ISSN 2074-272X

науково-практичний журнал

2025/2

Електротехніка і Електромеханіка

Electrical Engineering & Electromechanics

Електричні машини та апарати
Електротехнічні комплекси та системи
Промислова електроніка
Теоретична електротехніка
Техніка сильних електричних та магнітних полів, інженерна електрофізика
Електроізоляційна та кабельна техніка

Журнал включено до найвищої категорії «А» Переліку фахових видань України

З 2019 р. журнал індексується у Scopus

З 2015 р. журнал індексується у Web of Science Core Collection: Emerging Sources Citation Index

Electrical Engineering & Electromechanics

Scientific Journal was founded in 2002
Co-founders: National Technical University «Kharkiv Polytechnic Institute» (Kharkiv, Ukraine);
Anatolii Pidhornyi Institute of Power Machines and Systems of NAS of Ukraine (Kharkiv, Ukraine)

From no. 1 2019 Journal «Electrical Engineering & Electromechanics» is indexing in **Scopus**
and from no. 1 2015 Journal is indexing in **Web of Science Core Collection: Emerging Sources Citation Index (ESCI)**
Also included in DOAJ (Directory of Open Access Journals), in EBSCO's database, in ProQuest's databases – Advanced Technologies & Aerospace Database and Materials Science & Engineering Database, in Gale/Cengage Learning databases.

Editorial office address:
National Technical University «Kharkiv Polytechnic Institute», Kyrpychova Str., 2, Kharkiv, 61002, Ukraine
phone: +380 67 3594696, **e-mail:** a.m.grechko@gmail.com (**Grechko O.M.)**
ISSN (print) 2074-272X
ISSN (online) 2309-3404

Approved for printing on 28 February 2025. Format 60 × 90 ⅛. Paper – offset. Laser printing. Edition 50 copies.
Printed by Printing house «Madrid Ltd» (18, Gudanova Str., Kharkiv, 61024, Ukraine)

Electrical Engineering & Electromechanics
Scientific Journal

no. 2, 2025

Table of Contents

UDC 621.314 https://doi.org/10.20998/2074-272X.2025.2.01

Y. Lee

Online detection of phase resistance of switched reluctance motor by sinusoidal signal injection

Introduction. *Switched reluctance motors (SRMs) are widely used in various applications due to their simplicity, robustness, and cost-effectiveness. However, the performance of SRMs can be significantly influenced by variations in their phase resistance, especially under high current and saturated conditions. Accurate knowledge of this parameter is crucial for optimal control and efficient operation.* ***Problem.*** *During operation, SRM parameters, particularly phase resistance, can vary considerably. These variations pose challenges to control strategies that rely on precise parameter values, leading to potential inefficiencies and degraded performance. There is a need for an effective method to monitor and identify these changes in real-time.* ***Goal.*** *This paper aims to develop and validate a method for the online detection and identification of phase resistance in SRMs. The method should work under varying operational conditions without requiring additional hardware, thereby maintaining the system's simplicity and cost-effectiveness.* ***Methodology.*** *The proposed method injects a sinusoidal signal into the inactive phase of the SRM using Sinusoidal Pulse Width Modulation (SPWM) via the main converter. The phasor method is then applied to determine the impedance of the phase circuit, from which the phase resistance can be identified. This approach eliminates the need for extra circuits, making it an efficient solution.* ***Results.*** *Simulations were conducted to evaluate the proposed method. The results demonstrate that the method can accurately track the variation in phase resistance under different operational conditions, validating its effectiveness.* ***Originality.*** *The originality of this work lies in its innovative use of the phasor method combined with SPWM for online phase resistance detection in SRMs, without the need for additional hardware components.* ***Practical value.*** *This method provides a practical solution for real-time phase resistance identification in SRMs, enhancing the reliability and performance of control strategies in various industrial applications.* References 17, table 1, figures 6.
Key words: **parameter identification, signal injection, switched reluctance motor.**

Вступ. *Вентильні реактивні двигуни (SRMs) широко використовуються в різних сферах завдяки своїй простоті, надійності та економічній ефективності. Однак на продуктивність SRMs можуть суттєво впливати зміни їх фазового опору, особливо в умовах сильного струму та насичення. Точне знання цього параметра має вирішальне значення для оптимального управління та ефективної роботи.* ***Проблема***. *Під час роботи параметри SRM, зокрема фазовий опір, можуть значно змінюватися. Ці зміни створюють проблеми для стратегій управління, які покладаються на точні значення параметрів, що призводить до потенційної неефективності та погіршення продуктивності. Існує необхідність ефективного методу моніторингу та ідентифікації цих змін у режимі реального часу.* ***Метою*** *статті є розробка та перевірка методу онлайн-виявлення та ідентифікації фазового опору у SRMs. Метод повинен працювати в різних робочих умовах без необхідності використання додаткового обладнання, тим самим зберігаючи простоту та економічну ефективність системи.* ***Методологія***. *Пропонований метод вводить синусоїдальний сигнал у неактивну фазу SRM за допомогою синусоїдальної широтно-імпульсної модуляції (SPWM) через головний перетворювач. Потім застосовується метод векторів визначення імпедансу фазового кола, з якого можна визначити опір фази. Такий підхід усуває потребу у додаткових колах, що робить його ефективним рішенням.* ***Результати***. *Для оцінки запропонованого методу було здійснено моделювання. Результати показують, що метод може точно відслідковувати зміну опору фази у різних робочих умовах, підтверджуючи його ефективність.* ***Оригінальність*** *цієї роботи полягає в інноваційному використанні методу векторів у поєднанні з SPWM для визначення опору фази в режимі реального часу SRMs без необхідності використання додаткових апаратних компонентів.* ***Практична цінність***. *Цей метод забезпечує практичне рішення для визначення опору фази SRMs в реальному часі, підвищуючи надійність і продуктивність стратегій управління в різних промислових застосуваннях.* Бібл. 17, табл. 1, рис. 6.
Ключові слова: **ідентифікація параметрів, подача сигналу, вентильний реактивний двигун.**

Introduction. In recent years, the switched reluctance motor (SRM) has experienced significant development and has become increasingly popular due to its robust structure and low cost, making it appealing for both industrial and domestic applications [1–3]. However, during motor operation, key parameters such as phase inductance and phase resistance can vary significantly. Parameters measured at standstill may differ from those when the motor is running, necessitating real-time identification of these values to ensure optimal performance [4, 5].

A neural network-based method for SRM parameter identification was proposed in [6–12], utilizing a more precise circuit model that includes an extra RL branch connected in parallel to account for saturation and losses. This method, however, requires complex modeling and does not directly address the need for real-time resistance identification without additional hardware.

Modulation techniques, such as phase and amplitude modulation, have been employed to detect rotor position without using encoders or Hall sensors [13–17]. These techniques leverage phase inductance information but assume constant phase resistance, requiring additional circuitry such as signal generators, amplifiers, and resistors, which add bulk and complexity to the motor drive. While effective, these methods are not ideal for applications where compactness and cost are critical concerns.

Purpose of the work. This paper proposes a novel method for detecting variations in the phase resistance of SRMs in real time. Unlike previous approaches, our method does not require additional hardware; instead, it utilizes the existing main converter to inject a small sinusoidal signal during the negative inductance slope region of the unenergized phase. By adjusting the signal frequency to make the inductive reactance comparable to the phase resistance, this method enhances the sensitivity of resistance detection.

Proposed online detection method of phase resistance of SRM. The phase resistance of a SRM is typically measured when the motor is not in operation. This is done by connecting the phase terminals to a dedicated instrument. After obtaining the phase resistance, the winding is disconnected from the instrument and

reconnected to the main converter to drive the motor. Knowing the phase resistance is crucial for various applications, including calculating copper loss, determining flux linkage, and performing sensorless control. However, this offline measurement method cannot be applied while the motor is running. Moreover, the phase resistance may change significantly during operation, especially under high load conditions. Relying on the value measured at standstill may lead to inaccurate calculations, as the resistance might have varied. Therefore, it is essential to measure the phase resistance online.

To achieve online detection of the phase resistance, a low-amplitude sinusoidal voltage is injected into the inactive phase of the motor – meaning the phase that is not currently contributing to torque during the inductance falling region. The resulting small current in the inactive phase produces a minimal negative torque, which has negligible impact on the overall motor performance. Assuming that the self-inductance and resistance of the phase remain constant over a short period, the circuit model of a motor phase can be represented as a first-order RL circuit with an alternating voltage source, inductor, and resistor in series (Fig. 1).

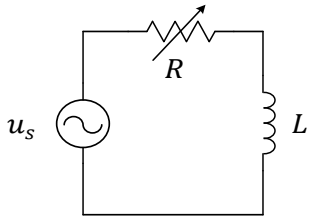

Fig. 1. One-phase model of SRM

The voltage equation for a single-phase circuit can be expressed as:

$$u(t) = Ri(t) + \mathrm{d}\psi/\mathrm{d}t\,, \tag{1}$$

where u is the phase voltage; R is the phase resistance; i is the phase current; ψ is the flux linkage. Under unsaturated conditions, the flux linkage can be expressed as:

$$\psi(t) = Li(t)\,, \tag{2}$$

where L is the phase self-inductance. Substituting (2) into (1), the voltage equation becomes:

$$u(t) = Ri(t) + L\frac{\mathrm{d}i}{\mathrm{d}t}\,. \tag{3}$$

If a sinusoidal voltage is applied, it can be described as:

$$u_s(t) = \sqrt{2}U_S\cos\left(2\pi\cdot f\cdot t + \varphi_{u_s}\right), \tag{4}$$

where U_s, f, φ_{us} are the RMS value, the frequency and the phase angle of u_s, respectively.

Since the voltage u_s is chosen as the reference, φ_{us} equals 0. It should be noted that, in practice, the actual voltage applied to the phase is a pulse width modulated voltage, whose effect is equivalent to that of the sinusoidal voltage described above. The resulting current in the circuit is expected to take the form:

$$i(t) = \sqrt{2}I\cos\left(2\pi\cdot f\cdot t + \varphi_i\right), \tag{5}$$

where I and φ_i are the RMS value and phase angle of i, respectively.

The magnitude of the circuit's impedance Z is given by:

$$|Z| = U_s/I = \sqrt{R^2 + X_L^2}\,, \tag{6}$$

where $X_L = 2\pi f L$ is the inductive reactance.

The phase resistance R can be determined as:

$$R = \sqrt{\frac{U_s^2}{I^2} - X_L^2}\,. \tag{7}$$

Alternatively, the resistance can also be calculated using the impedance angle φ as follows:

$$R = |Z|\cos\varphi\,, \tag{8}$$

where φ is the phase shift between the applied voltage and the resulting current.

It is important to note that the variable resistor in the circuit model (Fig. 1) indicates that the resistance may differ from the value measured at standstill, though it is assumed to be constant while solving the sinusoidal circuit. The response current in this time-invariant circuit will also take on a sinusoidal form.

As illustrated in Fig. 2, both the amplitude and angle of the impedance will change if the phase resistance varies during motor operation.

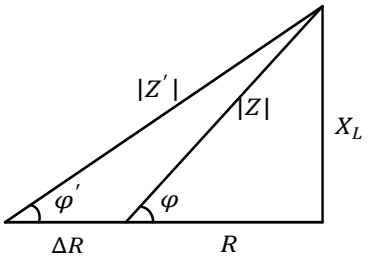

Fig. 2. Change in impedance due to variation in phase resistance

The phasor diagram of the circuit (Fig. 3) highlights that any change in phase resistance during motor operation will result in variations in the angle and amplitude of the response current vector.

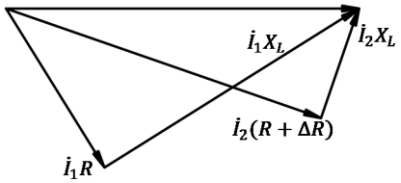

Fig. 3. Phasor diagram of the single-phase circuit

The sinusoidal voltage injection can be performed using the main converter. In this study, a full-bridge converter is employed to drive the SRM, as depicted in Fig. 4. This converter allows phase current to flow in both directions. The sinusoidal voltage is injected using Sinusoidal Pulse Width Modulation (SPWM) technique, where a bipolar triangle wave serves as the carrier wave and the desired sinusoidal voltage acts as the signal wave.

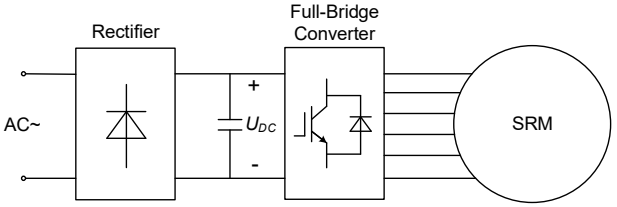

Fig. 4. SRM drive system utilizing a full-bridge converter

The selection of the sinusoidal voltage frequency is critical for the effectiveness of the proposed phase resistance detection method. The frequency must be high enough so that the phase self-inductance remains

constant, thereby validating the simplified circuit model shown in Fig. 1. However, the frequency should also be chosen such that the inductive reactance is comparable to the phase resistance. This balance ensures that any variation in phase resistance results in a noticeable change in the phase and amplitude of the response current, leading to improved sensitivity in detecting phase resistance changes.

Simulation results and discussion. To validate the effectiveness of the proposed online phase resistance detection method for a SRM, simulations were conducted using MATLAB/Simulink. The motor used in the simulation is an outer rotor type SRM, with key dimensions provided in Table 1.

Table 1
Outer rotor SRM parameters

Parameters	Value
Number of phases	3
Pole combination	6/4
Stator outer radius	51 mm
Stator inner radius	20 mm
Stator yoke	15 mm
Stator pole arc	28°
Rotor outer radius	95 mm
Rotor inner radius	52 mm
Rotor yoke	15 mm
Rotor pole arc	32°
Stack length	50 mm
Turn number/pole	150

The motor operates at a low speed during the simulation. Once the tail current diminishes completely to zero, a 100 Hz SPWM voltage is injected into the phase during the negative inductance slope region. The reference signal for this injection is a 100 Hz sinusoidal wave with a RMS value of 5.55 V. Initially, the phase resistance is set at 2.56 Ω.

Before any change in resistance, the simulation results are depicted in Fig. 5. As expected in an inductive circuit, the response current lags behind the applied voltage. The current is small, with an RMS value around 1.15 A, producing only a negligible amount of negative torque. The rotor position is approximately 39°, where the inductance is around 6.5 mH. The resistance, calculated using (8), is found to be 2.57 Ω, which is within 1 % of the actual resistance value, demonstrating high accuracy.

When the phase resistance is doubled to 5.12 Ω, the simulation is repeated at the same rotor position of 39°. The results are shown in Fig. 6. Due to the unsaturated state of the circuit and the unchanged rotor position, the inductance remains constant at 6.5 mH. The impedance change is solely due to the increase in the resistive component. The figure reveals that the response current exhibits a smaller phase shift relative to the applied voltage and a reduced RMS value of approximately 0.85 A, compared to the previous simulation. This reduction in current amplitude indicates a change in phase resistance. The resistance calculated from (8) is 5.11 Ω, closely matching the actual resistance value.

These simulation results clearly demonstrate that the phase resistance information is effectively encoded in the sinusoidal response current. Consequently, the proposed method is capable of accurately extracting this information to detect and monitor variations in phase resistance in real-time.

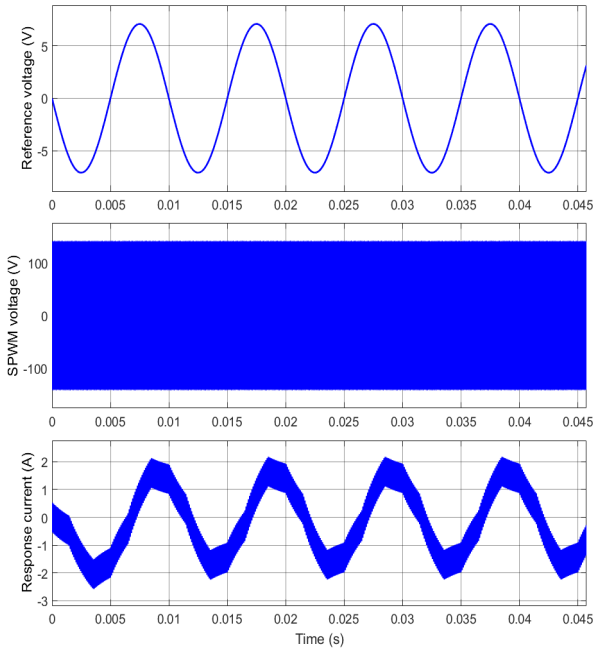

Fig. 5. Simulation results with the initial resistance

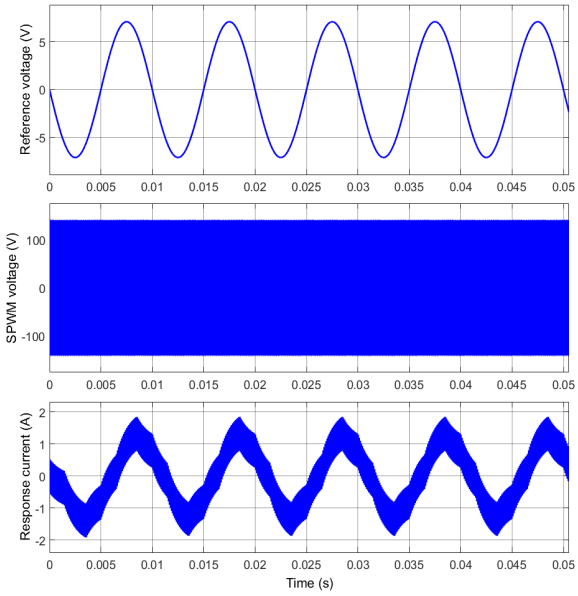

Fig. 6. Simulation results with the modified resistance

Conclusions. This paper presents a method for detecting phase resistance in switched reluctance motors (SRMs) using sinusoidal voltage injection via the main converter. Unlike conventional methods that require external instruments and can't monitor resistance changes during operation, this approach enables real-time detection, especially in high-current and saturated conditions.

By injecting a finely tuned sinusoidal-equivalent PWM voltage into the inactive phase, the method accurately identifies phase resistance through impedance or current analysis, without the need for additional circuitry.

Future prospects. Further research could focus on optimizing frequency tuning for greater detection accuracy under varying conditions and validating the method experimentally on physical SRM systems.

Additionally, integrating this detection method with advanced control strategies and expanding it to monitor other parameters like phase inductance could significantly enhance the performance and reliability of SRMs in industrial applications.

Acknowledgement. This work is supported by Seoul National University of Science and Technology.

Conflict of interest. The author declares no conflicts of interest.

REFERENCES

1. Fan J., Lee Y. Sensorless control of switched reluctance motor based on a simple flux linkage model. *Electrical Engineering & Electromechanics*, 2023, no. 3, pp. 36-39. doi: https://doi.org/10.20998/2074-272X.2023.3.05.

2. Quraan L.A., Saleh A.L., Szamel L. Indirect Instantaneous Torque Control for Switched Reluctance Motor Based on Improved Torque Sharing Function. *IEEE Access*, 2024, vol. 12, pp. 11810-11821. doi: https://doi.org/10.1109/ACCESS.2024.3355389.

3. Kumar P., Israyelu M., Sashidhar S. A Simple Four-Phase Switched Reluctance Motor Drive for Ceiling Fan Applications. *IEEE Access*, 2023, no. 11, pp. 7021-7030. doi: https://doi.org/10.1109/ACCESS.2023.3238068.

4. Fan J., Lee Y. Design Consideration to Achieve Wide-Speed-Range Operation in a Switched Reluctance Motor. *Canadian Journal of Electrical and Computer Engineering*, 2020, vol. 43, no. 4, pp. 290-294. doi: https://doi.org/10.1109/CJECE.2020.2978265.

5. Sree P.B., Bhavani N.P.G. Efficiency Improvement of Electrical Vehicles Using Novel Switched Reluctance Motor and Compared with Permanent Magnet Motor by Reducing Power Loss. *2023 6th International Conference on Contemporary Computing and Informatics (IC3I)*, 2023, pp. 1473-1477. doi: https://doi.org/10.1109/IC3I59117.2023.10398050.

6. Omar M., Bakr M., Emadi A. Switched Reluctance Motor Design Optimization: A Framework for Effective Machine Learning Algorithm Selection and Evaluation. *2024 IEEE Transportation Electrification Conference and Expo (ITEC)*, 2024, pp. 1-6. doi: https://doi.org/10.1109/ITEC60657.2024.10598839.

7. Omar M., Sayed E., Abdalmagid M., Bilgin B., Bakr M.H., Emadi A. Review of Machine Learning Applications to the Modeling and Design Optimization of Switched Reluctance Motors. *IEEE Access*, 2022, vol. 10, pp. 130444-130468. doi: https://doi.org/10.1109/ACCESS.2022.3229043.

8. Kandhasamy S. Machine learning based SRM control using FPGAs for torque ripple minimization. *2020 International Conference on Artificial Intelligence in Information and Communication (ICAIIC)*, 2020, pp. 675-680. doi: https://doi.org/10.1109/ICAIIC48513.2020.9065241.

9. Jha M.K., Seth N., Tyagi N., Khan S.A. SRM Torque Ripple Reduction Using Grey Wolf and Teaching and Learning Based optimization in Hysteresis Control. *2021 International Conference on Intelligent Technologies (CONIT)*, 2021, pp. 1-7. doi: https://doi.org/10.1109/CONIT51480.2021.9498374.

10. Matschek J., Bethge J., Findeisen R. Safe Machine-Learning-Supported Model Predictive Force and Motion Control in Robotics. *IEEE Transactions on Control Systems Technology*, 2023, vol. 31, no. 6, pp. 2380-2392. doi: https://doi.org/10.1109/TCST.2023.3262987.

11. Unluturk A., Aydogdu O. Machine Learning Based Self-Balancing and Motion Control of the Underactuated Mobile Inverted Pendulum With Variable Load. *IEEE Access*, 2022, vol. 10, pp. 104706-104718. doi: https://doi.org/10.1109/ACCESS.2022.3210540.

12. Kolb J., Hameyer K. Classification of Tolerances in Permanent Magnet Synchronous Machines With Machine Learning. *IEEE Transactions on Energy Conversion*, 2024, vol. 39, no. 2, pp. 831-838. doi: https://doi.org/10.1109/TEC.2023.3340337.

13. Ki Hong S., Lee Y. Optimizing Detection: Compact MobileNet Models for Precise Hall Sensor Fault Identification in BLDC Motor Drives. *IEEE Access*, 2024, vol. 12, pp. 77475-77485. doi: https://doi.org/10.1109/ACCESS.2024.3407766.

14. Mohanraj D., Aruldavid R., Verma R., Sathiyasekar K., Barnawi A.B., Chokkalingam B., Mihet-Popa L. A Review of BLDC Motor: State of Art, Advanced Control Techniques, and Applications. *IEEE Access*, 2022, vol. 10, pp. 54833-54869. doi: https://doi.org/10.1109/ACCESS.2022.3175011.

15. Zhang S., Wallscheid O., Porrmann M. Machine Learning for the Control and Monitoring of Electric Machine Drives: Advances and Trends. *IEEE Open Journal of Industry Applications*, 2023, vol. 4, pp. 188-214. doi: https://doi.org/10.1109/OJIA.2023.3284717.

16. Mousmi A., Abbou A., El Houm Y. Binary Diagnosis of Hall Effect Sensors in Brushless DC Motor Drives. *IEEE Transactions on Power Electronics*, 2020, vol. 35, no. 4, pp. 3859-3868. doi: https://doi.org/10.1109/TPEL.2019.2934794.

17. Huang Y., Zhao M., Zhang J., Lu M. The Hall Sensors Fault-Tolerant for PMSM Based on Switching Sensorless Control With PI Parameters Optimization. *IEEE Access*, 2022, vol. 10, pp. 114048-114059. doi: https://doi.org/10.1109/ACCESS.2022.3218325.

Received 28.08.2024
Accepted 09.10.2024
Published 02.03.2025

Yongkeun Lee[1]*, PhD, Professor,*
[1] Seoul National University of Science and Technology,
Seoul 01811, South Korea,
e-mail: yklee@seoultech.ac.kr (Corresponding Author)

How to cite this article:
Lee Y. Online detection of phase resistance of switched reluctance motor by sinusoidal signal injection. *Electrical Engineering & Electromechanics*, 2025, no. 2, pp. 3-6. doi: https://doi.org/10.20998/2074-272X.2025.2.01

UDC 621.313.33 https://doi.org/10.20998/2074-272X.2025.2.02

V.I. Milykh

Numerical-field analysis of differential leakage reactance of stator winding in three-phase induction motors

Introduction. *The differential leakage reactance (DLR) of the stator winding of three-phase induction motors (TIM) is considered. It is known that DLR is the sum of the self-induction resistances of the winding from all harmonics of its magnetic field, excluding the first one, and its analytical definition is too complicated. But this reactance is a mandatory design element, including for calculating a number of other parameters and characteristics of such motors.* ***Problem.*** *Because of this, in the current classical design methods, the DLR are determined by a simplified formula with the addition of a number of coefficients, tabular and graphical dependencies. As a result, not only the physical and mathematical meaning of DLR is lost, but even the accuracy of its calculation is difficult to assess.* ***Goal.*** *The purpose of the paper consists in the comparative verification of the classical design calculation of the DLR of the TIM stator winding by numerical-field analysis of the harmonic composition of the EMF of self-inductions in this winding and by the determination of the considered DLR on such a basis.* ***Methodology.*** *Harmonic analysis is performed by obtaining the angular and time discrete functions of the magnetic flux linkage (MFL) of the stator winding with their formation in two ways: single-position calculation of the magnetic field and conditional rotation of the phase zones of the winding, or multi-position calculations of the rotating magnetic field and determination of the MFL of stationary phase zones.* ***Results.*** *Computational analysis is performed for nine common variants of TIM, designed according to a single classical method with variation of their power and the number of poles.* ***Originality.*** *A comparison of the results of the classical and numerical-field calculations of the DLR using the FEMM program showed their large discrepancy, which is attributed to the indicated inadequacy of the first one, since the second option is devoid of the shortcomings of the first one due to the fact that it takes into account the dimensions of the TIM structures, the saturation of the magnetic circuit and the physical and mathematical essence of the parameters and values under consideration.* ***Practical value.*** *The presented method of numerical-field analysis and the obtained results of calculating the DLR of the TIM stator winding are recommended as a basis for improving the system of their design. At the same time, a similar approach can be applied to the DLR of the TIM rotor winding, but taking into account its features.* References 27, tables 13, figures 7.

Key words **induction motor, three-phase stator winding, differential leakage reactance, classical design, numerical-field calculations, magnetic flux linkage, harmonic analysis**

Вступ. *Розглядається диференціальний реактивний опір розсіювання (ДРОР) обмотки статора трифазних асинхронних двигунів (ТАД). Відомо, що ДРОР є сумою опорів самоіндукції обмотки від усіх гармонік її магнітного поля за виключенням першої і його аналітичне визначення є надто складним. Але цей опір є обов'язковим елементом проєктування, в тому числі для розрахунку низки інших параметрів та характеристик таких двигунів.* ***Проблема.*** *Через це в чинних класичних методиках проєктування ДРОР визначаються за спрощеною формулою з додаванням низки коефіцієнтів, табличних і графічних залежностей. У підсумку не тільки втрачається фізико-математичний сенс ДРОР, але навіть точність його розрахунку оцінити важко.* ***Мета*** *роботи полягає у порівняльній перевірці класичного проєктного розрахунку ДРОР обмотки статора ТАД шляхом чисельно-польового аналізу гармонічного складу ЕРС самоіндукцій в цій обмотці і визначення на такій основі ДРОР, що розглядається.* ***Методика.*** *Гармонічний аналіз відбувається за отриманням кутових та часових дискретних функцій магнітного потокозчеплення (МПЗ) обмотки статора з їхнім формуванням двома способами: однопозиційним розрахунком магнітного поля і умовним обертанням фазних зон обмотки, або багатопозиційними розрахунками обертового магнітного поля і визначенням МПЗ нерухомих фазних зон.* ***Результати.*** *Розрахунковий аналіз виконано для дев'яті поширених варіантів ТАД, запроєктованих за єдиною класичною методикою з варіюванням їхньої потужності та кількості полюсів.* ***Оригінальність.*** *Порівняння результатів класичного і чисельно-польового розрахунків ДРОР за програмою FEMM показало їхню велику розбіжність, що віднесено до зазначених умовностей і припущень першого, тому що другий варіант позбавлений недоліків першого завдяки тому, що він враховує розміри конструкцій ТАД, насичення магнітопроводу і фізико-математичну сутність параметрів і величин, що розглядаються.* ***Практична цінність.*** *Надана методика чисельно-польового аналізу і отримані результати розрахунку ДРОР обмотки статора ТАД рекомендуються як основа для удосконалення системи їхнього проєктування. При цьому аналогічний підхід можна застосувати і для ДРОР обмотки ротора ТАД, але з урахуванням її особливостей.* Бібл. 27, табл. 13, рис. 7.

Ключові слова: **асинхронний двигун, трифазна обмотка статора, диференціальний реактивний опір розсіювання, класичне проєктування, чисельно-польові розрахунки, магнітне потокозчеплення, гармонічний аналіз.**

Introduction. Three-phase induction motors (TIMs) are diverse and widespread in the technosphere around the world. Their improvement is always relevant and occurs due to various factors, including increasing the accuracy and efficiency of the design system.

Among the design parameters of the TIMs, the active and reactive resistances of its windings are mandatory and important. At the same time, calculations of the inductive resistances of their scattering are usually more complex and insufficiently adequate. This applies to the resistances of differential, slot and frontal scattering, for which specific magnetic conductivities are determined, but in classical design, for example in [1, 2], this is done using methods with fairly approximate formulas.

First of all, this is characteristic of the differential leakage reactance (DLR), which reflects the presence of higher harmonic components in the magnetic field in the gap between the stator and rotor cores. This reactance is determined by a simplified empirical formula that takes into account the minimum parameters of specific TIMs and does not affect the physical essence of the harmonic composition of the specified fields, but it is reinforced by a number of «opaque» coefficients, tabular and graphical dependencies. As a result, not only is the physical and mathematical meaning of DLR lost, but even the accuracy of its calculation is difficult to assess.

The problem of classical calculations of inductive leakage reactances is that their methods are based on simpler magnetic field models, oriented on the theory of magnetic circuits, which does not give sufficiently adequate results due to the complex geometry of the

electromagnetic system of TIMs and, accordingly, the structure of real magnetic fields.

In this sense, it is currently relevant to revise the conservative classical system of TIM design based on direct calculations of magnetic fields by numerical methods, for which there are appropriate software tools, for example, COMSOL Multiphysics, ANSYS Maxwell, FEMM, etc., which allow to avoid forced conventions and simplifications when determining the leakage reactances of TIM windings.

The use of various software complexes, as well as other experimental and computational studies of the characteristics and parameters of TIMs is reflected in a significant number of works, for example, in [3–21]. But, focusing on the implementation of a specific goal, each of them does not actually concern the analysis of the leakage reactances of TIM windings. This means that such works only use the data obtained during the classical design or creation of TIMs, but the analysis of these parameters does not occur. Therefore, the task of a detailed analysis of the methodology for calculating the leakage reactances of TIM windings remains insufficiently studied and is currently relevant.

This is especially true for the parameters of differential scattering of TIM windings, which are the least studied due to the complexity of the physical process of their formation, although the share of this scattering among its other components is usually predominant.

The goal of the work is to further develop the TIM design system through numerical-field calculation analysis of the differential leakage reactance of their stator winding, as well as a comparative check of the corresponding empirical formulas inherent in the methods of traditional design calculations.

Analysis of recent research. Despite the very long development and use of TIMs, research on their further study and improvement as such, as well as improving their operation in electric drive systems, continues on a fairly broad scale, for example, in works [3–10]. And these works to one degree or another affect the parameters of these motors.

Thus, in [3] for energy saving, an online estimation of TIM parameters using an extended Kalman filter is proposed. It is noted that to calculate the optimal value of the stator current for energy saving, its exact parameters are required, which are estimated in real time using an online estimator, and that this can ensure minimal power losses for the TIM drive.

The goal of the work [4] is to study the effectiveness of implementing fuzzy logic on FPGA programmable logic circuits for diagnosing failures of induction machines in case of phase asymmetry and their breaks. This is done on the basis of fuzzy logic and analysis of the motor stator current signals, its root-mean-square value.

In the article [5], a new method for diagnosing broken rotor bars in a lightly loaded induction machine in a stationary operation mode is provided. This method is used to solve the problem of using traditional methods, such as the Fourier transform signal processing algorithm, by analyzing the stator current envelope curve using discrete and continuous wavelet transform.

In [6], the development of a neural network model is presented, which allows generating a large database that can cover the maximum possible faults of the TIM stator. They take into account short circuits with large fluctuations in the machine load. The aim is also to automate the diagnostic algorithm using an artificial neural network classifier.

In [7], a comparative study of methods for taking into account the influence of loss processes in the stator steel of an asynchronous machine on the parameters of its operating mode was performed. This is done using mathematical modeling with the introduction of equivalent resistances connected in parallel to the equivalent circuit of the motor, as well as equivalent steel loss circuits.

The article [8] is devoted to the optimization of the design of an induction motor using multiparameter FEM methods. It is shown that the TIM parameters, including the types of rotor and stator slots, steel core sheets and rotor winding material, are optimized using the Rmxprt module in Maxwell.

In [9], the stages, methodology and means of complex design of electromechanical systems with induction motors are substantiated. A quantitative assessment of the possibilities of increasing their economic efficiency using complex design according to the criterion of maximum income is provided.

In [10], a flux linkage observer of an induction motor is considered, adaptive to variations in the active rotor resistance. Due to the redundant estimation of flux linkages introduced into the observer, under the conditions of persistence of excitation, the properties of global exponential stability of the estimation of the components of the flux linkage vectors and stator current and active rotor resistance are ensured.

The following cycle of works [11–21] mainly concerns the analysis of the active and reactive parameters of the stator winding, the use and improvement of TIM equivalent circuits, and operation with them.

In the work [11], the reactive (inductive) reactances of the scattering and active resistances of the TIM windings are investigated with the aim of further developing the TIM design system by means of numerical field calculation analysis of the active and reactive reactances of the TIM windings in the entire range of its slip change, and the calculation of the mechanical characteristics of the TIM to confirm the adequacy of the calculations of these resistances. The reactances of the TIM windings are determined by numerical calculations of the magnetic fields of scattering using the FEMM code, and in the core of the short-circuited rotor - with current displacement.

In the article [12], the magnetic fields and the corresponding magnetic conductivities of the slot scattering of the TIM stator winding are investigated for a comparative check of the analytical formulas from different classical design methods. The numerical field method shows that the classical design method can give both sufficiently accurate results and unacceptable errors in determining the magnetic conductivities of the slot scattering of the TIM.

In [13], it is emphasized that a deep understanding of the parameters of an induction machine is necessary for almost all program control methods to maintain high-quality dynamic and steady-state characteristics of the drive. This study presents a method for predicting the parameters of an induction machine during start-up without using any assumptions. The instantaneous waveforms of voltage and current recorded during direct start-up are used to estimate the parameters. In this way, all six main electrical parameters of induction machines can be independently determined.

In [14], a new simplified method for estimating the parameters of the equivalent T-circuit of induction motors is described, which is based solely on the manufacturer's data sheet and on the synergistic interaction of the numerical and analytical dimensionless approach using the Thevenin theorem. This provides accurate and stable results for a wide range of rotational speeds and power of induction motors.

In [15], the work is also devoted to estimating the parameters of the equivalent T-circuit. These parameters are necessary for many performance and planning studies involving these motors. For their evaluation, an iterative method is proposed that uses only motor nameplate data.

In [16] it is emphasized that for controlling the torque in high-performance operations in a wide speed range by vector control algorithms, the parameters of the equivalent circuit of an induction motor must be known precisely. The estimation method is based on information from the manufacturer's data and the principles of solving nonlinear equations obtained from the equivalent circuit of such a motor.

The article [17] is devoted to the identification of the parameters of an induction motor in a stopped state. A comprehensive identification procedure is analyzed, which describes a method for reliably determining the characteristics of the main flux saturation and transients when testing the parameters from the rotor side. The effect of the main flux saturation is studied based on the results of transient tests and the determined rotor parameters. The identification procedure is confirmed by experiments using specific induction motors.

How to design a TIM with the desired characteristics and how to implement high-performance control for a specific TIM has always been a hot topic for many researchers, as noted in [18]. Regardless of which control technology is used to achieve high-performance TIM drive, it depends on a deep understanding of the motor parametric characteristics and their accurate acquisition. An effective method for determining the parameters of the equivalent circuit for induction motors is proposed to improve the accuracy of the parameters by combining the non-rotor test with the double-load test and using this method to measure and analyze the parametric characteristics of TIM.

In [19], a study of the degree of unbalance and the differential magnetic leakage coefficient of electrical machines equipped with multiphase windings is presented. The analysis was carried out for 4800 combinations between slots/poles/phases/layers, considering the changes in the leakage factor for each condition and determining the optimal zone for minimizing the leakage. The results show that the leakage coefficient can be significantly reduced by using slightly asymmetrical windings.

In the article [20], an accurate and simple method for determining differential dissipation factors in multiphase AC electric machines with asymmetrical windings is provided. The method is based on the properties of Görges polygons, which are used to transform an infinite series expressing the differential dissipation factor into a finite sum in order to significantly simplify the calculations.

The work [21] introduces the estimation of TIM parameters based on a differential evolution algorithm aimed at estimating its electrical and mechanical parameters. A comparative study of the results using three different input signals is carried out. Such an algorithm is able to estimate the parameters of the equivalent electrical circuit, such as stator and rotor resistances and leakage inductances, magnetizing inductance, as well as mechanical parameters, such as the moment of inertia and the friction coefficient.

Object of study. To generalize the research of DLR, they are performed for a number of TIM variants, which have in common the nominal phase voltage U_{sN} = 220 V and frequency f_s = 50 Hz; accordingly, the number of phases m_s = 3.

The basic one is a four-pole TIM with nominal power P_N = 7.5 kW, which is interesting in that it is a test object in the design methodology [1], which is still widespread at enterprises and Universities of the corresponding profile.

A total of nine similarly designed TIM variants with variable power of 4; 7.5 and 11 kW are considered, each of which is considered with the number of pole pairs p equal to 1, 2 and 3.

Motors with such parameters are quite common in modern production of TIM of general industrial execution [22, 23]. Thus, the nine adopted variants will allow us to sufficiently fully demonstrate the results of calculations using the numerical field method adopted here and compare them with the results using the classical method.

The main design parameters of the selected TIM variants are given in Table 1. They were obtained using the classical method [1], which was converted into an author's Lua script included in a single software package based on the FEMM code [24]. This script was tested on the specified basic TIM variant, which eliminates design errors of various origins.

Table 1

The most important design data of TIN

P_N	p	h	d_s	l_s	δ	q_s	Q_s	N_s	Q_r	I_{sN}
kW	–	mm	mm	mm	mm	–	–	–	–	A
4	1	100	96	110	0,45	4	24	132	19	7,92
	2	100	109	145	0,30	3	36	144	28	8,74
	3	112	134	140	0,30	3	54	171	51	9,29
7,5	1	112	109	140	0,50	4	24	88	19	15,42
	2	132	147	120	0,35	3	36	126	34	15,31
	3	132	158	155	0,35	3	54	135	51	15,94
11	1	132	129	135	0,60	4	24	76	19	22,23
	2	132	147	165	0,35	3	36	90	34	22,26
	3	160	192	135	0,40	3	54	126	51	22,85

Table 1 indicates the TIM parameters: h – height of the rotation axis, d_s, l_s – inner diameter of the stator core bore and its axial length; δ – air gap; q_s – number of slots per pole and stator phase; N_s – number of consecutive turns in the phase winding; Q_s, Q_r – number of stator and rotor slots; I_{sN} – nominal stator phase current.

The general layout of the TIM is given in Fig. 1.

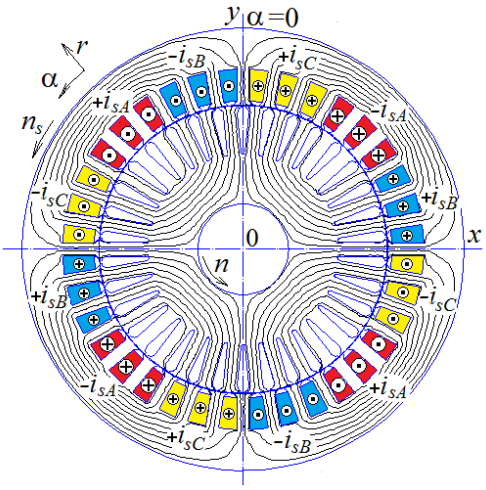

Fig. 1. The electromagnetic system of the TIM with the distribution of currents in its windings and the pattern of the magnetic field lines of the stator winding

The stator winding is single-layer, diametrical, which is typical for TIMs of the specified powers, the rotor winding is short-circuited, cast from aluminum alloy. This TIM uses common shapes of stator and rotor slots of general industrial TIMs [1, 2, 22, 23], which are shown in Fig. 1.

Design methodology for determining the differential inductive reactance of the stator winding of the TIM. For the transparency of the research performed, the classical methodology for calculating the DLR according to [1] and the results obtained by it are first given.

Differential scattering magnetic conductivity coefficient

$$\lambda_{sd} = 0{,}9\frac{(\tau_s \cdot K_{Ws})^2 \cdot K_{r\,dm} \cdot K_{ns} \cdot K_{dif\,s}}{\delta \cdot K_C}, \qquad (1)$$

where $K_{ns} = 1 - \dfrac{0{,}033 \cdot b_{s1}^2}{\tau_s \cdot \delta}$ is the coefficient that takes into account the effect of opening the stator slots; b_{s1} is the slot width of its slots; τ_s is the stator tooth pitch; $K_{dif\,s}$ is the stator differential dissipation coefficient, equal to the ratio of the total EMF from the higher harmonics of the stator magnetic field to the EMF from the first harmonic, determined by Table 2; $K_{r\,dm}$ is the damping reaction coefficient of currents induced in the short-circuited rotor winding by the higher harmonics of the stator magnetic field, determined by Table 3 for the given TIM variants; K_{Ws} is the stator winding coefficient; K_c is the air gap coefficient.

Table 2

Determination of the stator differential dissipation coefficient

q_s	2	3	4	5	6
$K_{dif\,s}$	0,0285	0,0141	0,0089	0,0065	0,0052

Table 3

Determination of the damping reaction coefficient of rotor winding currents (fragment of the general table)

q_s	Values $K_{r\,dm}$ at Q_r / p				
	10	15	20	25	30
3	0,98 / 0,92	0,93 / 0,87	0,88 / 0,84	0,85 / 0,78	–
4	–	0,90 / 0,81	0,84 / 0,77	0,8 / 0,75	0,77 / 0,72
Value: in the numerator – with bevel of the rotor slots, in the denominator– with no bevel.					

Data for (1) for all TIM variants according to Table 1 are collected in Table 4.

The intrinsic conductivity coefficient of differential scattering λ_{sd} of the stator winding together with other similar values are given in Table 5, where it is indicated: λ_{sn}, λ_{sfh} – magnetic conductivity coefficients of slot and frontal scattering; $\lambda_{\sigma s}$ – total scattering coefficient; R_s, $X_{\sigma s}$ – total active and reactive resistances of the stator winding in the nominal operating mode of the TIM, and also X_{sd} – reactive resistance of differential scattering.

Table 4

Data for design calculation of the coefficient of magnetic conductivity of differential scattering of TIM

P_N	p	τ_s	b_{s1}	K_c	K_{Ws}	$K_{r\,dm}$	$K_{n\,s}$	K_{dif}
kW	–	mm	mm	–	–	–	–	–
4	1	12,6	3,0	1,204	0,958	0,852	0,95	0,0089
	2	9,5	3,0	1,349	0,960	0,940	0,90	0,0141
	3	7,8	3,2	1,521	0,960	0,910	0,86	0,0141
7,5	1	14,3	3,2	1,179	0,958	0,852	0,95	0,0089
	2	12,8	3,5	1,283	0,960	0,910	0,91	0,0141
	3	9,2	3,5	1,433	0,960	0,910	0,88	0,0141
11	1	16,9	3,5	1,150	0,958	0,852	0,96	0,0089
	2	12,8	3,5	1,283	0,960	0,910	0,91	0,0141
	3	11,2	3,8	1,360	0,960	0,910	0,89	0,0141

Table 5

Calculated design resistances of TIM

P_N	p	λ_{sn}	λ_{sd}	λ_{sfh}	$\lambda_{\sigma s}$	R_s	X_{sd}	$X_{\sigma s}$
kW	–	p.u.	p.u.	p.u.	p.u.	Ω	Ω	Ω
4	1	1,261	1,729	1,805	4,794	1,771	0,654	1,815
	2	1,377	2,200	0,704	4,281	1,842	0,871	1,695
	3	1,521	1,215	0,676	3,413	2,103	0,437	1,226
7,5	1	1,257	2,060	1,575	4,892	0,744	0,441	1,047
	2	1,365	3,55	1,089	6,014	0,834	0,893	1,508
	3	1,532	1,573	0,704	3,809	0,941	0,390	0,945
11	1	1,254	2,487	1,884	5,625	0,452	0,383	0,866
	2	1,355	3,559	0,789	5,704	0,487	0,626	1,004
	3	1,653	2,180	0,958	4,791	0,673	0,410	0,901

Note that the relative value of the differential scattering conductivity coefficient λ_{sd} in $\lambda_{\sigma s}$ is a fraction within 0.361–0.624, which shows a high specific weight of this type of scattering against the background of its other types.

The inductive resistance of the scattering of the phase winding of the stator is calculated by the well-known formula [1]:

$$X_{\sigma s} = 1{,}58 \cdot \frac{f_s \cdot l_s \cdot N_s^2 \cdot \lambda_{\sigma s}}{p \cdot q_s \cdot 10^8}, \qquad (2)$$

and the differential leakage reactance X_{sd} – according to a similar formula when replacing $\lambda_{\sigma s}$ with λ_{sd}.

The provision in Table 5 of the active resistance R_s of the stator winding along with its total reactive reactance $X_{\sigma s}$ indicates their proportionality and importance of both in calculating important operational parameters and characteristics of TIMs and their operating modes [1, 2].

Numerical field calculations of the parameters of differential scattering of the stator winding of the TIM. The physically transparent path to the DLR lies through the direct calculation of the harmonic composition of the EMF of the stator winding, which are determined directly through the time functions of its own magnetic flux linkage (MFL) [25]. All this can be done in the most reliable form on the basis of numerical calculations of the corresponding magnetic fields of the stator winding itself.

These magnetic fields in the TIM are calculated in the popular free software package FEMM [24]. Given the multivariate complex calculations that include the design of the TIM, the construction of its physical and geometric models in the FEMM software environment, control of magnetic field calculations, determination of the time functions of the MFL and EMF and their harmonic analysis, all of them were automated. For this, following the example in [26] and other works of the author, a single script was created in the algorithmic language Lua, integrated into the FEMM code.

The FEMM code solves a large system of algebraic equations, which are formed on the basis of the Finite Element Method and a differential equation describing the magnetic field in the cross section of the TIM electromagnetic system, namely [24]:

$$\nabla\times\left[\frac{1}{\mu(B)}\nabla\times(\vec{k}A_z)\right]=\vec{k}J_z\,, \qquad (3)$$

where J_z, A_z are the axial components of the current density vectors and the magnetic vector potential (MVP); μ is the magnetic permeability depending on the magnetic flux density B; $\vec{k}$ is the unit vector along the axial axis z.

To limit the TIM calculation zone, which is given in Fig. 1, the Dirichlet boundary condition is set on the outer surface of the stator core for the MVP, i.e. $A_z = 0$.

A feature of this study is that to determine the differential inductive resistance of the stator winding, the basis is the calculation of the magnetic field of this winding in the presence of a symmetrical three-phase system of phase currents in it

$$\begin{aligned} i_{sA} &= I_{ms}\cos(\omega t)\,; \\ i_{sB} &= I_{ms}\cos(\omega t-\tfrac{2}{3}\pi)\,; \\ i_{sC} &= I_{ms}\cos(\omega t+\tfrac{2}{3}\pi)\,, \end{aligned} \qquad (4)$$

where $I_{ms}=\sqrt{2}\cdot I_s$ is the amplitude of the currents; I_s, $\omega = 2\pi f_s$ are their effective value and angular frequency; t is time.

When forming the current system (4) in specific calculations of magnetic fields, the question arises of choosing the calculated effective value of the current I_s.

The guideline for the calculations is that the saturation of the magnetic system of the TIM should be at the same level as in its nominal operating mode. Accordingly, for the stator winding, the value of the current of the idealized idle mode (IIM) is taken as a first approximation, which provides this condition. Naturally, there are no currents in the rotor winding in this mode.

The model in Fig. 1 shows the accepted distribution of the phase zones of the stator winding, and the values of the phase currents in them are given by (4) for specific moments of time. So at $t = 0$ we have the corresponding instantaneous values of the currents: is $i_{sA}=I_{ms}$; $i_{sB}=i_{sC}= -0.5I_{ms}$, and their directions at the specified time are also indicated.

The conditional distribution of currents in the slots of the stator winding is shown in Fig. 2 as a discrete function in the angular coordinate α, which is indicated in Fig. 1, and in the pole steps τ_p. The points that reflect the currents in the slots are meaningful, and the connecting lines are drawn for clarity of the current structure.

For the FEMM code, the numerical solution of equation (1) by the Finite Element Method is a trivial problem. As a result, in the cross section of the TIM, the distribution of the MVP is obtained, which in Fig. 1 gives a picture of the magnetic field lines in the idealized idle mode. Here and further, current illustrations are provided on the example of the adopted basic TIM model.

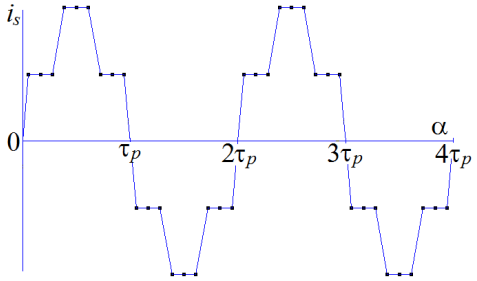

Fig. 2. Angular discrete distribution of currents is of the stator winding of the TIM along its slots on the scan of the cylindrical surface in the gap

The next step of the calculations is to determine the magnetic flux linkage (MFL) of the stator phase winding, as which, as usual, the phase winding A with current i_{sA} is taken. For the MFL in the FEMM code and the Lua script there are corresponding procedures. But what is needed is not just one value of the MFL, but its angular, and then the time function.

For this, there are two ways of calculations: fast and long-term, which we will consider in turn.

A fast method for forming time functions of the MFL and EMF is appropriate at the initial stage of numerical field studies of the DLR.

In this case, the angular function of the MFL is first obtained after a one-time calculation of the magnetic field at $t = 0$, the picture of which is already shown in Fig. 1 and corresponds to a fixed distribution of the MVP.

Specifically, according to the distribution of the MVP in the cross section of the TIM, the values of the MFL of the phase winding A are «collected» with the alternate selection of the «mask» of the phase zone with its movement in the angular direction along the slot structure of the stator.

Figure 3 shows the sequence of such actions for moving the «mask» within two pole steps, which corresponds to the period of the angular function of the MFL.

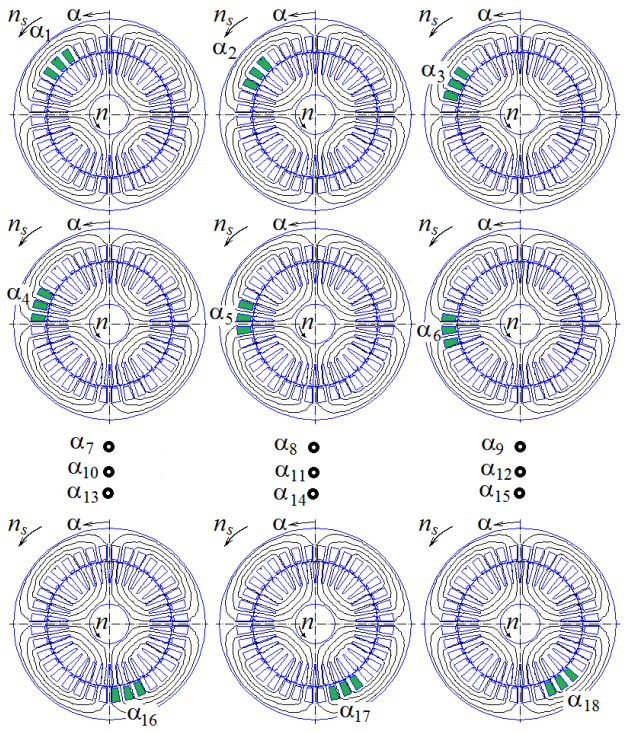

Fig. 3. The process of moving the «mask» of the phase zone of the stator winding to collect the MFL within the period of its angular function against the background of the calculated magnetic field

In each selected position, the Lua commands Ak=mo_blockintegral(1) and Sk=mo_blockintegral(5) read the surface integral of the MVP and the area of the selected block of rods, which makes it possible to determine the MFL of the conditional phase zone with number k:

$$\Psi_k = N_s A_k / S_k. \quad (5)$$

Thus, a discrete angular function of the MFL appears

$$\Psi_k(\alpha_k); \quad \alpha_k = (k-1)\tau_s; \quad k = 1, 2, 3, \ldots K, \quad (6)$$

where k is the counter of the positions of the conditionally movable «mask» of the phase zone; $K=Q_s/p$ is the number of such positions within two pole steps τ_p, which is the period T of the function (6); $\tau_s=360°/Q_s$ is the stator tooth step.

The resulting numerical array of the MFL is given in Table 6.

Table 6

Angular discrete function of the MFL Ψ_k of phase zones of phase winding A in 18 angular positions, Wb

k	1	2	3	4	5	6
Ψ_k	0,4858	0,4555	0,3708	0,2418	0,0840	–0,0840
k	7	8	9	10	11	12
Ψ_k	–0,2418	–0,3707	–0,4554	–0,4858	–0,4512	–0,3644
k	13	14	15	16	17	18
Ψ_k	–0,2366	–0,0819	0,0819	0,2366	0,3644	0,4512

The angular function at two pole steps, i.e. at its period (Table 6), is in principle sufficient to give an idea of its essence, but for the first attempt similar actions were performed at two more pole steps and the result was completely repeated. The resulting discrete function Ψ is shown in Fig. 4.

The angular discrete function of the $\Psi_k(\alpha_k)$ of the phase zones according to Table 6 is transformed into a similar function for the phase winding A entirely at its period:

$$\Psi_{s,k} = \Psi_k(\alpha_k) - \Psi_{k+K/2}(\alpha_k + \tau_p); \; k = 1, 2, 3, \ldots K. \quad (7)$$

Here it is taken into account that the winding branches are formed by conductors in phase zones with different current directions, located through the pole step τp. In addition, the averaging of the MFL values of the phase zones located through two pole steps is obtained, due to which instead of the function Ψ in Fig. 4 over two periods, the averaged MFL function Ψ_s over one period within two pole steps is obtained. This function is illustrated in the same Fig. 4.

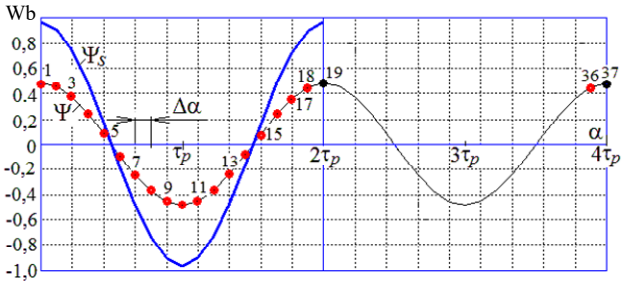

Fig. 4. Angular function of the MFL phase zones of half of the phase winding – Ψ and the phase winding in full – Ψ_s

It turned out that the angular function of the MFL is close to the cosine, as well as the time functions of the phase currents (4), but it is fundamentally different from the angular function of the current distribution in the slots (Fig. 2). However, in the theory of TIM, based on the step function of the stator currents is(α), it is customary to form similar functions of the distribution of the magnetomotive force (MMF) in the gap, then – of the magnetic induction and magnetic fluxes. And all this is laid down as the basis for the harmonic analysis of magnetic and electrical quantities, including – the EMF in the phase windings of the stator.

But the inadequacy of this approach is shown in [27] on the example of a three-phase stator winding of a turbogenerator. This is confirmed by the practically harmonic function of the MFL (Fig. 4), from which there is only one step left to a similar, but time, EMF function.

The function Ψ_s (7) is periodic, therefore it is subject to expansion into a harmonic Fourier series on its period in two pole steps (see Fig. 4), on which the MFL is calculated at K points (their specific number in this TIM is 18, and point 19 is already included in the next period and repeats point 1).

The expansion begins with the determination of the sine and cosine amplitudes of the harmonic components:

$$s_\nu = \frac{2}{K}\sum_{k=1}^{K}\Psi_k \sin(\nu\alpha_k); \quad c_\nu = \frac{2}{K}\sum_{k=1}^{K}\Psi_k \cos(\nu\alpha_k), \quad (8)$$

where ν is the number of the current harmonic; k is the number of the angular position in Fig. 3, 4; α_k is its angular coordinate.

It is known from mathematical foundations that the maximum number of harmonics allowed is $N_g = K/2$.

Considering that cosine functions (4) are adopted for the stator winding currents, then for the MFL, the harmonic series of cosine functions is also determined by the coefficients (8):

$$\Psi = \sum_{v=1,3,5...}^{N_g} \Psi_{mv} \cos(v\alpha + \gamma_{\psi v}), \qquad (9)$$

where this series for each harmonic includes the following amplitude and argument (initial phase):

$$\Psi_{mv} = \sqrt{s_v^2 + c_v^2}\ ; \quad \gamma_{\psi v} = -\text{arctg}\frac{s_v}{c_v}. \qquad (10)$$

The angular function (9) is converted into a time function by the relation $\alpha=\Omega_s t$, where $\Omega_s=\omega/p$ is the angular velocity of the rotating magnetic field of the TIM. As a result, for the MFL, a harmonic time function is obtained, which corresponds to the stationary phase winding *A–A*:

$$\Psi = \sum_{v=1,3,5...}^{N_g} \Psi_{mv} \cos(v\omega t + \gamma_{\psi v}). \qquad (11)$$

Note that in (9) the quantities $v\alpha$ and $\gamma_{\psi v}$ are measured in angular radians or degrees, and in (11) the quantities $v\omega t$ and $\gamma_{\psi v}$ are measured in electrical radians or degrees, taking into account the known transition of geometric angles α into electrical α_{el}, i.e. $\alpha_{el}=p\alpha$.

From the MFL function (11) based on the law of electromagnetic induction according to the general expression $e = -d\Psi/dt$, a transition is made to the harmonic time function of the EMF of the stator phase winding:

$$e_s = \sum_{v=1,3,5...}^{N_g} v\omega\Psi_{mv} \cos\left(v\omega t + \gamma_{\psi v} - \pi/2\right). \qquad (12)$$

In this formula, the amplitude of the EMF of the *v*-th harmonic is extracted

$$E_{mv}=v\omega\,\Psi_{mv} \qquad (13)$$

and its corresponding initial phase

$$\gamma_{ev} = \gamma_{\psi v} - \pi/2. \qquad (14)$$

Also, according to the known relationship for a sinusoidal function, the effective value of the EMF of the *v*-th harmonic is obtained through the amplitude, namely:

$$E_{sv} = \sqrt{2}\pi f_s v\Psi_{mv}, \qquad (15)$$

where it is taken into account that the angular frequency $\omega=2\pi f_s$; f_s is the frequency of electromagnetic quantities in the TIM.

The angular functions (6), (7) in Table 6 and Fig. 4, respectively, have a semi-periodic asymmetry:

$$\Psi_{s,k}(\alpha_k) = -\Psi_{s,k}(\alpha_k + \tau_p);\ k = 1, 2, 3, ...K, \qquad (16)$$

therefore, the harmonic series (9), (11), (12) contain only odd harmonics.

According to the provided method in the form of formulas (5)–(15), a corresponding software implementation of the formation and expansion of the periodic MFL function into a harmonic Fourier series and obtaining a similar EMF function was made on the Lua script.

Determination of the magnetizing current of the stator winding. As noted, the magnetic field calculations are performed in the IIM under the condition of saturation of the magnetic core equivalent to the nominal mode. For this, the search for the corresponding current is introduced into the calculation structure after the design of the TIM. This occurs iteratively provided that the nominal voltage of the stator winding U_{sN} is reached.

The initial current value for the first iteration is the design value of the magnetizing component of the stator winding current I_{so}, which is equal to 5.65 A.

After calculating the magnetic field, the time function of the MFL (11) and then the EMF (12) are determined using the above method, for which the first harmonic is isolated and used, namely, for the EMF – its effective value E_{s1} (15) and the initial phase γ_{e1} (14).

This is enough to determine the phase voltage complex in symbolic form according to the voltage balance equation in the stator phase winding circuit.

$$\underline{U}_s = -\underline{E}_{s1} + \underline{U}_{Rs} + \underline{U}_{s\sigma dif} + \underline{U}_{s\sigma fh}, \qquad (17)$$

where the complexes are applied: EMF $\underline{E}_{s1} = E_1 e^{j\gamma_{e1}}$; voltage drop across the active resistance of the stator winding $\underline{U}_{Rs} = R_s\underline{I}_{so}$ and on the inductive resistances of its differential $\underline{U}_{s\sigma dif} = jX_{sd}\underline{I}_{so}$ and frontal $\underline{U}_{s\sigma fh} = jX_{sfh}\underline{I}_{so}$ scattering (the inductive resistance of the slot scattering is already taken into account in the EMF $\underline{E}_{s1}$ due to the definition of the full MFL of the stator winding (5) within its active part along the length of the TIM cores); the stator winding current complex has the form $\underline{I}_{so}=I_{so}$ due to the fact that a zero initial phase is assumed for it.

After determining the voltage at the current iteration, the magnetizing current at the next iteration is corrected by linear interpolation, and everything is repeated until the voltage deviation dU_s from its nominal value is reduced to the permissible level. The course of the iterative process is illustrated in Table 7, where n_i is the iteration number.

Table 7

Changes in magnetizing current in the iterative process of bringing the voltage to the nominal value

n_i	I_{so}, A	U_s, V	dU_s, V
0	5,65	240,9	20,86
1	5,16	224	4,01
2	5,05	221,2	1,25
3	4,99	219,9	–0,06
4	4,99	220	0

In this example, it is clear that at the design value of the magnetizing current, the voltage deviates quite significantly from the nominal, which is a consequence of the use of magnetic calculation based on the theory of magnetic circuits in the design. But the iterative process showed that to operate with the nominal voltage, and therefore with the corresponding saturation of the TIM magnetic core, the magnetizing current should be 4.99 A. This is the value of I_{so} that is used for further calculations of the test TIM in the IIM and determining its DLR.

As a result of further calculations and harmonic analysis of the angular functions of the MFL and EMF on the period, the following calculated data are obtained: amplitude and initial phase of the first harmonic of the MFL Ψ_{m1}= 0.9640 Wb; $\gamma_{\psi 1}$=0; effective value and initial

phase of the same harmonic of the EMF E_{s1}= 214.1 V; γ_{e1}= –90°.

The harmonic composition of these quantities in relative units (p.u. is given in Table 8 (the value of their first harmonics is taken as the basis), and the allowed number of harmonics N_g was 9.

Table 8

Harmonics composition of MFL and EMF

ν	–	1	3	5	7	9
$\Psi_{m\nu}$	p.u.	1,000	0,0047	0,0017	0,0010	0,0009
$E_{m\nu}$	p.u.	1,000	0,0141	0,0087	0,0070	0,0078
$E_{s\nu}$	V	214,1	3,02	1,87	1,51	1,68

In general, the harmonic composition is estimated by the distortion factor (using the example of EMF)

$$d_{distE} = \sqrt{\sum_{\nu=1}^{N_g} E_{m\nu}^2} \Big/ E_{m1}\,, \qquad (18)$$

which for the functions of MFL and EMF received the corresponding values: $d_{distΨ}$= 1.0000; d_{distE}=1.0002.

Taking into account the entire determined harmonic composition, the equivalent effective value of the phase EMF of the stator winding is found

$$E_s = \sqrt{\sum_{\nu=1,3,5...}^{N_g} E_{s\nu}^2}\,, \qquad (19)$$

as well as differential EMF, which consists only of higher harmonics,

$$E_{sdif} = \sqrt{\sum_{\nu=3,5...}^{N_g} E_{s\nu}^2}\,. \qquad (20)$$

The last EMF allows to determine the desired differential inductive resistance of the stator phase winding:

$$X_{sdif} = \frac{E_{sdif}}{I_{so}}. \qquad (21)$$

Calculations using (19)–(21) gave the following results: E_s= 214.2 V; E_{sdif} = 4.21 V; X_{sdif} = 0.84 Ω.

If we compare the obtained differential inductive resistance X_{sdif} = 0.84 Ω with its design value X_{sd} = 0.893 from Table 5, we can think about the closeness of the two calculation options.

But this is until similar calculations have been performed for all planned TIM options (Table 1): all the results obtained are given in Table 9, where for different options, according to their data, the number of available harmonics N_g was 9 or 11.

Table 9

Differential parameters of TIM obtained by a single numerical-field calculation of the magnetic field

P_N	p	I_{so}	Ψ_{m1}	E_{s1}	E_s	E_{sdif}	X_{sdif}
kW	–	A	Wb	V	V	V	Ω
4	1	2,56	0,9747	216,5	216,5	1,99	0,78
	2	3,84	0,9700	215,5	215,7	10,16	2,65
	3	6,34	0,9691	215,3	215,8	14,54	2,29
7,5	1	4,39	0,9749	216,6	216,6	1,99	0,45
	2	4,99	0,9640	214,1	214,2	4,21	0,84
	3	7,99	0,9694	215,3	215,6	10,01	1,25
11	1	5,95	0,9723	216,0	216,0	2,05	0,34
	2	7,17	0,9655	214,5	214,5	4,25	0,59
	3	9,06	0,9658	214,6	214,6	6,33	0,70

In relation to the data in Table 9, we note that the distortion coefficients are within the limits: $d_{distΨ}$=1.0000–1.0002; d_{distE}=1.0000–1.0023, i.e. the corresponding angular functions of the MFL and EMF, as in Fig. 4, are close to their first harmonics. This is also evidenced by the closeness of the values of E_{s1} and E_s.

As for the main quantity considered here, i.e. the differential leakage reactance, its values X_{sd} та X_{sdif}, obtained by different methods in Table 5 and 9, can be both close and significantly diverge.

This indicates the absence of strict determinism of the empirical formula (1) and a number of coefficients included in it.

At the same time, the numerical-field method does not have such drawbacks, because it has fewer weighty conventions and assumptions. But in the considered form, it also has a serious drawback, namely – a small number of harmonics, which is associated with a limited number of calculation positions (see Fig. 3) due to the available number of stator slots at two pole steps, that is, at the period of the MFL and EMF functions.

To solve the identified problem, it is necessary to involve a more accurate calculation method. And as such, the numerical-field method is again adopted, but one that allows you to involve the desired number of calculation positions and, accordingly, the number of harmonics in the calculations.

The long-term method of forming the time functions of the MFL and EMF is appropriate at the final stage of numerical field studies of the DLR.

In this case, the time function of the MFL of the stator winding is considered directly without its previous angular function.

To obtain the time function of the MFL, multi-position calculations of the magnetic field are performed alternately, as shown in [25, 27], for a time series with a step Δt:

$$t_k = \Delta t\,(k–1); \quad k = 1,2,...,K, \qquad (22)$$

where K is the number of positions that allows forming a time function at a given time interval.

Substituting these values of t_k into (4), we obtain the corresponding changes in the stator phase currents is and their wave, which moves in angular $\Delta\alpha=\Omega_s\cdot\Delta t$, where $\Omega_s=2\pi f_s/p$ is the already mentioned angular velocity of the rotating magnetic field.

The calculation of the stator currents (4) at given moments of time (22), as well as the calculation and collection of the MFL values (5) were performed automatically during the operation of the FEMM code using the already mentioned program in the Lua language.

In this case, the magnetic field rotates, and the phase zones for collecting MFL values are stationary, which is partially shown in Fig. 5.

As before, the phase zones were selected for phase winding A (see Fig. 1), but in the order that explains Fig. 6.

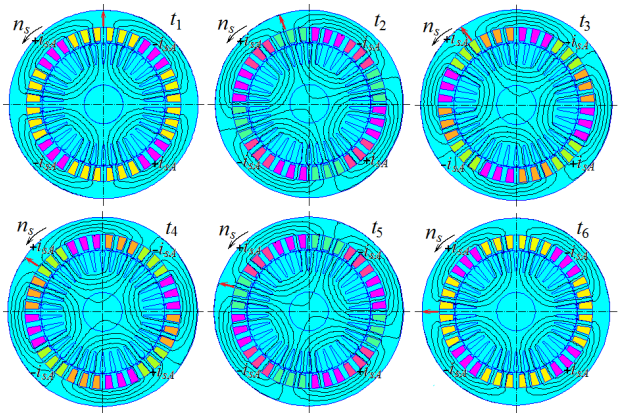

Fig. 5. Pictures of the rotating magnetic field of the stator winding at fixed moments of time:
t_1=0; t_2=0.1T; t_3=0.2T; t_4=0.3T; t_5=0.4T; t_6=0.5T

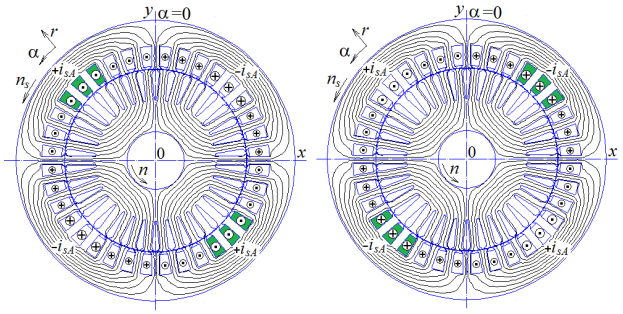

Fig. 6. Selection of phase zones of the stator winding to obtain the MFL of the stator phase winding

First, phase zones with a conditional positive current direction $+i_{sA}$ are distinguished and their MFL Ψ_{is+} is obtained, then phase zones with a conditional negative current direction $-i_{sA}$ are distinguished and their MFL Ψ_{is-}. is obtained.

As a result, a time discrete function of the MFL of the phase winding of the TIM stator at specific moments of time with a change in their number k is obtained:

$$\Psi_{s,k} = \Psi_{is+,k} - \Psi_{is-,k}\ ;\ t_k;\ \ k = 1, 2, 3, ...K. \qquad (23)$$

Then everything happens as in the previous calculation method, that is, according to (10)–(15), starting with the harmonic expansion of the discrete time function (23) instead of the similar function (9).

It is determined that it is enough to step by step (22) pass one pole step of the TIM τ_p, which will correspond to half the period T of the time function of the MFL $\Psi(t)$ and the calculation zone (in degrees):

$$\alpha_z = 360° / 2p, \qquad (24)$$

and in the test four-pole TIM α_z = 90° specifically turns out.

To justify a sufficient number of calculated positions K, comparative calculations were performed at different values of K. Thus, it was determined that the value of K = 27 is sufficient, and then the angular step (in degrees):

$$\Delta\alpha = \alpha_z / K = 3.333°. \qquad (25)$$

This provides a satisfactory detailing of time functions of type (23). At the same time, the calculation time for one TIM on a sufficiently high-level computer lasted about 1 hour.

The obtained time function of the stator phase winding is shown in Fig. 7: in the first half of the period, this is what was obtained by calculation, in the second half, the full period is drawn for clarity under the condition of semi-periodic asymmetry of type (16). With the selected number of points, the graph of the MFL function looks quite smooth (unlike the similar function in Fig. 5), and the number of its harmonic components can be taken up to N_g = 27, which corresponds to the number of points in half the period.

To analyze the MFL function, it was decomposed into a harmonic series similar to (11), and then a transition was made to the EMF harmonic series (12). The values of the amplitudes of the EMF harmonics in p.u. and their corresponding effective values in absolute terms are given in Table 10, but only up to the 19th harmonic out of 27 possible, because the higher harmonics were then negligible.

Calculations using (19)–(21) gave the results: E_s= 215.4 V; E_{sdif} = 4.59 V; X_{sdif} = 0.92 Ω.

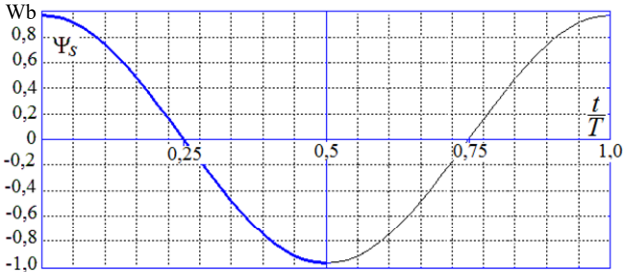

Fig. 7. Time function of the MFL of the phase winding of the TIM stator

Table 10

Harmonic composition of the stator winding EMF

ν	–	1	3	5	7	9
E_{mv}	p.u.	1,000	0,0144	0,0155	0,0020	0,0011
E_{sv}	V	215,3	3,10	3,33	0,43	0,25
ν	–	11	13	15	17	19
E_{mv}	p.u.	–	0,0012	0,0006	0,0000	0,0005
E_{sv}	V	0,04	0,26	0,14	0,09	0,11

These results are again quite close to those obtained by other calculation methods (X_{sdif} = 0.84 Ω, X_{sd} = 0.893 Ω), although they differ from them, with a discrepancy of X_{sdif} of 9.5 %.

But the same closeness of the results by comparative calculation methods is not maintained for other TIM variants, for which the results are summarized in Table 11.

Table 11

Differential parameters of different TIMs obtained by multiple numerical-field calculations of the rotating magnetic field

P_N	p	I_{so}	Ψ_{m1}	E_{s1}	E_s	E_{dif}	X_{sdifm}
kW	–	A	Wb	V	V	V	Ω
4	1	2,56	0,9818	218,1	218,2	5,51	2,15
	2	3,84	0,9815	218,0	218,2	7,93	2,07
	3	6,34	0,9696	215,4	215,9	14,67	2,31
7,5	1	4,39	0,9819	218,1	218,2	5,53	1,26
	2	4,99	0,9692	215,3	215,4	4,59	0,92
	3	7,99	0,9717	215,9	216,1	10,17	1,27
11	1	5,95	0,9791	217,5	217,6	5,28	0,89
	2	7,17	0,9712	215,7	215,8	4,71	0,66
	3	9,06	0,9703	215,5	215,6	6,46	0,71

Now we can compare the main calculation results for all TIM variants obtained by three different methods, which is done by the values of the differential inductive resistance of the TIM stator winding by collecting their values from Tables 5, 8, 11 to Table 12.

This table indicates: M1 – design data according to the standard method; M2 – data using a single numerical field calculation based on the angular functions of the MPZ; M3 – data using multi-position numerical field calculations based on the time functions of the MFL.

Table 12

Comparison of differential reactances of TIM obtained by different calculation methods

Calculation method			M1	M2	M3
P_N	p	I_{so}	X_{sd}	X_{sdif}	X_{sdif}
kW	–	A	Ω	Ω	Ω
4	1	2,56	0,654	0,78	2,15
	2	3,84	0,871	2,65	2,07
	3	6,34	0,437	2,29	2,31
7,5	1	4,39	0,441	0,45	1,26
	2	4,99	0,893	0,84	0,92
	3	7,99	0,390	1,25	1,27
11	1	5,95	0,383	0,34	0,89
	2	7,17	0,626	0,59	0,66
	3	9,06	0,410	0,70	0,71

Recall that for the M2 method, only 9 or 11 calculation points and the same number of harmonics was used, for the M3 method - 27 points, but it was even possible to limit ourselves to a smaller number.

The discrepancy between the values of X_{sd} and X_{sdif} by the M1 and M3 methods is impressive and excessively large in the majority of TIMs, which indicates the limitations of the classical method for calculating the differential reactance of the TIM stator winding. The same applies to the M2 calculation method in two-pole TIM variants.

The rather close correlation of the results of classical and numerical-field calculations for the basic TIM variant can be explained by the fact that in the methodology [1] the coefficients recommended for (1) were adapted specifically for this variant, but, unfortunately, they have not become universal for other TIM variants and still mislead their designers.

Upon completion of the studies of the differential parameters of the TIM when its magnetic system is saturated according to the nominal operating mode, calculated estimates of the effect of saturation on these parameters were made using the example of the basic TIM variant.

First of all, an example of a TIM with a completely unsaturated magnetic system was considered. For this, in the IIM, the current I_{so} was set to 1 A, and multi-position numerical field calculations were performed based on the time function of the MFL (23). The results of the calculations are given in the corresponding row of Table 13.

Table 13

Assessment of the effect of saturation of the TIM magnetic system on the differential reactance of the stator winding

I_{so}	$B_{r,ts}$	$B_{r,tr}$	$\mu_{r,ts}$	$\mu_{r,tr}$	E_s	E_{dif}	X_{sdifm}
A	T	T	p.u.	p.u.	V	V	Ω
1	0,44	0,38	2500	2490	48	0,04	0,04
5	1,84	1,61	787	1265	208	4,38	0,88
5,5	1,89	1,70	530	1010	224	7,05	1,28
6	1,96	1,78	414	835	238	10,1	1,68
10	2,21	2,06	132	265	302	36,7	3,67
15	2,30	2,20	64	238	339	59,7	3,98
50	2,36	2,28	29	77	369	83,5	3,34

To assess the saturation level of the magnetic system, the table provides the averaged values obtained for the sections of the magnetic core: $B_{r,ts}$, $B_{r,tr}$ – magnetic flux density in the stator and rotor teeth; $\mu_{r,ts}$, $\mu_{r,tr}$ – relative magnetic permeability in them (in the backs of the stator and rotor cores, the values of similar values were $\mu_{r,ys} = 5200$; $\mu_{r,yr} = 4920$).

The very weak saturation (or its absence) is also confirmed by the value of the phase EMF E_s, which turned out to be much lower than the nominal voltage of the TIM. As a result, the differential EMF E_{dif} and, accordingly, the DLR of the stator winding X_{sdifm} compared to the nominal saturation mode (see Table 12) almost did not appear.

The studies were continued at saturation levels of the magnetic core from the nominal to the one that can be at the start of the TIM. But in this case, it was necessary to take into account that with increased slips of the TIM from critical to 1, the stator and rotor currents simultaneously increase, and the voltage remains unchanged. Therefore, with increasing currents, the voltage drops on the active and reactive resistances of the windings increase, and the EMF has a reduced share. In proportion to the EMF, the main magnetic flux decreases and, accordingly, the value of the magnetic induction in the magnetic circuit.

The distribution of the magnetic field in the magnetic circuit in such a case and the level of its saturation require a careful analysis, which is difficult to conduct in detail within the framework of this article, and this can be performed and published separately.

In order to preliminarily assess how much such an analysis will give significant results and makes sense to perform, some conventions were adopted when calculating the magnetic field of the stator winding to determine the DLR.

Namely, that the saturation of the backs of the stator and rotor cores also maintains its level, as in the nominal mode. In fact, taking into account the remarks made, the saturation will be much lower, but this is not of principle, because even with a completely unsaturated magnetic core, the DLR does not differ very much from the results at nominal saturation. But the teeth of these cores saturate very strongly due to a significant increase in the magnetic fields of the slot and differential scattering, as explained in [2].

These assumptions provided the basis for organizing an artificial mode of calculating the DLR with strong saturation of the tooth portion of the TIM magnetic system.

Specifically, for the estimated calculations of the DLR with increased slips, the relative magnetic permeabilities in the backs of the stator and rotor cores were taken $\mu_{r,ys} = 1256$; $\mu_{r,yr} = 3666$ and they did not change when calculating the magnetic field. At the same time, the magnetic permeabilities in the core teeth were determined by the FEMM code as is customary in the process of such calculations.

The results of calculations of the specified variants of the TIM magnetic circuit are summarized in Table 13 at the specified values of the I_{so} current from 5 to 50 A. The data on the differential parameters at a value of 5 A

in principle correspond to the data in Table 11 at the standard operation of the FEMM code in the IIM of the TIM mode at current of 4.99 A.

The level of further saturation growth is reflected by the given averaged values of magnetic induction and relative magnetic permeability in the teeth of the stator and rotor cores. At the same time, the differential parameters of the TIM (EMF and DLR) increase significantly, which is associated with the redistribution of the magnetic field in the gap between the stator and rotor cores with an increase in the saturation of their teeth. And because of this, the higher harmonic components of the MFL and EMF of the stator winding increase significantly.

It can be seen from Table 13 that with an increase in current in the stator winding, the rate of DLR growth slows down compared to the increase in current, and even in the case of oversaturation of the teeth, this reactance reaches a maximum and even begins to decrease.

Conclusions.

1. In the system of design and theoretical research of TIMs, a significant place is given to the leakage reactances of their windings. They are determined on the basis of the theory of magnetic circuits, which in the conditions of complex tooth-and-groove structures does not guarantee the desired accuracy of calculations. This especially applies to the differential leakage reactance of the stator winding, the determination of which requires a detailed calculation of the magnetic field in the gap between the stator and rotor cores, and a harmonic analysis of the EMFs of this winding induced by it.

2. It is shown that in the current classical methods of designing DLR, they are determined by a simplified formula with the addition of a number of coefficients, tabular and graphical dependencies. As a result, not only is the physical and mathematical meaning of DLR lost, but even the accuracy of its calculation is difficult to assess. Therefore, verification of the calculation results by classical methods is relevant, and in modern conditions this can be done on the basis of numerical methods for calculating magnetic fields by available software complexes and the accompanying harmonic analysis.

3. The absence of such studies is explained by their complexity and significant labor intensity, which is practically impossible to carry out in the «manual» mode. Therefore, to overcome the problems of calculations, an automated software complex was created in the form of a single Lua script, which provides a physically transparent path to the DLR, which runs through the design of the TIM of its physical and geometric model in the FEMM software environment, control of magnetic field calculations, determination of the time functions of the MFL and EMF and their harmonic analysis.

4. Comparison of the results of classical and numerical-field calculations of DLR using the FEMM code showed their large discrepancy, which is attributed to the above-mentioned conventions and assumptions of the first. But the second option is devoid of the shortcomings of the first due to the fact that it takes into account the dimensions of the TIM structures, the saturation of the magnetic core and the physical and mathematical essence of the parameters and quantities under consideration. To exclude the randomness of the assessment, the computational analysis was performed for nine common TIM options, designed using a single classical method with varying their power and number of poles.

5. It was found that the DLR of the TIM stator winding significantly depends on the saturation level of its magnetic system, increasing with increasing saturation of the tooth zone. If we take a completely unsaturated system, then in the stator winding there remains practically only the first harmonic of the EMF, and differential scattering becomes insignificant. The classical method does not focus on this and provides a universal formula for calculating the DLR.

6. The conducted studies have shown that numerical-field calculations of differential parameters of the TIM stator winding are universal, therefore they can be proposed for similar calculations for both the stator and the rotor of various AC electric machines. Moreover, given the software implementation based on the FEMM code and the Lua script, such calculations can be built into automated design methods for these machines.

Conflict of interest. The author declares no conflict of interest.

REFERENCES

1. Goldberg O.D., Gurin Ya.S., Sviridenko I.S. *Design of electrical machines. 2nd ed., revised and additional*. Moscow, Higher School Publ., 2001. 430 p. (Rus).

2. Kopylov I.P., Goryainov F.A., Klokov B.K. *Electrical machines designing*. Moscow, Yurait Publ., 2011. 767 p. (Rus).

3. Udomsuk S., Areerak K., Areerak T., Areerak K. Online Estimation of Three-Phase Induction Motor Parameters Using an Extended Kalman Filter for Energy Saving. *Energies*, 2024, vol. 17, no. 9, art. no. 2115, pp. 1-17. doi: https://doi.org/10.3390/en17092115.

4. Aib A., Khodja D.E., Chakroune S., Rahali H. Fuzzy current analysis-based fault diagnostic of induction motor using hardware co-simulation with field programmable gate array. *Electrical Engineering & Electromechanics*, 2023, no. 6, pp. 3-9. doi: https://doi.org/10.20998/2074-272X.2023.6.01.

5. Abu Ibaid O.Z.I., Belhamdi S., Abid M., Chakroune S., Mouassa S., Al-Sagar Z.S. Wavelet packet analysis for rotor bar breakage in an inverter induction motor. *Electrical Engineering & Electromechanics*, 2023, no. 3, pp. 3-11. doi: https://doi.org/10.20998/2074-272X.2023.3.01.

6. Sakhara S., Brahimi M., Nacib L., Layadi T.M. Application of a wavelet neural network approach to detect stator winding short circuits in asynchronous machines. *Electrical Engineering & Electromechanics*, 2023, no. 3, pp. 21-27. doi: https://doi.org/10.20998/2074-272X.2023.3.03.

7. Popovych O.M., Golovan I.V. Modeling of induction motors in electromechanical systems considering stator iron losses. *Technical Electrodynamics*, 2024, no. 5, pp. 24-29. (Ukr). doi: https://doi.org/10.15407/techned2024.05.024.

8. Tumbek M., Oner Y., Kesler S. Optimal design of induction motor with multi-parameter by FEM method. *2015 9th International Conference on Electrical and Electronics Engineering (ELECO)*, 2015, pp. 1053-1056. doi: https://doi.org/10.1109/ELECO.2015.7394483.

9. Popovych O.M., Golovan I.V. Complex design tools for improvement of electromechanical systems with induction motors. *Technical Electrodynamics*, 2022, no. 2, pp. 52-59. doi: https://doi.org/10.15407/techned2022.02.052.

10. Peresada S.M., Nikonenko Y.O., Kovbasa S.M., Kuznietsov O. Flux observer adaptive to induction motors active rotor

resistance variations. *Technical Electrodynamics*, 2022, no. 5, pp. 45-51. (Ukr). doi: https://doi.org/10.15407/techned2022.05.045.
11. Milykh V.I. Numerical-field analysis of active and reactive winding parameters and mechanical characteristics of a squirrel-cage induction motor. *Electrical Engineering & Electromechanics*, 2023, no. 4, pp. 3-13. doi: https://doi.org/10.20998/2074-272X.2023.4.01.
12. Milykh V. Numerical-field analysis of the magnetic conductivity of the slot dispersion of the stator winding of induction motors. *Bulletin of NTU «KhPI». Series: Problems of electrical machines and apparatus perfection. Theory and practice*, 2023, no. 2 (10), pp. 13-19. (Ukr). doi: https://doi.org/10.20998/2079-3944.2023.2.03.
13. Diarra M.N., Li Y., Zhao X. Induction Motors Parameters Identification by Starting Process Using Quantum Particle Swarm Optimization-Trust Region Algorithm (QPSO-TRA). *2023 International Conference on Applied Intelligence and Sustainable Computing (ICAISC)*, 2023, pp. 1-6. doi: https://doi.org/10.1109/ICAISC58445.2023.10200090.
14. Rajput S., Bender E., Averbukh M. Simplified algorithm for assessment equivalent circuit parameters of induction motors. *IET Electric Power Applications*, 2020, vol. 14, no. 3, pp. 426-432. doi: https://doi.org/10.1049/iet-epa.2019.0822.
15. Lee K., Frank S., Sen P.K., Polese L.G., Alahmad M., Waters C. Estimation of induction motor equivalent circuit parameters from nameplate data. *2012 North American Power Symposium (NAPS)*, 2012, pp. 1-6. doi: https://doi.org/10.1109/NAPS.2012.6336384.
16. Gülbahçe M.O., Karaaslan M.E. Estimation of induction motor equivalent circuit parameters from manufacturer's datasheet by particle swarm optimization algorithm for variable frequency drives. *Electrica*, 2022, vol. 22, no. 1, pp. 16-26. doi: https://doi.org/10.5152/electrica.2021.21122.
17. Mölsä E., Tiitinen L., Saarakkala S., Peretti L., Hinkkanen M. Standstill Self-Commissioning of an Induction Motor Drive. *2020 IEEE Energy Conversion Congress and Exposition (ECCE)*, 2020, pp. 3044-3050. doi: https://doi.org/10.1109/ECCE44975.2020.9236035.
18. Chen H., Bi C. An effective method for determination and characteristic analysis of induction motor parameters. *IET Electric Power Applications*, 2022, vol. 16, no. 5, pp. 605-615. doi: https://doi.org/10.1049/elp2.12180.
19. Caruso M., Tommaso A.O.D., Giangrasso L., Marignetti F., Miceli R., Rizzo R. Differential Leakage Factor in Electrical Machines Equipped with Asymmetrical Multiphase Windings: a General Investigation. *2019 Fourteenth International Conference on Ecological Vehicles and Renewable Energies (EVER)*, 2019, pp. 1-7. doi: https://doi.org/10.1109/EVER.2019.8813617.
20. Di Tommaso A.O., Genduso F., Miceli R., Ricco Galluzzo G. An Exact Method for the Determination of Differential Leakage Factors in Electrical Machines With Non-Symmetrical Windings. *IEEE Transactions on Magnetics*, 2016, vol. 52, no. 9, pp. 1-9. doi: https://doi.org/10.1109/TMAG.2016.2562602.
21. Guedes J.J., Castoldi M.F., Goedtel A., Agulhari C.M., Sanches D.S. Parameters estimation of three-phase induction motors using differential evolution. *Electric Power Systems Research*, 2018, vol. 154, pp. 204-212. doi: https://doi.org/10.1016/j.epsr.2017.08.033.
22. *Slobozhansky Electromechanical Plant «SLEMZ»*. Available at: https://slemz.com.ua (Accessed: 26 August 2024).
23. *DNEPRORESURS LLC*. Available at: https://elmo.ua/uk (Accessed: 26 August 2024).
24. *Finite Element Method Magnetics: Download – Stable Distribution (21Apr2019) – 64-bit Executable.* Available at: https://www.femm.info/wiki/Download (Accessed: 22 July 2024).
25. Milykh V.I. Numerical-field analysis of temporal functions and harmonic composition of EMF in windings of a three-phase asynchronous motor. *Technical Electrodynamics*. 2018, no. 3, pp. 56-65. (Rus). doi: https://doi.org/10.15407/techned2018.03.056.
26. Milykh V.I. The system of automated formation of electrical machines computational models for the FEMM software environment. *Technical Electrodynamics*. 2018, no. 4, pp. 74-78. (Ukr). doi: https://doi.org/10.15407/techned2018.04.074.
27. Milykh V.I., Polyakova N.V. Harmonious analysis of electromagnetic sizes three-phase winding of stators of turbogenerator on basis classic and numeral field methods. *Technical Electrodynamics*, 2013, no. 3, pp. 40-49. (Rus).

Received 02.09.2024
Accepted 05.11.2024
Published 02.03.2025

V.I. Milykh[1]*, Doctor of Technical Science, Professor,*
[1] National Technical University «Kharkiv Polytechnic Institute», 2, Kyrpychova Str., Kharkiv, 61002, Ukraine,
e-mail: mvikemkpi@gmail.com

How to cite this article:
Milykh V.I. Numerical-field analysis of differential leakage reactance of stator winding in three-phase induction motors. *Electrical Engineering & Electromechanics*, 2025, no. 2, pp. 7-18. doi: https://doi.org/10.20998/2074-272X.2025.2.02

UDC 621.314 https://doi.org/10.20998/2074-272X.2025.2.03

I.I. Alnaib, A.N. Alsammak, K.K. Mohammed

Brushless DC motor drive with optimal fractional-order sliding-mode control based on a genetic algorithm

Introduction. *Brushless DC (BLDC) motor is a type of permanent magnet synchronous motor that operates without brushes employed in many applications owing to its efficiency and control in electric cars. One of the main reasons BLDC motors are better than brushed DC motors is that they employ an electronic commutation circuit instead of a mechanical one. The fractional order sliding mode controller (FOSMC) was used, which is characterized by high durability and is not affected by the disturbances that the motor is exposed to during operation, as well as overcoming the chattering phenomenon present in the conventional sliding mode controller (CSMC).* ***The novelty*** *of the proposed work consists of to use FOSMC by genetic algorithm (GA) to mitigate the chattering phenomena in sliding mode control (SMC) for optimal response for speed control and regeneration braking control in BLDC motor by using single stage by voltage source inverter and decrease energy use during motor starting.* ***Purpose.*** *Improvement FOSMC techniques for the regulation of BLDC motor's driving control system.* ***Methods.*** *Employing the GA to optimize the parameters of FOSMC to mitigate the chattering phenomenon in SMC to regulate BLDC motor's driving control system.* ***Results.*** *A comparison was made between two types of sliding controllers to obtain the best performance of the control system in speed control operations and motor braking operations, the FOSMC, through parameter optimization via the GA, surpasses the CSMC in achieving optimal performance in driving the BLDC motor.* ***Practical value.*** *FOSMC exhibits superiority over the CSMC, as indicated by the reduced integral time absolute error in motor speed tracking and regenerative brake control, with values of (0.028, 0.046, and 0.075) for the FOSMC, in contrast to (2.72, 1.56, and 0.17) for the CSMC, the overshoot for FOSMC is (0, 0, and 11.4), but for CSMC it is (60.4, 43.7, and 11.2). During braking mode for FOSMC, the power recovery from the motor to the battery was (1.96, 9, and 17.76), but in CSMC, it was (0.99, 4.49, and 11.98). Moreover, the braking length was expedited, and the battery's initial power consumption diminished at the outset.* References 32, tables 5, figures 6.

Key words: **fractional order sliding mode control, brushless DC motor, genetic algorithm, sliding mode controller.**

Вступ. *Безщітковий двигун постійного струму (BLDC) – це тип синхронного двигуна з постійним магнітом, який працює без щіток і використовуються в багатьох сферах застосування завдяки своїй ефективності та контролю в електромобілях. Одна з головних причин, чому BLDC двигуни кращі за щіткові двигуни постійного струму, полягає в тому, що вони використовують електронну схему комутації замість механічної. Використовувався контролер режиму ковзання дробового порядку (FOSMC), який характеризується високою довговічністю та не залежить від збурень, яким піддається двигун під час роботи, а також подолав явище вібрації, присутнє у звичайному контролері режиму ковзання (CSMC).* ***Новизна*** *запропонованої роботи полягає у використанні FOSMC за допомогою генетичного алгоритму (GA) для пом'якшення явища вібрації в управлінні режимом ковзання (SMC) для оптимальної реакції для керування швидкістю та керування регенераційним гальмуванням у BLDC двигуні за допомогою одноступінчатого інвертора джерела напруги і зменшити споживання енергії під час запуску двигуна.* ***Призначення***. *Удосконалення методів FOSMC для регулювання системи керування приводом BLDC двигуна.* ***Методи***. *Використання GA для оптимізації параметрів FOSMC для пом'якшення явища вібрації в SMC для регулювання системи керування приводом BLDC двигуна.* ***Результати***. *Проведено порівняння між двома типами ковзних контролерів для отримання найкращої продуктивності системи керування в операціях регулювання швидкості та операцій гальмування двигуна. FOSMC, завдяки оптимізації параметрів через GA, перевершує CSMC у досягненні оптимальної продуктивності в керуванні BLDC двигуном.* ***Практична цінність***. *FOSMC демонструє перевагу над CSMC, на що вказує зменшена абсолютна похибка інтегрального часу у відстеженні швидкості двигуна та управлінні рекуперативним гальмом зі значеннями (0,028, 0,046 і 0,075) для FOSMC, на відміну від (2,72, 1,56 і 0,17) для CSMC, перевищення для FOSMC становить (0, 0 і 11.4), але для CSMC це (60.4, 43.7 і 11.2). Під час режиму гальмування для FOSMC відновлення потужності від двигуна до батареї було (1,96, 9 і 17,76), але в CSMC воно було (0,99, 4,49 і 11,98). Крім того, довжина гальмування була прискорена, а початкове енергоспоживання батареї зменшилося на початку.* Бібл. 32, табл. 5, рис. 6.

Ключові слова: **керування ковзним режимом дробового порядку, безщітковий двигун постійного струму, генетичний алгоритм, контролер ковзного режиму.**

Introduction. Brushless DC (BLDC) motor is widely used among the several permanent magnet synchronous motors (PMSMs) due to its enhanced efficiency and control in electric vehicles [1]. Recent trends indicate that BLDC motor technologies are utilized for variable-speed drives in global industrial applications and electric vehicles etc [2, 3]. PMSM characterized by a sinusoidal back electromagnetic force (EMF) waveform, is 15 % less efficient than a BLDC motor [4]. The flux distribution is the main differentiator between the PMSM and the BLDC motor. BLDC motor is a type of PMSM that is identified by a trapezoidal back-EMF waveform [5]. In contrast, BLDC motors have many benefits over brushed DC motors, including quiet operation, reduced size and weight, increased service life, reduced maintenance needs, a large torque capacity, reduced size and weight and improved dependability and efficiency [6]. The electronic commutation circuit, which takes the place of the mechanical commutated in brushed DC motors, is the source of BLDC motors' advantages. As a result, BLDC motors are currently the industry standard [7]. BLDC motor uses an electronic commutation technique instead of employing brushes [8]. Sliding mode control (SMC) has become known as a robust control technique that ensures superior tracking performance despite internal parameter fluctuations and external disruptions [9, 10]. Aside from that, SMC's notable attributes include its exceptional accuracy and straightforwardness. BLDC motors are only one example of the several machine kinds that have benefited from SMC's widespread use and effective implementation [11]. The use of SMC for BLDC motor speed control is the main topic of this paper.

The goal of the paper is to use FOSMC by genetic algorithm (GA) to mitigate the chattering phenomena in SMC for optimal response for speed control and regeneration braking control in BLDC motor by using single stage by voltage source inverter.

Review of the literature. Several speed control structures are suggested for regulating BLDC motors, encompassing PID controllers [12, 13], fuzzy logic controllers, sliding mode controllers, fractional order sliding mode controllers (FOSMC) and additional controller types [14]. Numerous researchers are engaged in this domain, employing metaheuristic algorithms to determine optimal values for these controllers. In [15] the researchers devised an adaptive integer sliding controller, which demonstrated superior performance to the conventional integer sliding controller regarding variations in reference speeds and motor load changes. Using a variable slope sliding mode observer (SMO), the study [16] presents a way to control the speed of a high-speed BLDC motor in a hand-stick Hoover cleaner. For irrational BLDC motor estimations, the SMO based on the signum function works wonders. The work [17] utilises the Dragonfly Algorithm (DA) to identify optimal configurations for the PI and SMC parameters. To optimise the controllers, simulation findings indicate that the DA-based SMC surpasses the optimised PI controller and SMC. The study [18] presents the design and use of the FOSMC to the quadrotor to demonstrate its fractional behaviour in response to disturbances. Additionally, to evaluate the FOSMC, the integer-order SMC (IOSMC) has been executed on the quadrotor for identical routes to regulate this unstable system. The experimental results indicate that the FOSMC exhibits reduced trajectory tracking error with minimal variations when following inclined circular and zigzag paths. In contrast, the IOSMC has more tracking errors and increased overshoot and undershoot. The work [19] compares the conventional PI controller and a sliding mode controller for closed-loop speed regulation of a BLDC motor. The results demonstrate that the SMC surpasses the PID controller. The study [20] examines the regenerative braking of a BLDC motor for electric vehicle applications using PI controller. The paper [21] a predictive senseless driving system based on SMO for a BLDC motor with regenerative capabilities in electric vehicle applications is given. The rotor speed and location calculation by SMO is highly precise and resilient under fluctuating solar insulation. This paper thoroughly analyses diverse control techniques aimed at reducing torque ripples in BLDC motors for electric vehicles, rigorously analyzed for their functionality and control methodologies, using the SMC controller employed for motor regulation [22].

Mathematical model of BLDC motor. BLDC motor regulates the currents flowing through the armature with the use of position sensors and an inverter (Fig. 1). Its streamlined size, high efficiency, dependability, quiet operation, and low maintenance requirements make it excellent for use in industrial applications. There are several configurations of BLDC motors; however, the three-phase variant is the most popular because to its fast speed and little torque ripple [23]. It is driven by a six-switch inverter, whereby two phases operate concurrently during each control step, while the third phase is deactivated. Pulses (S_1, ... , S_6) generated at 60 electrical degree intervals control these switches from the 120-degree-displaced Hall effect position sensor signals (H_r, H_s, H_t). Using a sequence of Hall effect sensors and transistors, the rotor's evolution may be switched between 0 and 360° in angular position, as detailed in Table 1 [24].

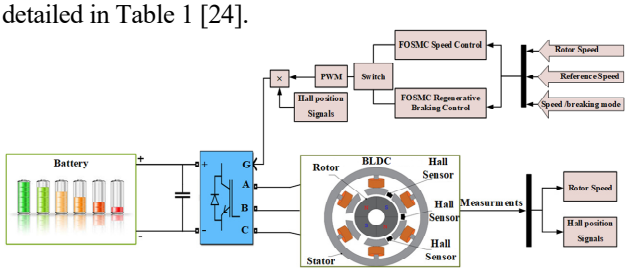

Fig. 1. The control drive for BLDC motor

Table 1

The sequence of switching utilizing Hall effect outcomes

Angle, deg.	Cycle	Hall sensors (H_a, H_b, H_c)	Phase current (i_a, i_b, i_c)	Switch active
0–60	1	(1, 0, 1)	(+DC, –DC, off)	T_1–T_4
60–120	2	(1, 0, 0)	(+DC, off, –DC)	T_1–T_6
120–180	3	(1, 1, 0)	(off, +DC, –DC)	T_3–T_6
180–240	4	(0, 1, 0)	(–DC, +DC, off)	T_3–T_2
240–300	5	(0, 1, 1)	(–DC, off, +DC)	T_5–T_2
300–360	6	(0, 0, 1)	(off, –DC, +DC)	T_5–T_4

The model of the BLDC motor is [24]:

$$\begin{bmatrix} \mathrm{d}i_a/\mathrm{d}t \\ \mathrm{d}i_b/\mathrm{d}t \\ \mathrm{d}\omega_m/\mathrm{d}t \\ \mathrm{d}\theta_m/\mathrm{d}t \end{bmatrix} = \begin{bmatrix} -R/L & 0 & 0 & 0 \\ 0 & -R/L & 0 & 0 \\ 0 & 0 & -k_f/J & 0 \\ 0 & 0 & 1 & 0 \end{bmatrix} \begin{bmatrix} i_a \\ i_b \\ \omega_m \\ \theta_m \end{bmatrix} + \begin{bmatrix} 2/3L & 1/3L & 0 \\ -1/3L & 1/3L & 0 \\ 0 & 0 & 1/J \\ 0 & 0 & 0 \end{bmatrix} \begin{bmatrix} v_{ab} - e_{ab} \\ v_{bc} - e_{bc} \\ T_e - T_l \end{bmatrix}; \quad (1)$$

$$i_c = -(i_a + i_b),$$

where $e_{ab} = e_a - e_b$; $e_{bc} = e_b - e_c$; e_a, e_b, e_c are the motor back-EMFs; i_a, i_b, i_c are the stator phase currents; v_a, v_b, v_c are the stator phase voltages; v_{ab}, v_{bc}, v_{ca} are the stator phase to phase voltages; R, L are the resistance and inductance of a stator phase; ω_m is the rotor speed; θ_m is the mechanic angle; k_f is the friction constant; J is the rotor inertia; T_e, T_l are the electromagnetic and load torque.

Improvements to BLDC drive control via sliding mode controllers. SMC is an effectively recognized control technique in the domain of electric drives. It is a variable structure nonlinear discontinuous control method distinguished by precision, resilience, and straightforward implementation [25, 26]. The mathematical equation for SMC is:

$$s(t) = e(t) + \Delta e(t), \quad (2)$$

where $s(t)$ is the sliding surface for SMC; $e(t)$ is the difference between the reference speed and the actual speed of the motor; $\Delta e(t)$ is the rate of variation of the error signal.

The current theory views chattering problems in SMC as the main challenge to SMC's recognition as a significant theoretical advancement. Researchers have suggested different methods for dealing with this issue (Fig. 2).

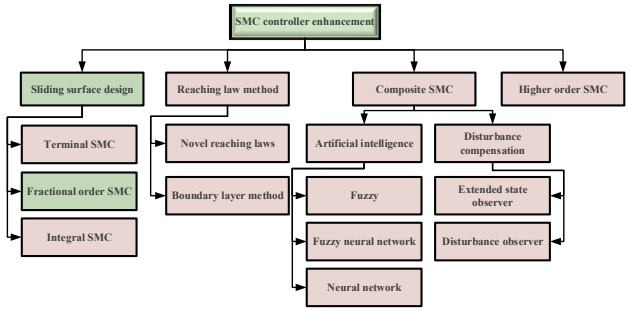

Fig. 2. Techniques to mitigate the chattering phenomenon in CSMC [26]

Figure 2 shows that the FOSMC surface is used as a nonlinear sliding surface design method in this study to reduce chattering problems [27]. GA was employed to improve the functionality of FOSMC by identifying the most effective components for regulating motor speed and breaking in all scenarios [28]. For speed mode the FOSMC is:

$$s_1(t) = k_1 \cdot |e(t)|^{v_1} \cdot \text{sign}(e(t)) + \text{d}e(t)/\text{d}t \,, \tag{3}$$

braking mode the FOSMC is:

$$s_2(t) = k_2 \cdot |e(t)|^{v_2} \cdot \text{sign}(e(t)) + \text{d}e(t)/\text{d}t \,, \tag{4}$$

where k_1, v_1, k_2, v_2 are the parameter of FOSMC tuning by GA.

Genetic algorithm (GA). The evolutionary algorithm known as a GA is based on the ideas of natural selection and how the strongest individuals reproduce [29]. GA has earned a stellar reputation as an optimization method among its many real-world uses. GA generates the optimal solution for several generations by randomly populating the candidate solutions. GA uses a set of genetic operators during its search procedure, including mutation, selection and crossover [30]. GA was used in this work to find the best elements for FOSMC in BLDC motor speed control and braking operations. Table 2 explains the parameters of GA algorithm.

Table 2

Selection of the settings for the GA

Parameters	Values
Crossover function	Arithmetic
Selection function	Tournament size 4
Scaling function	Rank
Mutation rate	0.1
Population size and iteration number	20 (double vector) and 20
Range of FOSMC tuning parameters k, v	$0 \le k \le 400$, $0 \le v \le 5$

The training process of the GA to find the best parameters for a FOSMC is shown in Fig. 3.

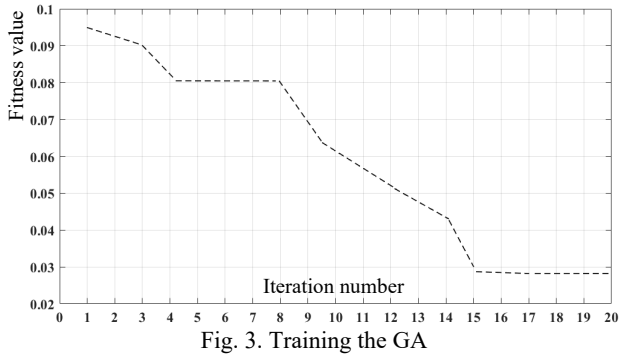

Fig. 3. Training the GA

Simulation and results. This section shows the simulation method for driving BLDC motor with parameters from Table 3.

Table 3

Parameters of the BLDC motor

Parameters	Value
Rated power P, kW	0.4712
Voltage V, V	400
Frequency f, Hz	50
Angular speed ω_r, rpm	1500
Stator resistance R_s, Ω	0.0485
Stator self-inductance L_s, mH	3.045
Magnetizing inductance L_m, H	0.1194
Inertia J, kg·m^2	0.0027
Friction factor F, N·m·s	0.0004924
Number of pole pairs p	4

It implements an SMC with the proposed FOSMC surface types, this is due to the chattering phenomena in SMC. The proposed type was used to control the motor speed (speed mode) and the braking motor (braking mode) using the regeneration braking technique, when the machine is under regenerative braking (RB), the motor inverter transfers power from the DC-link side to the low-voltage source known as back-EMF, much like a boost converter. Whenever the top diodes of the voltage source converter are operational, energy is returned to the battery pack [31]. GA was used in both models to find the best values for the FOSMC at a different reference speed during the motor's full load.

The power reinstated to the battery pack may be calculated by assessing the DC bus voltage $v_{DC\text{-}link}$ and current i_{brake}. The average power restored during the RB operation is calculated as

$$P_r = \frac{1}{T_b} \int_0^{T_b} v_{DC-link}(t) \cdot i_{brake}(t) \text{d}t \,. \tag{5}$$

Equation (5) is used to determine the average power output generated by the drive when it is in RB mode [32].

The performance Integral Time Absolute Error (ITAE) index was used:

$$ITAE = \int_0^t t|e(t)|\text{d}t \,. \tag{6}$$

Table 4 explains the parameters of all modes of FOSMC by tuning GA.

Table 4

Tuning the FOSMC controller using GA

n, rpm	k_1	v_1	k_2	v_2	*ITAE*
500	382.23	1.016	338.35	3.254	0.028
1000	296.019	1.155	69.475	4.431	0.046
1500	299.625	2.480	158.192	3.073	0.075

Table 5 compares between FOSMC and CSMC the time response of the BLDC motor.

Table 5

Comparison of FOSMC and SMC controllers at different reference speeds in terms of the time characteristics of the speed response

SMC controller type	Speed reference, rpm	Overshoot speed, %	Settling time T_s, ms	Error steady state, %	Braking time T_b, ms	Power recovery P_r, W
FOSMC	500	0	28	0	27	1.96
	1000	0	15	0	39.4	9
	1500	11.4	20	0	58.5	17.76
SMC	500	60.4	6	0.4	38	0.99
	1000	43.7	45	0.2	65.5	4.49
	1500	11.2	21	0.2	88.33	11.98

Figures 4–6 show the time response of the motor in the case of speed control mode and braking mode for each figure using 2 types of sliding controllers. The results show the superiority of the FOSMC in the speed control process, in addition to the fast braking process and less energy consumption from the battery when starting the motor.

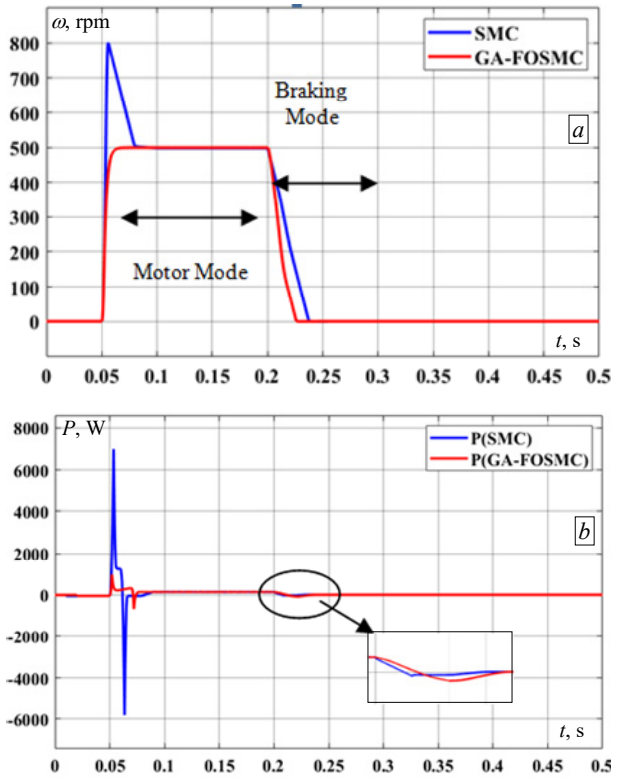

Fig. 4. Response of BLDC by GA-FOSMC and CSMC controllers: *a* – speed reference 500 rpm; *b* – battery power

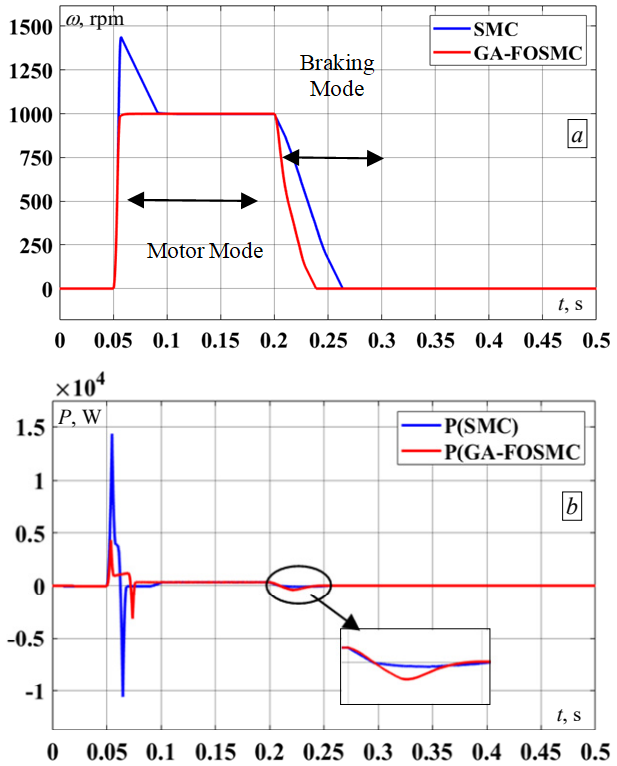

Fig. 5. Response of BLDC by GA-FOSMC and CSMC controllers: *a* – speed reference 1000 rpm; *b* – battery power

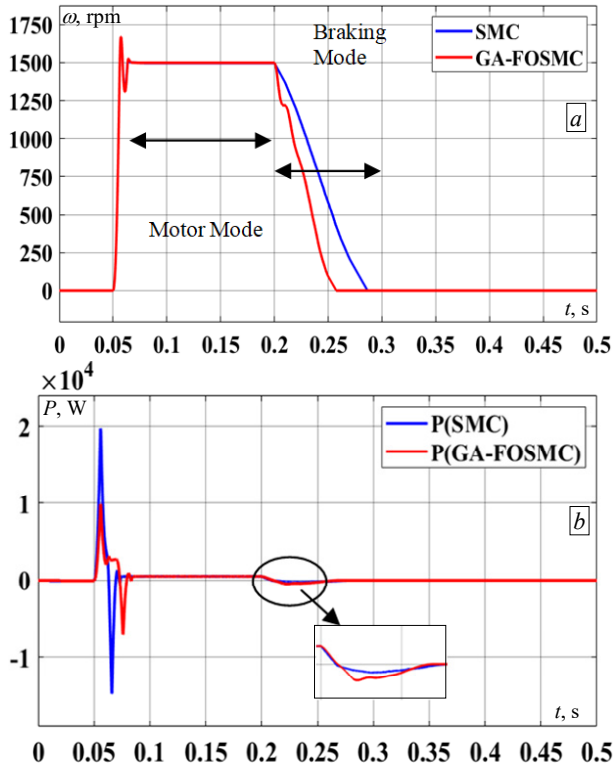

Fig. 6. Response of BLDC by GA-FOSMC and CSMC controllers: *a* – speed reference 1500 rpm; *b* – battery power

Conclusions. Fractional order sliding mode controller (FOSMC) treats the chattering phenomena in conventional sliding mode controller (CSMC) to optimally control the speed and regenerative braking of the brushless DC motor via the voltage source inverter circuit, where the firing signal is generated using the pulse-width modulation method. The comparison between the FOSMC and CSMC, which includes several levels of speed references, and using the genetic algorithm to find the best parameters of the FOSMC through the results of the simulation turns out the superior FOSMC over the CSMC where the lowest integral time absolute error in tracking the motor speed 500, 1000 and 1500 rpm for the FOSMC (0.028, 0.046 and 0.075) respectively. The overshoot by FOSMC is (0 and 11.4), while in CSMC (60.4, 43.7, and 11.2). In braking mode for FOSMC was the power recovery from motor to battery (1.96, 9, and 17.76), while in CSMC, it was (0.99, 4.49, and 11.98). Furthermore, the braking duration was quicker, and the initial power consumption from the battery decreased at the starting.

Acknowledgements. The authors would like to sincerely thank the College of Engineering Department of Electrical at the University of Mosul for the tremendous help they provided during this work.

Conflict of interest. The authors declare that there is no conflict of interest.

REFERENCES

1. Saiteja P., Ashok B., Mason B., Kumar P.S. Assessment of Adaptive Self-Learning-Based BLDC Motor Energy Management Controller in Electric Vehicles Under Real-World Driving Conditions for Performance Characteristics. *IEEE Access*, 2024, vol. 12, pp. 40325-40349. doi: https://doi.org/10.1109/ACCESS.2024.3375753.

2. Mohanraj D., Aruldavid R., Verma R., Sathiyasekar K., Barnawi A.B., Chokkalingam B., Mihet-Popa L. A Review of BLDC Motor: State of Art, Advanced Control Techniques, and Applications. *IEEE Access*, 2022, vol. 10, pp. 54833-54869. doi: https://doi.org/10.1109/ACCESS.2022.3175011.

3. Patel A.N. Slot opening displacement technique for cogging torque reduction of axial flux brushless DC motor for electric two-wheeler application. *Electrical Engineering & Electromechanics*, 2023, no. 2, pp. 7-13. doi: https://doi.org/10.20998/2074-272X.2023.2.02.
4. Prabhu N., Thirumalaivasan R., Ashok B. Design of sliding mode controller with improved reaching law through self-learning strategy to mitigate the torque ripple in BLDC motor for electric vehicles. *Computers and Electrical Engineering*, 2024, vol. 118, art. no. 109438. doi: https://doi.org/10.1016/j.compeleceng.2024.109438.
5. Akrami M., Jamshidpour E., Nahid-Mobarakeh B., Pierfederici S., Frick V. Sensorless Control Methods for BLDC Motor Drives: A Review. *IEEE Transactions on Transportation Electrification*, 2024, pp. 1–1. doi: https://doi.org/10.1109/TTE.2024.3387371.
6. Saha B., Singh B. Torque Ripple Mitigation in Sensorless PMBLDC Motor Drive With Adaptive Observer for LEV. *IEEE Transactions on Power Electronics*, 2025, vol. 40, no. 1, pp. 1739-1747. doi: https://doi.org/10.1109/TPEL.2024.3457677.
7. Khemis A., Boutabba T., Drid S. Model reference adaptive system speed estimator based on type-1 and type-2 fuzzy logic sensorless control of electrical vehicle with electrical differential. *Electrical Engineering & Electromechanics*, 2023, no. 4, pp. 19-25. doi: https://doi.org/10.20998/2074-272X.2023.4.03.
8. Lee H.-Y., Cha K.-S., Kwon S.-O., Yoon S.-Y., Seok C.-H., Lim M.-S. Efficiency Analysis of BLDC Motor With Delta Connection According to Magnitude of Circulating Current. *IEEE Transactions on Magnetics*, 2024, vol. 60, no. 12, pp. 1-5. doi: https://doi.org/10.1109/TMAG.2024.3465879.
9. Sakri D., Laib H., Farhi S.E., Golea N. Sliding mode approach for control and observation of a three phase AC-DC pulse-width modulation rectifier. *Electrical Engineering & Electromechanics*, 2023, no. 2, pp. 49-56. doi: https://doi.org/10.20998/2074-272X.2023.2.08.
10. Mohammed H.A., Alsammak A.N.B. An Intelligent Hybrid Control System using ANFIS-Optimization for Scalar Control of an Induction Motor. *Journal Européen Des Systèmes Automatisés*, 2023, vol. 56, no. 5, pp. 857-862. doi: https://doi.org/10.18280/jesa.560516.
11. Li K., Ding J., Sun X., Tian X. Overview of Sliding Mode Control Technology for Permanent Magnet Synchronous Motor System. *IEEE Access*, 2024, vol. 12, pp. 71685-71704. doi: https://doi.org/10.1109/ACCESS.2024.3402983.
12. Ibrahim M.A., Alsammak A.N.B. Adaptive PID Control for 8/6 Switched Reluctance Motor Drive Based on BFO. *Journal Européen Des Systèmes Automatisés*, 2023, vol. 56, no. 4, pp. 539-546. doi: https://doi.org/10.18280/jesa.560403.
13. Ibrahim M.A., Alsammak A.N.B. Switched Reluctance Motor Drives Speed Control Using Optimized PID Controller. *Przeglad Elektrotechniczny*, 2022, vol. 98, no. 11, pp. 46-50. doi: https://doi.org/10.15199/48.2022.11.7.
14. Alnaib I.I., Alsammak A.N. Optimization of fractional PI controller parameters for enhanced induction motor speed control via indirect field-oriented control. *Electrical Engineering & Electromechanics*, 2025, no. 1, pp. 3-7. doi: https://doi.org/10.20998/2074-272X.2025.1.01.
15. Younus S.M.Y., Kutbay U., Rahebi J., Hardalaç F. Hybrid Gray Wolf Optimization–Proportional Integral Based Speed Controllers for Brush-Less DC Motor. *Energies*, 2023, vol. 16, no. 4, art. no. 1640. doi: https://doi.org/10.3390/en16041640.
16. Ok S., Xu Z., Lee D.-H. A Sensorless Speed Control of High-Speed BLDC Motor Using Variable Slope SMO. *IEEE Transactions on Industry Applications*, 2024, vol. 60, no. 2, pp. 3221-3228. doi: https://doi.org/10.1109/TIA.2023.3348081.
17. Kheel A.M., Al-Shamaa N.K., Hawas M.N. Sliding Mode Controller Enchancement for Speed Control of BLDC Motor Based On Dragonfly Algorithm. *2023 International Conference on Converging Technology in Electrical and Information Engineering (ICCTEIE)*, 2023, pp. 135-141. doi: https://doi.org/10.1109/ICCTEIE60099.2023.10366754.
18. Basci A., Derdiyok A., Can K., Orman K. A Fractional-Order Sliding Mode Controller Design for Trajectory Tracking Control of An Unmanned Aerial Vehicle. *Elektronika Ir Elektrotechnika*, 2020, vol. 26, no. 4, pp. 4-10. doi: https://doi.org/10.5755/j01.eie.26.4.25846.
19. El Idrissi A.L., Bouchnaif J., Mokhtari M., Bensliman A. Comparative study between pi speed control and sliding mode control of bldc motor. *Lecture Notes in Electrical Engineering*, 2020, vol. 684 LNEE, pp. 309-317. doi: https://doi.org/10.1007/978-3-030-53187-4_35.
20. Soni N., Barai M. Performance Study of Regenerative Braking of BLDC Motor targeting Electric Vehicle Applications. *2022 2nd Asian Conference on Innovation in Technology (ASIANCON)*, 2022, pp. 1-6. doi: https://doi.org/10.1109/ASIANCON55314.2022.9909322.
21. Saha B., Singh B., Sen A. SMO Based Position Sensorless BLDC Motor Drive Employing Canonical Switching Cell Converter for Light Electric Vehicle. *IEEE Transactions on Industry Applications*, 2023, vol. 59, no. 3, pp. 2974-2984. doi: https://doi.org/10.1109/TIA.2023.3241607.
22. Prabhu N., Thirumalaivasan R., Ashok B. Critical Review on Torque Ripple Sources and Mitigation Control Strategies of BLDC Motors in Electric Vehicle Applications. *IEEE Access*, 2023, vol. 11, pp. 115699-115739. doi: https://doi.org/10.1109/ACCESS.2023.3324419.
23. Azab M. Comparative Study of BLDC Motor Drives with Different Approaches: FCS-Model Predictive Control and Hysteresis Current Control. *World Electric Vehicle Journal*, 2022, vol. 13, no. 7, art. no. 112. doi: https://doi.org/10.3390/wevj13070112.
24. Bazi S., Benzid R., Bazi Y., Rahhal M.M.Al. A Fast Firefly Algorithm for Function Optimization: Application to the Control of BLDC Motor. *Sensors*, 2021, vol. 21, no. 16, art. no. 5267. doi: https://doi.org/10.3390/s21165267.
25. Ullah A., Pan J., Ullah S., Zhang Z. Robust Speed Control of Permanent Magnet Synchronous Motor Drive System Using Sliding-Mode Disturbance Observer-Based Variable-Gain Fractional-Order Super-Twisting Sliding-Mode Control. *Fractal and Fractional*, 2024, vol. 8, no. 7, art. no. 368. doi: https://doi.org/10.3390/fractalfract8070368.
26. Mohd Zaihidee F., Mekhilef S., Mubin M. Robust Speed Control of PMSM Using Sliding Mode Control (SMC) – A Review. *Energies*, 2019, vol. 12, no. 9, art. no. 1669. doi: https://doi.org/10.3390/en12091669.
27. Lin X., Liu J., Liu F., Liu Z., Gao Y., Sun G. Fractional-Order Sliding Mode Approach of Buck Converters With Mismatched Disturbances. *IEEE Transactions on Circuits and Systems I: Regular Papers*, 2021, vol. 68, no. 9, pp. 3890-3900. doi: https://doi.org/10.1109/TCSI.2021.3092138.
28. Zaihidee F.M., Mekhilef S., Mubin M. Application of Fractional Order Sliding Mode Control for Speed Control of Permanent Magnet Synchronous Motor. *IEEE Access*, 2019, vol. 7, pp. 101765-101774. doi: https://doi.org/10.1109/ACCESS.2019.2931324.
29. Zhao B., Chen W.-N., Wei F.-F., Liu X., Pei Q., Zhang J. PEGA: A Privacy-Preserving Genetic Algorithm for Combinatorial Optimization. *IEEE Transactions on Cybernetics*, 2024, vol. 54, no. 6, pp. 3638-3651. doi: https://doi.org/10.1109/TCYB.2023.3346863.
30. Patel A.N., Suthar B.N. Performance optimisation of axial flux permanent magnet brushless DC motor for electric vehicle application with the genetic algorithm (GA) approach. *International Journal of Ambient Energy*, 2024, vol. 45, no. 1, art. no. 2370850. doi: https://doi.org/10.1080/01430750.2024.2370850.
31. Baszynski M., Pirog S. Unipolar Modulation for a BLDC Motor With Simultaneously Switching of Two Transistors With Closed Loop Control for Four-Quadrant Operation. *IEEE Transactions on Industrial Informatics*, 2018, vol. 14, no. 1, pp. 146-155. doi: https://doi.org/10.1109/TII.2017.2723962.
32. Mishra A.K., Singh A.K., Vishwanath G.M. A Fuel-Efficient BLDC Motor-Driven Light Electric Vehicle With Single-Stage Onboard Charging System. *IEEE Transactions on Transportation Electrification*, 2023, vol. 9, no. 4, pp. 4909-4921. doi: https://doi.org/10.1109/TTE.2022.3226536.

Received 11.12.2024
Accepted 20.01.2025
Published 02.03.2025

I.I. Alnaib [1]*, MSc., Lecturer,*
A.N. Alsammak [1]*, PhD, Professor,*
K.K. Mohammed [1]*, MSc., Assistant Lecturer,*
[1] Electrical Engineering Department,
College of Engineering, University of Mosul, Iraq,
e-mail: ibrahim-85353@uomosul.edu.iq (Corresponding Author);
ahmed_alsammak@uomosul.edu.iq
karam_alnakieb@uomosul.edu.iq

How to cite this article:
Alnaib I.I., Alsammak A.N., Mohammed K.K. Brushless DC motor drive with optimal fractional-order sliding-mode control based on a genetic algorithm. *Electrical Engineering & Electromechanics*, 2025, no. 2, pp. 19-23. doi: https://doi.org/10.20998/2074-272X.2025.2.03

UDC 621.314 https://doi.org/10.20998/2074-272X.2025.2.04

Z. Darsouni, S.E. Rezgui, H. Benalla, F. Rebahi, M.A.M. Boumandjel

Ensuring service continuity in electric vehicles with vector control and linear quadratic regulator for dual star induction motors

Introduction. *In this paper, the use of a Linear Quadratic Regulator (LQR) to control a Dual Star Induction Motor (DSIM) powered by dual three-level neutral point clamped inverters in electric vehicle (EV) propulsion systems is explored.* ***Purpose.*** *Ensuring both high performance against parameter sensitivity and service continuity in the event of faults is challenging in EV propulsion systems. The* ***aim*** *is to maximize both system performance and service continuity through the optimal design of the controller.* ***Methods.*** *DSIM is controlled by a LQR, which is replaced the traditional PI controller in the field-oriented control (FOC) system for speed regulation. Starting with FOC the optimal regulator is designed by introducing a minimization criterion into the Ricatti equation. The LQR control law is then employed as a speed regulator to ensure precise regulation and optimize DSIM operation under various load and speed conditions. The avoidance of linearization of the DSIM facilitates the exploitation of its true nonlinear dynamics.* ***Novelty.*** *Three tests are conducted to evaluate system performance. A precision test by varying the reference speed and analyzing speed response, settling time, precision and overshoot, a robustness test against parameter variations, assessing system robustness against changes in stator and rotor resistances and moment of inertia, and a fault robustness test evaluating system robustness against faults such as phase faults while maintaining load torque. The* ***results*** *show that this approach can keep the motor running smoothly even under parameter variations or degraded conditions. The precision and adaptability of the LQR technique enhance the overall efficiency and stability of the DSIM, making it a highly viable solution for modern EVs. This robust performance against parameter variations and loads is essential in ensuring the reliability and longevity of EV propulsion systems.* ***Practical value****. This approach holds significant potential for advancing EV technology, promising improved performance and reliability in real-world applications.* References 44, tables 2, figures 15.

Key words: **dual star induction motor, linear quadratic regulator, neutral point clamped, electric vehicle, field-oriented control.**

Вступ. *У цій статті досліджується використання лінійного квадратичного регулятора (LQR) для керування асинхронним двигуном із подвійною зіркою (DSIM), що живиться від подвійних трирівневих інверторів із закріпленням нейтральної точки в силових системах електромобілів.* ***Призначення***. *Забезпечення як високої продуктивності щодо чутливості до параметрів, так і безперервності роботи в разі несправностей є складним завданням для силових систем електромобілів.* ***Метою*** *є максимізація як продуктивності системи, так і безперервності обслуговування за допомогою оптимальної конструкції контролера.* ***Методи***. *DSIM керується LQR, який замінює традиційний PI-контролер у системі орієнтованого на поле керування (FOC) для регулювання швидкості. Починаючи з FOC, оптимальний регулятор розробляється шляхом введення критерію мінімізації в рівняння Рікатті. Потім закон керування LQR використовується як регулятор швидкості для забезпечення точного регулювання та оптимізації роботи DSIM за різних умов навантаження та швидкості. Уникнення лінеаризації DSIM полегшує використання його справжньої нелінійної динаміки.* ***Новизна***. *Для оцінки продуктивності системи проводяться три тести. Випробування на точність шляхом зміни еталонної швидкості та аналізу відповіді на швидкість, часу встановлення, точності та перерегулювання, випробування на стійкість щодо варіацій параметрів, оцінювання стійкості системи щодо змін опору статора та ротора та моменту інерції, а також тест на стійкість до несправностей, що оцінює стійкість системи проти несправностей, таких як замикання фаз, зберігаючи момент навантаження.* ***Результати*** *показують, що цей підхід може підтримувати безперебійну роботу двигуна навіть за коливань параметрів або погіршених умов. Точність і адаптивність техніки LQR підвищують загальну ефективність і стабільність DSIM, що робить його дуже життєздатним рішенням для сучасних електромобілів. Ця надійна робота проти коливань параметрів і навантажень є важливою для забезпечення надійності та довговічності силових систем електромобілів.* ***Практична цінність***. *Цей підхід має значний потенціал для вдосконалення технології електромобілів з точки зору покращеної продуктивності і надійності у реальних прикладах.* Бібл. 44, табл. 2, рис. 15.

Ключові слова: **асинхронний двигун з подвійною зіркою, лінійно-квадратичний регулятор, зафіксована нейтральна точка, електромобіль, керування з орієнтацією за полем.**

Introduction. Preserving the environment is a top priority in today's world. Pollution and climate change are forcing us to reconsider the way we travel. Electric Vehicles (EVs) unquestionably represent an efficient measure and a promising solution to this problem [1]. In the world of EVs, the core of this technology lies in their propulsion system, which separates it from combustion vehicle. It contains [2] (Fig. 1):

- the battery, which is an energy storage unit that powers the electric motor for vehicle propulsion. Often, EVs are equipped with Battery Management System (BMS) that supervise the performance of the battery and motor, optimize energy efficiency, and ensure safe operation;
- the electric motor is responsible for converting electric energy into mechanical energy to drive the vehicle's wheels;
- the inverter is an electronic converter that controls the direction and power of the electric current supplied to the motor;
- the embedded control system, that control the inverter state and hence the direction and the speed of the vehicle.

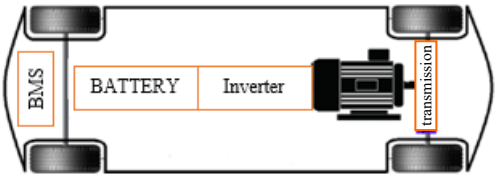

Fig. 1. Powertrain of EV

To control any AC motor, an essential step called Field-Oriented Control (FOC) is used. FOC allows us to decouple the electromagnetic torque from the flux, making AC motors behave similarly to DC motors [3]. This technique provides several advantages, including high efficiency, better torque control at low speeds, smooth operation, a wide speed range, and improved dynamic response [4]. Nevertheless, FOC requires an estimator to calculate angular velocity feedback for speed control [5].

Purpose. This paper aims to maximize the performance of EVs by improving the powertrain of the EV, and to do so a comparison between regulators such as

Sliding Mode Control (SMC) regulator, Model Reference Adaptive Control (MRAC) regulator and Linear Quadratic Regulator (LQR) to choose the most appropriate one. In the context of ensuring service continuity of EVs, it is essential to choose an appropriate type of motors from the commonly used types that are AC and DC motors.

Brushless (BLDC) motor. With the elimination of brushes, the BLDC motor has emerged as a solution to the old DC motor. This type of motor offers improved efficiency and requires less maintenance [6, 7]. Additionally, it has the ability to provide higher torque and power over a wide operating range, compared to the older DC motor. However, the BLDC motor has a relatively limited field weakening capability. Furthermore, high speeds pose a safety risk due to the potential for magnet breakage. They are also sensitive to high temperatures, which affects the overall motor performance [6, 8]. While the BLDC motor offers various advantages as mentioned, it may not ensure service continuity in the presence of motor faults, which make it not the most suitable motor in this case.

Induction motor. The simple structure, high reliability, robustness, reduced maintenance, low cost, and operation even in adverse conditions are all advantages that led Tesla Company to choose this type of motors for the Tesla S model [6]. Additionally, these motors offer an extended speed range through flux weakening in the constant power zone, as well as absence of commutation and the ability to recover energy during the braking phase [9, 10].

However, controlling this type of motor is also challenging, as it requires precise balancing of slip percentages and load quantity to ensure efficient operation at all times [6]. Additionally, while losses increase at high speeds, its efficiency decreases at both low and high speeds [8]. Furthermore, if the critical synchronous speed is reached, the motor may fail [11, 12]. In the context of selecting more suitable motor for an electric car to ensure continuous service, it appears that induction motors are not the optimal choice for this scenario.

Dual Star Induction Motor (DSIM). The robustness and low maintenance of the DSIM allow for the gradual replacement of the induction motor in industrial applications, even in high power scenarios such as railway traction, marine propulsion [13–15]. This type of motor consists of two windings with phases shifted by 30 electric degrees from each other, powered by a 6-phase inverter or 2 inverters of 3 phases [16].

Among its advantages, one can also note a higher torque density compared to traditional induction motors. Additionally, the DSIM reduces harmonic content and exhibits high reliability, allowing it to operate even in the presence of faults on one or more phases of the motor [17, 18]. It also offers power segmentation, minimizing torque ripple and rotor losses while reducing harmonic currents [19]. However, controlling the DSIM is considered complex, especially regarding achieving torque and flux decoupling [16, 17]. Despite this drawback, this type of motor is capable of operating under degraded conditions [20, 21]. In comparison between BLDC, induction motor and DSIM the last one stands out as the most suitable option for EVs in most scenarios and, particularly in ensuring service continuity.

Control methods. There are numerous control techniques classified into 2 categories: classic techniques and advanced techniques.

Starting with classical ones, the indirect and direct (IFOC and FOC) was proposed for the first time by K. Hasse in 1968 and Werner Leonard in 1971 [22], as a replacement for classic correctors. Many researches have focused on these 2 techniques [23–27], applying them to different types of machines, and according to the results obtained: FOC and IFOC control allow for control over the machine's flux and torque. They have a better effect on suppressing high-order harmonics, reference tracking with a good response time, and high precision in steady state. However, they are sensitive to parametric variations, and the transformation of variables is based on an estimator, making it sensitive [28]. For the several mentioned disadvantages, many researchers were proposed such as SMC, MRAC and optimal control with LQR to enhance FOC and mitigate high sensitivity to parameters variations, and ensure fault tolerant control [29].

SMC is intended for systems with variable structures because it is robust to parameter changes or parameter uncertainty and total suppression of external disturbances [30–32]. It provides also good reference tracking with fast response time [33]. On one hand, high-frequency switching causes chattering phenomenon which significantly affects the overall system performance. Additionally, it suffers from overshoot peaks and high stabilization times. Finally, it does not guarantee good performance in the presence of disturbances such as sudden changes in reference speed [30, 34].

MRAC is used to control systems with variable structures or unknown parameters [35, 36]. Many research has been conducted on MRAC and applied to various types of motors [37–40]. According to simulation results, MRAC is robust against parameter uncertainties such as stator and rotor resistance (R_s, R_r) and moment of inertia (J) [41], as well as parameter changes [42], and presents a good reference tracking and precision [37, 38, 40]. However, it suffers from high overshoot [42, 43], complexity and heavy computational time of the algorithms [41]. Real-time parameter updates lead to oscillations in the response and influence the desired dynamic response [43].

Optimal control. Thanks to its robustness, the LQR control has been widely used in the industry, especially from the 2000s to the present day [44]. It is based on maximizing or minimizing a performance criterion (depending on how the Hamiltonian is defined) [37]. Studies have already been conducted on the LQR control [38, 39, 44], where simulation results have shown that this technique offers high performance by eliminating the gap in the state trajectory. It also allows for tracking the reference with zero steady-state error in a settling time of less than one second, and with minimal effort [39]. Carried out robustness testing against parameter uncertainties and external disturbances, where the LQR control showed very satisfactory performance, with tolerance ranging from 30 % to 90 % uncertainty and complete rejection of external disturbances.

However, the only inevitable issue when designing an LQR controller for different dynamics lays in the systematic determination of the parameters of the performance matrices Q and R [44]. Therefore, it can be said that optimal control is a promising choice to control an EV.

This contribution not only focuses on ensuring high performance of the EV, but also on service continuity by combining the advantages of the DSIM and LQR. By leveraging the strengths of both LQR and the DSIM, such as precise speed tracking, minimal overshoot and high precision offered by LQR, along with the capability of working with DSIM even under phase faults, this approach ensures a seamless operation of the EV system, maintaining superior performance and robustness in various operating conditions.

Given the comparison above, the DSIM will be controlled by a LQR, which will replace the traditional PI controller in the FOC system for speed regulation.

Modeling of the DSIM. The stator consists of two pairs of windings shifted by 30°, and a short-circuited rotor as a classical induction motor. The spatial representation of the windings of the DSIM is illustrated on the Fig. 2, where L_r, L_s are the rotor and stator inductances, R_r, R_s are the rotor and stator resistances.

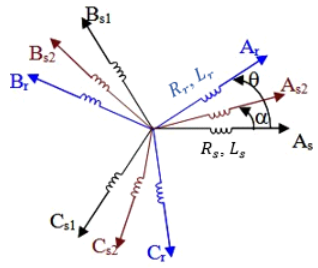

Fig. 2. Spatial representation of the DSIM windings

The dynamic of the DSIM in the *d-q* reference can be divided into three categories of equations.

1) Electric equations:

$$\begin{cases} V_{ds1} = R_{s1} i_{ds1} + \mathrm{d}\Phi_{ds1}/\mathrm{d}t - \omega_s \Phi_{qs1}; \\ V_{ds2} = R_{s2} i_{ds2} + \mathrm{d}\Phi_{ds2}/\mathrm{d}t - \omega_s \Phi_{qs2}; \\ V_{qs1} = R_{s1} i_{qs1} + \mathrm{d}\Phi_{qs1}/\mathrm{d}t + \omega_s \Phi_{ds1}; \\ V_{qs2} = R_{s2} i_{qs2} + \mathrm{d}\Phi_{qs2}/\mathrm{d}t + \omega_s \Phi_{ds2}; \\ 0 = R_r i_{dr} + \mathrm{d}\Phi_{dr}/\mathrm{d}t - (\omega_s - \omega_r)\Phi_{qr}; \\ 0 = R_r i_{qr} + \mathrm{d}\Phi_{qr}/\mathrm{d}t + (\omega_s - \omega_r)\Phi_{dr}, \end{cases} \quad (1)$$

where V_{ds1}, V_{qs1}, V_{ds2}, V_{qs2} are respectively the stator voltages in the *d-q* axis; R_{s1}, R_{s2} are the stator resistances; L_{s1}, L_{s2} are the stator inductances; i_{ds1}, i_{qs1}, i_{ds2}, i_{qs2} are the components of the stator currents in the *d-q* axis; i_{dr}, i_{qr} are the rotor currents in the *d-q* axis; Φ_{ds1}, Φ_{qs1}, Φ_{ds2}, Φ_{qs2} are the components of the stator flux in the *d-q* axis; Φ_{dr}, Φ_{qr} are the rotor fluxes in the *d-q* axis; R_r is the rotor resistance; ω_s, ω_r are the stator and rotor angular speeds.

2) Magnetic equations:

$$\begin{cases} \Phi_{ds1} = L_{s1} i_{ds1} + L_m (i_{ds1} + i_{ds2} + i_{dr}); \\ \Phi_{ds2} = L_{s2} i_{ds2} + L_m (i_{ds1} + i_{ds2} + i_{dr}); \\ \Phi_{qs1} = L_{s1} i_{qs1} + L_m (i_{qs1} + i_{qs2} + i_{qr}); \\ \Phi_{qs2} = L_{s2} i_{qs2} + L_m (i_{qs1} + i_{qs2} + i_{qr}); \\ \Phi_{dr} = L_r i_{dr} + L_m (i_{ds1} + i_{ds2} + i_{dr}); \\ \Phi_{qr} = L_r i_{qr} + L_m (i_{qs1} + i_{qs2} + i_{qr}), \end{cases} \quad (2)$$

where L_r is the rotor inductance; L_m is the mutual inductance.

3) Mechanical equations.

The electromagnetic torque is given as:

$$C_{em} = p\left(\Phi_{ds1} i_{qs1} - \Phi_{qs1} i_{ds1} + \Phi_{ds2} i_{qs2} - \Phi_{qs2} i_{ds2}\right), \quad (3)$$

where p is the number of pole pairs.

The rotation dynamic is given as:

$$\frac{\mathrm{d}\Omega}{\mathrm{d}t} = \frac{1}{J}\left(C_{em} - C_r - F_r \cdot \Omega\right), \quad (4)$$

where Ω is the rotor angular speed; J is the moment of inertia; C_r is the load torque; F_r is the friction coefficient.

Modeling of the three levels neutral point clamped (NPC) inverter. Figure 3 illustrates a three-level inverter. A multi-level inverter typically contains $(n–1)$ capacitors in the DC link, $(n–1)(n–2)$ clamping diodes, and $2(n–1)$ switches. Therefore, a three-level inverter requires 2 balancing capacitors, 2 clamping diodes, and 4 switches multiplied by 3 (number of phases). This gives us a total of 6 diodes and 12 switches. Table 1 summarizes the possible switching sequences.

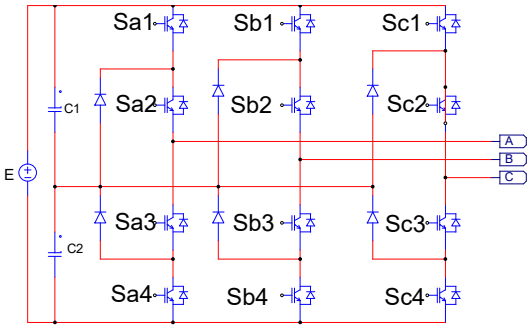

Fig. 3. Three phases three levels NPC inverter

Table 1

Possible sequences of three levels NPC inverter

K_1	K_2	K_3	K_4	V_{a0}
1	1	0	0	$E/2$
0	1	1	0	0
0	0	1	1	$–E/2$

Optimal control by LQR. In this section, instead of using PI regulator, the LQR will be used as a speed regulator to ensure service continuity and robustness against parameters variations. To accomplish this, several steps will be taken, beginning with the general state space representation of the DSIM:

$$\begin{cases} [\dot{x}(t)] = [A]\cdot[x(t)] + [B]\cdot[u(t)]; \\ [y(t)] = [C]\cdot[x(t)] + [D]\cdot[u(t)], \end{cases} \quad (5)$$

where $[x(t)]$ is the state variable matrix, $x \in \Re^n$; $[A]$ is the state parameters matrix, $A \in \Re^{n \times n}$; $[B]$ is the control matrix, $B \in \Re^{n \times m}$; $[u(t)]$ is the control vector, $u \in \Re^m$; $[C]$ is the observation matrix; $[D]$ is the direct action matrix; $[y(t)]$ is the output matrix. While:

$$[x(t)] = \begin{bmatrix} \Phi_{ds1} & \Phi_{ds2} & \Phi_{qs1} & \Phi_{qs2} & \Phi_{dr} & \Phi_{qr} \end{bmatrix}^T;$$

$$[u(t)] = \begin{bmatrix} V_{ds1} & V_{ds2} & V_{qs1} & V_{qs2} & 0 & 0 \end{bmatrix}^T.$$

The optimality criterion can be expressed as:

$$j(u(t)) = \int_0^\infty \left[x^T \cdot Q \cdot x + u^T \cdot R \cdot u\right] \mathrm{d}t. \quad (6)$$

In the case there are constraints, to obtain the optimal feedback coefficient, we must solve the following Ricatti matrix equation:

$$A^T \cdot P + P \cdot A - P \cdot B \cdot R^{-1} \cdot B^T \cdot P + Q = 0. \quad (7)$$

The introduction of the minimization criterion in Ricatti equation make it as follows:

$$A^T \cdot P + P \cdot A - P \cdot B \cdot R^{-1} \cdot B^T \cdot P + C^T \cdot Q \cdot C = 0. \quad (8)$$

While:

$$R = 0.1 \cdot \begin{bmatrix} 1 & 1 & 1 & 1 & 1 & 1 \\ 1 & 1 & 1 & 1 & 1 & 1 \\ 1 & 1 & 1 & 1 & 1 & 1 \\ 1 & 1 & 1 & 1 & 1 & 1 \\ 1 & 1 & 1 & 1 & 1 & 1 \\ 1 & 1 & 1 & 1 & 1 & 1 \end{bmatrix}; \quad Q = 2 \cdot \begin{bmatrix} 1 & 0 & 0 & 0 & 0 & 0 \\ 0 & 1 & 0 & 0 & 0 & 0 \\ 0 & 0 & 1 & 0 & 0 & 0 \\ 0 & 0 & 0 & 1 & 0 & 0 \\ 0 & 0 & 0 & 0 & 1 & 0 \\ 0 & 0 & 0 & 0 & 0 & 1 \end{bmatrix};$$

$$B = \begin{bmatrix} 1 & 0 & 0 & 0 & 0 & 0 \\ 0 & 1 & 0 & 0 & 0 & 0 \\ 0 & 0 & 1 & 0 & 0 & 0 \\ 0 & 0 & 0 & 1 & 0 & 0 \\ 0 & 0 & 0 & 0 & 0 & 0 \\ 0 & 0 & 0 & 0 & 0 & 0 \end{bmatrix};$$

$$C = \begin{bmatrix} \frac{\alpha_1}{\gamma} & \frac{-L_m L_r}{\gamma} & 0 & 0 & \frac{-L_m}{\delta} & 0 \\ \frac{-L_m L_r}{\gamma} & \frac{\alpha_1}{\gamma} & 0 & \frac{-L_m}{\delta} & 0 & 0 \\ 0 & 0 & \frac{\alpha_2}{\gamma} & \frac{-L_m L_r}{\gamma} & 0 & \frac{-L_m}{\delta} \\ 0 & 0 & \frac{-L_m L_r}{\gamma} & \frac{\alpha_2}{\gamma} & 0 & \frac{-L_m}{\delta} \\ \frac{-L_m}{\delta} & \frac{-L_m}{\delta} & 0 & 0 & \frac{2L_m L_s}{\delta} & 0 \\ 0 & 0 & \frac{-L_m}{\delta} & \frac{-L_m}{\delta} & 0 & \frac{2L_m L_s}{\delta} \end{bmatrix},$$

where:

$$\alpha_1 = L_m \cdot L_r + L_m \cdot L_{s1} + L_r \cdot L_{s1};$$
$$\alpha_2 = L_m \cdot L_r + L_m \cdot L_{s2} + L_r \cdot L_{s2};$$
$$\gamma = L_m \cdot L_s^2 + L_r \cdot L_s^2 + 2 \cdot L_m \cdot L_r \cdot L_s;$$
$$\delta = 2 \cdot L_m \cdot L_r + L_m \cdot L_s + L_r \cdot L_s;$$
$$L_s = L_{s1} = L_{s2},$$

where L_m is the magnetizing inductance.

The optimal gain can be expressed as:

$$K_{opt} = -R^{-1} \cdot B^T \cdot P. \quad (9)$$

New optimal gain will be calculated starting from K_{opt} which will equal the sum of elements of K_{opt}

$$K_{1opt} = \sum K_{opt}. \quad (10)$$

The control law equal:

$$U_{opt} = -K_{1opt} \cdot [X]. \quad (11)$$

As K_{1opt} is defined, also U_{1opt} will also be defined in the same way:

$$U_{1opt} = \sum U_{opt}. \quad (12)$$

The optimal controller will be used in the control loop as shown in Fig. 4, the global control scheme – in Fig. 5.

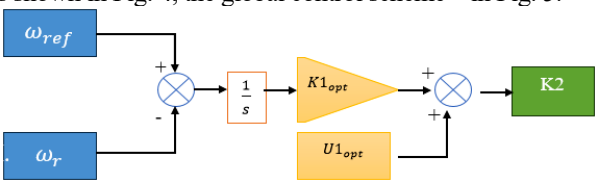

Fig. 4. Optimal control loop

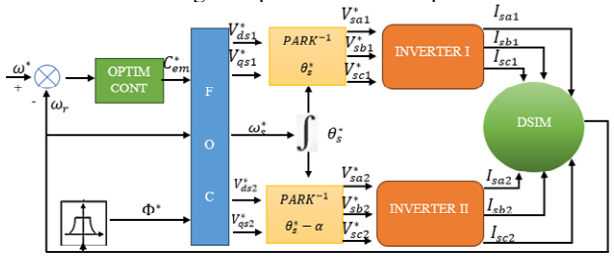

Fig. 5. LQR global regulation loop with FOC

Simulation results. The simulation investigates into the evaluation of the LQR implemented on a control system of the DSIM. It includes 3 distinct tests.

Test 1. The precision in tracking reference speed, settling time, and overshoot are examined to gauge the regulator's performance under different conditions.

Test 2. The regulator's resilience against parameter variations such as stator resistance, rotor resistance and inertia under load torque conditions is tested, aiming to ensure stable operation amidst the fluctuations that are encountered in the real world.

Test 3. The simulation examines the regulator and the DSIM robustness against phase disturbances for enhancing its reliability in practical scenarios.

Through these meticulous assessments, valuable insights are gained into the effectiveness and durability of the LQR regulator in controlling the DSIM system across diverse operating conditions in objective to ensure service continuity and high performance against parameters variations and external disturbances.

The parameters of the DSIM used in this study are defined in Table 2.

Table 2

Parameters of the DSIM

Parameter	Value	Parameter	Value
R_s, Ω	3.72	L_r, H	0.006
R_r, Ω	2.12	L_m, H	0.4092
L_s, H	0.022	J, kg·m^2	0.0625
p	1	F_r	0.001

Test 1. Speed tracking and disturbance rejection. The motor is initiated with a reference speed $\omega_{ref} = 200$ rad/s (Fig. 6). The response shows a settling time of 0.25 s, without overshoot and a precision level of 99 %. At the moment of 0.5 s, the speed reference is transitioned to 300 rad/s. Clearly, the system demonstrates the same stabilizing time of 0.25 s, coupled with an absence of overshoot (0 %) with a precision level of 99 %. These results underscore the LQR regulator's particular ability to quickly and accurately track reference speed changes.

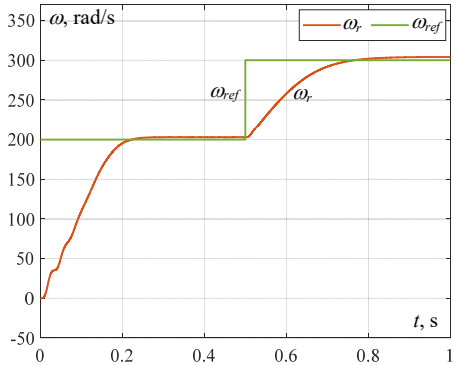

Fig. 6. Performance evaluation of LQR regulator in tracking

The current curves are observed to be non-ideal sinusoidal waveform and shifted by 120° (Fig. 7, 8). The currents of the second stator are shifted by 30° from the first stator. During the first 0.25 s, the currents undergo a transient phase before stabilizing at a peak value of 29 A. Then, at $t = 0.5$ s, the reference speed undergoes a sudden transition, reaching 300 rad/s. This change in speed results in a change in power, according to the relationship $P = C_{em} \cdot \Omega$. Consequently, the currents also evolve, reaching a lower peak value of 20 A in response to the change in speed.

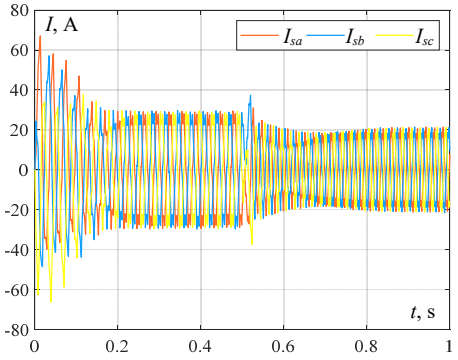

Fig. 7. Stator 1 currents

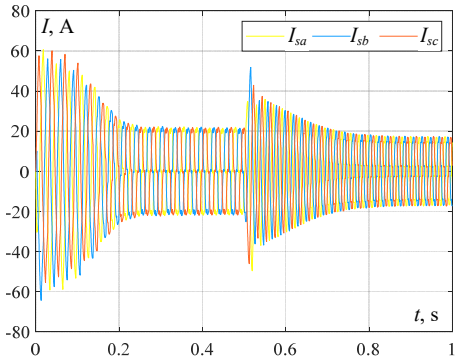

Fig. 8. Stator 2 currents

Figure 9 illustrates the response of the DSIM controlled by an LQR regulator. Initially, the system starts unloaded with a reference speed set to 150 rad/s. The DSIM reaches this target speed rapidly, within 0.2 s, achieving a precision of 99 %, with a resulting speed of 151.5 rad/s. At t = 0.5 s, a resistant torque of 10 N·m is applied, causing the speed to decrease to 148.8 rad/s. When the load torque is removed at t = 1 s, the speed recovers to 151.5 rad/s. Despite these disturbances, the DSIM demonstrates robust performance, maintaining a response precision of 99 %.

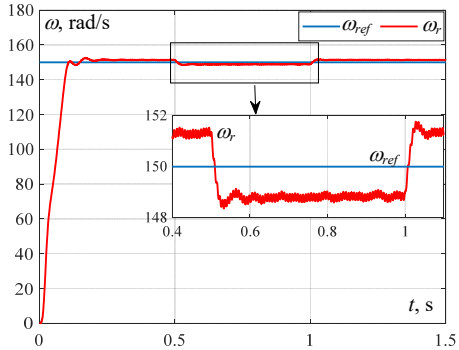

Fig. 9. Speed response of DSIM under load torque

Figure 10 shows that depicts the system's response when load torque is introduced at 0.5 s. DSIM promptly generates an electromagnetic torque equal to load torque. At t = 1 s, when the load torque is removed, the electromagnetic torque returns to 0. The system demonstrates a stabilization time of 0.1 s in both scenarios. Notably, small ripples of approximately ±8 N·m are observed around the generated torque, indicating minor fluctuations. This response highlights the DSIM's ability to swiftly adapt to load torque changes while maintaining overall stability within a tight time frame.

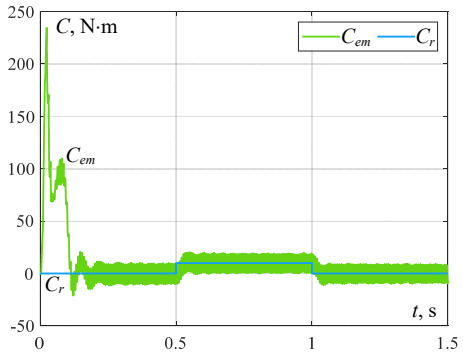

Fig. 10. DSIM torque response to load torque introduction

Test 2. Parameter variations evaluation. The simulation (Fig. 11–13) shows the response of the DSIM controlled with LQR regulator under parameters variations such as J, R_s and R_r. Initially, the motor operates with parameters R_s = 3.72 Ω, R_r = 2.12 Ω and J = 0.0625 kg·m^2. When these parameters are multiplied by 1.5 at instant t = 0.5 s, the new values become R_s = 5.58 Ω, R_r = 3.18 Ω and J = 0.09375 kg·m^2. Then, at t = 1 s, the parameters are doubled, resulting in R_s = 7.44 Ω, R_r = 4.24 Ω and J = 0.125 kg·m^2. Despite these substantial variations, the motor maintains stable performance in all scenarios. This constancy demonstrates the robustness of LQR controller against parametric changes, highlighting its ability to effectively regulate the system and minimize deviations from the set point, regardless of the conditions, thus ensuring precise and stable control of the system in changing conditions.

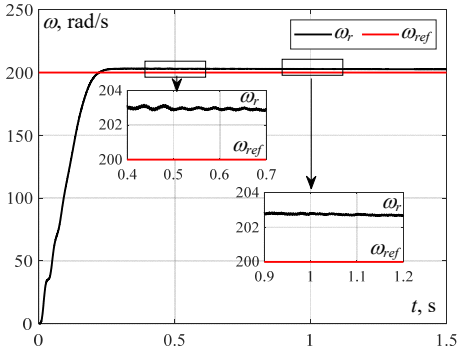

Fig. 11. Motor response under moment of inertia variations

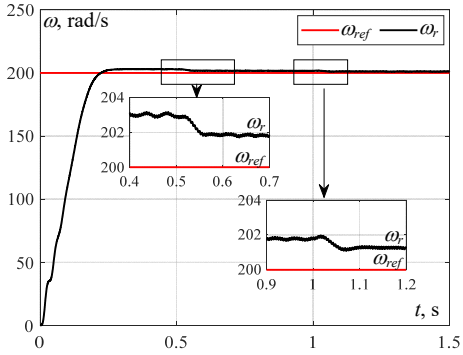

Fig. 12. Motor response under stator resistance variations

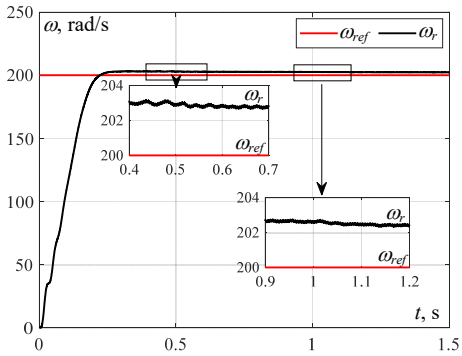

Fig. 13. Motor response under rotor resistance variations

Test 3. Phase fault evaluation. In the final test phase, the motor will start with a load torque 10 N·m, followed by the introduction of a phase fault at 1.5 s (V_a = 0), which represents challenging conditions, with a speed reference of 300 rad/s (Fig. 14). Despite the phase fault and the load torque, one can see that the DSIM continues operating with a speed value equal to 299 rad/s, ensuring service continuity. Additionally, small ripples of approximately ±1 rad/s around the reference speed are observed, highlighting the system's ability to maintain stability even under challenging and degraded conditions. The current in the faulty phase (phase A) is shown in Fig. 15. Ideally, the current in phase A should be 0, but due to interactions of magnetic fluxes, a current is induced in phase A. This phenomenon can be explained by mutual inductance, where the changing magnetic field produced by currents in other phases induces a current in the faulty phase.

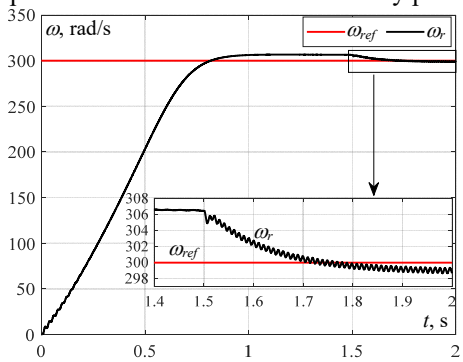

Fig. 14. Speed under load torque and phase fault

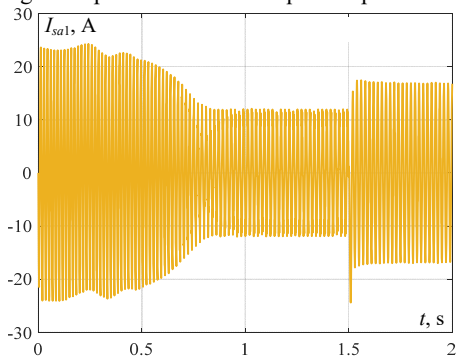

Fig. 15. Fault phase current I_{sa1}

Conclusions. The evaluation of the Linear Quadratic Regulator (LQR) applied to the dual star induction motor system (DSIM) through a series of rigorous tests has yielded promising results. In the precision test, the LQR regulator showcased high accuracy in tracking reference speed changes with zero overshoot and swift stabilization times, ensuring precise control. Furthermore, the robustness test against parameter variations demonstrated the regulator's resilience, maintaining stable motor performance even with doubled stator and rotor resistances and inertia. Additionally, the introduction of load torque displayed the system's ability to swiftly adapt while sustaining stable performance. Moreover, in the face of a phase fault and load torque at the same time, the DSIM maintained almost the same speed, with minor fluctuations around the reference speed, ensuring service continuity and stability. These results affirm the effectiveness and reliability of the LQR regulator and the DSIM in facilitating precise control and stability applications, without the need for simplifying assumptions, thereby contributing to the advancement of electric vehicle technology.

For further developments to enhance this technique, adaptive control algorithms such as fuzzy logic or neural networks can be used to improve precision and settling time by changing current classical PI regulators by one of the adaptive algorithms.

Conflict of interest. The authors declare that they have no conflicts of interest.

REFERENCES

1. Lasocki J., Krawczyk P., Kopczyński A., Roszczyk P., Hajduga A. Analysis of the strategies for managing extended-range electric vehicle powertrain in the urban driving cycle. *Electrical Engineering & Electromechanics*, 2022, no. 1, pp. 70-76. doi: https://doi.org/10.20998/2074-272X.2022.1.10.

2. Zhu X., Zhang H., Xi J., Wang J., Fang Z. Robust speed synchronization control for clutchless automated manual transmission systems in electric vehicles. *Proceedings of the Institution of Mechanical Engineers, Part D: Journal of Automobile Engineering*, 2015, vol. 229, no. 4, pp. 424-436. doi: https://doi.org/10.1177/0954407014546431.

3. Bhavik Brahmbhatt C.K.B. Indirect Field Oriented Control of Induction Motor. *Journal of Electrical Systems*, 2024, vol. 20, no. 3s, pp. 2013-2021. doi: https://doi.org/10.52783/jes.1793.

4. Kuczmann M., Horváth K. Tensor Product Alternatives for Nonlinear Field-Oriented Control of Induction Machines. *Electronics*, 2024, vol. 13, no. 7, art. no. 1405. doi: https://doi.org/10.3390/electronics13071405.

5. Phuong Duy Nguyen, An Van Vo, Thanh Lam Le, Giang Tuyet Thi Lai. Field-oriented control strategy for induction motor drives. *Proceedings of Eastern International University Scientific Conference (EIUSC 2023)*, 2023, pp. 438-445.

6. Ahmed H., Zaidi S.H., Khan F. A Comparative Study on Different Motors used in Electric Vehicles. *Journal of Independent Studies and Research Computing*, 2022, vol. 20, no. 2, pp. 32-39. doi: https://doi.org/10.31645/JISRC.22.20.2.5.

7. Ansari A.A. A Review of Different Motor Types and Selection of One Optimal Motor for Application in EV Industry. *International Journal of Electrical and Power Engineering*, 2022, vol. 16, no. 1, pp. 1-7.

8. Volkov V.A., Antonov N.L. Refined calculation of energy modes of a frequency-regulated induction motor. *Electrical Engineering & Electromechanics*, 2024, no. 5, pp. 3-13. doi: https://doi.org/10.20998/2074-272X.2024.5.01.

9. Yildirim M., Polat M., Kurum H. A survey on comparison of electric motor types and drives used for electric vehicles. *2014 16th International Power Electronics and Motion Control Conference and Exposition*, 2014, pp. 218-223. doi: https://doi.org/10.1109/EPEPEMC.2014.6980715.

10. Hashemnia N., Asaei B. Comparative study of using different electric motors in the electric vehicles. *2008 18th International Conference on Electrical Machines*, 2008, pp. 1-5. doi: https://doi.org/10.1109/ICELMACH.2008.4800157.

11. Zeraoulia M., Benbouzid M.E.H., Diallo D. Electric Motor Drive Selection Issues for HEV Propulsion Systems: A Comparative Study. *IEEE Transactions on Vehicular Technology*, 2006, vol. 55, no. 6, pp. 1756-1764. doi: https://doi.org/10.1109/TVT.2006.878719.

12. Madichetty S., Mishra S., Basu M. New trends in electric motors and selection for electric vehicle propulsion systems. *IET Electrical Systems in Transportation*, 2021, vol. 11, no. 3, pp. 186-199. doi: https://doi.org/10.1049/els2.12018.

13. Khadar S., Kouzou A., Rezzaoui M.M., Hafaifa A. Sensorless Control Technique of Open-End Winding Five Phase Induction Motor under Partial Stator Winding Short-Circuit. *Periodica Polytechnica Electrical Engineering and Computer Science*, 2019, vol. 64, no. 1, pp. 2-19. doi: https://doi.org/10.3311/PPee.14306.

14. Marouani K., Baghli L., Hadiouche D., Kheloui A., Rezzoug A. A New PWM Strategy Based on a 24-Sector Vector Space Decomposition for a Six-Phase VSI-Fed Dual Stator Induction Motor. *IEEE Transactions on Industrial Electronics*, 2008, vol. 55, no. 5, pp. 1910-1920. doi: https://doi.org/10.1109/TIE.2008.918486.
15. Sellah M., Abdellah K., Rezaoui M.M. Investigation of SVPWM Based Sliding Mode Control Application on Dual-Star Induction Motor and Dual Open-End Winding Induction Motor. *Periodica Polytechnica Electrical Engineering and Computer Science*, 2022, vol. 66, no. 1, pp. 80-98. doi: https://doi.org/10.3311/PPee.17910.
16. Boukhalfa G., Belkacem S., Chikhi A., Benaggoune S. Direct torque control of dual star induction motor using a fuzzy-PSO hybrid approach. *Applied Computing and Informatics*, 2022, vol. 18, no. 1/2, pp. 74-89. doi: https://doi.org/10.1016/j.aci.2018.09.001.
17. Pieńkowski K. Analysis and control of dual stator winding induction motor. *Archives of Electrical Engineering*, 2012, vol. 61, no. 3, pp. 421-438. doi: https://doi.org/10.2478/v10171-012-0033-z.
18. Bouziane M., Abdelkader M. A Neural Network Based Speed Control of a Dual Star Induction Motor. *International Journal of Electrical and Computer Engineering (IJECE)*, 2014, vol. 4, no. 6. pp. 952-961. doi: https://doi.org/10.11591/ijece.v4i6.6343.
19. Layadi N., Djerioui A., Zeghlache S., Houari A., Benkhoris M.-F., Berrabah F. A Hybrid Fuzzy Sliding Mode Controller for a Double Star Induction Machine. *2018 International Conference on Communications and Electrical Engineering (ICCEE)*, 2018, pp. 1-6. doi: https://doi.org/10.1109/CCEE.2018.8634439.
20. Hadiouche D., Baghli L., Rezzoug A. Space-vector PWM techniques for dual three-phase AC machine: analysis, performance evaluation, and DSP implementation. *IEEE Transactions on Industry Applications*, 2006, vol. 42, no. 4, pp. 1112-1122. doi: https://doi.org/10.1109/TIA.2006.877737.
21. Boukhalfa G., Belkacem S., Chikhi A., Bouhentala M. Fuzzy-second order sliding mode control optimized by genetic algorithm applied in direct torque control of dual star induction motor. *Journal of Central South University*, 2022, vol. 29, no. 12, pp. 3974-3985. doi: https://doi.org/10.1007/s11771-022-5028-3.
22. Benayache R. *Contribution à la commande robuste des systèmes non linéaires incertains application à un système hydraulique*. Thèse de doctorat, Université de Valenciennes et du Hainaut Cambrésis, France, 2007. 200 p. (Fra).
23. Yunfei L., Chengning Z. A Comparative Experimental Analysis of PMSM between Deadbeat Prediction Current Control and Field-oriented Control. *Energy Procedia*, 2019, vol. 158, pp. 2488-2493. doi: https://doi.org/10.1016/j.egypro.2019.01.382.
24. Guo Z., Zhang J., Sun Z., Zheng C. Indirect Field Oriented Control of Three-phase Induction Motor Based on Current-source Inverter. *Procedia Engineering*, 2017, vol. 174, pp. 588-594. doi: https://doi.org/10.1016/j.proeng.2017.01.192.
25. Akyol I.E., Soylemez M.T. Position Sensorless Field Oriented Control of IPMSM Under Parameter Uncertainties. *IFAC-PapersOnLine*, 2017, vol. 50, no. 1, pp. 14501-14506. doi: https://doi.org/10.1016/j.ifacol.2017.08.2301.
26. Bohari A.A., Utomo W.M., Haron Z.A., Zin N.M., Sim S.Y., Ariff R.M. Speed Tracking of Indirect Field Oriented Control Induction Motor Using Neural Network. *Procedia Technology*, 2013, vol. 11, pp. 141-146. doi: https://doi.org/10.1016/j.protcy.2013.12.173.
27. Chang G.W., Hespanha J.P., Morse A.S., Netto M.S., Ortega R. Supervisory field-oriented control of induction motors with uncertain rotor resistance. *International Journal of Adaptive Control and Signal Processing*, 2001, vol. 15, no. 3, pp. 353-375. doi: https://doi.org/10.1002/acs.671.
28. Pradeep Kumar M., Sirisha S., Chandramouly M. Design of PMSM base on DTC method with MRAS. *International Journal of Engineering Research and Applications*, 2013, vol. 3, no. 5, pp. 282-287.
29. Alwi H., Edwards C., Pin Tan C. *Fault Detection and Fault-Tolerant Control Using Sliding Modes*. Springer London, 2011. 340 p. doi: https://doi.org/10.1007/978-0-85729-650-4.
30. Li X., Zhang Z., An J., Zhou X., Hu G., Zhang G., Man W. Adaptive sliding mode control of modular self-reconfigurable spacecraft with time-delay estimation. *Defence Technology*, 2022, vol. 18, no. 12, pp. 2170-2180. doi: https://doi.org/10.1016/j.dt.2021.12.005.
31. Pal P., Jin G.G., Bhakta S., Mukherjee V. Adaptive chaos synchronization of an attitude control of satellite: A backstepping based sliding mode approach. *Heliyon*, 2022, vol. 8, no. 11, art. no. e11730. doi: https://doi.org/10.1016/j.heliyon.2022.e11730.
32. Ibrar A., Ahmad S., Safdar A., Haroon N. Efficiency enhancement strategy implementation in hybrid electric vehicles using sliding mode control. *Electrical Engineering & Electromechanics*, 2023, no. 1, pp. 10-19. doi: https://doi.org/10.20998/2074-272X.2023.1.02.
33. Li H.Y., Hu Y.A. Robust sliding-mode backstepping design for synchronization control of cross-strict feedback hyperchaotic systems with unmatched uncertainties. *Communications in Nonlinear Science and Numerical Simulation*, 2011, vol. 16, no. 10, pp. 3904-3913. doi: https://doi.org/10.1016/j.cnsns.2011.02.031.
34. Prasad K.M.A., Unnikrishnan A., Nair U. Fuzzy Sliding Mode Control of a Switched Reluctance Motor. *Procedia Technology*, 2016, vol. 25, pp. 735-742. doi: https://doi.org/10.1016/j.protcy.2016.08.167.
35. Najim K. *Commande adaptative des processus industriels*. Masson, Paris, 1997. 120 p. (Fra).
36. Nguyen N.T. *Model-Reference Adaptive Control*. Springer International Publishing, 2018. 444 p. doi: https://doi.org/10.1007/978-3-319-56393-0.
37. Alekseev V., Tikhomirov V., Fomin S. *Optimal control*. Moscow, Mir Publ., 1982. 447 p. (Rus).
38. Wu S., Zhang R. Improved LQ Tracking Control Design for Industrial Processes Under Uncertainty: The Extended Nonminimal State Space Approach. *IEEE Transactions on Systems, Man, and Cybernetics: Systems*, 2022, vol. 52, no. 2, pp. 1356-1360. doi: https://doi.org/10.1109/TSMC.2020.3014839.
39. Elkhatem A.S., Engin S.N. Robust LQR and LQR-PI control strategies based on adaptive weighting matrix selection for a UAV position and attitude tracking control. *Alexandria Engineering Journal*, 2022, vol. 61, no. 8, pp. 6275-6292. doi: https://doi.org/10.1016/j.aej.2021.11.057.
40. Khemis A., Boutabba T., Drid S. Model reference adaptive system speed estimator based on type-1 and type-2 fuzzy logic sensorless control of electrical vehicle with electrical differential. *Electrical Engineering & Electromechanics*, 2023, no. 4, pp. 19-25. doi: https://doi.org/10.20998/2074-272X.2023.4.03.
41. Yin Y., Liu L., Hu Z., Lin H., Wu L. Adaptive Optimal Control for PMSM Servo System. *Lecture Notes in Electrical Engineering*, 2024, vol. 1034, pp. 131-151. doi: https://doi.org/10.1007/978-3-031-53188-0_7.
42. El-samahy A.A., Shamseldin M.A. Brushless DC motor tracking control using self-tuning fuzzy PID control and model reference adaptive control. *Ain Shams Engineering Journal*, 2018, vol. 9, no. 3, pp. 341-352. doi: https://doi.org/10.1016/j.asej.2016.02.004.
43. Rajesh R., Deepa S.N. Design of direct MRAC augmented with 2 DoF PIDD controller: An application to speed control of a servo plant. *Journal of King Saud University - Engineering Sciences*, 2020, vol. 32, no. 5, pp. 310-320. doi: https://doi.org/10.1016/j.jksues.2019.02.005.
44. Ganesh V., Vasu K., Bhavana P. LQR based load frequency controller for two area power system. *International Journal of Advanced Research in Electrical, Electronics and Instrumentation Engineering*, 2012, vol. 1, no. 4, pp. 262-269.

Received 06.07.2024
Accepted 13.09.2024
Published 02.03.2025

Z. Darsouni [1], *PhD Student,*
S.E. Rezgui [1], *Doctor of Technical Science,*
H. Benalla [1], *Professor,*
F. Rebahi [2], *Doctor of Technical Science,*
M.A.M. Boumendjel [1], *PhD Student,*
[1] Laboratory of Electrical Engineering of Constantine (LEC), Technology Sciences Faculty,
University Freres Mentouri Constantine 1, Algeria,
e-mail: darsounizakaria@gmail.com (Corresponding Author).
[2] Department of Electronic, Electrical Engineering and Automatic, National Polytechnic School of Constantine, Algeria.

How to cite this article:
Darsouni Z., Rezgui S.E., Benalla H., Rebahi F., Boumandjel M.A.M. Ensuring service continuity in electric vehicles with vector control and linear quadratic regulator for dual star induction motors. *Electrical Engineering & Electromechanics*, 2025, no. 2, pp. 24-30. doi: https://doi.org/10.20998/2074-272X.2025.2.04

UDC 621.314 https://doi.org/10.20998/2074-272X.2025.2.05

N. Hadjidj, M. Benbrahim, D. Ounnas, L.H. Mouss

Global maximum power point tracking method for photovoltaic systems using Takagi-Sugeno fuzzy models and ANFIS approach

Introduction. *A new global maximum power point tracking (GMPPT) control strategy for a solar photovoltaic (PV) system, based on the combination of Takagi-Sugeno (T-S) fuzzy models and an ANFIS, is presented. The* ***novelty*** *of this paper lies in the integration of T-S fuzzy models and the ANFIS approach to develop an efficient GMPPT controller for a PV system operating under partial shading conditions.* ***Purpose****. The new GMPPT control strategy aims to extract maximum power from the PV system under varying weather conditions or partial shading.* ***Methods****. An ANFIS algorithm is used to determine the maximum voltage, which corresponds to the actual maximum power point, based on PV voltage and current. Next, the nonlinear model of the PV system is employed to design the T-S fuzzy controller. A reference model is then derived based on the maximum voltage. Finally, a tracking controller is developed using the reference model and the T-S fuzzy controller. The stability of the overall system is evaluated using Lyapunov's method and is represented through linear matrix inequalities expressions. The* ***results*** *clearly demonstrate the advantages of the proposed GMPPT-based fuzzy control strategy, showcasing its high performance in effectively reducing oscillations in various steady states of the PV system, ensuring minimal overshoot and a faster response time. In addition, a comparative analysis of the proposed GMPPT controller against conventional algorithms, such as Incremental Conductance, Perturb & Observe and Particle Swarm Optimization, shows that it offers a fast dynamic response in finding the maximum power with significantly less oscillation around the maximum power point.* References 20, tables 3, figures 14.
Key words: **photovoltaic system, maximum power point tracking, Takagi-Sugeno fuzzy model, linear matrix inequalities.**

Вступ*. Представлена нова глобальна стратегія відстеження точки максимальної потужності (GMPPT) для сонячної фотоелектричної (PV) системи, заснована на комбінації нечітких моделей Такагі-Сугено (T-S) і ANFIS.* ***Новизна*** *статті полягає в інтеграції нечітких моделей T-S і підходу ANFIS для розробки ефективного контролера GMPPT для PV системи, що працює в умовах часткового затінення.* ***Мета****. Нова стратегія контролю GMPPT спрямована на отримання максимальної потужності від PV системи за змінних погодних умов або часткового затінення.* ***Методи****. Алгоритм ANFIS використовується для визначення максимальної напруги, яка відповідає фактичній точці максимальної потужності, на основі PV напруги та струму. Далі нелінійна модель PV системи використовується для розробки нечіткого контролера T-S. Потім на основі максимальної напруги виводиться еталонна модель. Нарешті, контролер стеження розроблено з використанням еталонної моделі та нечіткого контролера T-S. Стійкість системи в цілому оцінюється за допомогою методу Ляпунова і представляється у вигляді лінійних матричних нерівностей.* ***Результати*** *чітко демонструють переваги запропонованої стратегії нечіткого керування на основі GMPPT, демонструючи її високу продуктивність щодо ефективного зменшення коливань у різних сталих станах PV системи, забезпечуючи мінімальне перерегулювання та швидший час відгуку. Крім того, порівняльний аналіз пропонованого контролера GMPPT із звичайними алгоритмами, такими як Incremental Conductance, Perturb and Observe та Particle Swarm Optimization, показує, що він пропонує швидку динамічну реакцію у пошуку максимальної потужності зі значно меншими коливаннями навколо точки максимальної потужності.* Бібл. 20, табл. 3, рис. 14.
Ключові слова: **фотоелектрична система, відстеження точки максимальної потужності, нечітка модель Такагі-Сугено, лінійні матричні нерівності.**

Introduction. Fossil energy has several drawbacks, such as environmental pollution, climate change contributions, and resource depletion. In contrast, renewable energy, like solar and wind power, offers advantages like reduced environmental impact, sustainability, and the potential for job creation and innovation in clean energy technologies. Photovoltaic (PV) solar energy offers compelling advantages. It is a clean and sustainable source with zero emissions, reducing environmental impact. Moreover, solar modules are durable, low-maintenance, and cost-effective over their long lifespan. Scalability makes PV systems versatile for diverse applications, from homes to large-scale projects. Abundant sunlight in many regions promotes energy independence, diminishing reliance on finite resources. Ongoing technological advancements further enhance efficiency and affordability, making PV solar an increasingly attractive and accessible choice for renewable energy [1, 2].

The PV system consists of solar modules that transform sunlight into DC electricity and a DC-DC converter, which plays a pivotal role by facilitating the efficient power transfer from the solar modules to the load. Its primary function is to match the varying voltage levels between the PV module and the load or storage system [3]. In essence, it optimizes power extraction from the solar modules by maintaining the output voltage at the maximum power point V_{mpp} a task typically controlled by the Maximum Power Point Tracking (MPPT) algorithm [4, 5].

Many conventional MPPTs methods have been proposed in the literature, these include Perturb and Observe (P&O) [6, 7], Incremental Conductance (InCond) [8, 9] and Hill Climbing [10]. However, each method has its application challenges and inherent disadvantages. For instance, P&O is susceptible to oscillations around the maximum power point and may result in power losses, especially under rapidly changing irradiance conditions. InCond, while more efficient, can exhibit sensitivity to noise and instability. Hill Climbing methods may struggle in partially shaded conditions and exhibit slow convergence to the optimal operating point.

Additionally, these conventional MPPT approaches may not fully exploit the potential of PV systems under dynamic environmental conditions. As a result, exploring advanced and adaptive MPPT techniques becomes crucial to overcoming these limitations and improving overall performance [11]. On the other hand, shading introduces multiple peaks and valleys in the power-voltage characteristic, leading to inaccurate MPPT operation. These conventional methods may experience slow

convergence and oscillations and may even be trapped in local maximum power points, resulting in sub-optimal energy harvesting. To address these limitations, advanced MPPT techniques, often incorporating intelligent algorithms and adaptive strategies, are increasingly explored to enhance performance in partial shading conditions [12].

Over the past few years, numerous fuzzy MPPT controllers have been suggested, leveraging Takagi-Sugeno (T-S) fuzzy models [13, 14]. The fundamental concept behind T-S fuzzy models is to represent a process by aggregating linear models, facilitating the construction of fuzzy controllers using a technique called parallel-distributed compensation (PDC) [15]. Determination of fuzzy controller gains is dependent on the stability conditions of the augmented T-S fuzzy system, which can be readily formulated as linear matrix inequalities and efficiently solved through convex optimization techniques. In [16] the InCond algorithm is utilized to ascertain the reference voltage. Subsequently, it is combined with a T-S MPPT-based fuzzy controller. Other studies, such as [17], calculated the reference voltage employing a T-S reference model incorporating, as inputs measurements of temperature and irradiation. An alternative approach involves, an MPP searching algorithm, which evaluates the changing levels of irradiation and temperature. This algorithm instantly calculates the partial power derivative which respect to the PV cell current and generates the reference state required for tracking with a PDC controller.

Purpose. This work aims to design a Global Maximum Power Point Tracking (GMPPT) controller using the adaptive ANFIS technique to accurately track the global maximum power point in the presence of partial shading. ANFIS uses PV current and PV voltage as inputs to generate the maximum voltage. Subsequently, a T-S fuzzy controller ensures maximum energy transmission, enhancing the PV system's efficiency. The efficacy of the proposed T-S fuzzy method is assessed through the total-cross-tied configuration, partial shading as well as under sudden solar irradiance changes.

PV system modeling. As seen in Fig. 1, the PV system under consideration is made up of a PV panel, a DC/DC boost converter, and a DC load.

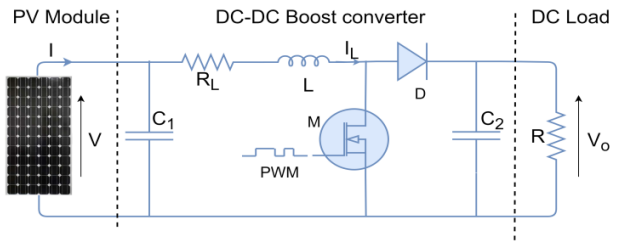

Fig. 1. PV system

PV system parameters applied in this study are as follows:

- I and V denote, respectively, the PV output current and voltage;
- i_L, i_0, V_0 and u denote, respectively, the converter's self-inductance current, load current, load voltage and duty cycle;
- C_1, C_2, L, R_L, R_m and v_d denote, respectively, the input capacitor, output capacitor, boost inductance, resistance of self-inductance, resistance characterizing the loss through the electronic switch (MOSFT) and diode's forward voltage.

PV panel model. According to the electrical circuit of PV panel (Fig. 2), the PV current can be described by [17, 18]:

$$I = n_p I_{ph} - n_p I_s \left(\exp\left(\frac{q(V + IR_s)}{AkT} \right) - 1 \right) - \frac{V + IR_s}{R_{sh}}, \quad (1)$$

where I_s is the cell saturation current in the dark; I_{ph} is the light-generated current; R_{sh} and R_s are the shunt and the cell series resistances respectively; q, k, T, n_p, A are, respectively, the electron charge, Boltzmann constant ($1.38 \cdot 10^{-23}$ J/K), cell temperature, number of parallel solar cells and the ideal factor.

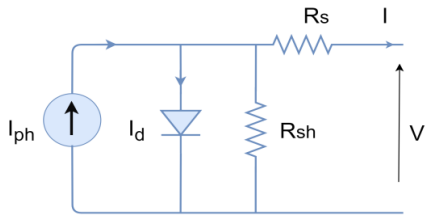

Fig. 2. Electrical equivalent model of PV module

Equation (2) describes the light-generated current I_{ph}, which is dependent on cell temperature T and sun irradiation G:

$$I_{ph} = G(I_{sc} + K_I(T - T_r)), \quad (2)$$

where I_{sc} is the cell short-circuit current at $T = 25$ °C and $G = 1$ kW/m^2; K_I, T_r, G are, respectively, the cell's short-circuit current temperature coefficient, cell's reference temperature and solar irradiation.

Conversely, the saturation current is dependent on cell temperature according to the following expression:

$$I_s = I_{rs} \left(\frac{T}{T_r} \right)^3 \exp\left[\frac{qE_g}{kA} \left(\frac{1}{T_r} - \frac{1}{T} \right) \right], \quad (3)$$

where E_g is the band-gap energy of the semiconductor used in the cell; I_{rs} is the reverse saturation current given by:

$$I_{rs} = \frac{I_{sc}}{\exp\left(\frac{qV_{oc}}{n_s kAT} \right) - 1}, \quad (4)$$

where V_{oc} is the open-circuit voltage.

The considered PV panel is simulated using the MATLAB/Simulink model illustrated in Fig. 3 with the values provided in Table 1. The PV panel is composed of 36 cells, as shown in Fig. 4.

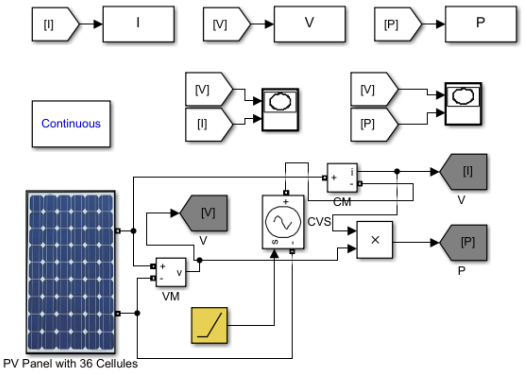

Fig. 3. Simulink model of PV panel

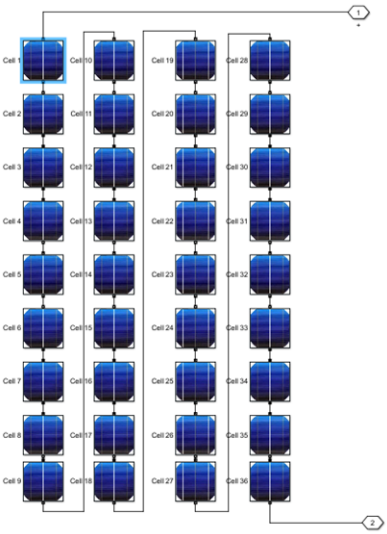

Fig. 4. Simulink model of PV panel cells

Table 1

PV panel parameters

Parameter	Value
Ideal factor of PV cell A, V	1.1
Shunt resistance R_{sh}, Ω	360
Cells connected in series n_s	36
Number of module in parallel n_p	1
Series resistance R_s, Ω	0.18
Temperature reference T_0, K	298
Irradiation reference G_0, W/m^2	100
Nominal short-circuit current I_{scn}, A	3.8
Open-circuit voltage V_{oc}, V	21.6

P-V characteristic (Fig. 5) shows the significant impact of solar irradiation and cell temperature on the fluctuation of the PV module's maximum power $P_{\max}$, which translates to an ideal PV output voltage $V_{\max} = V_{mpp}$. On the other hand, when the PV module is partially shaded, it gives rise to the occurrence of multiple operating points on its P-V characteristic plot.

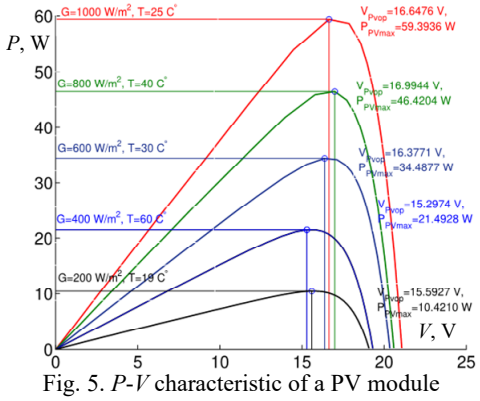

Fig. 5. P-V characteristic of a PV module

DC-DC boost converter model. The dynamic model of DC-DC boost converter can be described as [17]:

$$\begin{cases} \dot{i}_L = -\dfrac{R_L}{L} i_L + \dfrac{1}{L} V - \left(\dfrac{1-u}{L}\right)\left(V_0 + v_d - R_m i_L\right); \\ \dot{V} = -\dfrac{1}{C_1} i_L + \dfrac{1}{C_1} I. \end{cases}, \quad (5)$$

By using (5) and adding a new state, such as $\dot{u} = u_{pv}$, the PV system can be described as:

$$\dot{x}(t) = f(x(t)) + Bu(t) + \eta(t), \quad (6)$$

where

$$f(x(t)) = \begin{bmatrix} -\dfrac{R_L}{L} i_L + \dfrac{1}{L} V - \left(\dfrac{1-u}{L}\right)\left(\dfrac{V_0 + v_d - R_m i_L}{L} u_{pv}\right) \\ -\dfrac{1}{C_1} i_L \\ 0 \end{bmatrix};$$

$$x = \begin{bmatrix} i_L \\ V \\ u_{pv} \end{bmatrix}; \quad B = \begin{bmatrix} 0 \\ 0 \\ 1 \end{bmatrix}; \quad \eta = \begin{bmatrix} -\dfrac{V_0 + v_d}{L} \\ -\dfrac{1}{C_1} I \\ u_{pv} \end{bmatrix}.$$

The considered boost converter parameters are given in Table 2.

Table 2

Boost converter parameters

Parameter	Value
Output capacitor C_1, μF	50
Input capacitor C_2, μF	220
Resistance of self-inductance R_L, Ω	0.5
Resistance of IGBT characterizing R_m, Ω	0.05
Load resistance R, Ω	35
Inductor L, μH	180
Diode's forward voltage v_d, V	1.9

Proposed GMPPT method. The purpose of this study is to design a feedback controller using T-S fuzzy models and ANFIS technique that permit to maximize the output power of the PV Panel. The primary objective is to ensure that the PV system states follow $x = [i_L \;\; V \;\; u_{pv}]^T$ precisely a desired reference $x_d = [i_{Ld} \;\; V_d \;\; u_{pvd}]^T$ regardless of varying weather conditions and partial shading. The initial stage involves designing a T-S fuzzy controller using the nonlinear mathematical model of the PV system. Subsequently, a desirable reference model and a nonlinear tracking controller are determined using a maximum voltage $V_{\max} = V_{mpp}$ which can be determined using an ANFIS. Consequently, the control scheme depicted in Fig. 6 is proposed.

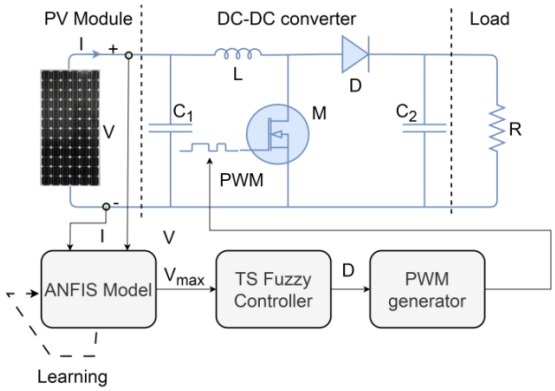

Fig .6. Control scheme of proposed GMPPT method

ANFIS design. The implementation of an ANFIS for the prediction of the maximum voltage is illustrated in Fig 7.

Simulink/SimPower models of the PV module operating in diverse climatic conditions and under various partial shading, scenarios are employed to create the training dataset for the ANFIS. These datasets encompass predictor inputs and corresponding desired output values. The system

involves two inputs, the PV voltage and PV current and a single output representing the maximum PV voltage which corresponds to the actual maximum power point. The ANFIS network formulates fuzzy rules based on a provided input-output dataset, utilizing suitable membership functions whose shape parameters are adjusted in the learning phase. The training process employs a hybrid learning method that integrates the least squares approach with the back-propagation gradient descent algorithm.

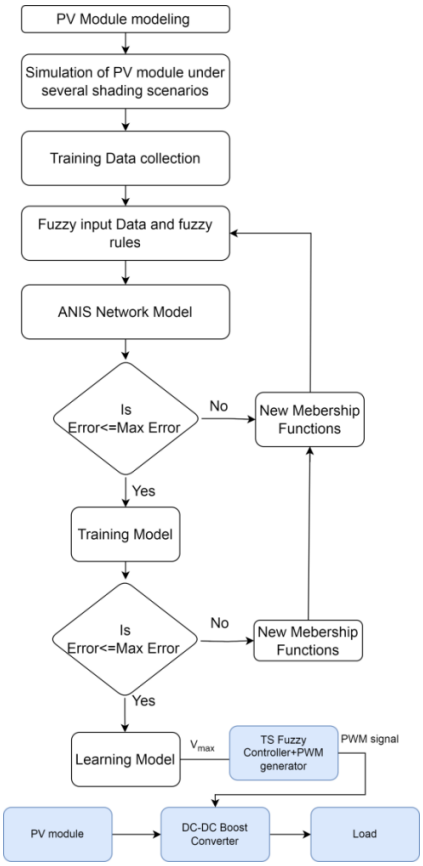

Fig. 7. ANFIS flowchart

Fuzzy modeling of the PV system. To design the feedback T-S controller, the nonlinear system given by (6) is converted into a T-S fuzzy model. This transformation is achieved by considering the converter inductance current i_L and the load voltage V_0 as decision variables. Consequently, the following state space representation is produced:

$$\dot{x}(t) = A(i_L, V_0)x(t) + Bu(t) + \eta(t), \tag{7}$$

where:

$$A = \begin{bmatrix} -\frac{R_L}{L} & \frac{1}{L} & \frac{V_0 + v_d - R_m i_L}{L} \\ -\frac{1}{C_1} & 0 & 0 \\ 0 & 0 & 0 \end{bmatrix}, B = \begin{bmatrix} 0 \\ 0 \\ 1 \end{bmatrix}, \eta = \begin{bmatrix} -\frac{V_0 + v_d}{L} \\ \frac{1}{C_1} i_{pv} \\ 0 \end{bmatrix}.$$

Assuming that the output load voltage and the boost inductance current are bounded as:

$$\underline{i}_L \le i_L \le \bar{i}_L, \quad \underline{V}_0 \le V_0 \le \overline{V}_0, \tag{8}$$

and using the nonlinearity transformation sector approach [19], the mathematical model of the PV system (7) can be given by a fuzzy models with $r = 2^n = 2^2 = 4$ If-Then rules, as follows: Rule i: If $z_1(t)$ is F_{1i} and $z_2(t)$ is F_{2i}. Then

$$\dot{x}(t) = A_i x(t) + B_i u(t) + \eta(t), \; i = 1,...,r,$$

where $z_1 = i_L$ and $z_2 = V_0$ are the premise variables, F_{11}, F_{12}, F_{21}, F_{22} are the membership functions given by:

$$\begin{cases} F_{11}(i_L) = \dfrac{i_L(t) - \underline{i}_L}{\bar{i}_L(t) - \underline{i}_L}, \quad F_{12}(i_L) = 1 - F_{11}(i_L); \\ F_{21}(V_0) = \dfrac{V_0(t) - \underline{V}_0}{\overline{V}_0(t) - \underline{V}_0}, \quad F_{22}(V_0) = 1 - F_{21}(V_0). \end{cases} \tag{9}$$

The sub-matrices are defined as:

$$A_1 = \begin{bmatrix} -\frac{R_L}{L} & \frac{1}{L} & \frac{\overline{V}_0 + v_d - R_m \underline{i}_L}{L} \\ -\frac{1}{C_1} & 0 & 0 \\ 0 & 0 & 0 \end{bmatrix}, A_2 = \begin{bmatrix} -\frac{R_L}{L} & \frac{1}{L} & \frac{\underline{V}_0 + v_d - R_m \underline{i}_L}{L} \\ -\frac{1}{C_1} & 0 & 0 \\ 0 & 0 & 0 \end{bmatrix},$$

$$A_3 = \begin{bmatrix} -\frac{R_L}{L} & \frac{1}{L} & \frac{\overline{V}_0 + v_d - R_m \underline{i}_L}{L} \\ -\frac{1}{C_1} & 0 & 0 \\ 0 & 0 & 0 \end{bmatrix}, A_4 = \begin{bmatrix} -\frac{R_L}{L} & \frac{1}{L} & \frac{\underline{V}_0 + v_d - R_m \underline{i}_L}{L} \\ -\frac{1}{C_1} & 0 & 0 \\ 0 & 0 & 0 \end{bmatrix},$$

$$B_1 = B_2 = B_3 = B_4 = \begin{bmatrix} 0 \\ 0 \\ 1 \end{bmatrix}.$$

The overall output of the T-S fuzzy model can be given by:

$$\dot{x}(t) = \sum_{i=1}^{r} h_i(z(t))(A_i x(t) + B_i u(t)) + \eta(t), \tag{10}$$

where $h_i(z) = w_i(z) \Big/ \sum_{i=1}^{r} w_j(z), w_i(z) = \prod_{j=1}^{n} F_{ij}(z_j)$ for all $t > 0$, $h_i(z) \ge 0$ and $\sum_{i=1}^{r} h_i(z) = 1$.

T-S fuzzy controller gains. The aim is to develop a feedback fuzzy controller that can steer the state of the PV system, denoted as $x(t)$, to closely match a reference model $x_d(t)$. Subsequently, the feedback tracking control must adhere to the following conditions:

$$x(t) - x_d(t) \to 0 \text{ as } t \to \infty. \tag{11}$$

The derivative of the tracking error $\dot{\tilde{x}}(t)$ can be defined as:

$$\dot{\tilde{x}}(t) = \dot{x}(t) - \dot{x}_d(t). \tag{12}$$

By substituting (10) in (12) and adding the term $\sum_{i=1}^{r} h_i(z) A_i(x(t) - x_d(t))$, equation (12) becomes:

$$\dot{\tilde{x}}(t) = \sum_{i=1}^{r} h_i(z)(A_i \tilde{x} + B_i u + A_i x_d) + \eta(t) - \dot{x}_d(t). \tag{13}$$

Equation (13) can be written as:

$$\dot{\tilde{x}}(t) = \sum_{i=1}^{r} h_i(z(t))(A_i \tilde{x}(t) + B_i \tau_u(t)), \tag{14}$$

where

$$\sum_{i=1}^{r} h_i B_i \tau_u(t) = \sum_{i=1}^{r} h_i(z)(A_i x_d(t) + B_i u(t) + \eta - \dot{x}_d(t)). \tag{15}$$

T-S feedback controllers are developed to solve the control problem as outlined below.

Controller rule i: If $z_1(t)$ is F_{1i} and $z_2(t)$ is F_{2i} Then $\tau_u(t) = -K_i \tilde{x}(t)$.

The final output of the fuzzy controller is given as:

$$\tau_u(t) = -\sum_{i=1}^{r} h_i(z(t)) K_i \tilde{x}(t). \quad (16)$$

By applying T-S control law (16) to model (14), the closed-loop system is represented as:

$$\dot{\tilde{x}}(t) = \sum_{i=1}^{r}\sum_{j=1}^{r} h_i(z(t)) h_j(z(t)) (A_i - B_i K_j) \tilde{x}(t). \quad (17)$$

By letting $G_{ij} = (A_i - B_i K_j)$, equation (17) can be expressed as:

$$\dot{\tilde{x}}(t) = \sum_{i=1}^{r}\sum_{j=1}^{r} h_i(z(t)) h_j(z(t)) G_{ij} \tilde{x}(t). \quad (18)$$

To compute the feedback controller gains K_i, the subsequent theorem is taken into consideration [20].

Theorem: T-S fuzzy system described by (18) is globally asymptotically stable if there exists a matrix $X > 0$, a diagonal matrix Q, matrices M_i and matrices Z_{ij} with: $Z_{ii} = Z_{ii}^T$ and $Z_{ji} = Z_{ij}^T$ for $i \neq j$, such that:

$$\begin{bmatrix} XA_i^T + A_i X - B_i M_i - M_i^T B_i^T + Y_{ii} & XQ^T \\ QX & -X \end{bmatrix} < 0. \quad (19)$$

$$\begin{aligned} & XA_i^T + A_i X + XA_j^T + A_j X - B_i M_j - M_j^T B_i^T \\ & - B_j M_i - M_i^T B_j^T + 2Z_{ij} \le 0, \quad i < j < r. \end{aligned} \quad (20)$$

$$\begin{bmatrix} Z_{11} & Z_{12} & \cdots & Z_{1r} \\ Z_{12} & Z_{22} & \cdots & Z_{2r} \\ \vdots & \ddots & \vdots & \vdots \\ Z_{1r} & Z_{2r} & \cdots & Z_{rr} \end{bmatrix} \equiv \tilde{z} > 0. \quad (21)$$

The feedback controller gains can be extracted as:

$$K_i = M_i X^{-1}. \quad (22)$$

Controller law and reference model. The controller law $u(t)$ and the variables of the desired reference model, represented by $x_d(t)$, can be determined through the utilization of (15), which is restated as:

$$\sum_{i=1}^{r} h_i B_i (u(t) - \tau_u(t)) = -\sum_{i=1}^{r} h_i A_i x_d(t) - \eta(t) + \dot{x}_d(t). \quad (23)$$

Noting that:

$$A(i_L, V_0) = \sum_{i=1}^{r} h_i A_i, \quad B = \sum_{i=1}^{r} h_i B_i. \quad (24)$$

Then, equation (23) can be rewritten as the following compact form:

$$B(u - \tau_u) = -A(i_L, V_0) x_d - \eta + \dot{x}_d. \quad (25)$$

In matrix notation, the equation (25) can be given as:

$$\begin{bmatrix} 0 \\ 0 \\ 1 \end{bmatrix} (u - \tau_u) = -\begin{bmatrix} -\frac{R_L}{L} & \frac{1}{L} & \alpha \\ -\frac{1}{C_1} & 0 & 0 \\ 0 & 0 & 0 \end{bmatrix} \begin{bmatrix} i_d \\ V_d \\ u_d \end{bmatrix} - \begin{bmatrix} -\beta \\ \frac{1}{C_1} i_{pv} \\ 0 \end{bmatrix} + \frac{\mathrm{d}}{\mathrm{d}t} \begin{bmatrix} i_d \\ V_d \\ u_d \end{bmatrix}. \quad (26)$$

where

$$\alpha = \frac{V_0 + V_d - R_m i_L}{L}, \quad \beta = \frac{V_0 + V_d}{L}.$$

It is important to highlight that the optimal reference and the nonlinear controller are calculated based on the optimal voltage reference which corresponds to the maximum voltage $V_d = V_{\max}$. The second equation of (26) implies:

$$i_d(V_d) = i_{pv} - C_1 \dot{V}_d. \quad (27)$$

From the initial equation in (26), it can be inferred that:

$$u_d(V_d) = \frac{1}{\alpha}\left(\frac{R_L}{L} i_d - \frac{1}{L} V_d + \beta + \dot{i}_d\right). \quad (28)$$

The nonlinear tracking control is derived from the third equation in (26), as outlined below:

$$u(V_d) = \dot{u}_d(V_d) + \tau_u. \quad (29)$$

Figure 8 shows the configuration of the proposed MPPT controller and its key components. The first block is dedicated to the calculation of the maximum voltage $V_{\max}$. This computation involves a fuzzy inference system that takes PV voltage V and PV current I measurements as inputs. Next, $V_{\max}$ is utilized by the desired reference block to produce x_d using (27) and (28). Following this, the fuzzy controller generates the fuzzy control signal utilizing (16), derived from the error $e(t)$ between the current and desired states. This generated signal is then utilized by the nonlinear controller block, employing (29) to produce the ultimate control signal. Further insights into the fuzzy inference system block will be provided in the subsequent section.

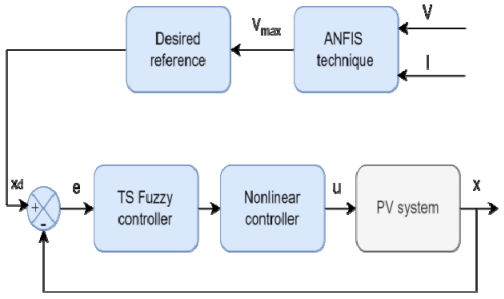

Fig. 8. Diagram of the control strategy

Simulation results. To validate the proposed method's efficacy, simulation tests of the PV system were conducted using the Simulink model (Fig. 9).

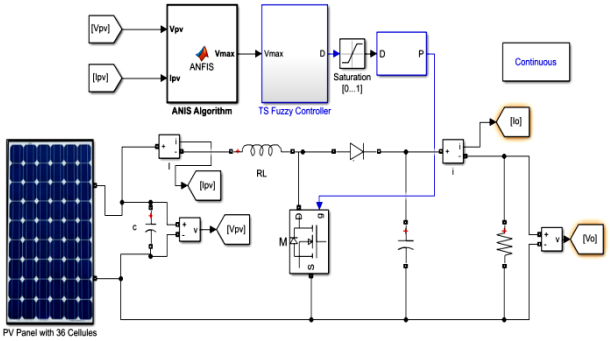

Fig. 9. Simulink model of the proposed control method

The obtained T-S feedback gains are computed as:

$$K_1 = [155.0075 \quad -0.6106 \quad 633.6307];$$
$$K_2 = [92.6114 \quad -0.1194 \quad 570.2396];$$
$$K_3 = [282.7187 \quad -0.4403 \quad 616.0382];$$
$$K_4 = [103.4164 \quad 0.3952 \quad 577.9426].$$

The maximum voltage, which corresponds to the peak power corresponding to the peak power, is calculated using an MPPT algorithm based on the ANFIS algorithm (see Fig. 7). This algorithm relies on a database constructed from the *P-V* characteristic, where fuzzy membership functions model the PV voltage and PV current. This method establishes a fuzzy relationship between these parameters and the maximum voltage.

The initial simulation is conducted under diverse conditions with variable solar radiance and temperature, assuming temperatures and irradiation levels as illustrated in Fig. 10,*a* and Fig. 10,*b*, respectively.

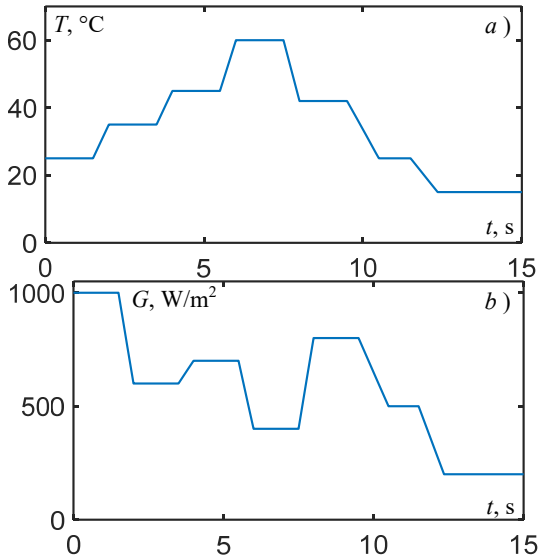

Fig. 10. Temperature (*a*) and radiance (*b*) profiles for the first test

Figures 11,*a*,*b* display the responses of PV voltage and PV power, respectively, while Fig. 11,*c*,*d* depict the responses of the boost converter current and control signal. Notably, the steady states align precisely, with the desired trajectories, remaining unaffected by variations in solar irradiation and cell temperature. This precision in tracking optimal paths contributes significantly to the enhanced extraction of available solar power and the overall performance of the system.

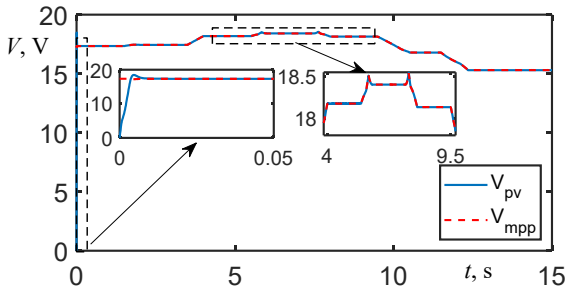

a) PV output voltage

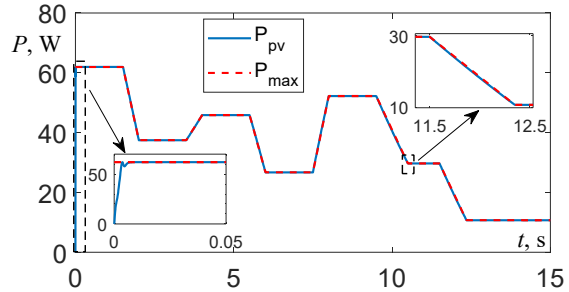

b) PV output power

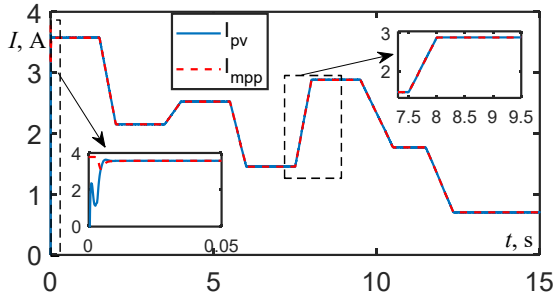

c) Inductance current of boost converter

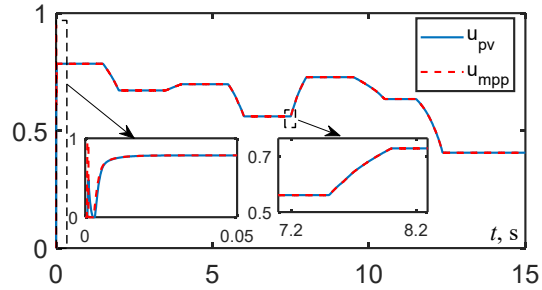

d) Duty cycle

Fig. 11.Simulation results for various atmospheric conditions

The second test involves maintaining a constant temperature while varying irradiation levels as shown in Fig. 12,*a*. The corresponding response of the output power is depicted in Fig. 12,*b*. One can clearly see that the steady states of the system exactly follow the optimal trajectories and remain consistent despite in cell temperature and sun irradiation. The precision with which the system stays on the best courses is critical to optimizing solar energy use and raising the overall system's efficiency.

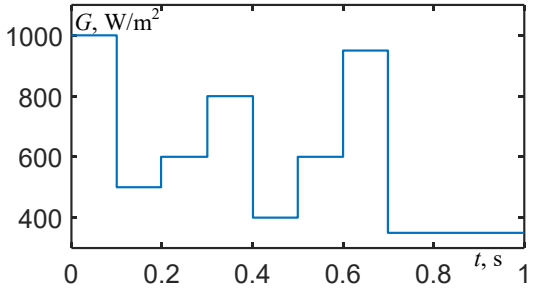

a) Irradiation profile

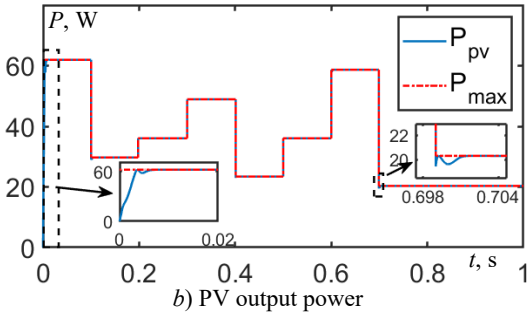

b) PV output power

Fig. 12. Simulation results for sudden change of atmospheric conditions

The third test is conducted under partial shading conditions for a PV panel consisting of 36 cells, with 4 cells shaded, maintaining a constant temperature of $T = 25$ °C and solar irradiation of $G = 1000$ W/m². *P-V* characteristic curve reveals 2 maximum power points: a local maximum of 29.91 W and a global maximum of 52.76 W (Fig. 13,*a*). To assess its performance, the proposed fuzzy method is

compared to conventional methods such as P&O, IncCond, and Particle Swarm Optimization (PSO). Figure 13,*b* presents the responses of the PV output power under partial shading conditions.

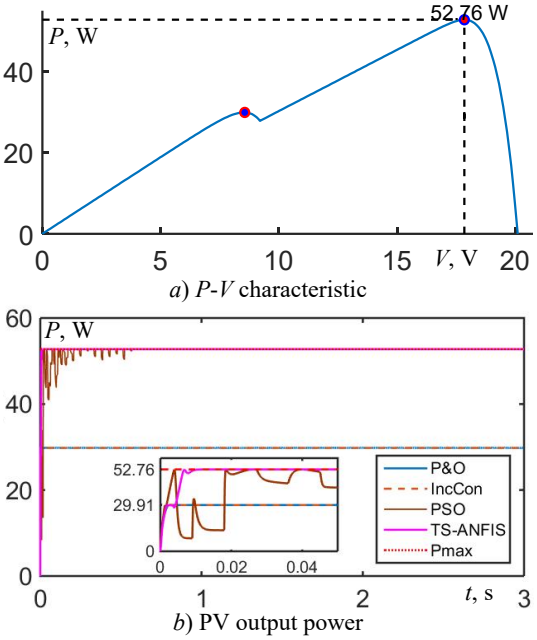

Fig. 13. Simulation results for the third test

One can clearly see that the PSO as well as the proposed methods can identify the global maximum amid various local maxima and quickly stabilize at the maximum global. However, the proposed controller exhibits a rapid response time, efficiently locating and maintaining the global maximum without oscillations. Moreover, conventional methods such as P&O and IncCond tend to stabilize at the minimum power.

The fourth test is conducted under partial shading conditions for a PV panel consisting of 36 cells, with 8 cells shaded, maintaining a constant temperature of $T = 25$ °C and solar irradiation of G = 1000 W/m². P-V characteristic curve reveals 3 maximum power points, including 2 local maxima of 37.86 W and 21.37 W, along with a global maximum of 40.86 W (Fig. 14). Performance evaluation involves a comparison of the proposed fuzzy method with well-known methods such as P&O, IncCond and PSO.

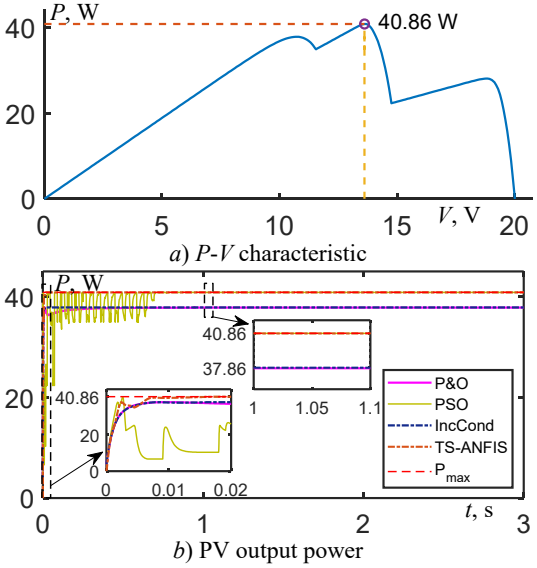

Fig. 14. Simulation results for the fourth test

Simulation tests confirm that the developed MPPT-based controller effectively guides the steady states to closely match the optimal operating points, displaying minimal oscillation. Conversely, the PV system responses under the compared methods exhibit notable fluctuations across different states.

Additionally, the performance of the proposed and comparative methods is evaluated through many indexes such as root mean square error, MPPT energetic efficiency, and MPPT energetic error.

The root mean square error is defined as:

$$E_{rms} = \sqrt{\frac{\sum_{i=1}^{N}\left(P_{pv,i} - P_{\max,i}\right)^2}{N}}. \quad (30)$$

The static efficiency:

$$\eta = \left(\frac{P_{pv}}{V_{\max}}\right)\cdot 100. \quad (31)$$

The relative tracking error:

$$\varepsilon = \left(\frac{P_{pv}}{V_{\max}}\right) - 1. \quad (32)$$

The obtained indexes for the proposed and compared methods are summarized in Table 3.

Table 3

Comparison of different MPPT methods

Index	P&O	InCond	PSO	Proposed
E_{rms}	0.2891	0.2182	0.0575	0.0215
η	46.2568	46.8910	97.1906	98.1256
e	5.2918	5.3109	2.8094	1.0295

This comparative study demonstrates the effectiveness of the proposed control strategy in overcoming the limitations associated in traditional controllers. It is demonstrates also that the proposed controller delivers a faster dynamic response, significantly reduced oscillation around the maximum power point, and overall superior performance.

Conclusions. This paper presents a highly effective Takagi-Sugeno fuzzy controller for global maximum power point tracking in PV conversion systems. This controller demonstrates the capability to guide the PV system in swiftly tracking a desired reference model with minimal oscillations during rapid weather changes and under partial shading conditions.

The desired reference model is determined by the ANFIS algorithm based on the maximum voltage. Fuzzy controller gains are computed according to specific conditions shown in linear matrix inequalities and are determined using optimization tools. Simulation results, alongside comparisons to classic Incremental Conductance, Perturb & Observe and Particle Swarm Optimization algorithms, demonstrate the effectiveness of the proposed fuzzy tracking control scheme in managing the PV system across various operating conditions. Addressing practical implementation and robustness concerns remains a focus for future research endeavors.

Conflict of interest. The authors declare that they have no conflicts of interest.

REFERENCES

1. Chen X.H., Tee K., Elnahass M., Ahmed R. Assessing the environmental impacts of renewable energy sources: A case study on air pollution and carbon emissions in China. *Journal of Environmental*

Management, 2023, vol. 345, art. no. 118525. doi: https://doi.org/10.1016/j.jenvman.2023.118525.
2. Osman A.I., Chen L., Yang M., Msigwa G., Farghali M., Fawzy S., Rooney D.W., Yap P.-S. Cost, environmental impact, and resilience of renewable energy under a changing climate: a review. *Environmental Chemistry Letters*, 2023, vol. 21, no. 2, pp. 741-764. doi: https://doi.org/10.1007/s10311-022-01532-8.
3. Youcef H., Touhami G., Omar O., Essama G.A., Slimane L. Sliding Mode based PSO MPPT for Solar PV System. *Przeglad Elektrotechniczny*, 2024, no. 1, pp. 86-90. doi: https://doi.org/10.15199/48.2024.01.18.
4. Juma'a H.G., Atyia T.H. Design a 91-Multilevel Inverter Circuit Using Solar PV System Sources. *Przeglad Elektrotechniczny*, 2023, no. 11, pp. 127-133. doi: https://doi.org/10.15199/48.2023.11.22.
5. Paquianadin V., Navin Sam K., Koperundevi G. Maximizing solar photovoltaic system efficiency by multivariate linear regression based maximum power point tracking using machine learning. *Electrical Engineering & Electromechanics*, 2024, no. 1, pp. 77-82. doi: https://doi.org/10.20998/2074-272X.2024.1.10.
6. Guiza D., Ounnas D., Soufi Y., Bouden A., Maamri M. Implementation of Modified Perturb and Observe Based MPPT Algorithm for Photovoltaic System. *2019 1st International Conference on Sustainable Renewable Energy Systems and Applications (ICSRESA)*, 2019, pp. 1-6. doi: https://doi.org/10.1109/ICSRESA49121.2019.9182483.
7. Zerzouri N., Ben Si Ali N., Benalia N. A maximum power point tracking of a photovoltaic system connected to a three-phase grid using a variable step size perturb and observe algorithm. *Electrical Engineering & Electromechanics*, 2023, vol. 5, pp. 37-46. doi: https://doi.org/10.20998/2074-272X.2023.5.06.
8. Dhaouadi G., Djamel O., Youcef S., Salah C. Implementation of Incremental Conductance Based MPPT Algorithm for Photovoltaic System. *2019 4th International Conference on Power Electronics and Their Applications (ICPEA)*, 2019, pp. 1-5. doi: https://doi.org/10.1109/ICPEA1.2019.8911186.
9. Louarem S., Kebbab F.Z., Salhi H., Nouri H. A comparative study of maximum power point tracking techniques for a photovoltaic grid-connected system. *Electrical Engineering & Electromechanics*, 2022, no. 4, pp. 27-33. doi: https://doi.org/10.20998/2074-272X.2022.4.04.
10. Jately V., Azzopardi B., Joshi J., Balaji Venkateswaran V., Sharma A., Arora S. Experimental analysis of hill-climbing MPPT algorithms under low irradiance levels. *Renewable and Sustainable Energy Reviews*, 2021, vol. 150, art. no. 111467. doi: https://doi.org/10.1016/j.rser.2021.111467.
11. Ounnas D., Guiza D., Soufi Y., Maamri M. Design and Hardware Implementation of Modified Incremental Conductance Algorithm for Photovoltaic System. *Advances in Electrical and Electronic Engineering*, 2021, vol. 19, no. 2, pp. 100-111. doi: https://doi.org/10.15598/aeee.v19i2.3881.
12. Wang Q., Chang X. Maximum Power Point Tracking of PV System Under Partial Shading Conditions Based on TSO-IP&O Algorithm. *2023 3rd International Conference on Energy, Power and Electrical Engineering (EPEE)*, 2023, pp. 155-159. doi: https://doi.org/10.1109/EPEE59859.2023.10351794.
13. Chaibi R., Bachtiri R.E., Hammoumi K.E., Yagoubi M. Photovoltaic System's MPPT Under Partial Shading Using T-S Fuzzy Robust Control. *IFAC-PapersOnLine*, 2022, vol. 55, no. 12, pp. 214-221. doi: https://doi.org/10.1016/j.ifacol.2022.07.314.
14. Moussaoui L., Aouaouda S., Rouaibia R. Fault tolerant control of a permanent magnet synchronous machine using multiple constraints Takagi-Sugeno approach. *Electrical Engineering & Electromechanics*, 2022, no. 6, pp. 22-27. doi: https://doi.org/10.20998/2074-272X.2022.6.04.
15. Guiza D., Soufi Y., Ounnas D., Metatla A. Design and Implementation of Takagi-Sugeno Fuzzy Tracking Control for a DC-DC Buck Converter. *Advances in Electrical and Electronic Engineering*, 2019, vol. 17, no. 3, pp. 234-243. doi: https://doi.org/10.15598/aeee.v17i3.3126.
16. Sekhar P.C., Mishra S. Takagi–Sugeno fuzzy-based incremental conductance algorithm for maximum power point tracking of a photovoltaic generating system. *IET Renewable Power Generation*, 2014, vol. 8, no. 8, pp. 900-914. doi: https://doi.org/10.1049/iet-rpg.2013.0219.
17. Ounnas D., Ramdani M., Chenikher S., Bouktir T. An Efficient Maximum Power Point Tracking Controller for Photovoltaic Systems Using Takagi–Sugeno Fuzzy Models. *Arabian Journal for Science and Engineering*, 2017, vol. 42, no. 12, pp. 4971-4982. doi: https://doi.org/10.1007/s13369-017-2532-0.
18. Kahsay A.H., Regulski P., Derugo P. AI-based control techniques for maximum power point tracking of photovoltaic systems using a boost converter. *Przeglad Elektrotechniczny*, 2023, no. 11, pp. 1-6. doi: https://doi.org/10.15199/48.2023.11.01.
19. Ohtake H., Tanaka K., Wang H.O. Fuzzy modeling via sector nonlinearity concept. *Integrated Computer-Aided Engineering*, 2003, vol. 10, no. 4, pp. 333-341. doi: https://doi.org/10.3233/ICA-2003-10404.
20. Ounnas D., Ramdani M., Chenikher S., Bouktir T. Optimal reference model based fuzzy tracking control for wind energy conversion system. *International Journal of Renewable Energy Research*, 2016, vol. 6, no. 3, pp. 1129-1136. doi: https://doi.org/10.20508/ijrer.v6i3.4258.g6896.

Received 25.08.2024
Accepted 24.10.2024
Published 02.03.2025

N. Hadjidj[1]*, PhD,*
M. Benbrahim[1]*, PhD, Associate Professor,*
D. Ounnas[2]*, PhD, Associate Professor,*
L.H. Mouss[1]*, Professor,*
[1] Industrial Engineering Department,
Laboratory of Automation and Manufacturing Engineering,
University of Batna 2, Algeria,
e-mail: n.hadjidj@univ-batna2.dz (Corresponding Author);
m.benbrahim@univ-batna2.dz;
h.mouss@univ-batna2.dz
[2] LABGET Laboratory, Department of Electrical Engineering,
Faculty of Technology, University of Tebessa, Algeria,
e-mail: djamel.ounnas@univ-tebessa.dz

How to cite this article:
Hadjidj N., Benbrahim M., Ounnas D., Mouss L.H. Global maximum power point tracking method for photovoltaic systems using Takagi-Sugeno fuzzy models and ANFIS approach. *Electrical Engineering & Electromechanics*, 2025, no. 2, pp. 31-38. doi: https://doi.org/10.20998/2074-272X.2025.2.05

UDC 621.314 https://doi.org/10.20998/2074-272X.2025.2.06

K. Sabhi, M. Talea, H. Bahri, S. Dani

Integrating dual active bridge DC-DC converters: a novel energy management approach for hybrid renewable energy systems

Introduction. *Hybrid renewable energy systems, which integrate wind turbines, solar PV panels, and battery storage, are essential for sustainable energy solutions. However, managing the energy flow in these systems, especially under varying load demands and climatic conditions, remains a challenge. The* ***novelty*** *of this paper is introduces a hybrid renewable energy system structure using Dual Active Bridge (DAB) DC-DC converters and an energy management strategy (EMS) to control power flow more effectively. The approach includes a dump load mechanism to handle excess energy, offering a more efficient and flexible system operation. The* ***purpose*** *of this study is to develop a novel approach to managing and controlling hybrid renewable energy systems, specifically through the use of a DAB DC-DC converter. Unlike traditional methods that may struggle with efficiency and flexibility, our approach introduces an innovative EMS that leverages a reduced neural network block for real-time optimal power tracking and a sophisticated control system to adapt to dynamic conditions. This approach aims to improve the flexibility of the system, enhance energy utilization, and address the limitations of existing methods by ensuring rapid and efficient responses to changes in load and climatic conditions. The primary goal of this study is to improve the performance and reliability of hybrid renewable energy systems by optimizing energy distribution and battery management. The strategy aims to ensure continuous energy availability, enhance battery lifespan, and improve system response to dynamic changes.* ***Methods.*** *The proposed EMS was developed and tested using MATLAB/Simulink. The system's control mechanism prioritizes battery charging when renewable energy output exceeds demand and redirects excess energy to a dump load when necessary. Simulations were conducted under various load and climatic conditions to assess system performance.* ***Results.*** *The simulation results demonstrate that the proposed strategy effectively manages energy flow, ensuring optimal power distribution, quick adaptation to load changes, and maintaining the battery's state of charge within safe limits.* ***Practical value****. The system showed improved stability and efficiency, validating the effectiveness of the control strategy in enhancing the overall performance of hybrid renewable energy systems.* References 33, tables 3, figures 13.

Key words: **hybrid renewable energy system, dual active bridge DC-DC converter, energy management strategy, maximum power point tracking.**

Вступ*. Гібридні системи відновлюваної енергетики, які об'єднують вітряні турбіни, сонячні фотоелектричні панелі та акумуляторні батареї, є важливими для стійких енергетичних рішень. Однак управління потоком енергії в цих системах, особливо за змінних вимог до навантаження та кліматичних умов, залишається проблемою.* ***Новизна*** *цієї статті полягає в представленні гібридної структури системи відновлюваної енергії з використанням подвійних активних мостів (DAB) DC-DC перетворювачів і стратегії управління енергією (EMS) для більш ефективного контролю потоку електроенергії. Цей підхід включає механізм скидання навантаження для обробки надлишкової енергії, що забезпечує більш ефективну та гнучку роботу системи.* ***Метою*** *цього дослідження є розробка нового підходу до управління та контролю гібридних систем відновлюваної енергії, зокрема за допомогою перетворювача DAB DC-DC. На відміну від традиційних методів, які можуть мати проблеми з ефективністю та гнучкістю, наш підхід запроваджує інноваційну EMS, яка використовує зменшений блок нейронної мережі для відстеження оптимальної потужності в реальному часі та складну систему керування для адаптації до динамічних умов. Цей підхід спрямований на покращення гнучкості системи, покращення використання енергії та усунення обмежень існуючих методів шляхом забезпечення швидкої та ефективної реакції на зміни навантаження та кліматичних умов. Основною метою цього дослідження є покращення продуктивності та надійності гібридних систем відновлюваної енергії шляхом оптимізації розподілу енергії та керування батареями. Стратегія спрямована на забезпечення безперервної доступності енергії, збільшення терміну служби акумулятора та покращення реакції системи на динамічні зміни.* ***Методи****. Запропонована EMS була розроблена та протестована за допомогою MATLAB/Simulink. Механізм керування системою надає пріоритет зарядці батареї, коли вихід відновлюваної енергії перевищує попит, і за необхідності перенаправляє надлишкову енергію на скидання. Для оцінки продуктивності системи було проведено моделювання за різних навантажень і кліматичних умов.* ***Результати*** *моделювання демонструють, що запропонована стратегія ефективно керує потоком енергії, забезпечуючи оптимальний розподіл потужності, швидку адаптацію до змін навантаження та підтримку стану заряду батареї в безпечних межах.* ***Практична значимість****. Система продемонструвала покращену стабільність та ефективність, підтверджуючи ефективність стратегії керування для підвищення загальної продуктивності гібридних систем відновлюваної енергії.* Бібл. 33, табл. 3, рис. 13.

Ключові слова: **гібридна система відновлюваної енергії, подвійний активний мостовий DC-DC перетворювач, стратегія управління енергією, відстеження точки максимальної потужності.**

Introduction. Renewable energy sources (RESs) are gaining increasing attention as a sustainable alternative to traditional fossil fuels, which have negative environmental impacts and limited availability. Various RESs, such as solar, wind, and hydropower, have been developed to harness clean and abundant energy from natural resources [1–5]. However, single source renewable energy systems have several limitations, such as intermittency, variability, and low efficiency. To overcome these limitations, hybrid renewable energy system (HRES) is an effective solution [6–8].

HRESs combine two or more RESs to improve the system's reliability, stability, and performance [9–11]. These systems can be configured in various ways, depending on the available RESs, system requirements, and design constraints. The most common configurations include PV/wind hybrid systems [9], PV/hydropower hybrid systems, and wind/fuel cell hybrid systems [6].

Several studies have been conducted to evaluate the performance and efficiency of different HRESs. These studies employ various methodologies, including simulation, optimization and experimental analysis [10].

In recent years, significant progress has been made in the field of HRESs, with numerous studies reporting successful implementation of these systems in various applications, such as rural electrification, microgrids and building integration [11]. However, challenges such as cost-effectiveness, scalability, and reliability still need to be addressed to facilitate the widespread adoption of HRESs [12].

In the literature we can distinguish several structures of hybrid systems based on renewable energies, there are two more useful types of hybrid system structures, specifically the DC bus structure [1–12] and the multiport converter structure [13], irrespective of their operating mode, standalone and grid-connected mode.

HRES based on ordinary DC-DC converters is a configuration that combines various RESs, including solar panels, wind turbines (WTs) and batteries [14], integrating them into a shared DC bus. This approach involves converting the energy generated by these sources into DC and merging them into a unified bus, enabling efficient energy management and optimal resource utilization [15].

Another approach looks at the implementation of a new secondary structure designed to streamline protection measures, minimizing the need for protection circuits. Another advantage of this type of structure is to ensure galvanic isolation without additional circuits [16], thereby enhancing safety and reducing electromagnetic interference.

This research embarks on a comprehensive exploration of a specific HRES configuration, strategically integrating solar panels, WT, a load and a dump load. At the heart of this integration is a battery storage system, the latter is connected to the other elements by a DC-DC Dual Active Bridge (DAB) converter, a technological cornerstone streamlining the interconnection of various energy sources [17–19]. The DAB converter, equipped with a single-phase high-frequency transformer, also strengthens the system against voltage fluctuations and other operational challenges.

The orchestration of this energetic symphony relies largely on a sophisticated control strategy. The crux of this strategy lies in the manipulation of the phase shift within each transformer. This control ensures optimal contributions from each energy source to interconnected loads, aligning with constantly fluctuating power demands. The battery storage system, the central element of this arrangement, seamlessly transitions between charging and discharging modes, acting as a stabilizing force that mitigates the impact of intermittent renewable sources.

The impact of climatic conditions on power availability is uncertain; the operating point often changes, to control the latter the DABs are controlled by a PI regulator, whose reference is precomputed by a reduced neural network block and a structural approximation which makes it possible to extract the maximum power point (MPP) of photovoltaic (PV) array [20] and WT energy [21].

The goal of the paper is to enhance the flexibility and efficiency of HRESs by developing an advanced control strategy. This approach aims to improve the adaptability of the system's structure and streamline the management of currents supplied or consumed by different components. The paper introduces a novel method for optimizing the use of RESs, utilizing a reduced neural network block for precise reference calculation. It focuses on effective energy management based on the State of Charge (SOC) of the battery and the load requirements. The proposed strategy ensures a rapid and adaptive response to load fluctuations, sudden changes in climatic conditions, and variations in energy availability. Performance evaluation is conducted through simulations using MATLAB/Simulink, with results compared to existing control strategies and management approaches.

System performance is simulated using the MATLAB/Simulink software; results were compared to the control approach to management organization charts.

System description. This paper carries out a HRES, depicted in Fig. 1, comprises a permanent magnet synchronous generator (PMSG) WT, solar PV panels, a variable load, and a dump load, these components are interconnected with a battery energy storage system each through a DAB DC-DC converter [19].

With the PV panel as the first input, the PMSG WT as the second input, the third input linked to the load, the fourth is gave to the dump load and the common and the fifth designated for the battery. The system operates independently in standalone mode.

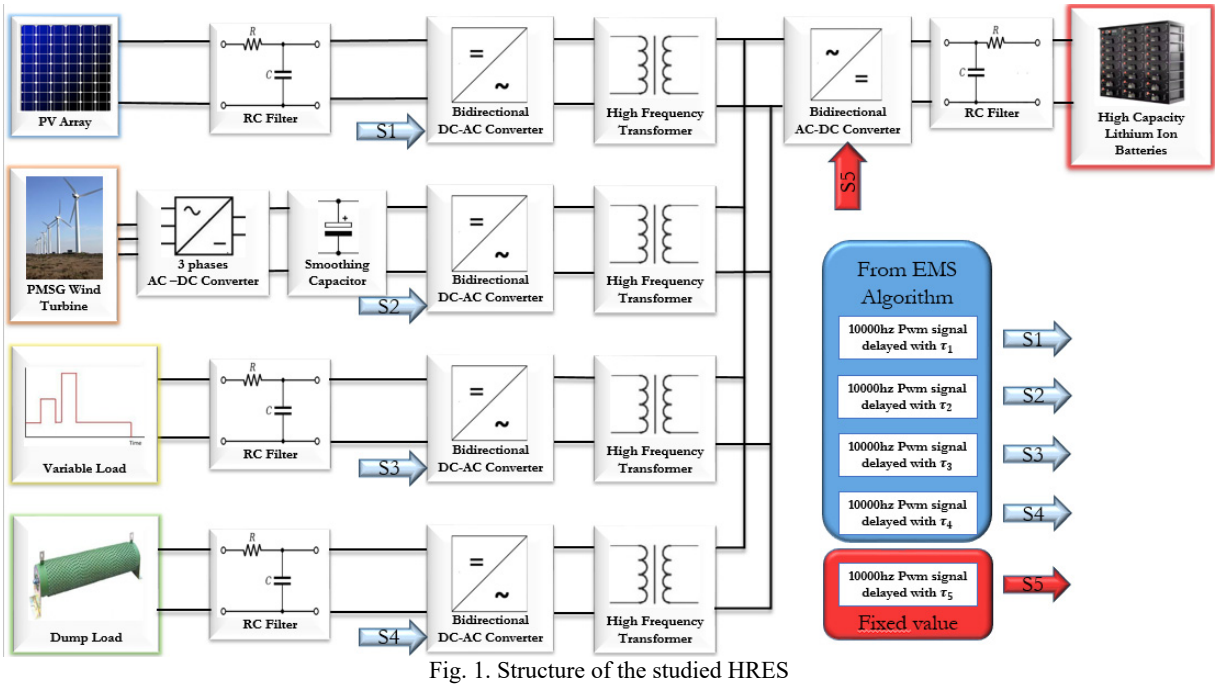

Fig. 1. Structure of the studied HRES

To regulate both the quantity and direction of power transfer, the rectangular waveforms generated exhibit controlled phase shifts with respect to each other. The relative delays, namely τ_{15} (controlling power flow from PV to the battery), τ_{25} (for power flow from the WT to the battery), τ_{35} (variable load to the battery) and τ_{45} (dump load to the battery), τ_{jk} determine the extent of phase shift. Positive values of indicate that the voltage in port j is leading the reference voltage in port k, while negative values imply the opposite.

The proposed energy management system is illustrated in Fig. 2 as a block diagram, showing its inputs and outputs. The management method in this study relies

on several key elements: it prioritizes charging the batteries when the load demand exceeds what the RESs can supply and pass the excess of power through a fixed dump resistor when the battery is maximally charged. This approach ensures the continuous availability of energy, extends the battery life cycle, and improves system efficiency.

Fig. 2. Block diagram of the energy management system

Modeling and sizing of electrical system parameters.

1. PV source. PV cell's equivalent diagram (Fig. 3) features a generator current that simulates illumination and a parallel diode representing the PN junction. The practical circuit also takes into account parasitic resistive effects due to manufacturing [22, 23].

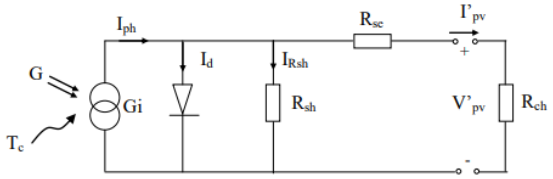

Fig. 3. Equivalent diagram of a PV cell

The solar PV module is formed by connecting PV cells in both series and parallel configurations. The current output I_{pv} from the solar PV module is determined as:

$$I_{pv} = N_p(I_{ph} - I_d e^{\left(\frac{qV_d}{N_s AkT}\right)} - 1) - \frac{V_d}{R_{sh}}, \quad (1)$$

where N_p is the number of cells in parallel; N_s is the number of cells in series; I_{ph} is the photocurrent; I_d is the reverse saturation current; V_d is the diode voltage; A is the diode ideality factor; k is the Boltzmann's constant; T is the temperature; q is the elementary charge; R_{sh} is associated with the non-ideal characteristics of the p-n junction and the presence of defects along the cell's edges that create a short-circuit path around the junction; R_{se} is the overall resistance encountered by the electrons along their path.

PV array used in this study under standard testing conditions of solar irradiance G = 1000 W/m² and a temperature of T = 25 °C (Table 1).

Table 1

Specification of the PV

Parameter	Value
Maximum power of the solar panel P_{mpp}, kW	64
Current at MPP I_{mpp}, A	110.25
Voltage at the MPP V_{mpp}, V	580
Short-circuit current I_{sc}, A	117.6
Open circuit voltage value V_{0cs}, V	726

2. WT model. Numerous mathematical models have been developed to describe the relationship between wind speed and the mechanical power generated from wind. In this study, the WT is represented as [24]:

$$P_w = \frac{1}{2}\rho A_r C_p v^3, \quad (2)$$

where P_w is the wind power extracted; ρ is the air density; A_r is the rotor area of the WT; v is the wind speed; C_p is the power coefficient. The power coefficient is influenced by the tip speed ratio λ and the pitch angle β.

Numerical approximations are utilized to compute C_p for specified values of λ and β, as shown in [24] with the following expression:

$$C_p(\lambda,\beta) = c_1\left(\frac{c_2}{\lambda_i} - c_3\beta - c_4\right)e^{-\frac{c_5}{\lambda_i}} + c_6\lambda; \quad (3)$$

$$\lambda_i = \left[\left(\frac{1}{\lambda + 0.08\beta}\right) - \left(\frac{0.035}{\beta^3 + 1}\right)\right]^{-1}. \quad (4)$$

The coefficient C_p utilized for the simulation, as referenced in [25], are: c_1=0.5176, c_2=116, c_3=0.4, c_4=5, c_5=21, c_6=0.0068. Notably, the maximum C_p (C_{pmax}) is achieved at an optimal tip speed ratio (λ_{opt}) and a pitch angle of β = 0. Additionally, a relationship linking the rotor speed to the tip speed ratio [3] is expressed as:

$$\lambda = \frac{\omega_r \cdot R}{v}, \quad (5)$$

where R is the length of the WT blade.

The characteristics of the WT at V = 12 m/s and β=0 used are presented in Table 2.

Table 2

WT specification

Parameter	Value
Maximal power P_{mpp}, kW	100
Density of air ρ, kg/m^3	1.12
Radius of rotor R, m	8.28
Turbine total inertia, kg·m^2	0.1
Total viscous friction, N·s/m^2	0.0004924

3. Dual active bridge. Figure 4 shows a typical full-bridge DAB DC/DC converter that interfaces between two voltage sources and its equivalent circuit. The two actively controlled full bridges are connected via a high-frequency transformer [26]. The power inductor L_s, which includes the leakage inductance, serves as the main energy transfer device.

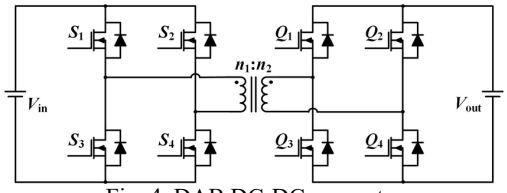

Fig. 4. DAB DC-DC converter

DAB converter is characterized by its easy control, high efficiency, high power density and galvanic isolation ensures by the transformer.

The power transfer between the two windings, represented as P_{jk}, is regulated using a simple-phase-shift technique [27]. This relationship is described by the following equation, while admitting that n_1=n_2:

$$P_{jk} = \frac{V_j V_k D_{jk}(1-|D_{jk}|)}{2 f_s L_{jk}}; \quad |D_{jk}| \le 1, \tag{6}$$

$$D_{jk} = 2\frac{\tau_{jk}}{T_s}; \tag{7}$$

$$\tau_{jk} = (\tau_k - \tau_j), \tag{8}$$

where τ_{jk} is the relative delay between the square wave signals from inverters j and k; τ_k and τ_j are the absolute delays of the signals V_k and V_j, respectively; T_s is the period of the square wave signals, also known as the switching period [27].

Assuming the following equality based on (7), (8):

$$D_{jk} = D_k - D_j. \tag{9}$$

MPPT method. Application on PV generator. This part of the energy management process begins with setting the irradiance G = 1000 W/m². It uses a simplified neural network block that takes temperature T and irradiance G as inputs and provides I_{opt} as the output.

The nntool Toolbox in MATLAB is used for designing, training, validating and testing a neural network. The dataset is divided into 3 parts: 70 % for training, 15 % for validation and 15 % for testing. The neural network is trained using the Levenberg-Marquardt algorithm, which is a very fast and accurate method for minimizing the mean square error (Fig. 5). This algorithm provides superior results compared to others. The regression results are depicted in Fig. 6.

Train a neural network to map predictors to continuous responses.

Data

Predictors: in - [1x61 double]
Responses: inn - [1x61 double]

in: double array of 61 observations with 1 features.
inn: double array of 61 observations with 1 features.

Algorithm

Data division: Random
Training algorithm: Levenberg-Marquardt
Performance: Mean squared error

Training Results

Training start time: 30-Jul-2024 20:24:43
Layer size: 10

	Observations	MSE	R
Training	43	0.0127	0.9947
Validation	9	0.0059	0.9969
Test	9	0.0109	0.9975

Fig. 5. ANN model summary

In the second step, an adaptation block is developed to calculate I_{opt} for any irradiance level by referencing the value obtained at 1000 W/m². We will validate this adaptation with experimental results.

The idea stems from the observed proportionality in the PV graphs at a constant temperature. Using the case presented in Table 3, for a fixed temperature T = 25°C, we compare the relative value G/1000 with I_{opt}/I_{opt}(1000) for irradiances ranging from 100 to 1000. According to the neural network block at T = 25°C, I_{opt}(1000) = 110 A.

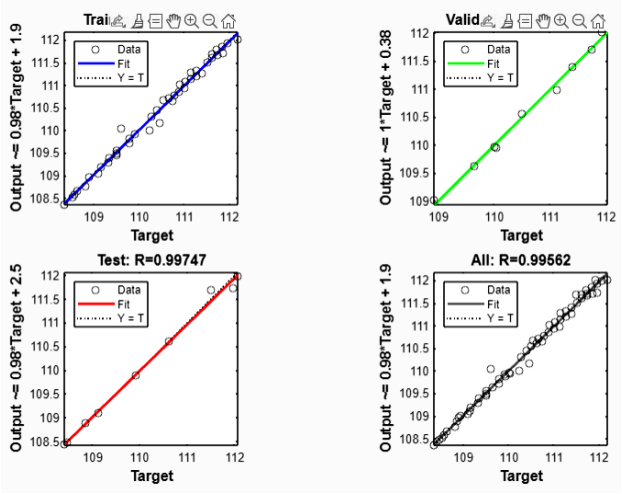

Fig. 6. The regression results

Table 3 demonstrates the approximate equality of G/1000 and $I_{opt}(G)/I_{opt}$(1000). Therefore, the adaptation we adopted involves first determining I_{opt} at any temperature for G = 1000 W/m² and then multiplying it by G/1000. The effectiveness of this technique will be validated in the results discussion section.

Table 3

Optimal current I_{opt} at different irradiance values G and T = 25°C

G	G/1000	I_{opt}	I_{opt} / I_{opt}(1000)
100	0.1	11.07	0.10063636363
200	0.2	22.155	0,20140909090
300	0.3	33.1763	0,30160272727
400	0.4	44.226	0,40205454545
500	0.5	55.2232	0,50202909090
600	0.6	66.2241	0,60203727272
700	0.7	77.2974	0,70270363636
800	0.8	88.2805	0,80255000000
900	0.9	99.6837	0,90621545454
1000	1	110	1

Figure 7 shows the circuit configuration between the PV and the battery this kind of techniques is represented in [28–32].

The energy management system is a computerized system, which allows, firstly, to find the current instructions to extract the maximum power from RESs, while referring to the SoC of the battery and secondly a regulation system which makes it possible to control the three converters in order to guarantee the performance of the powers in each element of our system.

The flowchart shown in Fig. 8 deploys the energy management strategy (EMS) proposed by our work. The management algorithm is designed to adjust the 4 phase shifts based on the reference, which is the battery, as mentioned in the system description. These adjustments are driven by 2 key factors: SOC of the battery and the comparison between the power demanded by the load and the power supplied in real time by the RESs.

The algorithm presented in Fig. 8 is summarized in the following situations:

1. Situation 1. When the total power produced by RESs is less than the power demanded by the load, and

SoC is greater than 85 %, the battery discharges and contributes to meeting the demand.

2. Situation 2. In this case, if SoC of the battery is greater than 85 % and the load demand is lower than the production from the RES, the battery is isolated, and the excess power produced is directed towards the dump load.

3. Situation 3. In this situation [33], if the SoC is between 15 % and 85 % and the power produced by the RES is lower than the load demand, the battery discharges to cover the remaining demand.

4. Situation 4. When the load demand is lower than the power produced by the RESs and the battery's SoC is between 15 % and 85 % [33], the excess power is directed to the battery, indicating that the battery is charging.

5. Situation 5. If the SoC is now less than 15 % and the power from the RESs exceeds the demand, the battery will be charged by the excess power.

6. Situation 6. The last situation involves isolating the load while the battery is charging when the battery's SoC is below 15 % and the RES cannot meet the load demand.

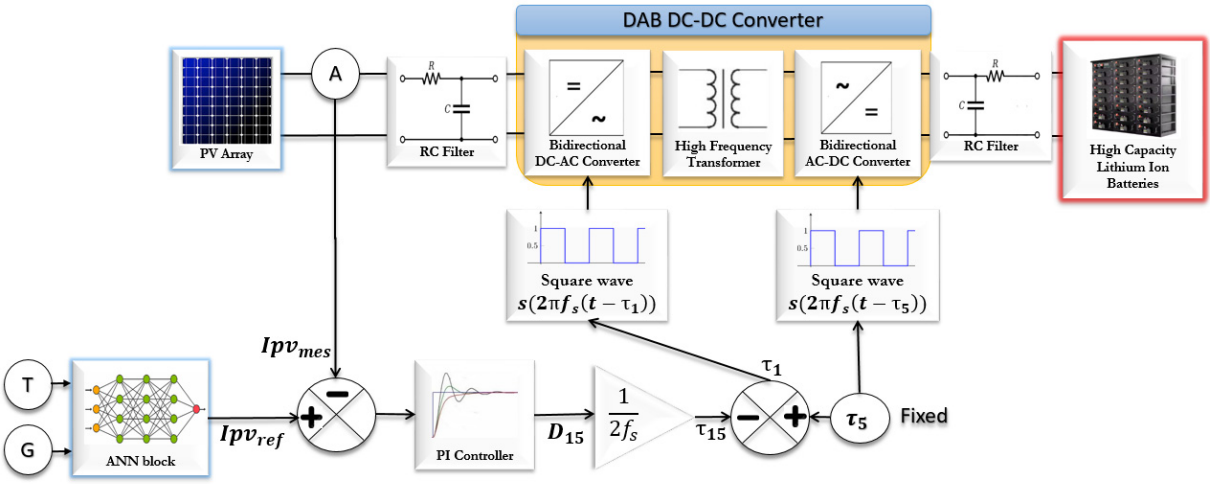

Fig. 7. Proposed MPPT control diagram block

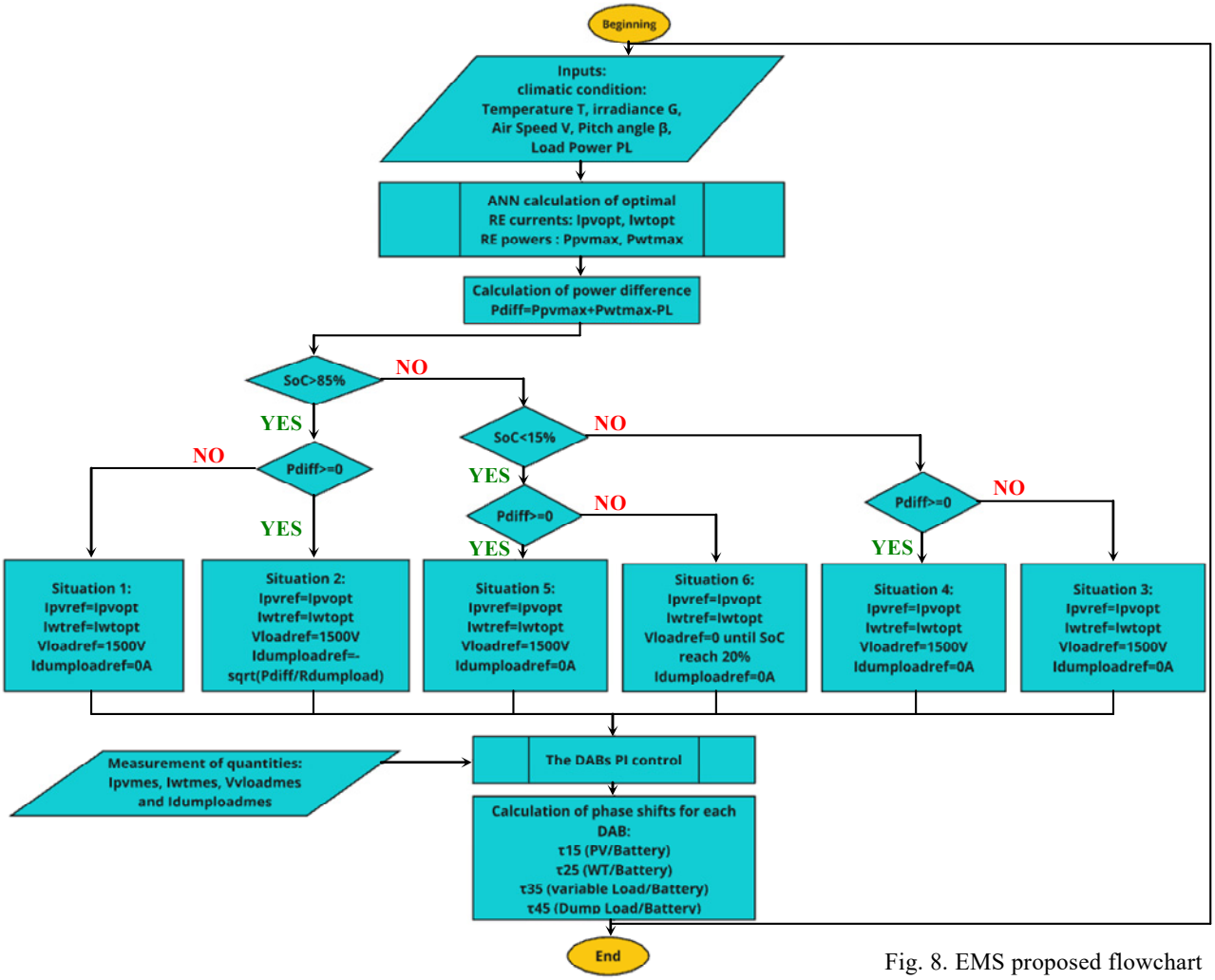

Fig. 8. EMS proposed flowchart

Results and discussion.

1. MPPT method validation. The test presented in Fig. 9,*a* assesses the reliability and capability of our control system to track maximum power. As previously mentioned, the optimal current under specific climatic conditions is calculated using a simplified neural network block and an adaptation method.

In this scenario, the PV system is subjected to a temperature $T = 30$°C and an irradiance $G = 850$ W/m².

The block provided 94 A as the reference current. To verify the block's reliability, we applied 3 reference currents to the PI regulation system with a 0.6 s delay: initially 94.5 A, then 94 A at 0.2 s (as calculated by the block), and finally 93.5 A at 0.4 s. The average power at the PV level was evaluated for the 3 cases. Figure 9,*b* summarizes these results.

After analyzing the residual graph, we see that the regulation system accurately followed the current references. For each current, the PV system developed an average power: approximately 53540 W for 94.5 A, 53552 W for 94 A (as calculated by the block), and 53539 W for 93.5 A. These results indicate that our system achieved maximum power for the reference calculated by our block, demonstrating that the MPPT approach is both efficient and reliable. It is worth noting that the system produced consistent results under different climatic conditions, which should be considered in the optimization algorithm.

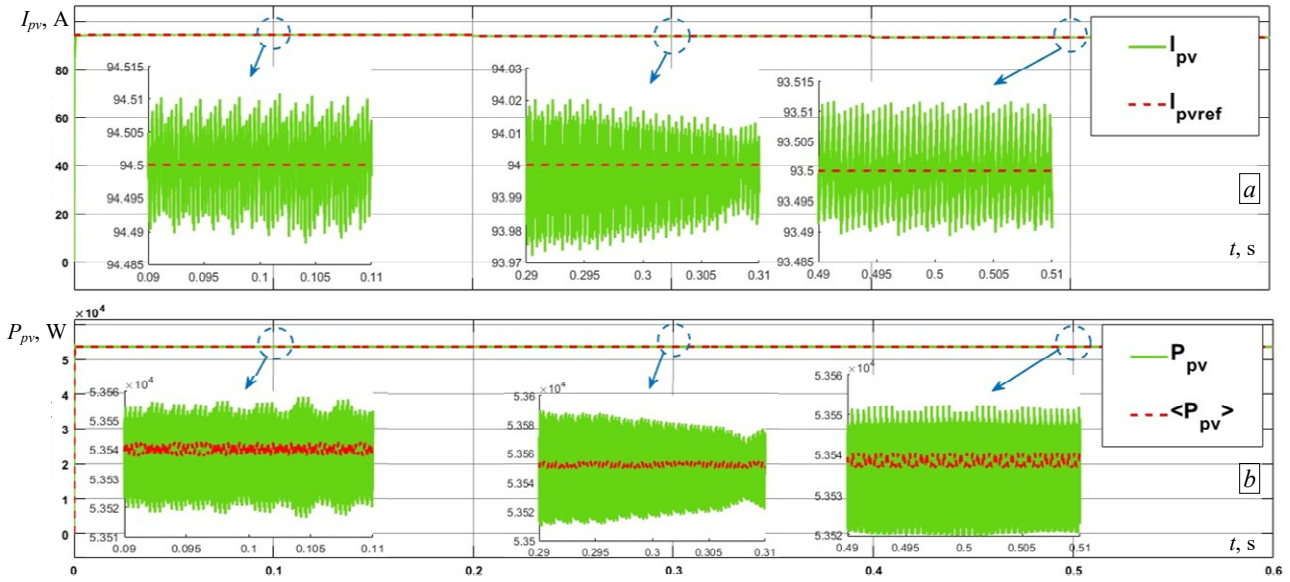

Fig. 9. MPPT PV results

2. EMS scenarios. In this section, we will evaluate the developed algorithm under different scenarios. One important thing to consider is that we did not vary the climatic conditions of the WT.

In a 4-second simulation, we evaluated the system's performance across the first 4 situations by adjusting the irradiation G, temperature T and changing the load demand. The results are presented in Fig. 9, 10.

Regarding the load, it requires 125 kW between 0 and 2 s, and 186.5 kW between 2 s and 4 s.

Between 0 and 1.33 s, the PV system operated at a temperature of 22 °C and an irradiance of 600 W/m², producing 39,32 kW. From 1.33 s to 2.66 s, with the temperature at 27 °C and irradiance at 1000 W/m², the power output increased to 63,35 kW. Finally, between 2.66 s and 4 s, at 25 °C and 900 W/m², the PV system generated 57,75 kW.

The climatic conditions for the WT were fixed throughout the simulation, with a wind speed of 12 m/s and a pitch angle of 0°, resulting in an average power output of 98,5 kW.

Based on the data provided, we can conclude that between 0 and 2 s, the power generated by the RESs exceeds the load demand, while between 2 s and 4 s, the opposite is true.

We began with the SoC of 84.9972 % to ensure a smooth transition between situations. Initially, we were in situation 4, which was confirmed by the simulation. At 0.91 s the battery reached 85 % (Fig. 11). At this point, we transitioned to situation 2 by isolating the battery through a command and diverting the excess power to the dump load. In Fig. 10, the dump load is represented by the power P_{dl}.

At 2 s, the SoC is still slightly above 85 %, and as the power demand exceeds production, the system shifts to situation 1. In this scenario, the battery becomes the power source, and the dump load is isolated again. However, this situation only lasts for 0.02 s before the SoC drops below 85 %, moving the system to situation 3, which follows the same instructions as situation 1.

This demonstrates the system's efficiency in regulation and control, as it dynamically adjusts based on the battery's status. For instance, at 2 s (Fig. 10) the load changes its setpoint, yet the system successfully adapts to the new setpoint, while the PV and WT maintain their average values, proving the system's resilience against load disturbances.

To avoid too much repetition, we kept the simulation conditions, including those for the PV, WT, and load, almost the same. This time, we focused on evaluating the energy management system with the SoC around 15 %.

Figure 12 shows the power levels in different situations when the SoC is close to 15 % (Fig. 13).

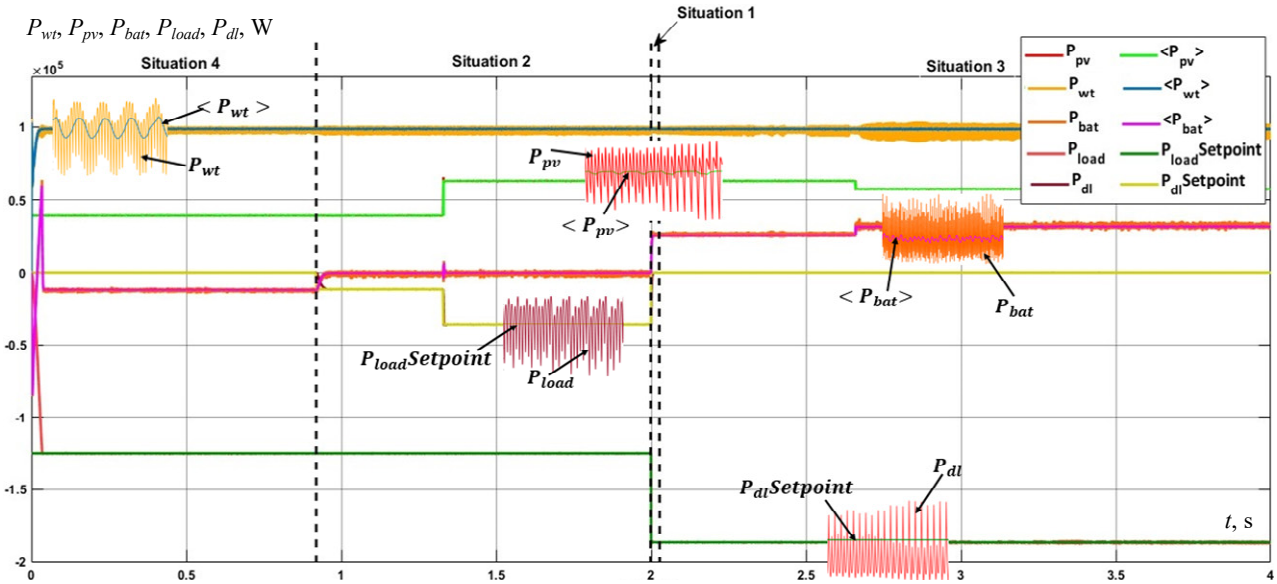

Fig. 10. EMS situations between 1 and 4

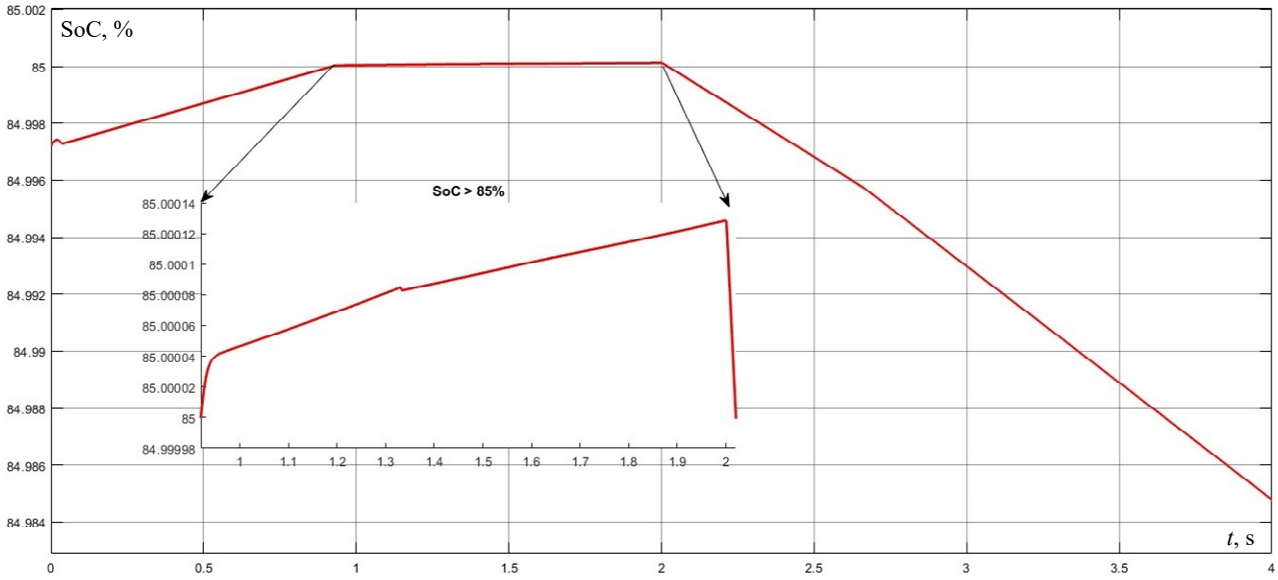

Fig. 11. Battery SOC corresponding situations between 1 and 4

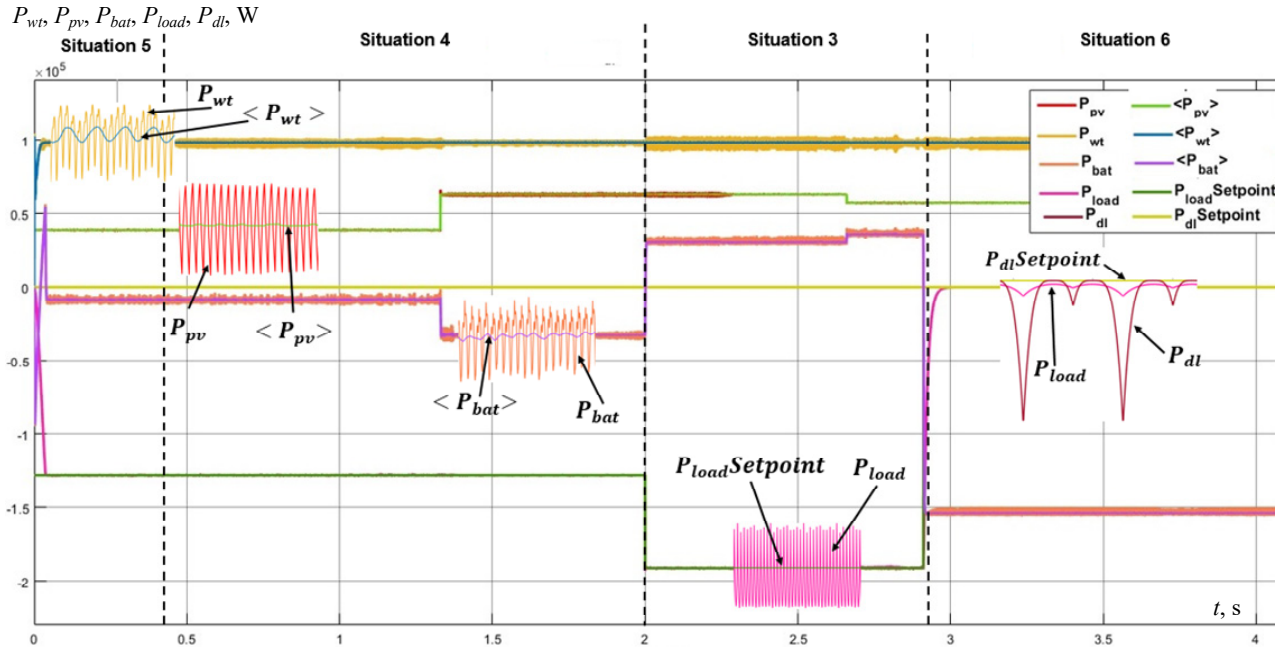

Fig. 12. EMS situations between 3 and 6

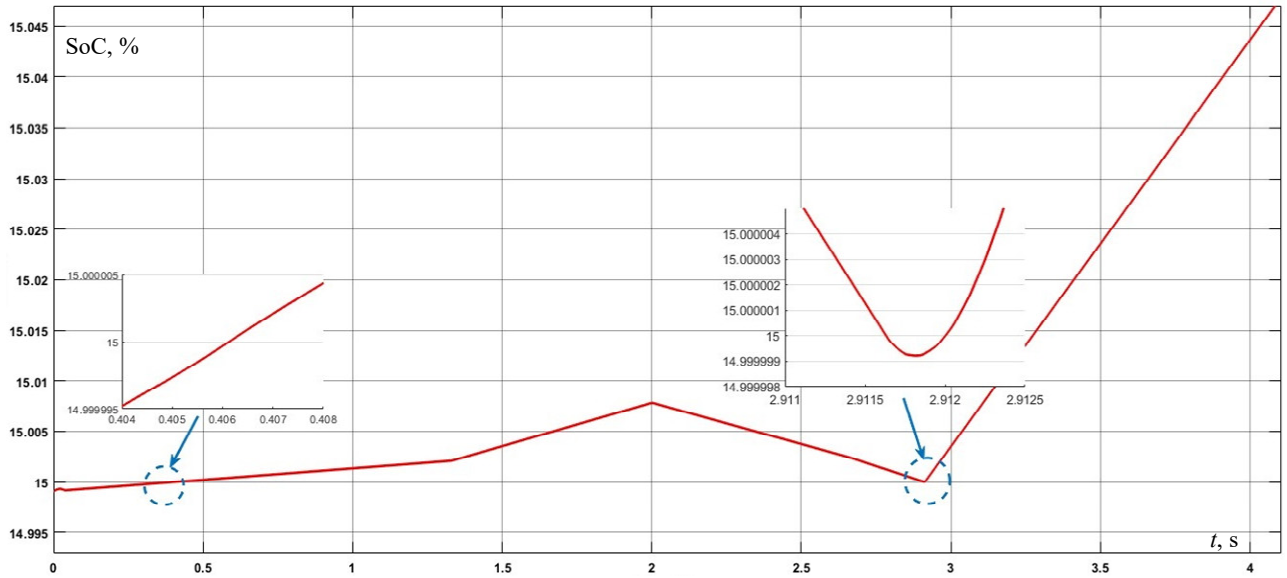

Fig. 13. Battery SOC corresponding situations between 3 and 6

As shown in Fig. 13, the SoC is below 15 % between 0 and 0.406 s. During this time, Fig. 12 indicates that the load's power demand is lower than the combined output of the PV and WT, triggering situation 5. After 0.406 s, the SoC surpasses 15 % under the same conditions, causing a switch to situation 4, which maintains the same outputs as situation 5. The battery continues to charge in this situation until 2 s, when the power demand exceeds what the sources can supply, as long as the SoC remains between 15 % and 85 %, situation 3 is activated, causing the battery to discharge until 2.9115 s, when the SoC reaches 15 %, At this point, a critical situation arises: the battery is at its minimum level, and the load demands more power than is being produced. This triggers situation 6, where charging the battery becomes the priority.

In the scenario shown in Fig. 12, the charging voltage is cut off to allow the battery to charge. To prevent the system from oscillating around 15 % (switching between situations 3 and 6), we implemented a strategy to stabilize the process, we introduce a tolerance band (hysteresis) in SoC levels to avoid frequent switching between charging and discharging modes. In this case, we might wait until SoC rises to 20 % before resuming power to non-critical loads. This prevents short cycling of the battery.

In the scenario shown in Fig. 12, the charging voltage is cut off to allow the battery to charge. To prevent the system from oscillating around 15 % (switching between situations 3 and 6), we implemented a strategy to stabilize the process, we introduce a tolerance band (hysteresis) in SoC levels to avoid frequent switching between charging and discharging modes. In this case, we might wait until the SoC rises to 20 % before resuming power to non-critical loads. This prevents short cycling of the battery.

Conclusions. This research has successfully created and tested a hybrid renewable energy system that combines solar panels, wind turbines, and a battery storage system. The system uses a smart control strategy with a dual active bridge DC-DC converter and an energy management system to effectively manage the energy from different sources and supply it to the load.

One of the main advantages of this system is its flexibility in managing energy. The control strategy adjusts the energy distribution based on changing power demands and environmental conditions, ensuring that all energy sources work together efficiently.

The energy management system is designed to prioritize when to charge or discharge the battery based on its state of charge and the energy demands in real time. This helps to keep the system reliable, extend the battery's lifetime, and improve overall efficiency.

We validated the MPPT method through simulations, showing that it accurately tracks the maximum power available under different weather conditions. The energy management system was also tested under various scenarios, proving its ability to adapt to changes in load and energy generation.

The simulations conducted using MATLAB/Simulink showed that the system performs consistently across different situations. By using a simplified neural network for MPPT and effectively managing the state of charge, the system maintains stable operation and optimizes energy use.

In summary, this hybrid renewable energy system, with its advanced control and management strategies, offers a practical solution for integrating renewable energy sources in a flexible and efficient way. Future research could focus on optimizing the system and on developing other control techniques to further improve the performance of the system.

Conflict of interest. The authors declare that there is no conflict of interest.

REFERENCES

1. Das S., Akella A.K. Power Flow Control of PV-Wind-Battery Hybrid Renewable Energy Systems for Stand-Alone Application. *International Journal of Renewable Energy Research*, 2018, vol. 8, no. 1, pp. 36-43. doi: https://doi.org/10.20508/ijrer.v8i1.6534.g7278.

2. Lu J., Siaw F.L., Thio T.H.G., Wang J.J. Capacity optimization of independent hybrid renewable energy system under different operational strategies based on improved gray wolf algorithm. *AIP Advances*, 2024, vol. 14, no. 5, art. no. 055205. pp. doi: https://doi.org/10.1063/5.0198446.

3. Gajewski P., Pieńkowski K. Control of the Hybrid Renewable Energy System with Wind Turbine, Photovoltaic Panels and Battery Energy Storage. *Energies*, 2021, vol. 14, no. 6, art. no. 1595. doi: https://doi.org/10.3390/en14061595.

4. Vinothkumar J., Thamizhselvan R. Efficient Power Management and Control Strategy of Hybrid Renewable Energy System in Microgrid. *International Journal on Applied Physics and Engineering*, 2023, vol. 2, pp. 106-127. doi: https://doi.org/10.37394/232030.2023.2.11.

5. Jamal S., Pasupuleti J., Ekanayake J. A rule-based energy management system for hybrid renewable energy sources with battery bank optimized by genetic algorithm optimization. *Scientific Reports*, 2024, vol. 14, no. 1, art. no. 4865. doi: https://doi.org/10.1038/s41598-024-54333-0.
6. Ayat Y., Badoud A.E., Mekhilef S., Gassab S. Energy management based on a fuzzy controller of a photovoltaic/fuel cell/Li-ion battery/supercapacitor for unpredictable, fluctuating, high-dynamic three-phase AC load. *Electrical Engineering & Electromechanics*, 2023, no. 3, pp. 66-75. doi: https://doi.org/10.20998/2074-272X.2023.3.10.
7. Bourouis B., Djeghloud H., Benalla H. An innovative algorithm for a hybrid fc/battery system energy management. *Electrical Engineering & Electromechanics*, 2020, no. 6, pp. 35-44. doi: https://doi.org/10.20998/2074-272X.2020.6.06.
8. Tahiri F.E., Chikh K., Khafallah M. Optimal Management Energy System and Control Strategies for Isolated Hybrid Solar-Wind-Battery-Diesel Power System. *Emerging Science Journal*, 2021, vol. 5, no. 2, pp. 111-124. doi: https://doi.org/10.28991/esj-2021-01262.
9. Ndeke C.B., Adonis M., Almaktoof A. Energy management strategy for a hybrid micro-grid system using renewable energy. *Discover Energy*, 2024, vol. 4, no. 1, art. no. 1. doi: https://doi.org/10.1007/s43937-024-00025-9.
10. Iqbal M.M., Kumar S., Lal C., Kumar C. Energy management system for a small-scale microgrid. *Journal of Electrical Systems and Information Technology*, 2022, vol. 9, no. 1, art. no. 5. doi: https://doi.org/10.1186/s43067-022-00046-1.
11. Maaruf M., Khan K., Khalid M. Robust Control for Optimized Islanded and Grid-Connected Operation of Solar/Wind/Battery Hybrid Energy. *Sustainability*, 2022, vol. 14, no. 9, art. no. 5673. doi: https://doi.org/10.3390/su14095673.
12. Cabrane Z., Lee S.H. Control and Management of Railway System Connected to Microgrid Stations. *IEEE Access*, 2022, vol. 10, pp. 40445-40455. doi: https://doi.org/10.1109/ACCESS.2022.3165832.
13. Mechnane F., Drid S., Nait-Said N., Chrifi-Alaoui L. Robust Current Control of a Small-Scale Wind–Photovoltaic Hybrid System Based on the Multiport DC Converter. *Applied Sciences*, 2023, vol. 13, no. 12, art. no. 7047. doi: https://doi.org/10.3390/app13127047.
14. Moghaddam S., Bigdeli M., Moradlou M. Optimal design of an off-grid hybrid renewable energy system considering generation and load uncertainty: the case of Zanjan city, Iran. *SN Applied Sciences*, 2021, vol. 3, no. 8, art. no. 732. doi: https://doi.org/10.1007/s42452-021-04718-x.
15. Menzri F., Boutabba T., Benlaloui I., Khamari D. Optimization of Energy management using a particle swarm optimization for hybrid renewable energy sources. *2022 2nd International Conference on Advanced Electrical Engineering (ICAEE)*, 2022, pp. 1-5. doi: https://doi.org/10.1109/ICAEE53772.2022.9962065.
16. Jafari M., Malekjamshidi Z. A Topology of DC-DC Converter Based on Multi-Winding Transformer for Grid Integration of Multiple Renewable Energy Resources. *Inventions*, 2020, vol. 5, no. 3, art. no. 31. doi: https://doi.org/10.3390/inventions5030031.
17. Dong Z., Yang P., Li Q., Zhang M., Chang Y., Wang S. Fractional order modelling and optimal control of dual active bridge converters. *Systems Science & Control Engineering*, 2024, vol. 12, no. 1, art. no. 2347886. doi: https://doi.org/10.1080/21642583.2024.2347886.
18. Effah E.K., Anto E.K., Okyere P.Y., Effah F.B. Model Reference Adaptive Control of SPS-Based Dual Active Bridge Converter with Constant Power Loading. *Power Electronics and Drives*, 2024, vol. 9, no. 1, pp. 348-357. doi: https://doi.org/10.2478/pead-2024-0022.
19. Henao-Bravo E.E., Ramos-Paja C.A., Saavedra-Montes A.J., González-Montoya D., Sierra-Pérez J. Design Method of Dual Active Bridge Converters for Photovoltaic Systems with High Voltage Gain. *Energies*, 2020, vol. 13, no. 7, art. no. 1711. doi: https://doi.org/10.3390/en13071711.
20. Hessad M.A., Bouchama Z., Benaggoune S., Behih K. Cascade sliding mode maximum power point tracking controller for photovoltaic systems. *Electrical Engineering & Electromechanics*, 2023, no. 1, pp. 51-56. doi: https://doi.org/10.20998/2074-272X.2023.1.07.
21. Chen Q., Wang L., Sun Y., Xie S., Wang R. Adaptive integral sliding mode MPPT control for wind turbines with fixed-time convergence. *IET Renewable Power Generation*, 2024, vol. 18, no. S1, pp. 4265-4276. doi: https://doi.org/10.1049/rpg2.12935.
22. Bahri M., Talea M., Bahri H., Aboulfatah M. An efficient scanning algorithm for photovoltaic systems under partial shading. *International Journal of Electrical and Computer Engineering (IJECE)*, 2022, vol. 12, no. 6, pp. 5799-5807. doi: https://doi.org/10.11591/ijece.v12i6.pp5799-5807.
23. Bendib D., Laour M. Modified incremental conductance MPPT using SEPIC converter for PV system, simulation and Arduino implementation. *Studies in Engineering and Exact Sciences*, 2024, vol. 5, no. 2, art. no. e6614. doi: https://doi.org/10.54021/seesv5n2-090.
24. Benhacine T.Z., Dali A., Tata M., Kherbachi A., Boudraf M., Kaabeche A. Design of a test bench for a small wind turbine emulator. *Journal of Renewable Energies*, 2024, vol. 27, no. 1, pp. 5-13. doi: https://doi.org/10.54966/jreen.v27i1.1113.
25. Abo-Khalil A.G., Alobaid M. Optimized Control for PMSG Wind Turbine Systems under Unbalanced and Distorted Grid Voltage Scenarios. *Sustainability*, 2023, vol. 15, no. 12, art. no. 9552. doi: https://doi.org/10.3390/su15129552.
26. Ríos S.J., Pagano D.J., Lucas K.E. Bidirectional Power Sharing for DC Microgrid Enabled by Dual Active Bridge DC-DC Converter. *Energies*, 2021, vol. 14, no. 2, art. no. 404. doi: https://doi.org/10.3390/en14020404.
27. Sabhi K., Talea M., Bahri H. Improving Power Precision in Hybrid Renewable Energy Systems with a Quad Active Bridge DC-DC Converter and Neural Network-Based Decoupling. *2024 International Conference on Intelligent Systems and Computer Vision (ISCV)*, 2024, pp. 1-8. doi: https://doi.org/10.1109/ISCV60512.2024.10620155.
28. Mahamat C., Bechet J., Linguet L. Artificial Neural Network Control Applied to a Photovoltaic-Battery Microgrid System. *AI, Computer Science and Robotics Technology*, 2024, vol. 3, no. 1, pp. 1-20. doi: https://doi.org/10.5772/acrt.34.
29. Vamsi Krishna A., Sateesh B., Sai Sankar M., Sravanthi P., Vanaja Suvarna P., Devendra Goud E. A novel MPPT method for a standalone PV System. *International Journal for Modern Trends in Science and Technology*, 2024, vol. 10, no. 4, pp. 60-66. doi: https://doi.org/10.46501/IJMTST1004010.
30. Bana P.R., D'Arco S., Amin M. ANN-Based Robust Current Controller for Single-Stage Grid-Connected PV With Embedded Improved MPPT Scheme. *IEEE Access*, 2024, vol. 12, pp. 100251-100262. doi: https://doi.org/10.1109/ACCESS.2024.3429347.
31. Hichem L., Leila M., Amar O. The effectiveness of a hybrid MPPT controller based on an artificial neural network and fuzzy logic in low-light conditions. *Bulletin of Electrical Engineering and Informatics*, 2024, vol. 13, no. 3, pp. 1453-1464. doi: https://doi.org/10.11591/eei.v13i3.6416.
32. Costanzo L., Rubino G., Rubino L., Vitelli M. PFC Control Signal Driven MPPT Technique for Grid-Connected PV Systems. *IEEE Transactions on Power Electronics*, 2024, vol. 39, no. 8, pp. 10368-10379. doi: https://doi.org/10.1109/TPEL.2024.3393294.
33. Jasim A.M., Jasim B.H., Bureš V. A novel grid-connected microgrid energy management system with optimal sizing using hybrid grey wolf and cuckoo search optimization algorithm. *Frontiers in Energy Research*, 2022, vol. 10, art. no. 960141. doi: https://doi.org/10.3389/fenrg.2022.960141.

Received 23.08.2024
Accepted 19.11.2024
Published 02.03.2025

K. Sabhi[1], *PhD,*
M. Talea[1], *Professor,*
H. Bahri[1], *Professor,*
S. Dani[1], *PhD,*
[1] Department of Physics,
Hassan II University of Casablanca, Morocco,
e-mail: sabhi.khalid.imt@gmail.com (Corresponding Author);
taleamohamed@yahoo.fr; hbahri.inf@gmail.com;
said_dani@hotmail.fr

How to cite this article:
Sabhi K., Talea M., Bahri H., Dani S. Integrating dual active bridge DC-DC converters: a novel energy management approach for hybrid renewable energy systems. *Electrical Engineering & Electromechanics*, 2025, no. 2, pp. 39-47. doi: https://doi.org/10.20998/2074-272X.2025.2.06

UDC 621.3.013 https://doi.org/10.20998/2074-272X.2025.2.07

B.I. Kuznetsov, T.B. Nikitina, I.V. Bovdui, K.V. Chunikhin, V.V. Kolomiets, B.B. Kobylianskyi

Method for reduction of magnetic field of uncertain extended technical objects based on their multyspheroidal model and compensating magnetic dipoles

Problem. *The implementation of strict requirements for magnetic silence of elongated energy-saturated objects such as naval vessel and submarines is an important scientific and technical problem of magnetism of technical objects.* ***Purpose***. *Development of method for reduction of magnetic field of uncertain extended technical objects based on their multyspheroidal model and optimization of parameters of compensating dipoles for compensate of spheroidal harmonics of external magnetic field of technical object.* ***Methodology.*** *Number, coordinates of spatial arrangement and magnitudes of spherical harmonics of compensating dipole of magnetic field sources calculated as magnetostatics geometric inverse problems solution in the form of nonlinear minimax optimization problem based on multyspheroidal model of magnetic field of extended technical objects. Nonlinear objective function calculated as the weighted sum of squared of resulting magnetic field COMSOL Multiphysics software package used. Nonlinear minimax optimization problems solutions calculated based on particle swarm nonlinear optimization algorithms.* ***Results.*** *The results of reduction of the initial magnetic field of extended technical objects based on their multyspheroidal model and optimization of parameters of compensating magnetic dipoles for compensate of spheroidal harmonics of external magnetic field of technical object using multyspheroidal model of the magnetic field in the form of spatial prolate spheroidal harmonics in the prolate spheroidal coordinate system and taking into account the uncertainty of the magnetic characteristics of extended technical objects.* ***Originality.*** *For the first time the method for reduction of magnetic field of uncertain extended technical objects based on their multyspheroidal model and optimization of parameters of compensating magnetic dipoles for compensate of spheroidal harmonics of external magnetic field of technical object using multyspheroidal model of the magnetic field developed. Unlike known methods, the developed method makes it possible to increase the efficiency of magnetic field reduction of uncertain extended technical objects.* ***Practical value.*** *It is theoretically shown the possibility to reduce by almost 100 times of modulus of induction and horizontal component of the induction of the original magnetic field of uncertain extended technical objects based on optimization of parameters of compensating magnetic dipoles for compensate of spheroidal harmonics of external magnetic field of technical object using multyspheroidal model of the magnetic field.* References 48, figures 6.

Key words: **extended technical objects, magnetic field, multyspheroidal model, magnetic silencing, prolate spheroidal coordinate system, spatial prolate spheroidal harmonics, control, uncertainty.**

Проблема. *Реалізація жорстких вимог щодо магнітної тиші витягнутих енергонасичених об'єктів, таких як військові кораблі та підводні човни, є важливою науковою та технічною проблемою магнетизму технічних об'єктів.* ***Мета.*** *Розробка методу зменшення магнітного поля невизначених протяжних технічних об'єктів на основі їх мультісфероїдальної моделі і оптимізації параметрів компенсуючих магнітних диполів для компенсації сфероїдальних гармонік зовнішнього магнітного поля технічного об'єкта.* ***Методологія.*** *Параметри компенсуючих дипольних джерел магнітного поля розраховані як рішення обернених геометричних задач магнітостатики у формі нелінійної задачі мінімаксної оптимізації на основі мультисфероїдальної моделі магнітного поля витягнутих технічних об'єктів. Нелінійна цільова функція розрахована як зважена сума квадратів результуючого магнітного поля з використанням програмного пакету COMSOL Multiphysics. Розв'язки задач нелінійної мінімаксної оптимізації розраховані на основі алгоритмів нелінійної оптимізації роєм частинок.* ***Результати.*** *Результати компенсації вихідного магнітного поля витягнутих технічних об'єктів на основі їх мультісфероїдальної моделі і оптимізації параметрів компенсуючих магнітних диполів для компенсації сфероїдальних гармонік зовнішнього магнітного поля технічного об'єкта з використанням мультисфероїдальної моделі магнітного поля в вигляді просторових витягнутих сфероїдальних гармонік в витягнутій сфероїдній системі координат та з врахуванням невизначеності магнітних характеристик витягнутих технічних об'єктів.* ***Оригінальність***. *Вперше розроблено метод зменшення магнітного поля невизначених протяжних технічних об'єктів на основі їх мультісфероїдальної моделі і оптимізації параметрів компенсуючих магнітних диполів для компенсації сфероїдальних гармонік зовнішнього магнітного поля технічного об'єкта з використанням мультисфероїдальної моделі магнітного поля . На відміну від відомих методів, розроблений метод дозволяє підвищити ефективність зменшення магнітного поля невизначених протяжних технічних об'єктів.* ***Практична цінність***. *Показана теоретична можливість зменшення майже в 100 разів модуля індукції та горизонтальної складової індукції вихідного магнітного поля невизначених протяжних технічних об'єктів на основі оптимізації параметрів компенсуючих магнітних диполів для компенсації сфероїдальних гармонік зовнішнього магнітного поля. поля технічного об'єкта з використанням мультисфероїдальної моделі магнітного поля.* Бібл. 48, рис. 6.

Ключові слова: **витягнуті технічні об'єкти, магнітне поле, мультисфероїдальна модель, магнітна тиша, витягнута сфероїдна система координат, просторові витягнуті сфероїдні гармоніки, управління, невизначеність.**

Introduction. Strict requirements are imposed on the accuracy of the description of the magnetic field near a technical object in shipboard magnetism such as naval vessel and submarines, when solving problems of electromagnetic compatibility, as well as in developing means of magnetic orientation and ensuring the magnetic cleanliness of spacecraft [1–3]. The main threat to naval vessel and submarines in modern naval warfare are naval mines. The magnetic protection complex of naval vessel and submarines from naval mines designed to reduce the magnetic field level at the control depth at which mine fuses do not operate through the following channels: magnetic, responding to the magnetic induction of a constant and slowly changing of magnetic field induction, responding to changes in the induction of a constant and slowly changing magnetic field during the movement of the naval vessel and submarines, electromagnetic, responding to the low-frequency electromagnetic field of the naval vessel and submarines [4–8].

The requirements for magnetic protection of naval vessel and submarines formulated as follows: the maximum value of the magnetic induction module of a

constant and slowly changing magnetic field calculated from the magnetic signature (pass-through characteristic) of the naval vessel and submarines at the control depth, should not exceed the specified value; the maximum value of the change in the horizontal component of the magnetic induction of a constant and slowly magnetic field changing over a certain period of time, calculated from the magnetic signature of the naval vessel and submarines, at the control depth when it moves at the nominal speed, should not exceed the specified value; the maximum value of the magnetic induction module of the low-frequency magnetic field of 50 Hz, calculated from the magnetic signature of the naval vessel and submarines at the control depth should not exceed the specified value.

To meet these stringent requirements for magnetic silence, all ships periodically carry out the demagnetization (degaussing) process on special magnetodynamic stands. To enhance the demagnetization process, a special solenoidal winding is installed on the ship's hull. To compensate the magnetic field of naval vessel and submarines a system of compensation windings are used in three orthogonal coordinates associated with the ship – in the longitudinal, transverse and vertical directions [4–7]. Compensation of the magnetic field of the main magnetization of the ship in the vertical direction is carried out using main parallel coils designed to compensate for the large magnetizations of the bow and stern of the ship. In addition to the general ship compensation windings, separate local electromagnetic compensators are also used.

Naval vessel and submarines are elongated energy-saturated objects and have a cigar-shaped appearance. The use of a spherical expansion of the scalar potential for objects with a predominant overall size does not make it possible to describe the magnetic field near their surface [9–13]. It seems relevant at present to use of spatial harmonic analysis in an extended spheroidal coordinate system, where the shape of the coordinate surfaces makes it possible to bring the description area closer to the surface of the object itself [14–16].

To compensate of initial magnetic field generated by these energy-saturated elongated object, it is theoretically possible to use compensating spheroidal magnetic field sources located at points in the space of the technical object, calculated when designing a multyspheroidal model of the original magnetic field of the technical object.

Multyspheroidal sources of the magnetic field should be taken equal in magnitude, but opposite in sign to the corresponding spheroidal harmonics of the spheroidal sources of the original magnetic field of the technical object. However, the technical implementation of such compensating spheroid magnetic field sources presents certain difficulties [16]. Therefore, we will consider the generation of a compensating magnetic field using compensating dipole magnetic field sources.

In various operating modes of an energy-saturated elongated technical object, as well as during operation, its signature changes, therefore, when reducing it, it is necessary to take into account the uncertainties of the magnetic signature of a technical object [17–19].

Optimization of parameters of compensating dipoles based on multyspheroidal model of magnetic field of energy-saturated elongated objects will improve the efficiency of reduction of original magnetic field of such uncertain objects.

The purpose of the work is to develop a method for reduction of magnetic field of uncertain extended technical objects based on their multyspheroidal model and optimization of parameters of compensating dipoles for compensate of spheroidal harmonics of external magnetic field of technical object.

Definition of forward multyspheroidal magnetostatics problem. Let's consider a multyspheroidal model of the original magnetic field of an energy-saturated extended technical object in an elongated spheroidal coordinate system. Let us assume that the initial magnetic field of an extended energy-saturated object is generated using I spheroidal magnetic field sources located at points in space of the technical object with coordinates (x_i, y_i, z_i) in a rectangular coordinate system associated with the center of the technical object as shown in Fig. 1.

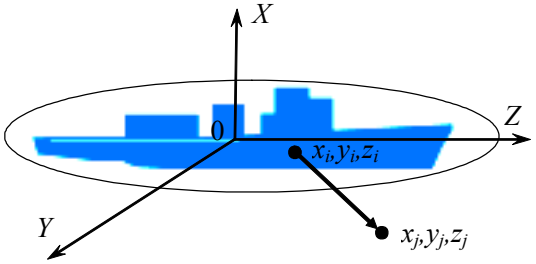

Fig. 1. Energy-saturated extended technical object

Then the components $H_{\xi ij}$, $H_{\eta ij}$, $H_{\varphi ij}$ of the magnetic field generated by these I spheroidal sources at J measurement points are calculated at points with coordinates ξ_{ij}, η_{ij}, φ_{ij} in elongated spheroidal coordinate systems associated with the centers of these sources, according to the following dependencies [16]

$$
\begin{aligned}
H_{\xi ij} &= -\frac{\sqrt{\xi_{ij}^{\,2}-1}}{c_i\sqrt{\xi_{ij}^{\,2}-\eta_{ij}^{2}}}\sum_{n=1}^{\infty}\sum_{m=0}^{n}\frac{dQ_{ni}^{m}(\xi_{ij})}{d\xi_{ij}}\left\{c_{ni}^{m}\cos(m\varphi_{ij})+s_{ni}^{m}\sin(m\varphi_{ij})\right\}P_{ni}^{m}\left(\cos(\eta_{ij})\right),\\
H_{\eta ij} &= -\frac{\sqrt{1-\eta_{ij}^{\,2}}}{c_i\sqrt{\xi_{ij}^{\,2}-\eta_{ij}^{\,2}}}\sum_{n=1}^{\infty}\sum_{m=0}^{n}Q_{ni}^{m}(\xi_{ij})\frac{dP_{ni}^{m}\left(\cos(\eta_{ij})\right)}{d\eta_{ij}}\left\{c_{ni}^{m}\cos(m\varphi_{ij})+s_{ni}^{m}\sin(m\varphi_{ij})\right\},\\
H_{\varphi ij} &= \frac{m}{c_i\sqrt{\left(\xi_{ij}^{\,2}-1\right)\left(1-\eta_{ij}^{\,2}\right)}}\sum_{n=1}^{\infty}\sum_{m=0}^{n}Q_{ni}^{m}(\xi)P_{ni}^{m}\left(\cos(\eta_{ij})\right)\left\{c_{ni}^{m}\sin(m\varphi_{ij})-s_{ni}^{m}\cos(m\varphi_{ij})\right\},
\end{aligned}
\qquad (1)
$$

here are the spheroidal coordinates ξ_{ij}, η_{ij}, φ_{ij} of observation points of the space of a technical object with coordinates (x_j, y_j, z_j) in rectangular coordinate systems associated with the center of the technical object, from the

location points of spheroidal magnetic field sources with coordinates (x_i, y_i, z_i) in an orthogonal system coordinates associated with the center of the technical object are related by the relation

$$\begin{aligned} x_j - x_i &= c_i \cdot \sqrt{\xi_{ij}^{\,2}-1} \cdot \sqrt{1-\eta_{ij}^{\,2}} \cdot \cos(\varphi_{ij}); \\ y_j - y_i &= c_i \cdot \sqrt{\xi_{ij}^{\,2}-1} \cdot \sqrt{1-\eta_{ij}^{\,2}} \cdot \sin(\varphi_{ij}); \\ z_j - z_i &= c_i \cdot \xi_{ij} \cdot \eta_{ij}; \end{aligned} \Rightarrow \begin{aligned} \xi_{ij} &\in [1,\infty[; \\ \eta_{ij} &\in [0,1]; \\ \varphi_{ij} &\in [0,2\pi]; \end{aligned} \tag{2}$$

where $P_{ni}^{m}(\xi_{ij})$, $Q_{ni}^{m}(\xi_{ij})$ associated Legendre functions of the first and second kind, respectively, with degree n and order m; c_i, c_{ni}^{m}, s_{ni}^{m} – constant coefficients characterizing the amplitudes of external spheroidal harmonics of the magnetic field.

Measurements and calculations of magnetic field components it is more convenient to carry out in the orthogonal coordinate system (x_j, y_j, z_j), the transition to which for the components H_{xij}, H_{yij}, H_{zij} is carried out using the formulas [16]:

$$\begin{aligned} H_{xij} &= \xi_{ij} \cdot \frac{\sqrt{1-\eta_{ij}^{\,2}}}{\sqrt{\xi_{ij}^{\,2}-\eta_{ij}^{\,2}}} \cdot \cos(\varphi_{ij}) \cdot H_{\xi ij} - \eta_{ij} \cdot \frac{\sqrt{\xi_{ij}^{\,2}-1}}{\sqrt{\xi_{ij}^{\,2}-\eta_{ij}^{\,2}}} \cdot \cos(\varphi_{ij}) \cdot H_{\eta ij} - \sin(\varphi_{ij}) \cdot H_{\varphi ij} \\ H_{yij} &= \xi_{ij} \cdot \frac{\sqrt{1-\eta_{ij}^{\,2}}}{\sqrt{\xi_{ij}^{\,2}-\eta_{ij}^{\,2}}} \cdot \sin(\varphi_{ij}) \cdot H_{\xi ij} - \eta_{ij} \cdot \frac{\sqrt{\xi_{ij}^{\,2}-1}}{\sqrt{\xi_{ij}^{\,2}-\eta_{ij}^{2}}} \cdot \sin(\varphi_{ij}) \cdot H_{\eta ij} + \cos(\varphi_{ij}) \cdot H_{\varphi ij}, \\ H_{zij} &= \eta_{ij} \cdot \frac{\sqrt{\xi_{ij}^{\,2}-1}}{\sqrt{\xi_{ij}^{\,2}-\eta_{ij}^{\,2}}} \cdot H_{\xi ij} + \cdot \xi_{ij} \cdot \frac{\sqrt{1-\eta_{ij}^{\,2}}}{\sqrt{\xi_{ij}^{\,2}-\eta_{ij}^{\,2}}} \cdot H_{\eta ij} \end{aligned} \tag{3}$$

Harmonic analysis in elongated spheroidal coordinate system based on (1) or (3) requires the calculation of associated Legendre polynomials of the first $P_{ni}^{m}(\xi_{ij})$ and second $Q_{ni}^{m}(\xi_{ij})$ kind. Polynomials $Q_{ni}^{m}(\xi_{ij})$ of the second kind calculated using the well-known formula with a limitation on the number of terms of the infinite series [18]

$$Q_{ni}^{m}(\xi_{ij}) = \frac{(-1)^m \cdot (2)^{m-1} \cdot (\xi_{ij}^{\,2}-1)^{\frac{m}{2}}}{\xi_{ij}^{\,n+m+1}} \times \sum_{k=0}^{\infty} \frac{\Gamma_i\left(\frac{n}{2}+\frac{m}{2}+k+\frac{1}{2}\right)! \cdot \Gamma_i\left(\frac{n}{2}+\frac{m}{2}+k+1\right)}{\Gamma_i(k+1) \cdot \Gamma_i\left(n+k+\frac{3}{2}\right) \cdot \xi_{ij}^{\,2k}}. \tag{4}$$

The region $\xi \in [\xi_o, 4]$ places strict demands on the accuracy of $Q_{ni}^{m}(\xi_{ij})$ function calculations. Algorithms for direct calculation $Q_{ni}^{m}(\xi_{ij})$ obtained in the form of finite sums [16]

$$\begin{aligned} Q_{ni}^{m}(\xi_{ij}) &= \frac{P_{ni}(\xi_{ij})}{2} \cdot \ln\left(\frac{\xi_{ij}+1}{\xi_{ij}-1}\right) - \sum_{k=1}^{n} \frac{1}{k} \cdot \sum_{\lambda=0}^{m} C_{mi}^{\lambda} \cdot P_{k-1}^{\lambda}(\xi_{ij}) \cdot P_{n-k}^{m-\lambda}(\xi_{ij}) + \frac{(1-\delta(m,0))}{2} \times \ldots \\ &\ldots \times \sum_{q=0}^{m-1} C_{mi}^{q} \cdot P_{ni}^{q}(\xi_{ij}) \cdot (m-q-1)! \cdot \frac{(\xi_{ij}-1)^{m-q} - (\xi_{ij}+1)^{m-q}}{(-1)^{m-q-1}(\xi_{ij}^{\,2}-1)^{\frac{m-q}{2}}}; \end{aligned}$$

$$Q_{ni}^{m}(\xi_{ij}) = \frac{(\xi_{ij}^{\,2}-1)^{\frac{m}{2}} n!\,m!}{2^{n+1}} \sum_{k=0}^{m} \frac{(k+n)!\,\Omega(m-k,\xi_{ij})}{k!\,(m-k)!} \sum_{\lambda=k}^{n} \frac{(\xi_{ij}-1)^{n-\lambda}(\xi_{ij}+1)^{\lambda-k}}{\lambda!\,(n+k-\lambda)!\,(\lambda-k)!\,(n-\lambda)!} - \sum_{k=1}^{n} \frac{1}{k} \sum_{\lambda=0}^{m} C_{mi}^{\lambda} P_{k-1}^{\lambda}(\xi_{ij}) P_{n-k,i}^{m-\lambda}(\xi_{ij});$$

$$\Omega(\nu,\xi_{ij}) = \begin{cases} \nu = 0 & \ln\left(\frac{\xi_{ij}+1}{\xi_{ij}-1}\right) \\ \nu \neq 0 & (-1)^{\nu-1}(\nu-1)! \frac{(\xi_{ij}-1)^{\nu} - (\xi_{ij}+1)^{\nu}}{(\xi_{ij}^{\,2}-1)^{\nu}} \end{cases}, \quad C_n^k = \frac{n!}{(n-k)!\,k!}. \tag{5}$$

Note that the calculation of the components $H_{\xi ij}$, $H_{\eta ij}$, $H_{\varphi ij}$ of the magnetic field in spheroidal coordinates ξ_{ij}, η_{ij}, φ_{ij} using (1) or components H_{xij}, H_{yij}, H_{zij} in the orthogonal coordinate system (x_j, y_j, z_j) using (3) generated by spheroidal sources of the magnetic field for given values of parameters c_i and spatial spheroidal harmonics c_{ni}^{m}, s_{ni}^{m} at

measurement points with coordinates (x_j, y_j, z_j) is a forward problem of magnetostatics for spheroidal magnetic field sources [20–25].

Definition of forward multydipole magnetostatics problem. To compensate for the spheroidal spatial harmonics of magnetic field of an energy-saturated extended object, we introduce C dipole magnetic field sources located at the C points of space of the technical object with coordinates (x_c, y_c, z_c) in a rectangular coordinate system associated with the center of the technical object. Let us define the spherical harmonics g_{nc}^m, h_{nc}^m of these C compensating dipole magnetic field sources.

Let us consider the calculation of the components of the magnetic field generated by these C dipole magnetic field sources at the magnetic field measurement points with coordinates (x_j, y_j, z_j) in a rectangular coordinate system associated with the center of the technical object. Let us calculate the spherical angular coordinates r_{cj}, φ_{cj}, θ_{cj} under which the measurement points with coordinates (x_j, y_j, z_j) are «visible» from the location points of dipole magnetic field sources with coordinates(x_c, y_c, z_c) in a rectangular coordinate system, associated with the center of the technical object, from the following relationships

$$\begin{aligned} x_j - x_c &= r_{cj}\cdot\sin(\theta_{cj})\cos(\varphi_{cj}); \\ y_j - y_c &= r_{cj}\cdot\sin(\theta_{cj})\cdot\sin(\varphi_{cj}); \\ z_j - z_c &= r_{cj}\cdot\cos(\theta_{cj}). \end{aligned} \Rightarrow \begin{aligned} r_{cj} &\in [0,\infty[\\ \theta_{cj} &\in [0,\pi] \\ \varphi_{cj} &\in [0,2\pi] \end{aligned} \quad (6)$$

Then the components H_{rcj}, $H_{\varphi cj}$, $H_{\theta cj}$ of the magnetic field in the spherical coordinate system r_{cj}, φ_{cj}, θ_{cj} associated with the center of location of the compensating dipole source of the magnetic field, are calculated using the following formulas [20]

$$\begin{aligned} H_{rcj} &= \sum_{n=1}^{\infty}\sum_{m=0}^{n}\frac{n+1}{r^{n+2}}\left\{g_{nc}^m\cos(m\varphi_{cj})+h_{nc}^m\sin(m\varphi_{cj})\right\}\cdot P_{nc}^m\left(\cos(\theta_{cj})\right); \\ H_{\theta cj} &= -\sum_{n=1}^{\infty}\sum_{m=0}^{n}\frac{1}{r^{n+2}}\left\{g_{nc}^m\cos(m\varphi_{cj})+h_{nc}^m\sin(m\varphi_{cj})\right\}\frac{dP_{nc}^m\left(\cos(\theta_{cj})\right)}{d\theta_{cj}}; \\ H_{\varphi cj} &= \sum_{n=1}^{\infty}\sum_{m=0}^{n}\frac{m}{r^{n+2}}\left\{g_{nc}^m\sin(m\varphi_{cj})-h_{nc}^m\cos(m\varphi_{cj})\right\}\frac{P_{nc}^m\left(\cos(\theta_{cj})\right)}{\sin(\theta_{cj})}. \end{aligned} \quad (7)$$

Using the calculated components H_{rcj}, $H_{\varphi cj}$, $H_{\theta cj}$ of the magnetic field in the spherical coordinate system r_{cj}, φ_{cj}, θ_{cj} we calculate the components H_{xcj}, H_{ycj}, H_{zcj} of magnetic field with orthogonal coordinate system, associated with the center of the compensating dipole magnetic field source according to the following formulas [20]

$$\begin{aligned} H_{xcj} &= H_{rcj}\sin(\theta_{cj})\cos(\varphi_{cj})+H_{\theta cj}\cos(\theta_{cj})\cos(\varphi_{cj})-H_{\varphi cj}\sin(\varphi_{cj}); \\ H_{ycj} &= H_{rcj}\sin(\theta_{cj})\sin(\varphi_{cj})+H_{\theta cj}\cos(\theta_{cj})\sin(\varphi_{cj})+H_{\varphi cj}\cos(\varphi_{cj}); \\ H_{zcj} &= H_{rcj}\cos(\theta_{cj})-H_{0cj}\sin(\theta_{cj}). \end{aligned} \quad (8)$$

Let us take the axes of the orthogonal coordinate systems of compensating dipole sources parallel to the corresponding axes of the orthogonal coordinate system associated with the center of the technical object. Then the magnetic field components H_{xc}, H_{yc}, H_{zc} in an orthogonal coordinate system associated with the center of a technical object generated by all compensating dipole sources of magnetic field in currents, measurements with coordinates (x_j, y_j, z_j) are calculated as sums of the corresponding components H_{xcj}, H_{ycj}, H_{zcj} of magnetic field generated by individual compensating dipole sources at measurement points with coordinates (x_j, y_j, z_j).

Note that the calculation of the components H_{rcj}, $H_{\varphi cj}$, $H_{\theta cj}$ of the magnetic field in the spherical coordinate system r_{cj}, φ_{cj}, θ_{cj} using (1) or components H_{xcj}, H_{ycj}, H_{zcj} of magnetic field with orthogonal coordinate system (x_j, y_j, z_j) using (3) generated by spherical sources of the magnetic field for given values of spherical harmonics g_{nc}^m, h_{nc}^m at measurement points with coordinates (x_j, y_j, z_j) is a forward problem of magnetostatics for spherical magnetic field sources [26–30].

Definition of prediction geometric inverse problems of magnetostatics. Let us now consider the definition of the prediction geometric inverse problems of magnetostatics based on a forward multyspheroidal model (1) of the initial magnetic field of an energy-saturated extended object [26–34]. As a result of solving the prediction of the geometric inverse problem of magnetostatics based on the multyspheroidal model (1) of the original magnetic field of the energy-saturated extended control object, it is necessary to calculate the following coordinates (x_i, y_i, z_i) of the location of the multyspheroidal sources of the original magnetic field in the space of the technical object and the parameters c_i and spatial spheroidal harmonics c_{ni}^m, s_{ni}^m in such a way that, based on this mathematical model (1), the values of the magnetic field at measurement points with coordinates (x_j, y_j, z_j) are close to the experimentally measured values of the magnetic field in these measuring points.

A feature of the energy-saturated extended technical objects are the uncertainty of the magnetic characteristics of their elements and their change in different operating modes [35–40]. Let us introduce the vector $\boldsymbol{G}$ of uncertainties of the parameters of the magnetic characteristics of energy-saturated extended technical object [41–44].

Let us introduce the vector $\boldsymbol{Y_M}(\boldsymbol{G})$ of the measured values of the magnetic field signature of a technical object, the components of which are the measured components $H_{xk}(\boldsymbol{G})$, $H_{yk}(\boldsymbol{G})$, $H_{zk}(\boldsymbol{G})$ of the magnetic field

of the technical object for given rectangular coordinates (x_j, y_j, z_j) associated with the center of the technical object. Note that the vector $\boldsymbol{Y_M(G)}$ of measured values of the magnetic field signature of a technical object depends on the operating modes of the technical object and on the vector $\boldsymbol{G}$ of uncertainties of the parameters of the magnetic cleanliness of the energy-saturated extended technical object units.

Let us introduce the vector $\boldsymbol{X}$ of the desired parameters of solving the prediction of the geometric inverse problem of magnetostatics, the components of which are the coordinates (x_i, y_i, z_i) of the location of spheroidal sources of the magnetic field at points in the space of a technical object in a rectangular coordinate system associated with the center of the technical object and given magnitudes of parameters c_i and spatial spheroidal harmonics c_{ni}^m, s_{ni}^m of these spheroidal magnetic field sources.

Then for given coordinate values (x_i, y_i, z_i) of the location of spheroidal magnetic field sources, at points in space of a technical object in a rectangular coordinate system associated with the center of the technical object and given values of parameters c_i and spatial spheroidal harmonics c_{ni}^m, s_{ni}^m components $H_{xkn}(\boldsymbol{X,G})$, $H_{ykn}(\boldsymbol{X,G})$, $H_{zkn}(\boldsymbol{X,G})$ H_{xij}, H_{yij}, H_{zij} of the magnetic field generated by these spheroidal magnetic field sources at measurement points with coordinates (x_i, y_i, z_i) in a rectangular coordinate system associated with the center of the technical object can be calculated based on forward multyspheroidal magnetic field model (1).

The values of parameters c_i and spatial spheroidal harmonics c_{ni}^m, s_{ni}^m of forward multyspheroidal magnetic field model (1) of an elongated energy-saturated object in an elongated spheroidal coordinate system ξ, η, φ depended on the operating modes of the energy-saturated extended technical object and, therefore, are functions of the components of the vector $\boldsymbol{G}$ of uncertainties of the parameters of the magnetic cleanliness of the energy-saturated extended technical object.

Therefore the components $\boldsymbol{H}_{xkn}(\boldsymbol{X,G})$, $\boldsymbol{H}_{ykn}(\boldsymbol{X,G})$, $\boldsymbol{H}_{zkn}(\boldsymbol{X,G})$, $\boldsymbol{H}_{xij}$, $\boldsymbol{H}_{yij}$, $\boldsymbol{H}_{zij}$ of the magnetic field generated by these spheroidal magnetic field sources at measurement points with coordinates (x_j, y_j, z_j) are also functions of the vector $\boldsymbol{G}$ of uncertainties of the parameters of the magnetic cleanliness of the energy-saturated extended technical object and the vector $\boldsymbol{X}$ of the desired parameters of solving the prediction of the geometric inverse problem of magnetostatics.

Let us introduce the vector $\boldsymbol{Y_C(X,G)}$ of calculated values of the magnetic field signature of a technical object, the components of which $\boldsymbol{H}_{xkn}(\boldsymbol{X,G})$, $\boldsymbol{H}_{ykn}(\boldsymbol{X,G})$, $\boldsymbol{H}_{zkn}(\boldsymbol{X,G})$, $\boldsymbol{H}_{xij}$, $\boldsymbol{H}_{yij}$, $\boldsymbol{H}_{zij}$ are calculated values components of the magnetic field of a technical object for given measurement points with coordinates (x_j, y_j, z_j) in a rectangular coordinate system associated with the center of the technical object.

Let us introduce the $\boldsymbol{E(X,G)}$ vector of the discrepancy between the vector $\boldsymbol{Y_M(G)}$ of the measured magnetic field and the vector $\boldsymbol{Y_C(X,G)}$ of the predicted by model (3) magnetic field

$$\boldsymbol{E(X,G) = Y_M(G) - Y_C(X,G)}. \qquad (9)$$

Then the solution of prediction geometric inverse problem of magnetostatics comes down to the standard approach of designing a robust prediction multyspheroidal model of magnetic field of an energy-saturated extended object, when the coordinates (x_i, y_i, z_i) of the location of spheroidal sources of the magnetic field at points in the space of a technical object in a rectangular coordinate system associated with the center of the technical object and magnitudes of parameters c_i and spatial spheroidal harmonics c_{ni}^m, s_{ni}^m of these spheroidal magnetic field sources are found from the conditions for minimizing the vector of the discrepancy between the vector of the measured magnetic field and the vector of the predicted by forward multyspheroidal model magnetic field, but for the «worst» the vector $\boldsymbol{G}$ of uncertainties of the parameters of the magnetic characteristics of energy-saturated extended technical object are found from the conditions for maximizing the same vector of the discrepancy between the vector of the measured magnetic field and the vector of the predicted by multyspheroidal model of magnetic field.

Definition of control geometric inverse problems of magnetostatics. Let us now consider the definition of control geometric inverse problem of magnetostatics based on a multydipole model (1) of the compensating magnetic field of an energy-saturated extended control object. As a result of solving the control of the geometric inverse problem of magnetostatics on the basis of a multy-dipole model (7) of the compensating magnetic field of an energy-saturated extended control object, it is necessary to calculate the coordinates (x_c, y_c, z_c) of the location C of multy-dipole sources of the compensating magnetic field in the space of energy-saturated extended control object and the magnitude g_{nc}^m, h_{nc}^m of their spherical spatial harmonics, in such a way that, on the basis of this, the control of the mathematical model (7) of components values $\boldsymbol{H}_{xc}$, $\boldsymbol{H}_{yc}$, $\boldsymbol{H}_{zc}$ of magnetic field at the measurement points with coordinates (x_j, y_j, z_j) were close in magnitude but oppositely directed to the values of the initial magnetic field calculated on the basis of the predictions of the multyspheroidal model (1) at the same J measurement points with coordinates (x_j, y_j, z_j).

Let us introduce the vector $\boldsymbol{X}$ of the desired parameters for solving the problem of compensating of initial magnetic field of energy-saturated extended control object, whose components are unknown values of coordinates (x_i, y_i, z_i) of the location of spherical sources of the compensating magnetic field at points in the space of a technical object in a rectangular coordinate system associated with the center of the technical object and unknown values magnitude g_{nc}^m, h_{nc}^m of their spherical spatial harmonics of magnetic field of these spherical compensating sources.

Then, for a given value of the vector $\boldsymbol{X}$ of the desired parameters of the compensating dipoles, based on (7), the vector $\boldsymbol{B}_c(\boldsymbol{X})$ of the compensating magnetic field generated by all compensating dipoles at the specified points in space, in particular at the control depth of a technical object generated by all compensating dipoles can be calculated.

Then we calculated the vector $\boldsymbol{B}_R(\boldsymbol{X},\boldsymbol{G})$ of resulting magnetic field at the specified points in space, in particular at the control depth of a technical object generated by energy-saturated extended control object and all compensating elements

$$\boldsymbol{B}_R(\boldsymbol{X},\boldsymbol{G})=\boldsymbol{B}(\boldsymbol{G})+\boldsymbol{B}_c(\boldsymbol{X}). \quad (10)$$

Then the problem of calculated unknown values of vector $\boldsymbol{X}$ of the desired parameters for solving the problem of compensating of initial magnetic field of energy-saturated extended control object, whose components are unknown values of coordinates (x_i, y_i, z_i) of the location of spherical sources of the compensating magnetic field at points in the space of a technical object in a rectangular coordinate system associated with the center of the technical object and unknown values magnitude g_{nc}^m, h_{nc}^m of their spherical spatial harmonics of magnetic field of these spherical compensating sources can be reduced to solving the problem of minimax optimization of resulting magnetic field (10) generated by energy-saturated extended control object and all compensating elements at the specified points in space, in particular at the control depth of a technical object.

This approach is also standard when designing of robust control by resulting magnetic field of an energy-saturated extended control object, when the coordinates of the spatial arrangement and the magnitudes of the compensating dipole calculated from the conditions for minimizing modulus of spacecraft resulting magnetic field (10) at the specified points in space, in particular at the control depth of a technical object, but for the «worst» values of the vector of uncertainty parameters of the energy-saturated extended technical object magnetic characteristics.

Inverse problems solution method. Components of the vector games (9), (10) are nonlinear functions of the vector $\boldsymbol{X}$ of required parameters and the vector $\boldsymbol{G}$ of uncertainty parameters of geometric inverse magnetostatics problem for prediction and control by magnetic signature of an energy-saturated extended object based on a multydipole model (1) taking into account forward problem uncertainties and calculated by COMSOL Multiphysics software.

A feature of the calculated solution problem is the multy-extremal nature of games payoff (9), (10) so that the considered region of possible solutions contains local minima and maxima. This due to fact that when minimizing the resulting magnetic field at one point in the signature of technical object, the magnetic field level at another point in signature of this technical object increases due to under compensation or overcompensation of the original magnetic field of technical object. Therefore, to calculate the solution this vector games (8) – (10) used stochastic multy-agent optimization algorithms [45].

To adapt the PSO method in relation to the problem of finding Pareto-optimal solutions on the set of possible values of a vector criterion, it is most simple to use binary preference relations that determine the Pareto dominance of individual solutions. To find a unique solution of a vector games (9), (10) from a set of Pareto-optimal solutions used information about the binary relationships of preferences of local solutions relative to each other [45]. To calculate one single global solution to the vector games (9), (10) individual swarms exchange information with each other during the calculation of optimal solutions to local games. Information about the global optimum obtained by particles from another swarm used to calculate the speed of movement of particles from another swarm, which allows calculated all Pareto-optimal solutions. To increase the speed of finding a global solution, special nonlinear algorithms of stochastic multy-agent optimization in which the motion of i particle of j swarm described by the following expressions [46]

$$\begin{aligned} v_{ij}(t+1) &= w_{1j}v_{ij}(t)+c_{1j}r_{1j}(t)\times\dots \\ &\dots\times H\left(p_{1ij}(\mathrm{t})-\varepsilon_{1ij}(t)\right)\left[y_{ij}(t)-\dots\right. \\ &\left.\dots-x_{ij}(t)\right]+c_{2j}r_{2j}(t)H\left(p_{2ij}(t)-\dots\right. \\ &\left.\dots-\varepsilon_{2ij}(t)\right)\left[y_j^*(t)-x_{ij}(t)\right]; \end{aligned} \quad (11)$$

$$\begin{aligned} u_{ij}(t+1) &= w_{2j}u_{ij}(t)+c_{3j}r_{3j}(t)H\times\dots \\ &\dots\times\left(p_{3ij}(t)-\varepsilon_{3ij}(t)\right)\left[z_{ij}(t)-\delta_{ij}(t)\right]+\dots \\ &\dots+c_{4j}r_{4j}(t)H\left(p_{4ij}(t)-\varepsilon_{4ij}(t)\right)\times\dots \\ &\dots\times\left[z_j^*(t)-\delta_{ij}(t)\right]; \end{aligned} \quad (12)$$

$$\begin{aligned} x_{ij}(t+1) &= x_{ij}(t)+v_{ij}(t+1); \\ g_{ij}(t+1) &= \delta_{ij}(t)+u_{ij}(t+1), \end{aligned} \quad (13)$$

where $x_{ij}(t)$, $g_{ij}(t)$ and $v_{ij}(t)$, $u_{ij}(t)$ is the position and velocity of i particle of j swarm.

In (11) – (13) $y_{ij}(t)$, $z_{ij}(t)$ and $y_j^*(t)$, $z_j^*(t)$ – the best local and global positions of the i–th particle, found respectively by only one i–th particle and all the particles of j swarm. Moreover, the best local position $y_{ij}(t)$ and the global position $y_j^*(t)$ of the i particle of j swarm are understood in the sense of the first player strategy $x_{ij}(t)$ for minimum of component $\boldsymbol{E}_i(\boldsymbol{X},\boldsymbol{G})$, $\boldsymbol{B}_R(\boldsymbol{X},\boldsymbol{G})$ of the vector payoff (9), (10). However, the best local position $z_{ij}(t)$ and the global position z_j^* of the i particle of j swarm are understood in the sense of the second player strategy $g_{ij}(t)$ for maximum of the same component $\boldsymbol{E}_i(\boldsymbol{X},\boldsymbol{G})$, $\boldsymbol{B}_R(\boldsymbol{X},\boldsymbol{G})$ of the vector payoff (9), (10).

Simulation results. Each naval vessel and each submarine has its own unique signature – a magnetic portrait, which can be used to determine not only the type of technical object, but also this particular technical object. Therefore, the magnetic signatures of specific naval vessel and submarines are a top secret [47, 48].

Measuring the magnetic field signature of naval vessel and submarines is usually carried out when a technical object moves against magnetic field sensors fixedly installed at various points in space. In particular, in the French marine laboratory 13 three-component magnetometers were installed along the body of the technical object being measured [13]. With linear geometric dimensions of a technical object ±100 m and measuring the magnetic field signature after 1 m, the number of measurement points will be 2613 pieces, and the number of measurements will be 7839 values of magnetic field components.

Based on these measurements, a mathematical model of the magnetic field signature is calculated. Recently, moving underwater drones equipped with

magnetometers have been used to measure the magnetic signatures of naval vessel and submarines [47, 48].

As an example, consider the magnetic signature of a technical object, the parameters of which are given in [6]. The technical object has linear dimensions from –100 m to +100 m. The initial magnetic field is generated by 16 dipole sources located at points in space of the technical object with the following coordinates. When measuring the magnetic field along the length of a technical object from –100 m to +100 m with an interval of 1 m along three lines with [6] coordinates, 603 measurement points are obtained. In this case, at each point three components of the magnetic field are measured in an orthogonal coordinate system associated with the center of the technical object, so that the total number of measurements is 1809 magnetic field values.

Let us first consider the design of a multyspheroidal model of the initial magnetic field. As a result of solving the predictions of the geometric inverse problem, the coordinates (x, y, z) of the spatial location and their values of the parameters c and the coefficients of the first spheroidal harmonics c_1^0, c_1^1, s_1^1 of 5 spheroidal sources of the multyspheroidal model of the initial magnetic field of the energy-saturated elongated technical object under consideration were calculated by magnetosystems.

1) Sources M_1 – x = 24.1775 m, y = 0.203945 m, z = 1.44653 m, c = 17.1245, c_1^0, = –840.073, c_1^1, = 13.9223, s_1^1 = –193.016;

2) Sources M_2 – x = –13.2818 m, y = 0.498642 m, z = 0.266331 m, c = 0.232014, c_1^0, = –58875.5, c_1^1, = 1373.1, s_1^1 = –7953.4;

3) Sources M_3 – x = –38.496 m, y = 0.276427 m, z = –1.03295 m, c = 0.337585, c_1^0, = –3620.08, c_1^1, = –11852.2, s_1^1 = –3933.69;

4) Sources M_4 – x = 241911 m, y = 0.203772 m, z = 1.4617 m, c = 16.9606, c_1^0, = 847.093, c_1^1, = –14.0885, s_1^1 = 194.566.

Figure 2 shows the signatures of the original (solid lines) and model (dashed lines) magnetic field components of the magnetic field for the following coordinate values: *a*) Y = –20 m, Z = 19 m; *b*) Y = 0, Z = 19 m; *c*) Y = 20 m, Z = 19 m; *d*) magnetic field induction modules. As seen in these figures, the signatures of the original and model magnetic fields practically coincide, which confirms the adequacy of the designed multyspheroidal model to the real signatures of the magnetic field.

One of the main technical requirements for the signature of ships and submarines is the limitation of the induction module of the magnetic field signature to the control depth. Technically, it is easiest to compensate for the initial magnetic field using local dipole-type compensators. Let us consider the reduction of the original magnetic field based on the designed multyspheroidal magnetic field model using compensating dipoles.

As a result of solving the control geometric inverse problem of magnetostatics, the spatial location coordinates and values of the magnetic moments of 5 compensating dipoles were calculated

$\{x_1, \ldots, x_5\}$ – {–13.4224, –38.4723, 38.3674, 29.2921, 11.2709} m;

$\{y_1, \ldots, y_5\}$ – {0.557271, 0.2328, –0.886435, –5.39425, 0.341033} m;

$\{z_1, \ldots, z_5\}$ – {0.37837, –1.00586, 0.809621, –1.51659, 0.0348981} m;

$\{M_{x1}, \ldots, M_{x5}\}$ – {1026.93, 136.8, 330.364, 99.726, 468.882} A·m^2;

$\{M_{y1}, \ldots, M_{y5}\}$ – { –48.7259, 900.474, 77.9282, –58.4812, –26.3114} A·m^2;

$\{M_{z1}, \ldots, M_{z5}\}$ – {263.642, 293.553, 135.072, 56.0585, 268.282} A·m^2.

Another technical requirement for the signature of ships and submarines is to limit the amount of change in the horizontal component of the magnetic field at a control depth over a certain period of time when passing a technical object at a given speed.

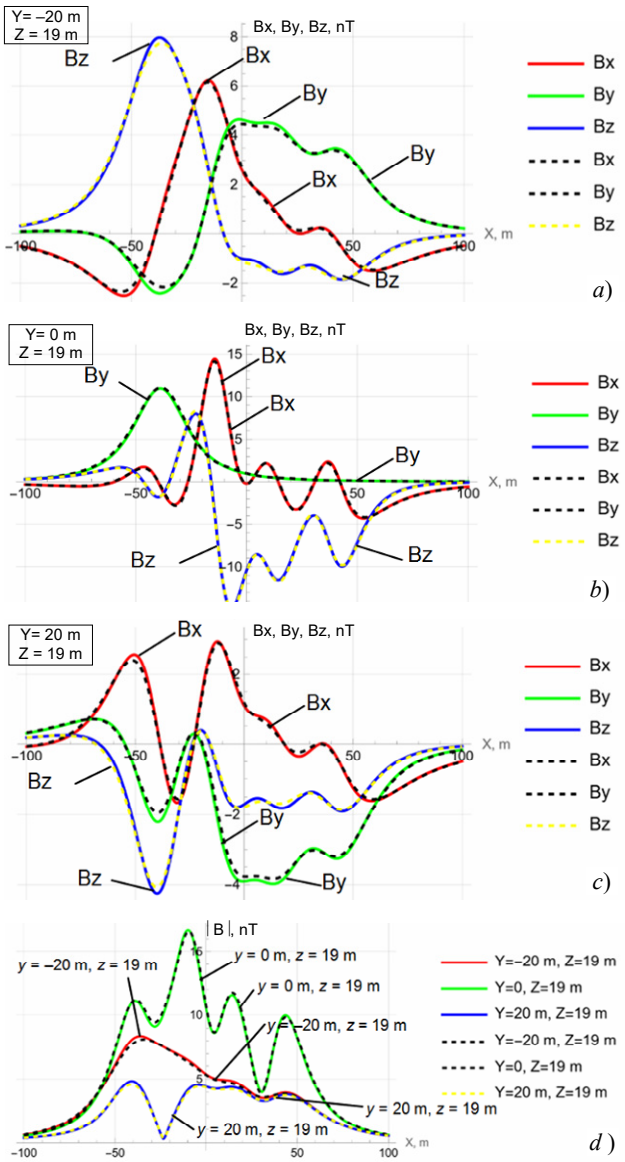

Fig. 2. Signatures of the original (solid lines) and model (dashed lines) magnetic field

Let us now consider the solution of the geometric inverse problem of magnetostatics based on the location of 5 compensation dipoles when introducing into the objective function, in addition to the magnetic field induction modules, also horizontal components at the control depth.

As a result of solving the control geometric inverse problem of magnetostatics, the spatial location

coordinates and values of the magnetic moments of 5 compensating dipoles were calculated

$\{x_1, \ldots, x_5\}$ – {11.081, –13.3971, 26.2429, 38.3417, –38.5133} m;

$\{y_1, \ldots, y_5\}$ – {0.148509, 0.547627, –9.81257, –0.832418, 0.288649} m;

$\{z_1, \ldots, z_5\}$ – {0.0697367, 0.302065, –2.47162, 0.512463, –1.01949} m;

$\{M_{x1}, \ldots, M_{x5}\}$ – {469.602, 1040.86, 84.7869, 347.086, 138.088} A·m^2;

$\{M_{y1}, \ldots, M_{y5}\}$ – {–37.4432, –50.1551, –22.2874, 59.2771, 904.151} A·m^2;

$\{M_{z1}, \ldots, M_{z5}\}$ – {252.922, 269.704, 30.4981, 164.38, 298.216} A·m^2.

Figure 3 shows the signatures of the modules: *a*) the initial and resulting magnetic field compensated using 5 dipole sources; *b*) taking into account only the module; *c*) taking into account the horizontal component of the resulting magnetic field at the control depth. The signatures are given for the following coordinate values: *a*) $Y = –20$ m, $Z = 19$ m; *b*) $Y = 0$, $Z = 19$ m; *c*) $Y = 20$ m, Z=19 m.

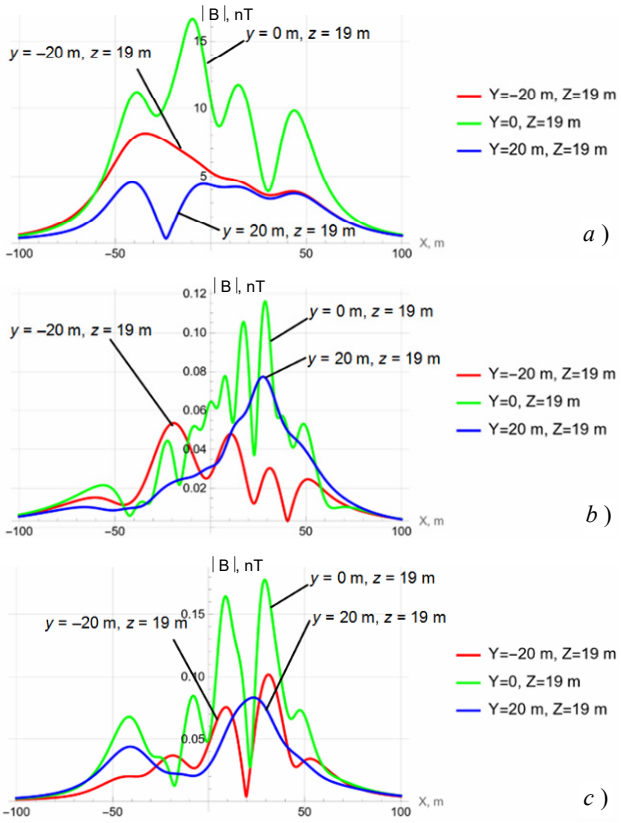

Fig. 3. Signatures of the modules of the initial and resulting magnetic fields

From a comparison of the signatures of the induction modules of the original magnetic field shown in Fig. 3,*a* and the resulting magnetic field shown in Fig. 3,*b*, it follows that with the help of 5 compensation dipoles it was possible to reduce the induction modulus of the original magnetic field by almost 100 times. Taking into account the horizontal component leads to a certain increase in the modulus of the resulting field, as follows from a comparison of Fig. 3,*b* and Fig. 3,*c*.

Figure 4 shows the signatures of the horizontal components of the induction of: *a*) the initial and resulting magnetic field using 5 compensating dipoles; *b*) taking into account only the module; *c*) taking into account the horizontal component of the resulting magnetic field at the control depth.

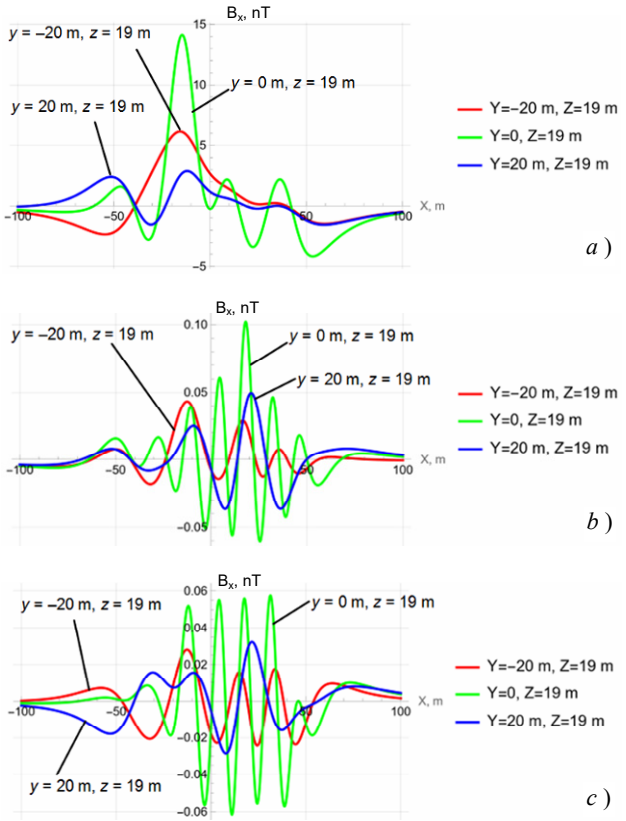

Fig. 4. Signatures of the horizontal components of the initial and resulting magnetic fields

From a comparison of these signatures it follows that with the help of 5 compensation dipoles it was also possible to reduce the horizontal component of the induction of the original magnetic field by almost 100 times. Moreover, taking into account the horizontal component of the magnetic field leads to an additional reduction in the horizontal component of the resulting field by approximately 1.5 times, as follows from a comparison of Fig. 4,*b* and Fig. 4,*c*.

Figure 5 shows the signatures of the longitudinal components of the induction of: *a*) the initial and resulting magnetic field using 5 compensating dipoles; *b*) taking into account only the module; *c*) taking into account the horizontal component of the resulting magnetic field at the control depth.

From a comparison of the signatures of the longitudinal components of the induction of the original magnetic field, shown in Fig. 5,*a* and the resulting magnetic field shown in Fig. 5,*b*, it follows that with the help of 5 compensation dipoles it was possible to simultaneously reduce the longitudinal components of the induction of the original magnetic field by almost 200 times. However, taking into account the horizontal component in the optimization criterion leads to an increase in the longitudinal components of the induction of the resulting field by more than two times, as follows from a comparison of Fig. 5,*b* and Fig. 5,*c*.

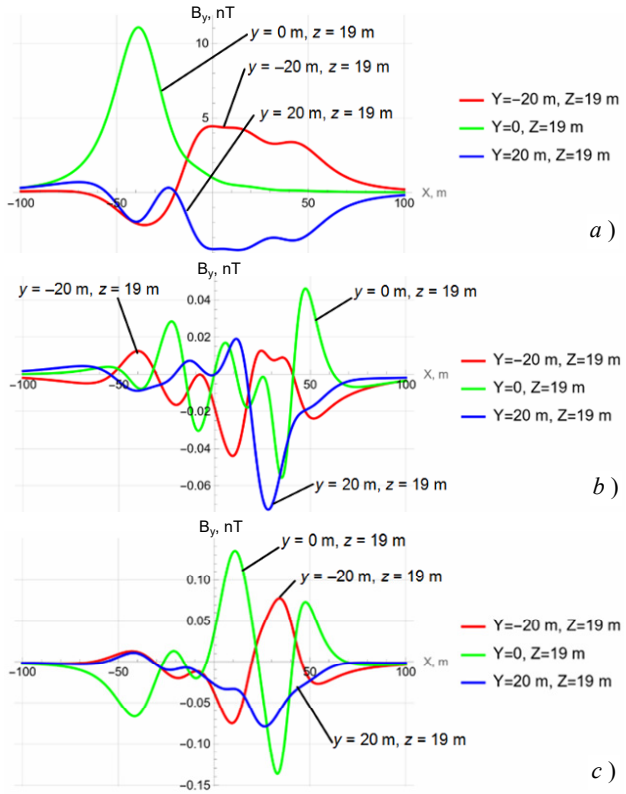

Fig. 5. Signatures of the longitudinal components of the initial and resulting magnetic fields

Figure 6 shows the signatures of the vertical components of induction: *a*) of the initial and resulting magnetic field using 5 compensating dipoles; *b*) when taking into account only the module; *c*) when taking into account the horizontal component of the resulting magnetic field at the control depth.

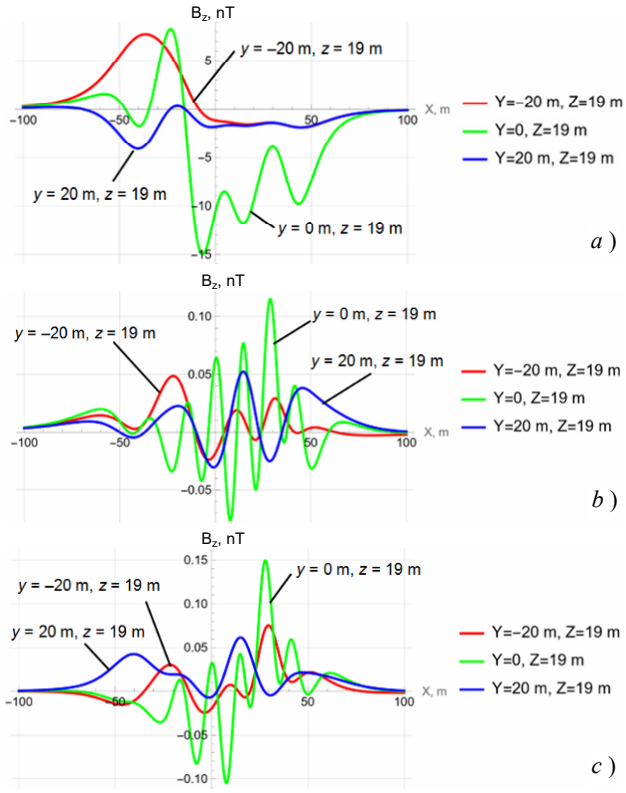

Fig. 6. Signatures of the vertical components of the initial and resulting magnetic fields

From a comparison of the signatures of the vertical components of the induction of the original magnetic field, shown in Fig. 6,*a* and the resulting magnetic field shown in Fig. 6,*b*, it follows that with the help of 5 compensation dipoles it was possible to simultaneously reduce the vertical components of the induction of the original magnetic field by almost 50 times. However, taking into account the horizontal component in the optimization criterion leads to an increase in the vertical components of the induction of the resulting field by more than 1.5 times, as follows from a comparison of Fig. 6,*b* and Fig. 6,*c*.

Thus, by minimizing the magnetic induction modules, a decrease in the module of the resulting magnetic field by more than 100 times is achieved, while simultaneously reducing the magnetic induction components of the resulting magnetic field, also by approximately 100 times. When simultaneously taking into account in the optimization criteria both the magnetic induction modules and the values of the horizontal components of the magnetic induction of the resulting magnetic field, the value of the horizontal component of the resulting magnetic field is additionally reduced by 1.5 times. However, in this case, the modules of the resulting magnetic field, as well as the longitudinal and vertical components of the magnetic field, increase by approximately 1.5 times.

Conclusions.

1. For the first time the method for reduction of magnetic field of uncertain extended technical objects based on their multyspheroidal model and optimization of parameters of compensating dipoles for compensate of spheroidal harmonics of external magnetic field of technical object. Unlike known methods, the developed method makes it possible to increase the efficiency of magnetic field reduction of uncertain extended technical objects.

2. Parameters of compensating dipole magnetic field sources calculated as magnetostatics geometric inverse problems solution in the form of nonlinear minimax optimization problem based on multyspheroidal model of magnetic field of extended technical objects. Nonlinear objective function calculated as the weighted sum of squared of resulting magnetic field COMSOL Multiphysics software package used. Nonlinear minimax optimization problems solutions calculated based on particle swarm nonlinear optimization algorithms

3. Based on the simulation results it is theoretically shown the possibility to reduce by almost 100 times of modulus of induction and horizontal component of the induction of the original magnetic field of uncertain extended technical objects based on optimization of compensating magnetic dipoles spatial arrangement for compensate of spheroidal harmonics of external magnetic field of technical object using multyspheroidal model of the magnetic field.

4. In the future it is planned to conduct experimental studies of the effectiveness of reducing of magnetic field of uncertain extended technical objects based on developed method.

Conflict of interest. The authors declare that they have no conflicts of interest.

REFERENCES

1. Rozov V.Yu., Getman A.V., Petrov S.V., Erisov A.V., Melanchenko A.G., Khoroshilov V.S., Schmidt I.R Spacecraft magnetism. *Technical Electrodynamics. Thematic issue «Problems of modern electrical engineering»*, 2010, part 2, pp. 144-147. (Rus).

2. *ECSS-E-HB-20-07A. Space engineering: Electromagnetic compatibility hand-book. ESA-ESTEC. Requirements & Standards Division*. Noordwijk, Netherlands, 2012. 228 p.

3. Droughts S.A., Fedorov O.P. Space project Ionosat-Micro. Monograph. Kyiv, Akademperiodika Publ., 2013. 218 p. (Rus).

4. Holmes J.J. *Exploitation of A Ship's Magnetic Field Signatures*. Springer Cham, 2006. 67 p. doi: https://doi.org/10.1007/978-3-031-01693-6.

5. Woloszyn M., Jankowski P. Simulation of ship's deperming process using Opera 3D. 2017 18th International Symposium on Electromagnetic Fields in Mechatronics, Electrical and Electronic Engineering (ISEF) Book of Abstracts, 2017, pp. 1-2. doi: https://doi.org/10.1109/ISEF.2017.8090680.

6. Birsan M., Holtham P., Carmen. Using global optimisation techniques to solve the inverse problem for the computation of the static magnetic signature of ships. *Defense Research Establishment Atlantic*, 9 Grove St., PO Box 1012, Dartmouth, Nova Scotia, B2Y 3Z7, Canada.

7. Zuo C., Ma M., Pan Y., Li M., Yan H., Wang J., Geng P., Ouyang J. Multi-objective optimization design method of naval vessels degaussing coils. *Proceedings of SPIE - The International Society for Optical Engineering*, 2022, vol. 12506, art. no. 125060J. doi: https://doi.org/10.1117/12.2662888.

8. Baranov M.I., Rozov V.Y., Sokol Y.I. To the 100th anniversary of the National Academy of Sciences of Ukraine – the cradle of domestic science and technology. *Electrical Engineering & Electromechanics*, 2018, no. 5, pp. 3-11. doi: https://doi.org/10.20998/2074-272X.2018.5.01.

9. Rozov V.Y. *External magnetic fields of power electrical equipment and methods for reducing them*. Kiev, The Institute of Electrodynamics Publ., 1995, no.772. 42 p. (Rus).

10. Rozov V.Yu. Methods for reducing external magnetic fields of energy-saturated objects. *Technical Electrodynamics*, 2001, no. 1, pp. 16-20.

11. Rozov V.Yu. Selective compensation of spatial harmonics of the magnetic field of energy-saturated objects. *Technical Electrodynamics*, 2002, no. 1, pp. 8-13. (Rus).

12. Rozov V.Yu., Dobrodeev P.N., Volokhov S.A. Multipole model of a technical object and its magnetic center. *Technical Electrodynamics*, 2008, no. 2, pp. 3-8. (Rus).

13. Rozov V.Yu., Getman A.V., Kildishev A.V. Spatial harmonic analysis of the external magnetic field of extended objects in a prolate spheroidal coordinate system. *Technical Electrodynamics*, 1999, no. 1, pp. 7-11. (Rus).

14. Rozov V.Yu. Mathematical model of electrical equipment as a source of external magnetic field. *Technical Electrodynamics*, 1995, no. 2, pp. 3-7. (Rus).

15. Volokhov S.A., Dobrodeev P.N., Ivleva L.F. Spatial harmonic analysis of the external magnetic field of a technical object. *Technical Electrodynamics*, 1996, no. 2, pp. 3-8. (Rus).

16. Getman A.V. *Analysis and synthesis of the magnetic field structure of technical objects on the basis of spatial harmonics*. Dissertation thesis for the degree of Doctor of Technical Sciences. Kharkiv, 2018. 43 p. (Ukr).

17. Xiao C., Xiao C., Li G. Modeling the ship degaussing coil's effect based on magnetization method. *Communications in Computer and Information Science*, 2012, vol. 289, pp. 62-69. doi: https://doi.org/10.1007/978-3-642-31968-6_8.

18. Wołoszyn M., Jankowski P. Ship's de-perming process using coils lying on seabed. *Metrology and Measurement Systems*, 2019, vol. 26, no. 3, pp. 569-579. doi: https://doi.org/10.24425/mms.2019.129582.

19. Fan J., Zhao W., Liu S., Zhu Z. Summary of ship comprehensive degaussing. *Journal of Physics: Conference Series*, 2021, vol. 1827, no. 1, art. no. 012014. doi: https://doi.org/10.1088/1742-6596/1827/1/012014.

20. Getman A.V. Spatial harmonic analysis of the magnetic field of the sensor of the neutral plasma component. *Eastern European Journal of Advanced Technologies*, 2010, vol. 6, no. 5(48), pp. 35-38. doi: https://doi.org/10.15587/1729-4061.2010.3326.

21. Getman A. Ensuring the Magnetic Compatibility of Electronic Components of Small Spacecraft. *2022 IEEE 3rd KhPI Week on Advanced Technology (KhPIWeek)*, 2022, no. 1-4. doi: https://doi.org/10.1109/KhPIWeek57572.2022.9916339.

22. Acuña M.H. *The design, construction and test of magnetically clean spacecraft – a practical guide*. NASA/GSFC internal report. 2004.

23. Junge A., Marliani F. Prediction of DC magnetic fields for magnetic cleanliness on spacecraft. *2011 IEEE International Symposium on Electromagnetic Compatibility*, 2011, pp. 834-839. doi: https://doi.org/10.1109/ISEMC.2011.6038424.

24. Lynn G.E., Hurt J.G., Harriger K.A. Magnetic control of satellite attitude. *IEEE Transactions on Communication and Electronics*, 1964, vol. 83, no. 74, pp. 570-575. doi: https://doi.org/10.1109/TCOME.1964.6539511.

25. Junge A., Trougnou L., Carrubba E. Measurement of Induced Equivalent Magnetic Dipole Moments for Spacecraft Units and Components. *Proceedings ESA Workshop Aerospace EMC 2009 ESA WPP-299*, 2009, vol. 4, no. 2, pp. 131-140.

26. Mehlem K., Wiegand A. Magnetostatic cleanliness of spacecraft. *2010 Asia-Pacific International Symposium on Electromagnetic Compatibility*, 2010, pp. 936-944. doi: https://doi.org/10.1109/APEMC.2010.5475692.

27. Messidoro P., Braghin M., Grande M. Magnetic cleanliness verification approach on tethered satellite. *16th Space Simulation Conference: Confirming Spaceworthiness into the Next Millennium*, 1991, pp. 415-434.

28. Mehlem K., Narvaez P. Magnetostatic cleanliness of the radioisotope thermoelectric generators (RTGs) of Cassini. *1999 IEEE International Symposium on Electromagnetic Compatability*, 1999, vol. 2, pp. 899-904. doi: https://doi.org/10.1109/ISEMC.1999.810175.

29. Eichhorn W.L. *Magnetic dipole moment determination by near-field analysis*. Goddard Space Flight Center. Washington, D.C., National Aeronautics and Space Administration, 1972. NASA technical note, D 6685. 87 p.

30. Matsushima M., Tsunakawa H., Iijima Y., Nakazawa S., Matsuoka A., Ikegami S., Ishikawa T., Shibuya H., Shimizu H., Takahashi F. Magnetic Cleanliness Program Under Control of Electromagnetic Compatibility for the SELENE (Kaguya) Spacecraft. *Space Science Reviews*, 2010, vol. 154, no. 1-4, pp. 253-264. doi: https://doi.org/10.1007/s11214-010-9655-x.

31. Boghosian M., Narvaez P., Herman R. Magnetic testing, and modeling, simulation and analysis for space applications. *2013 IEEE International Symposium on Electromagnetic Compatibility*, 2013, pp. 265-270. doi: https://doi.org/10.1109/ISEMC.2013.6670421.

32. Mehlem K. Multiple magnetic dipole modeling and field prediction of satellites. *IEEE Transactions on Magnetics*, 1978, vol. 14, no. 5, pp. 1064-1071. doi: https://doi.org/10.1109/TMAG.1978.1059983.

33. Thomsen P.L., Hansen F. Danish Ørsted Mission In-Orbit Experiences and Status of The Danish Small Satellite Programme. *Annual AIAA/USU Conference on Small Satellites*, 1999, pp. SSC99-I–8.

34. Kapsalis N.C., Kakarakis S.-D.J., Capsalis C.N. Prediction of multiple magnetic dipole model parameters from near field measurements employing stochastic algorithms. *Progress In Electromagnetics Research Letters*, 2012, vol. 34, pp. 111-122. doi: https://doi.org/10.2528/PIERL12030905.

35. Solomentsev O., Zaliskyi M., Averyanova Y., Ostroumov I., Kuzmenko N., Sushchenko O., Kuznetsov B., Nikitina T., Tserne E., Pavlikov V., Zhyla S., Dergachov K., Havrylenko O., Popov A., Volosyuk V., Ruzhentsev N., Shmatko O. Method of Optimal Threshold Calculation in Case of Radio Equipment Maintenance. *Data Science and Security. Lecture Notes in Networks and Systems*, 2022, vol. 462, pp. 69-79. doi: https://doi.org/10.1007/978-981-19-2211-4_6.

36. Ruzhentsev N., Zhyla S., Pavlikov V., Volosyuk V., Tserne E., Popov A., Shmatko O., Ostroumov I., Kuzmenko N., Dergachov K., Sushchenko O., Averyanova Y., Zaliskyi M., Solomentsev O., Havrylenko O., Kuznetsov B., Nikitina T. Radio-Heat Contrasts of UAVs and Their Weather Variability at 12 GHz, 20 GHz, 34 GHz, and 94 GHz Frequencies. *ECTI Transactions on Electrical Engineering, Electronics, and Communications*, 2022, vol. 20, no. 2, pp. 163-173. doi: https://doi.org/10.37936/ecti-eec.2022202.246878.

37. Havrylenko O., Dergachov K., Pavlikov V., Zhyla S., Shmatko O., Ruzhentsev N., Popov A., Volosyuk V., Tserne E., Zaliskyi M., Solomentsev O., Ostroumov I., Sushchenko O., Averyanova Y., Kuzmenko N., Nikitina T., Kuznetsov B. Decision Support System Based on the ELECTRE Method. *Data Science and Security. Lecture Notes in Networks and Systems*, 2022, vol. 462, pp. 295-304. doi: https://doi.org/10.1007/978-981-19-2211-4_26.

38. Shmatko O., Volosyuk V., Zhyla S., Pavlikov V., Ruzhentsev N., Tserne E., Popov A., Ostroumov I., Kuzmenko N., Dergachov K., Sushchenko O., Averyanova Y., Zaliskyi M., Solomentsev O., Havrylenko O., Kuznetsov B., Nikitina T. Synthesis of the optimal algorithm and structure of contactless optical device for estimating the parameters of statistically uneven surfaces. *Radioelectronic and Computer Systems*, 2021, no. 4, pp. 199-213. doi: https://doi.org/10.32620/reks.2021.4.16.

39. Volosyuk V., Zhyla S., Pavlikov V., Ruzhentsev N., Tserne E., Popov A., Shmatko O., Dergachov K., Havrylenko O., Ostroumov I., Kuzmenko N., Sushchenko O., Averyanova Yu., Zaliskyi M., Solomentsev O., Kuznetsov B., Nikitina T. Optimal Method for Polarization Selection of Stationary Objects Against the Background of the Earth's Surface. *International Journal of Electronics and Telecommunications*, 2022, vol. 68, no. 1, pp. 83-89. doi: https://doi.org/10.24425/ijet.2022.139852.

40. Zhyla S., Volosyuk V., Pavlikov V., Ruzhentsev N., Tserne E., Popov A., Shmatko O., Havrylenko O., Kuzmenko N., Dergachov K., Averyanova Y., Sushchenko O., Zaliskyi M., Solomentsev O., Ostroumov I., Kuznetsov B., Nikitina T. Practical imaging algorithms in ultra-wideband radar systems using active aperture synthesis and stochastic probing signals. *Radioelectronic and Computer Systems*, 2023, no. 1, pp. 55-76. doi: https://doi.org/10.32620/reks.2023.1.05.

41. Maksymenko-Sheiko K.V., Sheiko T.I., Lisin D.O., Petrenko N.D. Mathematical and Computer Modeling of the Forms of Multi-Zone Fuel Elements with Plates. *Journal of Mechanical Engineering*, 2022, vol. 25, no. 4, pp. 32-38. doi: https://doi.org/10.15407/pmach2022.04.032.

42. Hontarovskyi P.P., Smetankina N.V., Ugrimov S.V., Garmash N.H., Melezhyk I.I. Computational Studies of the Thermal Stress State of Multilayer Glazing with Electric Heating. *Journal of Mechanical Engineering*, 2022, vol. 25, no. 1, pp. 14-21. doi: https://doi.org/10.15407/pmach2022.02.014.

43. Kostikov A.O., Zevin L.I., Krol H.H., Vorontsova A.L. The Optimal Correcting the Power Value of a Nuclear Power Plant Power Unit Reactor in the Event of Equipment Failures. *Journal of Mechanical Engineering*, 2022, vol. 25, no. 3, pp. 40-45. doi: https://doi.org/10.15407/pmach2022.03.040.

44. Rusanov A.V., Subotin V.H., Khoryev O.M., Bykov Y.A., Korotaiev P.O., Ahibalov Y.S. Effect of 3D Shape of Pump-Turbine Runner Blade on Flow Characteristics in Turbine Mode. *Journal of Mechanical Engineering*, 2022, vol. 25, no. 4, pp. 6-14. doi: https://doi.org/10.15407/pmach2022.04.006.

45. Sushchenko O., Averyanova Y., Ostroumov I., Kuzmenko N., Zaliskyi M., Solomentsev O., Kuznetsov B., Nikitina T., Havrylenko O., Popov A., Volosyuk V., Shmatko O., Ruzhentsev N., Zhyla S., Pavlikov V., Dergachov K., Tserne E. Algorithms for Design of Robust Stabilization Systems. *Computational Science and Its Applications – ICCSA 2022. ICCSA 2022. Lecture Notes in Computer Science*, 2022, vol. 13375, pp. 198-213. doi: https://doi.org/10.1007/978-3-031-10522-7_15.

46. Zhyla S., Volosyuk V., Pavlikov V., Ruzhentsev N., Tserne E., Popov A., Shmatko O., Havrylenko O., Kuzmenko N., Dergachov K., Averyanova Y., Sushchenko O., Zaliskyi M., Solomentsev O., Ostroumov I., Kuznetsov B., Nikitina T. Statistical synthesis of aerospace radars structure with optimal spatio-temporal signal processing, extended observation area and high spatial resolution. *Radioelectronic and Computer Systems*, 2022, no. 1, pp. 178-194. doi: https://doi.org/10.32620/reks.2022.1.14.

47. Wang D., Yu Q. Review on the development of numerical methods for magnetic field calculation of ships. *Ships Science and Technology*, 2014, vol. 36, no. 3, pp. 1-6.

48. Jin H., Wang H., Zhuang Z. A New Simple Method to Design Degaussing Coils Using Magnetic Dipoles. *Journal of Marine Science and Engineering*, 2022, vol. 10, no. 10, art. no. 1495. doi: https://doi.org/10.3390/jmse10101495.

Received 16.05.2024
Accepted 18.09.2024
Published 02.03.2025

B.I. Kuznetsov[1], *Doctor of Technical Science, Professor,*
T.B. Nikitina[2], *Doctor of Technical Science, Professor,*
I.V. Bovdui[1], *PhD, Senior Research Scientist,*
K.V. Chunikhin[1], *PhD, Senior Research Scientist,*
V.V. Kolomiets[2], *PhD, Assistant Professor,*
B.B. Kobylianskyi[2], *PhD, Assistant Professor,*
[1] Anatolii Pidhornyi Institute of Power Machines and Systems of the National Academy of Sciences of Ukraine,
2/10, Komunalnykiv Str., Kharkiv, 61046, Ukraine,
e-mail: kuznetsov.boris.i@gmail.com (Corresponding Author)
[2] Bakhmut Education Research and Professional Pedagogical Institute V.N. Karazin Kharkiv National University,
9a, Nosakov Str., Bakhmut, Donetsk Region, 84511, Ukraine.

How to cite this article:
Kuznetsov B.I., Nikitina T.B., Bovdui I.V., Chunikhin K.V., Kolomiets V.V., Kobylianskyi B.B. Method for reduction of magnetic field of uncertain extended technical objects based on their multyspheroidal model and compensating magnetic dipoles. *Electrical Engineering & Electromechanics*, 2025, no. 2, pp. 48-58. doi: https://doi.org/10.20998/2074-272X.2025.2.07

UDC 621.365.51 https://doi.org/10.20998/2074-272X.2025.2.08

V.Yu. Grytsiuk, M.A.M. Yassin

Numerical modeling of coupled electromagnetic and thermal processes in the zone induction heating system for metal billets

Introduction. *For many modern manufacturing processes, induction heating provides an attractive combination of speed, consistency and control. Multi-inductor (zone) systems with continuous billets feed are the most promising, which keep the billet cross sectional average temperature equal. It allows to avoid overheating at low throughputs and reduces the number of rejected billets.* ***Problem.*** *With zone induction heating systems for metal billets developing it is necessary, at the design stage, to perform a quantitative analysis of the main characteristics of the electrothermal process and provide recommendations for optimal parameters and heating modes selections. Accurate calculations for induction heating systems involve considering the distribution of the magnetic field, current density, and changes of material properties throughout volume of the heated billet.* ***The goal*** *of the work is to develop the numerical model and analyze the coupled electromagnetic and thermal processes in zone induction heating system for metal billets to determine the optimal power ratio of the inductors and choose rational heating modes for the billets.* ***Methodology.*** *The spatiotemporal distribution of the electromagnetic field and temperature throughout the volume of the billet during the induction heating process is described by the system of Maxwell and Fourier equations. For numerical calculations by the finite element method, the COMSOL Multiphysics 6.1 software package was used. All three methods of heat transfer are taken into account – conduction, convection, and radiation. Multiphysics couplings use electromagnetic power dissipation as a heat sources, and the billet material properties are specified by temperature functions. The operation of the inductors' coils is modeled using the «Multi-Turn Coil» function, which uses a homogenized model. The translational motion of the billet is modeled by using the «Translational Motion» function.* ***Results.*** *The numerical 3D-model of coupled electromagnetic and thermal processes in the zone induction heating system for metal billets has been developed. Modeling was carried out for the design of a four-inductor system with the nominal capacity of 5000 kg/h. Data on the spatial distribution of the electromagnetic and temperature fields in the moving heated steel billet were obtained.* ***Originality.*** *Three-dimensional graphs of electrical conductivity and relative magnetic permeability change inside the moving heated steel billet are presented. Results of the temperature distribution calculations along the length of the steel billet for different inductors power ratios are provided. It is shown how the change in the power distribution of the inductors affects the billet heating parameters.* ***Practical value.*** *Analysis of the obtained data allows to determinate the necessary inductors powers to ensure the required heating mode. The results make it possible to reduce the time and resources required for the development, optimization of the design and improvement of the technological process of zone induction heating for metal billets.* References 20, table 1, figures 13.

Key words: **zone heating, numerical model, inductor, temperature field, finite element method, metal billet, electrical conductivity.**

Вступ. *Для багатьох сучасних виробничих процесів індукційний нагрів забезпечує привабливе поєднання швидкості, узгодженості та контролю. Найбільш перспективними є багатоіндукторні (зонні) установки з безперервною подачею заготовок, що підтримують середню температуру поперечного перетину заготовки рівною. Це дозволяє уникнути перегріву за низької продуктивності та зменшити кількість бракованих заготовок.* ***Постановка проблеми.*** *При розробці установок індукційного зонного нагріву металевих заготовок необхідно, на етапі проєктування, виконати кількісний аналіз основних характеристик електротеплового процесу та виробити рекомендації щодо вибору раціональних параметрів та режимів нагріву. Уточнений розрахунок індукційних нагрівальних установок передбачає врахування розподілу магнітного поля, густини струму та зміни властивостей матеріалу по всьому об'єму заготовки, що нагрівається.* ***Метою*** *роботи є розробка чисельної моделі та аналіз взаємопов'язаних електромагнітних і теплових процесів в установці індукційного зонного нагріву металевих заготовок для подальшого визначення оптимального співвідношення потужностей індукторів та вибору раціональних режимів нагріву заготовок.* ***Методика.*** *Просторово-часовий розподіл електромагнітного поля та температури по об'єму заготовки в процесі індукційного нагріву описується системою рівнянь Максвелла і Фур'є. Для проведення чисельних розрахунків методом скінченних елементів використано програмний комплекс COMSOL Multiphysics 6.1. Відтворюються всі три способи теплопередачі – теплопровідністю, конвекцією і випромінюванням. Мультифізичні зв'язки використовують розсіювання електромагнітної потужності як джерела тепла, а властивості матеріалу заготовки задані функціями температури. Робота котушок індукторів моделюється із застосуванням функції «Multi-Turn Coil», яка використовує гомогенізовану модель. Поступальний рух заготовки моделюється за допомогою функції «Translational Motion».* ***Результати.*** *Розроблено чисельну 3D-модель взаємопов'язаних електромагнітних і теплових процесів в установці індукційного зонного нагріву металевих заготовок. Розрахунок проведено для конструкції чотириіндукторної установки номінальною продуктивністю 5000 кг/год. Отримано дані просторового розподілу електромагнітного та температурного поля в рухомій сталевій заготовці, яка нагрівається.* ***Наукова новизна.*** *Представлено тривимірні картини зміни електропровідності та відносної магнітної проникності всередині рухомої сталевої заготовки, що нагрівається. Наведено розрахунки розподілу температури по довжині сталевої заготовки для різних співвідношень потужностей індукторів установки зонного нагріву. Показано, як зміна розподілу потужностей індукторів впливає на показники нагріву заготовки.* ***Практична значимість.*** *Аналіз отриманих даних дозволяє встановити необхідні потужності індукторів, за яких забезпечується необхідний режим нагрівання. Результати дозволяють зменшити час і ресурси, необхідні для розробки, оптимізації конструкції та вдосконалення технологічного процесу індукційного зонного нагріву металевих заготовок.* Бібл. 20, табл. 1, рис. 13.

Ключові слова: **зонний нагрів, чисельна модель, індуктор, температурне поле, метод скінченних елементів, металева заготовка, електропровідність.**

Introduction. A number of technological processes, including high-temperature processing of solid materials, liquid and granular substances, are based on the induction heating use [1–5]. The application area of induction heaters is quite wide: from hot water supply to process heating, including smelting and thermal processing of metals, thermal processing of bulk materials or liquid substances (for example, liquid fuel) placed in a metal container for its recycling. For many modern manufacturing processes, induction heating provides an attractive combination of speed, consistency and process control. In addition, induction heating is an environmentally friendly form of heating.

Modern induction heating installations are complex set of devices. Their main components are: an inductor with a billet, a control system, power supply, a billet supply system, etc. [1, 2]. The alternating magnetic field

of the inductor excites eddy currents of the same frequency inside the billet, which create internal heat sources in the billet. In industry, the following main methods of implementing through induction heating processes are used: periodic, methodical and continuous, as well as periodic heating with reciprocating movement of the billet (Fig. 1).

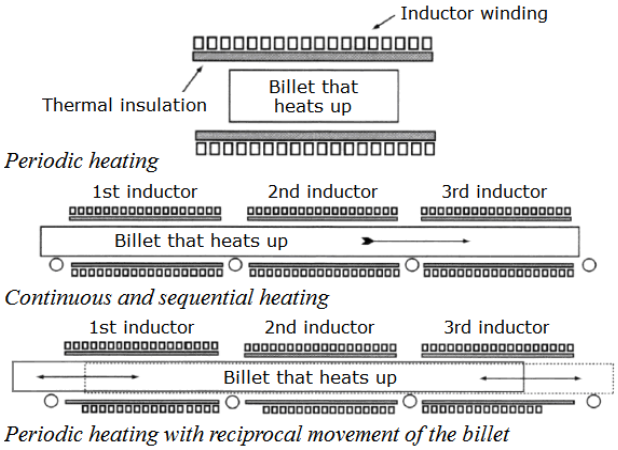

Fig. 1. Main methods of implementing through induction heating processes

In periodic heating systems, the billet is placed in the inductor for the time required to reach the desired temperature conditions, after which it is unloaded and transferred to the next technological operations, and a new billet is loaded in its place. The process is repeated with the periodic release of heated billets from the inductor. Methodical heating systems are designed for the sequential heating of two or more billets in a single- or multi-section inductor during their discrete movement (pushing) with a certain step in time and distance, with the step equal to the length of one billet from the entrance to the inductor to its exit.

Continuous heating systems provide heating of billets in an inductor of single- or multi-section design during their continuous movement at a constant speed inside the heater.

In systems with periodic heating and reciprocating movement of the billet, the depth of the billet inside the inductor periodically changes during heating. This compensates for undesirable longitudinal edge effects and helps to reduce temperature variations along the length of the billet. Such systems are used for heating long billets.

In mass production conditions, where it is necessary to ensure high productivity and heating quality, as well as the possibility of implementing different heating modes by changing the parameters of the heated billets, multi-inductor (zone) systems with continuous billets feed are the most promising [6–9]. In contrast to conventional billet heaters, zone heaters keep the billet cross sectional average temperature equal and independent of the throughput and billet dimensions. Due to that uniformity this technique avoids overheating at low throughputs and reduces the number of rejected billets. With the aid of a suitable control program the temperature profile can be modified in order to find the best compromise between low billet sticking and scaling rate, uniform temperature distribution within the billets and low energy consumption [6].

The accuracy of heating is ensured by the power supply system through the power distribution between the inductors and appropriate control of power in each inductor. The inductors can be either identical or differ from each other. The power supply system must include semiconductor power sources corresponding to the number of inductors. The most efficient power sources for induction heating devices before further plastic deformation are thyristor and transistor frequency converters [2, 4, 10].

Transistor inverters are predominantly used because they allow the transistor to be turned off not at the «zero» current point but when it is necessary. The use of resonant inverters with transistors and freewheeling diodes eliminates no-load pauses, significantly improving the harmonic composition of the output current. Additionally, the presence of freewheeling diodes eliminates the possibility of voltage overloads.

A generalized circuit of frequency converters is shown in Fig. 2. It includes an input rectifier that provides the required constant output voltage, a filter for coordination, a resonant inverter, and a load.

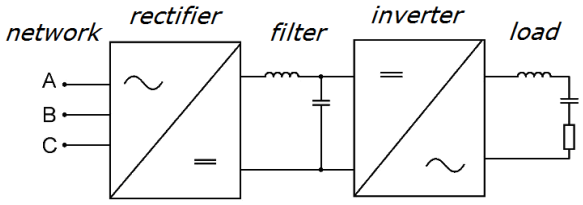

Fig. 2. Frequency converter circuit for induction heating

When developing automated complexes for zone induction heating for metal billets, it is necessary, at the design stage, to perform a quantitative analysis of the main characteristics of the electrothermal process and provide recommendations for selecting optimal parameters and heating modes. This will allow choosing the most efficient heating mode, and the obtained power values will serve as guidelines during the subsequent tuning of the technological cycle. The primary goal of achieving the specified temperature evenly throughout the volume of the billet must be attained with the highest possible performance indicators, which include process productivity, metal loss due to scaling, energy consumption, and the cost of the heating system.

Accurate calculations for induction heating systems involve considering the distribution of the magnetic field, current density, and changes of material properties throughout volume of the billet being heated [11, 12]. High precision in calculating thermal characteristics, which are necessary at the design stage of such systems, must be ensured.

Analysis of approaches to calculating electromagnetic and thermal processes in induction heating systems. Determining the distribution of the electromagnetic field and the temperature of the heated billet is generally performed by using numerical methods, such as the finite element method, considering skin effect, proximity effect, and ring effect [13]. This approach can be fully implemented with a small number of inductor turns (w = 1–5 turns). From the thermal calculation perspective, it is essential that the main part of the energy

is released within the depth of the magnetic field penetration into the conductor. For a large number of turns, the electromagnetic field of round massive conductors with current, representing a multi-turn coil model, has been studied by various authors. Is considered the high-frequency mode characterized by a pronounced skin effect and analyzed the case of using both massive conductors and multi-stranded litz wire. A method is proposed for calculating the resistance of the litz wire inductor winding for induction heating. The resistance is determined taking into account eddy current losses and winding temperature. The calculation of eddy currents and losses in the turns of high-frequency device inductors is carried out based on the experimental data analysis.

Solving the field electromagnetic problem for an induction heating system with a large number of massive inductor turns ($w \geq 10$) generally requires applying a fine computational mesh to cover the cross-section of all conductors and considering the aforementioned effects. Discretization the inductor turns in this case is associated with significant computational difficulties, and typically, each individual turn in the model ends up being too small to correctly account for the non-uniform current density distribution in its cross-section when calculating the entire system.

One approach to simplifying the task solution is to preliminarily calculate the frequency-dependent equivalent parameters of a separate inductor (assuming the heated billet is absent) and then use the found parameters in the overall system calculation [14]. However, in the case of a strong skin effect, using this approach may be ineffective since the inductor parameters significantly depend on the value of the resulting field created by the currents in the inductor turns and the billet.

We will consider a multi-scale modeling technique for calculating electrothermal processes in induction heating systems [13]. The traditional understanding of this approach involves sequentially considering hierarchical levels with information transfer both top-down and bottom-up, with refinement performed iteratively based on the system's main parameter – the equivalent resistance of the inductor. Two spatial levels are distinguished for the induction system. At the macro level, the electromagnetic process in the entire system volume is considered. At the micro level, the problem of the volume of a single inductor turn is solved. As a result of solving the electromagnetic task at the micro level, the equivalent resistance of the inductor is determined, which is then used as a set parameter for calculating the current value in the inductor at the macro level. Tasks that consider the electromagnetic process at two spatial levels are solved jointly using successive approximations, with the solution of the micro-level task refining the solution of the macro-level task.

Using multi-scale modeling, a numerical calculation of coupled electrothermal processes in the heated metal billet is performed [13, 15]. The dependence of the magnetic properties of its material on temperature is considered. An analysis of the processes occurring in the electrical circuit of the induction system's power supply is conducted.

The task of developing models for calculating electromagnetic and thermal processes in induction systems is relevant and allows determining their optimal parameters and efficient modes of electromagnetic controlled processing of conductive materials at the design stage of such systems [14].

Mathematical models for calculating such processes can be created based on both the theory of electromagnetic and thermal fields and the theory of equivalent thermal circuits. Models based on the theory of thermal circuits are widely used, for example, for analyzing thermal processes in electric machines. When constructing a thermal model of an induction system for heating a moving billet, the processes of convective heat transfer play an important role [14].

Field Theory Method: this method is characterized by high accuracy in calculating the temperature distribution within the billet volume, but it requires significant computational power and does not allow modeling electrical processes in a complex-structured power source, such as one with a rectifier and inverter.

Thermal Circuit Method: this method is simpler to implement, does not require significant computational power, and allows quickly obtaining the billet temperature values online as input parameters (billet movement speed, inductor current, etc.) change. By adding an electrical circuit of the power source to the model, this approach allows accurately modeling the processes in the inverter as part of the power source and in the compensating capacitor, as well as modeling the entire system, for example, the automatic control system of the billet temperature both at the inductor exit and along the billet length. The disadvantage of this method is its lower calculation accuracy compared to the field theory method.

The non-uniform current distribution in the inductor and the heated billet leads to the emergence of several specific effects that determine the main physical laws of induction heating [11, 12]. For typical induction heating systems of cylindrical billets placed inside the inductor, the ring effect, together with the skin effect and proximity effect, leads to current concentration on the inner surface of the inductor winding at the minimum distance from the heated billet. This increases the electrical efficiency coefficient in the electromagnetic system «inductor-billet» [8].

The highest accuracy in analyzing electromagnetic and thermal processes is ensured when solving a three-dimensional problem. This becomes possible when considering the influence of the aforementioned physical effects, which manifest more deeply under conditions reproducing the finite length and detailed geometry of the inductors and the billet. Such three-dimensional problems are of practical interest.

The goal of the work is to develop a numerical model and analyze the coupled electromagnetic and thermal processes in zone induction heating system for metal billets to determine the optimal power ratio of the inductors and choose rational heating modes for the billets.

Mathematical description of coupled electromagnetic and thermal processes. In general, the spatiotemporal distribution of the electromagnetic field and temperature throughout the volume of the billet during the induction heating process is described by the system of Maxwell and Fourier equations for electromagnetic and thermal fields [16, 17]:

$$\text{rot}\,\boldsymbol{H} = \boldsymbol{J} + \frac{\partial \boldsymbol{D}}{\partial \tau}; \quad (1)$$

$$\text{rot}\,\boldsymbol{E} = \boldsymbol{J} + \frac{\partial \boldsymbol{B}}{\partial \tau}; \quad (2)$$

$$\text{div}\boldsymbol{B} = 0; \quad (3)$$

$$\text{div}\boldsymbol{D} = \rho; \quad (4)$$

$$c(T)\gamma(T)\frac{\partial T}{\partial \tau}\text{div}(\lambda(T)\text{grad}T) + c(T)\gamma(T)\boldsymbol{V}\text{grad}T = F, \quad (5)$$

where $\boldsymbol{H}$ is the magnetic field strength vector; $\boldsymbol{E}$ is the electric field strength vector; $\boldsymbol{J}$ is the conduction current density; $\boldsymbol{B}$ is the magnetic flux density vector; $\boldsymbol{D}$ is the electric flux density vector; T is the temperature of the billet; τ is the time; $c(T)$, $\gamma(T)$, $\lambda(T)$ are the specific heat capacity, density, and thermal conductivity of the metal, respectively; $\boldsymbol{V}$ is the velocity vector of the billet's movement; F is the internal heat sources.

In the considered task, the source of heat is resistive losses in the billet due to the flow of eddy currents, as well as hysteresis losses. The power of heat generation per unit volume of the heated body can be found by calculating the transferred energy of the electromagnetic field:

$$F = \text{div}\left[\boldsymbol{E}\cdot\boldsymbol{H}\right]. \quad (6)$$

Obtaining a unique solution to the system (1) – (4) for all unknowns, whose number exceeds the number of equations, is possible if this system is supplemented with the following basic relationships [16, 17]:

$$\boldsymbol{D} = \varepsilon\varepsilon_0\boldsymbol{E}; \quad (7)$$

$$\boldsymbol{B} = \mu\mu_0\boldsymbol{H}; \quad (8)$$

$$\boldsymbol{J} = \sigma\boldsymbol{E}, \quad (9)$$

where ε is the relative permittivity of the billet material; ε_0 is the permittivity of vacuum; μ is the relative magnetic permeability of the billet material; μ_0 is the permeability of vacuum; σ is the electrical conductivity of the billet material.

Taking into account (7) and (9), equation (1) becomes:

$$\text{rot}\,\boldsymbol{H} = \sigma\boldsymbol{E} + \frac{\partial(\varepsilon\varepsilon_0\boldsymbol{E})}{\partial \tau}. \quad (10)$$

In the case of induction heating of metals at frequencies below 100 MHz, the density of the induced conduction current is much higher than the displacement current density. Therefore, the second term on the right side of (10) can be neglected. Thus, we get:

$$\text{rot}\,\boldsymbol{H} = \sigma\boldsymbol{E}. \quad (11)$$

The electrical conductivity σ and relative magnetic permeability μ of the billet material are functions of temperature, defined analytically and tabularly during numerical implementation. For induction heating, these dependencies are significant since the thermal power generated in the billet is related to σ and μ of the material. Their decrease when heating the billet leads to a reduction in heating power, a change in skin depth, and the efficiency of the heating process.

During induction heating, all three methods of heat transfer take place – conduction, convection, and radiation. Heat transfer within the heated billet from its more heated layers to less heated ones occurs due to the conduction process, described by the fundamental Fourier's law.

The convective heat exchange process between the heated billet and the surrounding environment is carried out according to Newton's law, which states that the heat transfer rate is directly proportional to the temperature difference between the billet surface T_1 and the surrounding environment T_0. Heat loss from the billet surface to the surrounding environment by radiation is described by the Stefan–Boltzmann law, which states that the heat transfer rate is proportional to the difference of the fourth powers of the absolute temperatures $T_1^4 - T_0^4$. Such a description of radiative heat losses is satisfactory when constructing mathematical models in most real tasks of studying induction heating processes.

The thermophysical parameters λ and c in (5) are nonlinear functions of temperature. In practice, the assumption of a constant thermal conductivity coefficient λ = const does not usually lead to significant errors when modeling temperature fields during induction heating. Similar approximation of the temperature dependence of specific heat capacity can lead to substantial errors in calculating the required power and thermal profile of the billet. Together with the corresponding boundary and initial conditions, equation (5) describes the three-dimensional temperature distribution at any time for any point throughout the volume of the heated billet. The solution to the system of equations (1) – (5) can only be realized by numerical methods. These methods are widely used in modern multiphysics simulation software packages such as Cedrat FLUX, COMSOL Multiphysics, ANSYS, and others.

Equations (1)–(6), (11) provide a general description of the coupled three-dimensional electromagnetic and thermal fields, allowing for the determination of all necessary structural characteristics of the induction system. In this case, equations (1), (2), (10) are rewritten in frequency domain [16]. This approach enables solving the tasks of optimal control of multidimensional temperature fields both in the process of continuous induction heating and in the optimal design of induction heating systems.

Numerical implementation of coupled electromagnetic and thermal processes calculation. For numerical calculations, the COMSOL Multiphysics 6.1 software package was used. The preparation of the calculation process can be divided into several stages. The first stage is the synthesis of the model, which begins with the selection of the model's dimensionality and physical modules. In this software package, there is an option to choose a module that is already highly adapted for calculations in induction heating devices – «Induction Heating». This can be selected through the «Electromagnetic Heating» branch. The multiphysics module (interface) «Induction Heating» is used for calculations of induction and eddy current heating and includes a magnetic fields interface and a heat transfer in solids interface. Multiphysics couplings add electromagnetic power dissipation as a heat source, and the electromagnetic properties of the material can depend on the temperature. Moreover, combinations of frequency domain modeling for the «Magnetic Fields» interface and stationary modeling for the «Heat Transfer in Solids» interface are supported, known as frequency-stationary and frequency-transient modeling.

The «Heat Transfer in Solids» interface allows modeling of heat transfer by conduction, convection, and radiation. The solid model is active by default in all

domains. The temperature equation defined in solid regions corresponds to the differential form of Fourier's law, which may include additional heat sources.

Model geometry synthesis. Each inductor heats a part of the billet in a specific area of space. Optimal heating programs and the required final temperature can be achieved by ensuring that each inductor individually transfers the corresponding power to the billet. This approach requires solving the task of forming the necessary power by the inductors, which determines the design of the inductors and the circuit design of the power part of the converter that powers them.

Modeling was carried out for the design of a multi-inductor system for zonal heating of steel billets with the nominal capacity of 5000 kg/h. The geometric dimensions and technical parameters of the zone induction heating system are presented in Table 1. The model consists of four cylindrical inductors and a cylindrical billet. Each inductor is 1,5 m long, and the billet has a length of 6,5 m and a radius of 0,05 m. The power distribution is such that all inductors have the same operating frequency and number of turns but different current values. For the initial modeling, the power ratios of the inductors were chosen as 1 : 0,8 : 0,8 : 0,6. The inductors are numbered according to the direction of the billet's movement.

Table 1

Geometric dimensions and technical parameters of the zone induction heating system

Parameters	Value
Length of one inductor l_1, m	1,5
Distance between inductors l_2, m	0,1
Inner radius of the inductor r_1, m	0,07
Outer radius of the inductor r_2, m	0,1
Length of the steel billet L_1, m	6,5
Radius of the steel billet R_1, m	0,05
Initial temperature of the billet T_1, °C	20
Ambient temperature T_0, °C	20
Required heating temperature T_2, °C	950
Velocity of the billet V, m/s	0,022
Frequency of the inductor current f, Hz	1000
Current density in the conductors of individual inductors J, A/m^2	
1st	$8{,}9\cdot10^6$
2nd	$7{,}12\cdot10^6$
3rd	$7{,}12\cdot10^6$
4th	$5{,}45\cdot10^6$
Electrical conductivity σ of the billet material at 20 °C, S/m	$5{,}56\cdot10^6$
Relative magnetic permeability μ of the billet material at 20 °C	16

The model geometry can be constructed using COMSOL Multiphysics tools or in AutoCAD, with subsequent importation.

Setting physical constants and properties. After creating the model's geometry, constants are defined. In our case, it is recommended to introduce several constants: $J_1 - J_4$ – the current density values for each inductor. These values equal the product of the current and the number of turns of the inductor divided by the cross-sectional area of the corresponding inductor. Also, f – the frequency of the current in the inductors. Using constants simplifies the subsequent reconfiguration of the model.

The calculation of the electromagnetic field is solved first in the frequency domain modeling step, and the calculation of the temperature field is solved in the subsequent stationary step.

The billet's movement speed is sufficiently low, so the induced current density due to the movement of the conductor is considered negligible compared to the current density induced by the alternating field. The operation of the inductors' coils is modeled using the «Multi-Turn Coil» function, which employs a homogenized coil model consisting of a large number of thin conductors [18, 19].

The boundary conditions applied to the radiating surface of the billet (the surfaces in contact with air) are a combination of thermal flux considering natural thermal convection in the air and a diffuse surface modeling radiative heat transfer to the environment. The translational motion of the billet at a constant speed is modeled using the «Translational Motion» function in the «Heat Transfer in Solids» module.

Finite element mesh construction. The minimum size of the finite elements (given the order of the approximating function polynomial) and the minimum calculation time should be chosen based on the required accuracy of the electromagnetic field calculation. The discretization requirements are applied to the conductive elements of the structure where eddy currents are calculated. Mesh step in these elements should be less than 1/4 of the field penetration depth. Reducing the size of the finite elements increases the calculation time, and the solution becomes more accurate.

Figure 3 shows a fragment of the finite element mesh, representing one of the four inductors and part of the steel billet (inside the inductor, shown in blue).

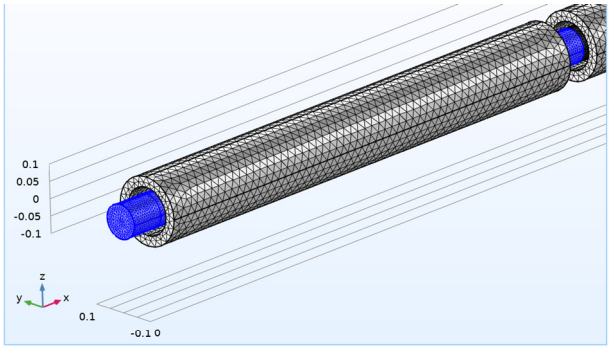

Fig. 3. Fragment of the finite element mesh representing one of the four inductors and part of the steel billet

Results of modeling and discussion. The results of determining the spatial distribution of eddy current density within the steel billet in the form of longitudinal and several transverse sections are presented in Fig. 4. According to the obtained results, the highest heat generation occurs in the layers of the steel billet adjacent to the inner surface of the inductor. In the operating zone of the first inductor, which initiates heating, the maximum current density on the surface of the billet reaches approximately $105\cdot10^6$ A/m². This value rapidly decreases along the axis of the billet and at a distance of 2 mm from the surface, it is around $45\cdot10^6$ A/m².

For comparison, these values in the billet at the edge of the fourth inductor are approximately $65\cdot10^6$ A/m² and $28\cdot10^6$ A/m², respectively. Presumably, this difference is solely due to the varying powers of the first and fourth

inductors (approximately 1,65 times difference). The influence of changes in σ and μ of the billet material on the redistribution of heat sources within it is minor, as this change primarily occurs within the operating zone of the first inductor. Figure 5 shows the change in temperature T and electrical conductivity σ along the length of the heated steel billet.

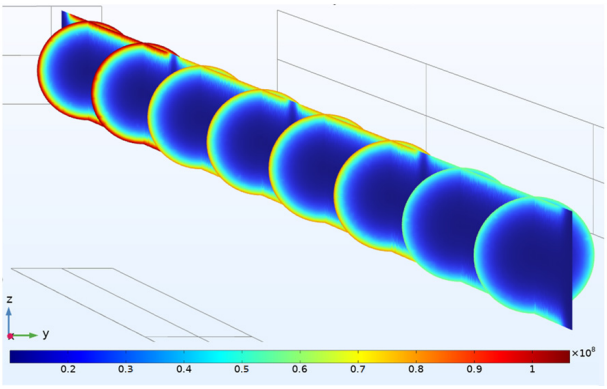

Fig. 4. Spatial distribution of eddy current density inside the billet in the form of longitudinal and several transverse sections

As observed, under such a power ratio between the inductors, the surface temperature of the billet at the end of the first inductor's working zone exceeds 660 °C, while it is 375 °C along the central axis. The electrical conductivity of the billet material in this section decreases by a factor of 5.5 on the surface and 3.1 along the axis compared to its initial values. However, until the completion of heating, the electrical conductivity of the billet decreases by only 25 % and 55 %, respectively.

Figures 6, 7 present the spatial change of σ and μ inside the billet in the form of longitudinal and several transverse sections. Due to skin effect, the surface of the billet transitions through the Curie point earlier than its center. This transition occurs gradually; however, Fig. 7 clearly shows a paramagnetic layer over the ferromagnetic layer within the heating zone of the second inductor, indicating a significant transition. From the perspective of magnetic properties, the billet material becomes two-layered over a length of approximately 1,25 m. Thus, these findings are crucial from a design standpoint. Specifically, the magnetic field strength and distribution of eddy currents, as well as changes in material properties, directly affect temperature control, heating rate, and the formation of localized heat treatment zones in billet.

Figure 8 shows typical curves of equivalent parameters changes of the inductor replacement circuit with the billet during heating for magnetic and non-magnetic metals.

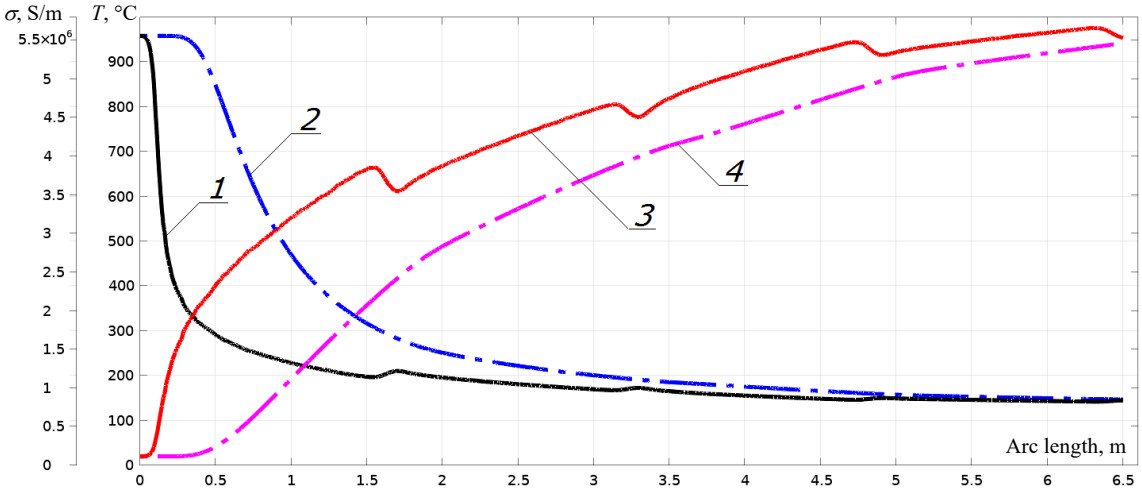

Fig. 5. Change in electrical conductivity and temperature along the heated steel billet length: *1* – value on the surface of billet $\sigma(L_1)$; *2* – value along of billet central axis $\sigma(L_1)$; *3* – value on the surface of billet $T(L_1)$; *4* – value along of billet central axis $T(L_1)$

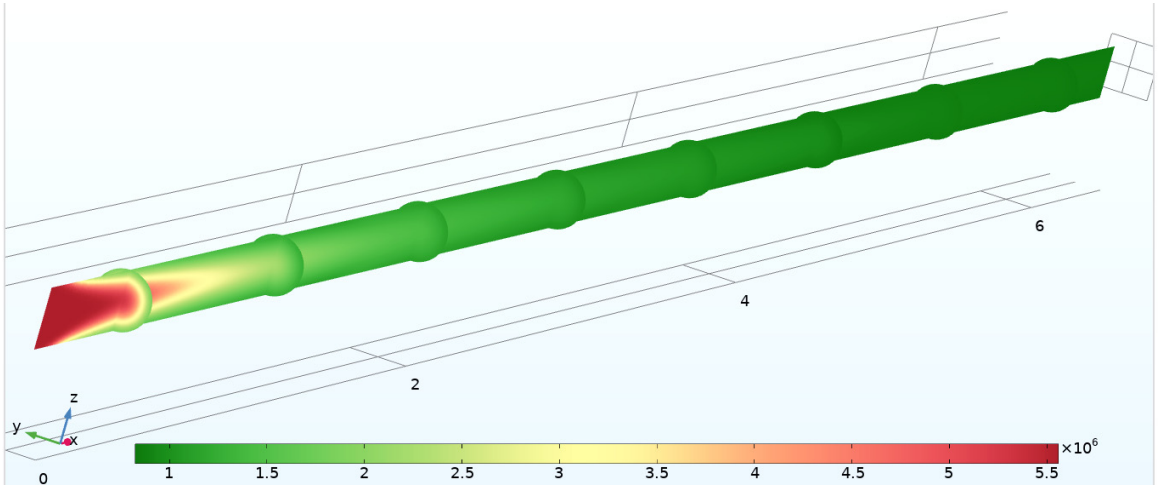

Fig. 6. Change in electrical conductivity σ inside the heated steel billet

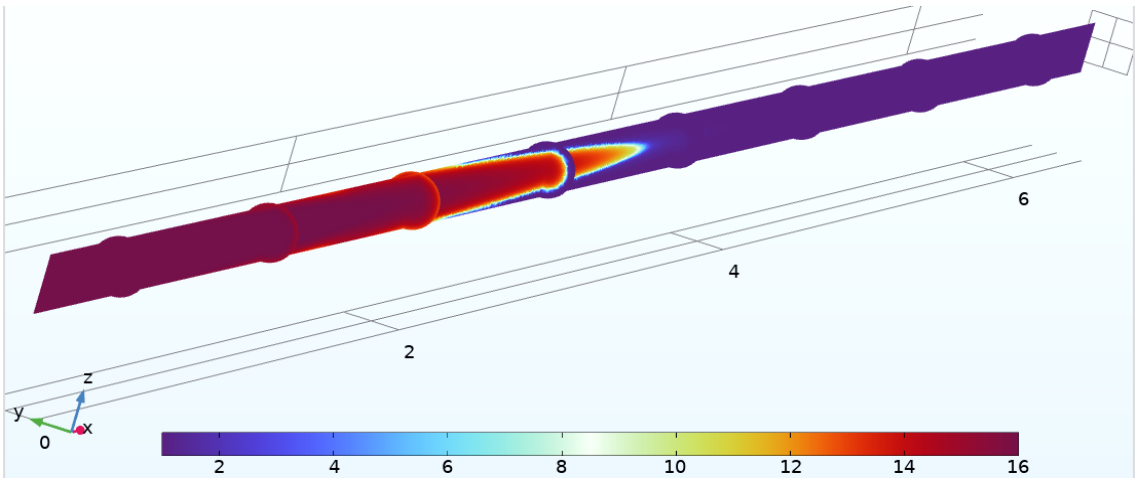

Fig. 7. Change in relative magnetic permeability μ inside the heated steel billet

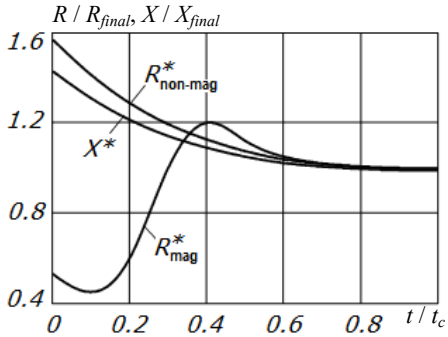

Fig. 8. Change of heating parameters for magnetic and non-magnetic billets (relative to final values) as a function of relative time t/t_C, where t_C – duration of the heating cycle

The curves of changes in R and X are provided for the parallel replacement circuit [10]. The parameters correspond to the complete filling of the inductor with fully heated metal. The ratio of the maximum R value to the minimum ranges from 1,5 to 2,5. The X value decreases during heating by 1,3 to 1,6 times. Accordingly, the quality factor can vary by 2 to 3 times.

The conclusion of the modeling involves obtaining comprehensive data on the spatial distribution of temperature inside the billet. Figure 9 presents temperature field maps of the billet at a time moment of 290,91 s (end of heating). The billet moves from left to right. Current density values in the inductors were chosen so that the exit temperature of the billet from the system would be approximately 950 °C.

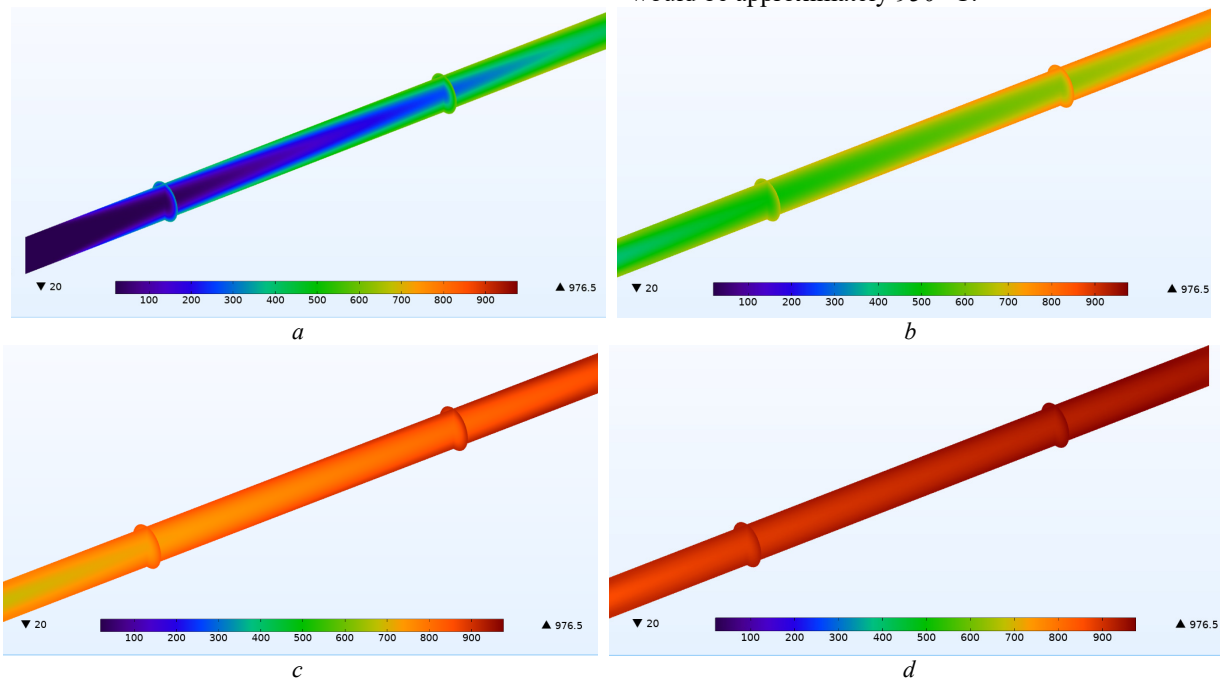

Fig. 9. Temperature spatial distribution in longitudinal and transverse sections of the steel billet for individual heating zones: *a* – heating zone of the first inductor; *b* – heating zone of the second inductor; *c* – heating zone of the third inductor (*c*); *d* – heating zone of the fourth inductor

Temperature spatial distribution in longitudinal and transverse sections of the steel billet for the four heating zones allows a visual assessment of the heating intensity as the billet moves into the zones influenced by individual inductors. For instance, the maximum temperature is found at the end of the heating zone of the fourth inductor (on the surface of the billet), reaching 976,6 °C. Due to skin effect, the center of the billet heats up slower than its surface, resulting in a temperature gradient between them during heating. Depending on the heat source power, this

gradient may exceed the allowable temperature uniformity specified for subsequent rolling or stamping processes, where permissible temperature gradients between the surface and center of a steel billet typically range from ±50 °C to ±25 °C, given the required heating temperature of 1000–1250 °C.

This temperature gradient is somewhat reduced due to heat losses from the billet surface through convective and/or radiative heat exchange with the surrounding environment. Analysis indicates that convective losses predominate in low-temperature heating setups, whereas in high-temperature heaters (for steel, titanium, cobalt, and nickel billets), heat loss predominates through radiation. In our case, the nature of the temperature gradient between the center and surface of the billet can be visually assessed using the temperature distribution across the radius of the billet at the output of each inductor (Fig. 10).

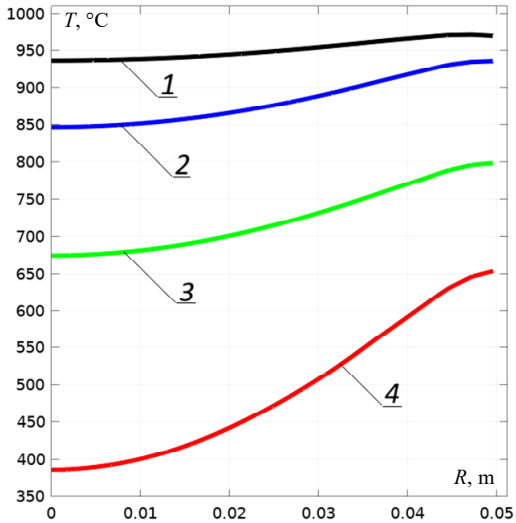

Fig. 10. The temperature distribution across the radius of the billet at the output of each inductor: *1* – the output of the 4th inductor; *2* – the output of the 3rd inductor; *3* – the output of the 2nd inductor; *4* – the output of the 1st inductor

The obtained temperature distribution closely resembles the distribution of eddy current density across the radius of the billet. The temperature difference between the center and the surface of the billet (under the edge of the fourth inductor) is 32 °C. However, this difference decreases rapidly, reaching about 11 °C within 4,5 s, explained by the rapid cooling of the billet surface. Figure 11 shows the temperature distribution across the end section of the billet as contours and surface plots at the exit of the zone heating system.

As we can see, after the billet exits the working zone of the last inductor, the temperature maximum of 960 °C is maintained at a distance of 5 mm from its surface.

Additionally, a series of numerical calculations were carried out to determine the optimal power distribution of the inductors when heating the steel billet. The conditions for comparing all calculations were as follows: the total power of all inductors (only the distribution changes), constant current frequency, productivity (speed), geometry (see Table 1), and cooling conditions. The required surface temperature of the billet at the output is 950 °C (within ±20 °C). Heating indicators such as the amount of heat loss in the billet (including the areas between inductors), overheating, and the temperature gradient along the length and cross-section of the billet are taken into account.

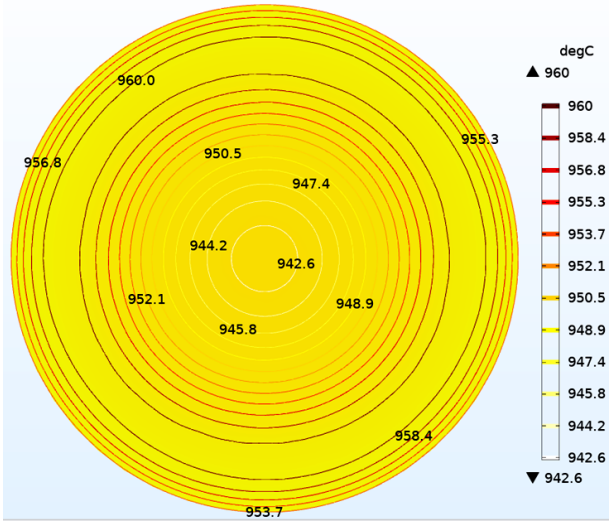

Fig. 11. Temperature distribution on the billet end part at the exit from the zone heating system

As previously established [20], to ensure an effective thermal process for heating billets, the power ratio of the inductors should be 1 : 0,5 : 0,25 : 0,125. The result of modeling such a power distribution for the inductors is overheating of the billet surface within the first inductor zone to 1150 °C (Fig. 12). However, subsequently, the billet begins to cool rapidly due to the lack of power from the other inductors, and the center (1009 °C) of the billet has a higher temperature than its surface (968 °C) at the output of the fourth inductor. In the forging industry is advantageous to achieve a homogeneous billet temperature at the outlet of the heater with the shortest possible coil line installation length while at the same time minimizing the scaling rate and energy consumption. These objectives should be obtained not only for the nominal billet diameter and throughput but also for smaller billets and throughputs. Since these requirements are partly in conflict the solution generally involves reaching a compromise [6].

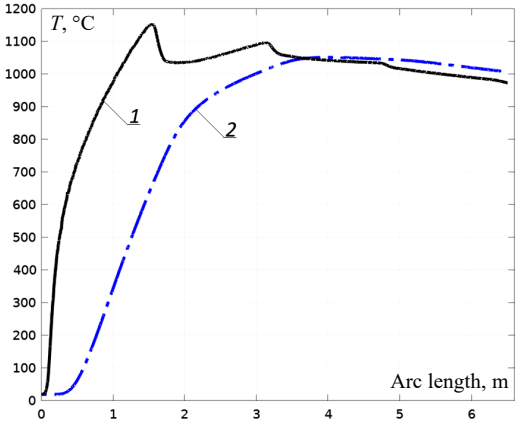

Fig. 12. Temperature along the billet length for the inductors power ratio 1 : 0,5 : 0,25 : 0,125: *1* – temperature on the surface of the billet; *2* – temperature along the central axis of the billet

From the standpoint of minimizing the temperature gradient across the cross-section of the billet, an acceptable power distribution for the inductors was found

to be when the power of each subsequent inductor decreases by 33 % compared to the power of the previous one. That is, the ratio is 1 : 0,67 : 0,45 : 0,3. In this case, the first inductor provides a rapid heating of the billet to 880 °C, and the temperature inside and on the surface of the billet equalizes at the beginning of the movement into the heating zone of the last inductor (Fig. 13). However, this design as a whole is characterized by thermal losses between the zones of individual inductors, which requires further improvement of the device.

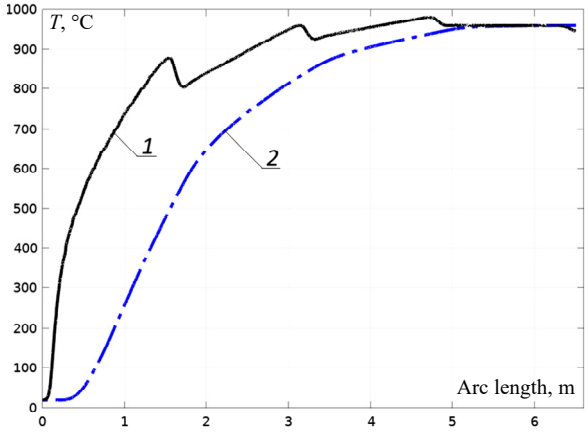

Fig. 13. Temperature along the billet length for the inductors power ratio 1 : 0,67 : 0,45 : 0,3: temperature on the surface of the billet (1); temperature along the central axis of the billet (2)

The task of defining the heating program for a multi-inductor heating complex generally involves subtasks to determine the power variation processes for each inductor. Determination of the inductors power ratio and heating programs for a multi-inductor complex presented in detail in works [6, 20].

The setup and resolution of the problem can be significantly simplified by predefining the function of power variation for each inductor over time. If the power of each inductor is assumed to be constant over time (taking into account data on changes in σ and μ throughout the billet volume), then the task of determining the inductor powers (power distribution among the inductors) can be solved using an iterative approach. This requires further modeling under various inductor power conditions to meet the heating requirements, gradually approaching the final result – power values. This approach significantly reduces resources when determining the optimal heating modes for a metal billet. The model can be represented as an m-file, describing geometric parameters, constants, global variables, nonlinear properties of the media, solver settings, and more.

Conclusions. This work presents the numerical 3D-model of coupled electromagnetic and thermal processes in zone induction heating system for metal billets. The model considers various effects that determine the fundamental physical principles of induction heating.

Using the finite element method and the COMSOL Multiphysics 6.1 software package, data on the spatial distribution of the electromagnetic and temperature fields in the moving heated steel billet were obtained. Three-dimensional graphs of electrical conductivity and relative magnetic permeability change inside the moving heated steel billet are presented.

Analysis of data on the distribution of the electromagnetic field, the temperature of the billet, and the changes in material properties allows for determining the necessary inductors powers to ensure the required heating mode. The established power distribution can serve as a reference for preliminary setup at the beginning of the zone heating system's operation.

Results of the temperature distribution calculations along the length of the steel billet for different inductors power ratios are provided. It is shown how the change in the power distribution of the inductors affects the billet heating parameters.

The thermal losses observed between the zones of individual inductors are a challenge that needs addressing. These losses can lead to inefficiencies and potential quality issues of the billet. Future work should focus on reducing these thermal losses, possibly through design modifications or improvement of thermal insulation and the heating process control system.

The presented 3D-model of coupled electromagnetic and thermal processes can be used for quickly readjusting initial parameters (frequency, power and number of inductors, billet dimensions and material, etc.) to obtain variations in numerical calculations. This allows for predicting the efficiency and performance indicators of zone heating, such as efficiency, speed, heating depth, temperature, and gradient.

The obtained results have practical application and make it possible to reduce the time and resources required for the development, optimization of the design and improvement of the technological process of zone induction heating for metal billets. Experimental validation of the developed technique and obtained numerical results is a prospect of further research.

Conflict of interest. The authors of the article declare that there is no conflict of interest.

REFERENCES

1. Rudnev V., Loveless D., Cook R.L. *Handbook of Induction Heating*. CRC Press, 2017. 722 p. doi: https://doi.org/10.1201/9781315117485.

2. Lucia O., Maussion P., Dede E.J., Burdio J.M. Induction Heating Technology and Its Applications: Past Developments, Current Technology, and Future Challenges. *IEEE Transactions on Industrial Electronics*, 2014, vol. 61, no. 5, pp. 2509-2520. doi: https://doi.org/10.1109/TIE.2013.2281162.

3. Shcherba A.A., Podoltsev O.D., Suprunovska N.I., Bilianin R.V., Antonets T.Y., Masluchenko I.M. Modeling and analysis of electro-thermal processes in installations for induction heat treatment of aluminum cores of power cables. *Electrical Engineering & Electromechanics*, 2024, no. 1, pp. 51-60. doi: https://doi.org/10.20998/2074-272X.2024.1.07.

4. Esteve V., Bellido J.L., Jordán J. State of the Art and Future Trends in Monitoring for Industrial Induction Heating Applications. *Electronics*, 2024, vol. 13, no. 13, art. no. 2591. doi: https://doi.org/10.3390/electronics13132591.

5. Jin Y., Yang N., Xu X. Innovative induction heating technology based on transformer theory: Inner heating of electrolyte solution via alternating magnetic field. *Applied Thermal Engineering*, 2020, vol. 179, art. no. 115732. doi: https://doi.org/10.1016/j.applthermaleng.2020.115732.

6. Walther A. Induction billet heaters with enthalpy controlled zone heating. *International Scientific Colloquium, Modelling for Electromagnetic Processing*, 2008, pp. 235-241.

7. *Induction Heating Systems for Precise Zone Heating & Temperature Control*. Available at: https://ultraflexpower.com/learn-about-induction-heating/zone-controlled-induction-heating (Accessed 02 July 2024).

8. Morozov D.I. Model of electrothermal processes in an induction plant for zone heating of a moving ferromagnetic billet. *Electrical and Computer Systems*, 2017, vol. 25, no. 101, pp. 245-252. doi: https://doi.org/10.15276/eltecs.25.101.2017.29.
9. Shih S.-Y., Nian S.-C., Huang M.-S. Comparison between single- and multiple-zone induction heating of largely curved mold surfaces. *International Communications in Heat and Mass Transfer*, 2016, vol. 75, pp. 24-35. doi: https://doi.org/10.1016/j.icheatmasstransfer.2016.03.020.
10. Beloha G.S., Morozov D.I. Resonance inverter for induction heating with stabilization of the load power. *Electrical and Computer Systems*, 2017, vol. 25, no. 101, pp. 132-138. doi: https://doi.org/10.15276/eltecs.25.101.2017.16.
11. Fisk M., Ristinmaa M., Hultkrantz A., Lindgren L.-E. Coupled electromagnetic-thermal solution strategy for induction heating of ferromagnetic materials. *Applied Mathematical Modelling*, 2022, vol. 111, pp. 818-835. doi: https://doi.org/10.1016/j.apm.2022.07.009.
12. Naar R., Bay F. Numerical optimisation for induction heat treatment processes. *Applied Mathematical Modelling*, 2013, vol. 37, no. 4, pp. 2074-2085. doi: https://doi.org/10.1016/j.apm.2012.04.058.
13. Podoltsev O.D., Kucheriava I.M. Multiphysics modeling of electrotechnical devices. *Technical Electrodynamics*, 2015, no. 2, pp. 3-15.
14. Shcherba A.A., Podoltsev O.D., Kucheriava I.M., Zolotaryov V.M., Belyanin R.V. Two approaches to the computation of electrothermal processes at induction heating of moving ingots – by field theory and thermal circuit theory. *Proceedings of the Institute of Electrodynamics of the National Academy of Sciences of Ukraine*, 2021, no. 59, pp. 5-10. (Ukr). doi: https://doi.org/10.15407/publishing2021.59.005.
15. Kovachki N., Liu B., Sun X., Zhou H., Bhattacharya K., Ortiz M., Stuart A. Multiscale modeling of materials: Computing, data science, uncertainty and goal-oriented optimization. *Mechanics of Materials*, 2022, vol. 165, art. no. 104156. doi: https://doi.org/10.1016/j.mechmat.2021.104156.
16. Kovetz A. *Electromagnetic Theory*. Oxford University Press, 2000. 368 p. doi: https://doi.org/10.1093/oso/9780198506041.001.0001.
17. Zhang Q., Cen S. *Multiphysics Modeling: Numerical Methods and Engineering Applications.* Elsevier and Tsinghua University Press Computational Mechanics, 2016. 440 p. doi: https://doi.org/10.1016/B978-0-12-407709-6.00001-8.
18. Khaleel D., Tang X., Abu-Zaher M. Advanced Simulation and Empirical Validation of High-Efficiency Induction Heating System Via COMSOL Multiphysics. *2024 IEEE 10th International Power Electronics and Motion Control Conference (IPEMC2024-ECCE Asia)*, 2024, pp. 2912-2917. doi: https://doi.org/10.1109/IPEMC-ECCEAsia60879.2024.10567372.
19. Chand S.K., Anand A., Gour A.S., Datta T.S., Bhunia U. A numerical study on homogeneity and central field with axial spacing between DP coils of HTS magnet at 65 K. *Cryogenics*, 2024, vol. 140, art. no. 103838. doi: https://doi.org/10.1016/j.cryogenics.2024.103838.
20. Morozov D.I., Rudnev E.S., Ushakov D.V. The algorithm of heating programs determination in multi-induction heating devices. *Electrotechnic and Computer Systems*, 2015, no. 20 (96), pp. 56-62.

Received 18.07.2024
Accepted 07.10.2024
Published 02.03.2025

V.Yu. Grytsiuk[1]*, PhD,*
M.A.M. Yassin[1]*, Senior Engineer,*
[1] University of South-Eastern Norway,
56, Kjølnes ring, Porsgrunn, 3918, Norway,
e-mail: Volodymyr.Grytsiuk@usn.no (Corresponding Author);
Mohammed.Yassin@usn.no

How to cite this article:
Grytsiuk V.Yu., Yassin M.A.M. Numerical modeling of coupled electromagnetic and thermal processes in the zone induction heating system for metal billets. *Electrical Engineering & Electromechanics*, 2025, no. 2, pp. 59-68. doi: https://doi.org/10.20998/2074-272X.2025.2.08

UDC 621.319 https://doi.org/10.20998/2074-272X.2025.2.09

G.V. Bezprozvannych, Y.S. Moskvitin, I.O. Kostiukov, O.M. Grechko

Dielectric parameters of phase and belt paper impregnated insulation of power cables

Introduction. *Medium voltage power cables with paper impregnated insulation remain an important component of power networks. The reliability and efficiency of such cables have been confirmed by their long service life also at nuclear power plants.* ***Problem***. *It is not possible to directly determine the dielectric parameters of phase and belt paper insulation of power cables. Effective electrical diagnostic systems are required to assess the technical condition of such types of power cable insulation. The* ***aim*** *of the work is to substantiate the methodology for determining the dielectric properties of phase and belt paper impregnated insulation based on cumulative measurements of the electrical capacitance and the tangent of the dielectric loss angle of power cables of nuclear power plants and power networks.* ***Methodology***. *The developed methodology is based on the solution of a system of linear algebraic equations of the sixth order for determining the dielectric properties of types of paper impregnated insulation of power three-core cables in a metal sheath.* ***Scientific novelty***. *The differences in the structure of the probing electric field in phase and belt paper insulation depending on the inspection scheme of three-core power cables with sector cores in a metal sheath have been established. The shares of electric energy in the types of insulation under different probing electric field schemes have been determined, which allows determining the tangent of the dielectric loss angle of phase and belt paper insulation.* ***Practical significance***. *The results of the practical implementation of the developed methodology for assessing the differences in the properties of phase and belt insulation of power cables of nuclear power plants and power network cables during spatial scanning of electrical insulation by frequency and voltage, respectively, are presented.* References 41, figures 4, table 6.

Key words: **power cables, aging of paper impregnated insulation, phase and belt insulation, electric field structure, aggregate measurements, commutation matrix, dielectric loss angle tangent, system of linear algebraic equations, self-discharge time constant.**

Вступ. *Силові кабелі середньої напруги з паперовою просоченою ізоляцією залишаються важливою складовою електроенергетичних мереж. Надійність та ефективність таких кабелів підтверджено тривалим терміном експлуатації також на АЕС.* ***Проблема***. *Безпосередньо визначити діелектричні параметри фазної та поясної паперової ізоляції силових кабелів не виявляється можливим. Для оцінки технічного стану таких видів ізоляції силових кабелів необхідні ефективні електричні системи діагностики.* ***Метою*** *роботи є обґрунтування методології визначення діелектричних властивостей фазної та поясної паперової просоченої ізоляції на підставі сукупних вимірювань електричної ємності та тангенсу кута діелектричних втрат силових кабелів АЕС та електричних мереж.* ***Методика***. *Розроблена методика ґрунтується на розв'язанні системи лінійних алгебраїчних рівнянь шостого порядку для визначення діелектричних властивостей видів паперової просоченої ізоляції силових трижильних кабелів у металевій оболонці.* ***Наукова новизна***. *Встановлено відмінності структури зондувального електричного поля у фазній та поясній паперовій ізоляції в залежності від схеми обстеження трижильних силових кабелів із секторними жилами у металевій оболонці. Визначено частки електричної енергії у видах ізоляції за різних схем зондувального електричного поля, що дозволяє визначити тангенс кута діелектричних втрат фазної та поясної паперової ізоляції.* ***Практична значимість***. *Представлено результати практичної реалізації розробленої методики для оцінки відмінностей властивостей фазної та поясної ізоляції силових кабелів АЕС та кабелів енергомереж при просторовому скануванні електричної ізоляції за частотою та напругою відповідно.* Бібл. 41, рис. 4, табл. 6.

Ключові слова: **силові кабелі, старіння паперової просоченої ізоляції, фазна та поясна ізоляція, структура електричного поля, сукупні вимірювання, матриця комутації, тангенс кута діелектричних втрат, система лінійних алгебраїчних рівнянь, стала часу саморозряду.**

Introduction.

Power systems include a significant number of important power cable systems. Paper insulated lead covered cables (PILC) have been used for more than 100 years in medium voltage systems from 6.6 to 36 kV, and even in high voltage systems. Such cable systems have advantages over cross-linked polyethylene cables, primarily in electrical characteristics: high electrical strength, low sensitivity to DC tests and proven operational reliability [1–10].

In modern medium voltage networks, cross-linked polyethylene insulated cables are increasingly used. Replacing paper impregnated cables is a long-term strategy. Paper impregnated cables remain vital components of distribution electrical networks and power systems for circulating pumps in NPP reactor cooling systems [4–7]. It should be noted that the cables have a specified service life of 25 years [7–13]. The actual term is determined by the technical condition of the cable insulation. The physical wear of medium voltage cables with paper impregnated insulation in the power systems of Ukraine is 80 % [7], in European countries it is at the level of 50 %. There are also cables in operation, the service life of which varies from 25 to 60 years. The extension of the service life of nuclear power plants to 60, and even up to 80, years determines the relevance of the problem of assessing the technical condition of cables to ensure reliable and safe operation of power units of stations [7–9].

Problem definition.

During operation, power cables are subject to the complex influence of various factors:

- electric field, which causes electrical aging of the insulation;

- thermal field, which causes thermal aging and oxidation of the insulation;
- wetting of the insulation leads to a deterioration of the electrophysical characteristics of the insulation;
- mechanical aging and damage under the influence of vibration, electrodynamic forces and mechanical loads;
- chemical aging under the influence of aggressive substances [4–13].

Aging of power cable insulation due to prolonged exposure to operational factors can lead to cable breakdown when the limit values of mechanical and electrical insulation characteristics are reached.

Network companies are trying to reduce the frequency of failures and associated costs by monitoring the condition of insulation and maintaining cable systems with paper impregnated insulation. To increase the reliability of power cables and cable lines under operating conditions, various electrical testing and diagnostic methods are used to assess the condition of electrical insulation of power cables, including traditionally used and new modern methods [14–26].

The technical condition of cable insulation is determined by applying constant test voltage that exceeds the nominal by 6 times. Testing cables with an increased test voltage does not allow obtaining reliable information about the real technical condition of power cables with paper impregnated insulation. Such tests of power cables that are operated for a long time often lead to a reduction in service life, untimely and unpredictable insulation breakdown.

Among modern methods, the following non-destructive electrical methods for diagnosing power cables with voltages up to 35 kV inclusive can be distinguished:

- method of measuring partial discharge characteristics [7, 21];
- measurement and analysis of recovery voltage [7, 22–24];
- method of measuring relaxation current (more often in cables with cross-linked polyethylene insulation);
- method of measuring dielectric characteristics of insulation at alternating voltage [23–33].

Measurements at DC voltage allow to detect local defects of the cable line, at AC – to detect general deterioration of the quality of insulation due to its aging.

Unlike short samples of NPP cables – with a length of about 10 m, the examination of which according to electrical characteristics in laboratory conditions can be performed in the frequency range up to 10 kHz [7, 25–27, 34], for long cables of power systems up to 5 km long, it is necessary to conduct an examination at power frequency of 50 (60) Hz to avoid resonance phenomena during the examination and reduce the error in the assessment of diagnostic results.

Power cables with paper impregnated insulation have two types of insulation – phase of each core and belt insulation of three cores together. Insulation is carried out by winding the cores with tapes of cable paper. In the initial state, the properties of the phase and belt insulation must be identical. In the process of cable aging, a synergistic effect of the influence of cable elements and external factors on the aging of paper impregnated insulation is manifested [27, 29, 30, 32].

This causes differences in the mechanical properties of phase and belt insulation, which are caused by the destruction of cellulose and the migration of low-molecular polar products of its decomposition (water, furans) into the colder part of the cable – to the shell, into the belt insulation [23]. As a result, the properties of the belt insulation deteriorate over time to a greater extent compared to the phase insulation. The mechanical strength of cable papers decreases, the dielectric loss tangent increases [7, 15, 27, 30].

It is important to identify signs of aging of each type separately: phase and belt paper electrical insulation, which determines the operability of power cables in operation as an important element of the network. Phase and belt insulation of cables are not available for direct measurements. This causes the averaging of insulation parameters, due to which the differences in their components become less noticeable [25, 27]. As a sign of the end of the period of normal cable operation, differences in the dielectric properties of phase and belt insulation that arise during prolonged operation should be considered. The change in properties can be caused by uneven aging of the specified types of insulation or by moisture due to loss of tightness of connecting and end couplings, protective sheath, etc.

The goal of the work is to substantiate the methodology for determining the dielectric properties of phase and belt paper impregnated insulation based on cumulative measurements of electrical capacitance and dielectric loss tangent of power cables of nuclear power plants and electrical networks.

Structure of the probing electric field in types of paper impregnated insulation of power cables.

The method for determining the dielectric properties of phase and belt paper impregnated insulation is based on establishing differences in the structure of the probing electric field in the type of insulation whose properties are of direct interest.

The density σ of surface electric charges at the interface of the media is found as a result of solving the system of linear algebraic equations (SLAE) in matrix form by the method of secondary sources [25]: Fredholm integral equations of the first kind for potentials on the surfaces of the cores, metal shell and of the second kind for jumps of the normal component of the field strength at the interface of phase and belt electrical insulation, respectively

$$\overline{A} \cdot \overline{\sigma} = \overline{U} , \qquad (1)$$

where $\overline{\sigma}$ is the column matrix of unknown values of the secondary charge density, C/m^2; in nodes of the total number N (order of SLAE), $\overline{U}$ is the column matrix, the first Ne members of which reflect the given potentials of nodes lying on the electrodes, the rest (N – Ne) – on the interface of dielectric media and are equal to zero;

$\overline{A}$ is the square matrix of coefficients, the elements of which a_{ij} are equal to [25]

$$a_{ij}=\left\{\begin{array}{l}\left(\begin{array}{l}\frac{1}{2\pi\varepsilon_0}\ln\frac{r_{0j}}{r_{ij}}\cdot\Delta l_j;\quad \forall i\neq j\\ \frac{1}{2\pi\varepsilon_0}\ln\frac{r_{0j}}{\Delta l_j/(2e)}\cdot\Delta l_j;\quad \forall i=j\end{array}\right) i=1\div N_e\\ \left(\begin{array}{l}\frac{1}{2\varepsilon_0};\quad \forall i=j\\ -\alpha\cdot\frac{1}{2\pi\varepsilon_0}\ln\frac{\cos\left(\overline{r}_{ij},\overline{n}_j\right)}{r_{ij}}\cdot\Delta l_j;\forall i\neq j\end{array}\right) i=N_e+1\div N\end{array}\right\},(2)$$

where i is the node number in which the field characteristics are sought; j is the node number in which the charge is located; r_{ij} is the distance between sections and j; r_{0j} is the distance from section j to point O, the potential of which can be taken to be zero; ε_0 = 8.85·10^{-12} F/m is the electric constant; Δl_j is the length of the segment of the cylinder generator with the center at point j; e is the base of the natural logarithm; α is the parameter associated with the dielectric permittivities of dielectric media: when the normal vector $\overline{n}_j$ is oriented from a medium with a dielectric permittivity ε_2 to a medium with ε_1, the parameter α is equal to:

$$\alpha=\frac{\varepsilon_2-\varepsilon_1}{\varepsilon_2+\varepsilon_1}.$$

During numerical modelling, the coordinates and areas of the sections, the centers of which are nodes located along the thickness of the insulation, are analytically determined, and the boundaries of the cores, phase and belt insulation, and metal sheath are analytically set [25]. The modelling was performed in the open-access software environments Lazarus and Octave.

Figure 1 shows the structure of the electrostatic field (Fig. 1,*a*,*c*,*e*) and the electric field intensity sweeps (Fig. 1,*b*,*d*,*f*) for different schemes of inspection of a power cable in a metal shell for linear voltage of 10 kV with paper impregnated insulation with sector-shaped cores with cross-section of 185 mm^2. The thickness of the phase insulation is 2.75 mm; of the belt insulation is 2 mm. The dielectric permittivity of the phase insulation is ε_1=4.5; of the belt insulation is ε_2=4; in dielectric wedges (in the center and on the periphery) filled with seeping liquid – ε_3=3. The applied phase voltage is 5774 V.

Figures 1,*a*,*c*,*e* show the patterns of electric field strength vectors when the nodes are located on the surface of the electrodes (cores, metal shell), in the thickness of the phase and belt insulation, dielectric wedges for different power cable inspection schemes. Figure 1,*a* corresponds to the cable inspection under the condition of applied electric voltage to one of the cores (*A*) and grounded two others (*B*, *C*) and metal sheath (*S*) – inspection scheme ***I***. Figure 1,*e* – inspection scheme ***II***: electric voltage applied to three cores (*A*, *B*, *C*) and grounded metal shell (*S*).

According to the specified inspection schemes in Fig. 1,*b*,*d*,*f* show the sweeps of the electrostatic field strength at nodes located in the thickness of the phase (*A*, *B*, *C*) and belt (*SA*, *SB*, *SC*) insulation. In the case of inspection scheme ***I***, the electric field is present in the phase and belt insulation (Fig. 1,*a*,*b*). In this scheme, the electrical properties of the phase insulation are more pronounced. The electric charge of the potential core is 2.9 μC/m, of the zero cores is 0.62 μC/m, and of the shell is 1.63 μC/m.

In the case of inspection scheme ***III***, under the condition of electric voltage applied to two cores and the grounded third core and metal shell, the electric field is present in the interphase insulation of the two cores, dielectric wedges, and belt insulation (Fig. 1,*c*,*d*). The electric charge of the potential cores is 2.29 μC/m and 2.29 μC/m, of the zero core is 1.23 μC/m and of the shell is 3.24 μC/m. The identity of the determined values of the electric charges of the two cores proves the high accuracy of the numerical calculations.

With the inspection scheme according to scheme ***II***, the electric field is present to a greater extent in the belt insulation (Fig. 1,*e*,*f*). In the interphase space, the electric field is absent (Fig. 1,*e*) The electric charge of each of the cores is 1.67 μC/m, of the metal shell is 4.98 μC/m.

The results of numerical simulation prove that for any inspection scheme, the electric field enters both the phase and belt insulation (compare Fig. 1,*a*, Fig. 1,*c* and Fig. 1,*e*). At the same time, the grounded cores and the metal shell located nearby significantly affect the value of the electric charge, i.e. the electric capacitance and losses of electric energy in the paper impregnated insulation of the core to which the electric voltage is applied.

Table 1 shows the distribution of the electric field energy (μW) in the phase and belt insulation of the cable determined by the results of numerical calculations for different inspection schemes: scheme ***I*** – «core - against the other two and the metal shell», scheme ***II*** – «three cores together - against the metal sheath».

For each of the selected inspection schemes, the structure of the cable insulation is scanned by an alternating electric field. The electric field is focused in different types of cable insulation: in phase (scheme *A–B*,*C*,*S* – Fig. 1,*a*), belt (scheme *A*,*B*,*C–S* – Fig. 1,*e*) insulation, in the interphase space (scheme *A*,*B – C*,*S* – Fig. 1,*c*).

Depending on the inspection scheme, the electrostatic field energy that accumulates in the types of electrical insulation differs. Thus, according to the scheme «each core against the other two and the shell», the share of energy accumulated in phase insulation is 76.4 %, while in belt insulation only 21.8 % of the total electric field energy in cable insulation is accumulated.

With inspection scheme ***III*** «two cores together – against the third and metal shell», the share of energy in phase insulation is 69.4 %, in belt insulation – 27.4 %. According to scheme ***II***, the share of energy accumulated in phase insulation is 59.4 %, in belt insulation – 43.07 %.

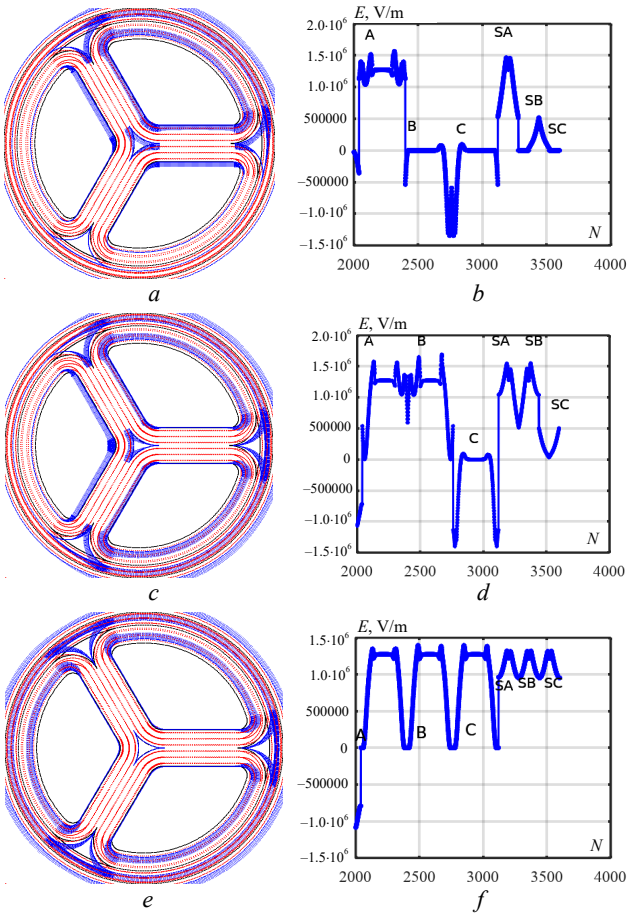

Fig. 1. Structure of the probing electrostatic field in types of paper impregnated electrical insulation under different inspection schemes of a three-core power cable with metal shell

The difference in energy accumulated in different parts of the cable under different schemes of the probing electric field allows to determine the electrical energy losses, i.e. the tangent of the dielectric loss angle directly of the phase and belt insulation. The question is in what way this can be done.

Power cable substitution circuit and methodology for combined capacitance and dielectric loss tangent measurements.

Figure 2 shows the substitution circuit of a three-core power cable in metal shell.

The circuit contains 6 links that reflect the dielectric properties of the insulation of three cores *A*, *B*, *C* to the shell *S* and between themselves $C_{A\text{-}S}$, $C_{B\text{-}S}$, $C_{C\text{-}S}$, $C_{A\text{-}B}$, $C_{B\text{-}C}$, $C_{C\text{-}A}$, respectively. In parallel with each of the partial capacitances, resistors are included that reflect the dielectric losses in the insulation: $\mathrm{tg}\delta_{A\text{-}S}$, $\mathrm{tg}\delta_{B\text{-}S}$, $\mathrm{tg}\delta_{C\text{-}S}$, $\mathrm{tg}\delta_{A\text{-}B}$, $\mathrm{tg}\delta_{B\text{-}C}$, $\mathrm{tg}\delta_{C\text{-}A}$.

To directly determine partial capacitances with the corresponding losses of electrical energy in insulation (Fig. 2), the method of cumulative measurements of dielectric parameters at alternating voltage of power cables using devices with two terminals is used.

The method of total measurements is more universal than the method of measuring partial capacitance with three terminals. The gap currents, which are discharged to the ground using the third terminal past the measuring circuit, affect the measurement results of the selected one. The error of the measurement results with three terminals can be significant, especially in operation [35].

Table 1

Electrostatic field energy shares in electrical insulation components depending on the inspection scheme of 10 kV power cable

Type of insulation	Inspection scheme					
	Scheme ***I***: «core *A* – against grounded cores *B*, *C* and metal shell *S*» applied voltage *U*=5774 V		Scheme ***III***: «cores *A*, *B* – against grounded core *C* and metal shell *S*» applied voltage *U*=5774 V		Scheme ***II***: «cores *A*, *B*, *C* – against grounded metal shell *S*» applied voltage *U*=5774 V	
	W_A, mJ/m	The share of energy stored in the type of insulation $\eta_A = W_A/W$	$W_{A,B}$, mJ/m	The share of energy stored in the type of insulation $\eta_{A,B} = W_{A,B}/W$	$W_{A,B,C}$, mJ/m	The share of energy stored in the type of insulation $\eta_{A,B,C} = W_{A,B,C}/W$
Phase insulation of the core *A*	4,73	0,5761	3,66	0,28	2,74	0,198
Phase insulation of the core *B*	0,81	0,099	3,70	0,28	2,76	0,198
Phase insulation of the core *C*	0,81	0,099	1,75	0,134	2,76	0,198
Belt insulation between the cores and shell	1,79	0,218	3,58	0,274	5,62	0,4307
Belt insulation between core *C* and shell	0,0453	0,0052	0,045	0,0034	0	0
Interphase insulation between cores *C* and *A*	0,1181	0,0144	0,0996	0,0077	0,0107	0,00082
Interphase insulation between cores *C* and *B*	$3{,}074\cdot10^{-9}$	0	0,1125	0,0086	0,0109	0,00083
Interphase insulation between cores *A* and *B*	0,1217	0,0148	0,1135	0,0087	0,0110	0,00084
Total energy *W*, mJ/m	8,21	1	13,071	1	13,913	1

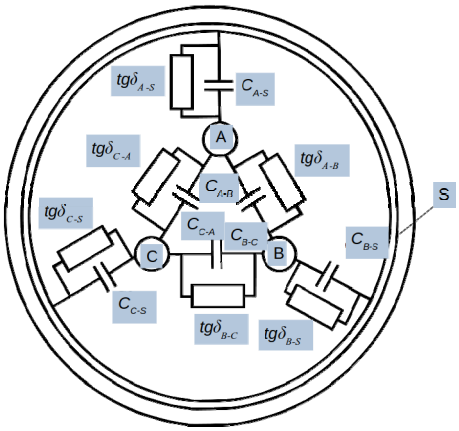

Fig. 2. Substitution circuit of a three-core power cable in a metal shell

The dielectric parameters of the controlled circuit are not found directly during the measurements, but as a result of solving the SLAE. The method can be implemented both using devices with three terminals (in this case, one terminal is not used) and using devices with two terminals. A two-position switch (*C*, Fig. 3) is placed between the object and the meter.

Each of the terminals of the three-core (*A*, *B*, *C*) power cable in a metal shell (*S*) is connected to one (*i*) or the other (*j*) input of the device (I).

The scheme of inspection of a three-core power cable with paper impregnated insulation in a metal shell using the method of cumulative measurements is presented in Fig. 3.

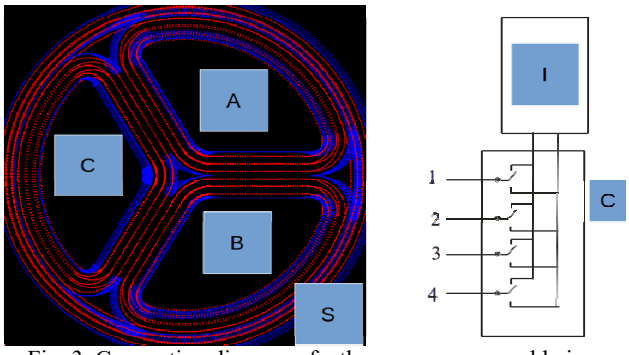

Fig. 3. Connection diagram of a three-core power cable in a metal shell to a two-position switch

In a three-core cable with a metal shell, 7 complete inspection schemes can be distinguished by the method of cumulative measurements for monitoring the electrical capacitance and dielectric loss tangent of the power cable.

Four schemes reflect the dielectric properties of the phase and belt insulation between the cores and the metal sheath for the cases: according to scheme ***I*** «each of the three cores – against the grounded two others and the metal shell» (Fig. 1,*a*) and according to scheme ***II*** «all three cores together – against the grounded metal shell» (Fig. 1,*e*). The corresponding total electrical capacitances $C_{A\text{-}B,C,S}$, $C_{B\text{-}A,C,S}$, $C_{C\text{-}A,B,S}$, $C_{A,B,C\text{-}S}$ and the total dielectric loss tangents $\mathrm{tg}\delta_{A\text{-}B,C,S}$, $\mathrm{tg}\delta_{B\text{-}A,C,S}$, $\mathrm{tg}\delta_{C\text{-}A,B,S}$, $\mathrm{tg}\delta_{A,B,C\text{-}S}$ are recorded.

Three inspection schemes ***III*** reflect the dielectric properties of the interphase insulation (Fig. 1,*c*). In this case, the device records the corresponding total electrical capacitances and total dielectric loss tangents: $C_{A,B\text{-}C,S}$, $C_{C,A\text{-}B,S}$, $C_{B,C\text{-}A,S}$, $\mathrm{tg}\delta_{A,B\text{-}C,S}$, $\mathrm{tg}\delta_{C,A\text{-}B,S}$, $\mathrm{tg}\delta_{B,C\text{-}A,S}$.

The state of the switch keys is determined by the switching matrix *AK*, the elements of which are equal to «1» in the case of connecting the object terminal, for example, to the left terminal of the device and «0» in the opposite case – to the right (Fig. 3):

$$AK=\begin{bmatrix} 0&1&0&1&0&1&0&1&0&1&0&1&0&1&0&1\\ 0&0&1&1&0&0&1&1&0&0&1&1&0&0&1&1\\ 0&0&0&0&1&1&1&1&0&0&0&0&1&1&1&1\\ 0&0&0&0&0&0&0&0&1&1&1&1&1&1&1&1 \end{bmatrix}. \quad (3)$$

The matrix contains 4 rows (by the number of terminals of the control object) and 2^4=16 columns (by the number of all possible options for the state of the switch keys). The first and last columns correspond to degenerate cases: 0000 – all poles of the object are connected to one terminal, and 1111 – to the other terminal of the meter. These experiments can be used to estimate the parasitic capacitance of the switch and connecting wires. The other experiments (there are a total of *Ne*=16 – 2 = 14) are divided into two groups. The first 7 experiments are the main ones (columns (2 – 8) in (3)), the others are inverse (columns (9–15) – correspond to a change in the polarity of the connection to all poles).

The unknown partial capacities are found based on the results of cumulative measurements from the SLAE:

$$AC\times Cx = Ce, \quad (4)$$

where *Ce* is the column matrix of the results of the cumulative measurements: $C_{A\text{-}B,C,S}$, $C_{B\text{-}A,C,S}$, $C_{C\text{-}A,B,S}$, $C_{A,B,C\text{-}S}$, $C_{A,B\text{-}C,S}$, $C_{C,A\text{-}B,S}$, $C_{B,C\text{-}A,S}$; *Cx* is the column matrix of unknown partial capacitances: $C_{A\text{-}B}$, $C_{B\text{-}C}$, $C_{C\text{-}A}$, $C_{A\text{-}S}$, $C_{B\text{-}S}$, $C_{C\text{-}S}$); *AC* is the matrix of the «participation» of the partial capacitance in the total capacitance for this experiment.

Element a_{ij} of the matrix *AC* is equal to 1 if the difference of the codes of poles *i* and *j* is different from zero, and is equal to 0 otherwise.

In experiment 2 (second column in (3): the first terminal «1», the rest are zero) the capacitances connected in parallel are measured: $C_{A\text{-}B} + C_{C\text{-}A} + C_{A\text{-}S}$. In experiment 3 (third column in (3): second terminal «1», the rest are zero) the capacitances connected in parallel are measured: $C_{A\text{-}B} + C_{B\text{-}C} + C_{B\text{-}S}$.

The partial capacitances that participate in the total capacitance for a particular experiment are found by multiplying the row of the matrix *AC* by the column matrix *Cx*:

$$AC\times Cx=\begin{bmatrix} 1&1&0&1&0&0\\ 1&0&1&0&1&0\\ 0&1&1&1&1&0\\ 0&1&1&0&0&1\\ 1&0&1&1&0&1\\ 1&1&0&0&1&1\\ 0&0&0&1&1&1 \end{bmatrix}\times\begin{bmatrix} C_{A-B}\\ C_{B-C}\\ C_{C-A}\\ C_{A-S}\\ C_{B-S}\\ C_{C-S} \end{bmatrix}.$$

The SLAE, similar to (4), is also written to find $\mathrm{tg}\delta$ of partial capacitances:

$$ATG \times TGx = TGe, \quad (5)$$

where TGe is the column matrix of measured total values of tgδ (the result of the total action of a number of partial capacitances with losses connected in parallel); TGx is the column matrix of values of tgδ of the partial capacitance with losses, which is **the purpose of the calculation**; ATG is the matrix of coefficients, similar in structure to the AC matrix, but instead of unit coefficients, contains fractions, in the numerator of which are the partial capacitances C_{ij}, found as a result of solving (4), and in the denominator – the sums of the partial capacitances participating in this experiment.

The coefficients of the ATG matrix determine the shares of the real values of the partial capacitances (with electrical energy losses) in the total losses for this experiment.

When implementing all 7 basic experiments according to (4), (5), the SLAE becomes overdetermined: the number of equations is greater than the number of unknowns [25]. Finding the solution requires the application of the least squares method:

$$Cx = (AC' \times AC)^{-1} \times AC' \times Ce, \quad (6)$$

where «′« means transposition; degree «–1» – finding the inverse matrix; sign «×« – matrix multiplication.

Similarly, the unknown values of the tangents of the angle of dielectric losses of partial capacitances are found, which is **the purpose of the study**:

$$TGx = (ATG' \times ATG)^{-1} \times ATG' \times TGe. \quad (6)$$

To find the dielectric parameters of phase and belt insulation, it is enough to perform 6 experiments out of the 7 main ones, for example: 2 – 7: $C_{A\text{-}B,C,S}$, $C_{B\text{-}A,C,S}$, $C_{C\text{-}A,B,S}$, $C_{A,B,C\text{-}S}$, $C_{A,B\text{-}C,S}$, $C_{C,A\text{-}B,S}$.

When implementing 6 experiments (columns (2–7) of the commutation matrix AK (3)), we obtain a 6th-order SLAE with the matrix AC of the form:

$$AC = \begin{bmatrix} 1 & 1 & 0 & 1 & 0 & 0 \\ 1 & 0 & 1 & 0 & 1 & 0 \\ 0 & 1 & 1 & 1 & 1 & 0 \\ 0 & 1 & 1 & 0 & 0 & 1 \\ 1 & 0 & 1 & 1 & 0 & 1 \\ 1 & 1 & 0 & 0 & 1 & 1 \end{bmatrix}.$$

The corresponding inverse matrix AC^{-1} is:

$$AC^{-1} = 0{,}5 \times \begin{bmatrix} 1 & 1 & -1 & 0 & 0 & 0 \\ 1 & 0 & 0 & 1 & -1 & 0 \\ 0 & 1 & 0 & 1 & 0 & -1 \\ 0 & -1 & 1 & -1 & 1 & 0 \\ -1 & 0 & 1 & -1 & 0 & 0 \\ -1 & -1 & 0 & 0 & 1 & 1 \end{bmatrix}.$$

The sought partial capacitances are found by multiplying the rows of the inverse matrix by the column of experimental data.

For example, the first unknown capacitance $C_{A\text{-}B}$ is found by multiplying the first row of the matrix AC^{-1} by the column of measurement results (8). This provides grounds to determine tg$\delta_{A\text{-}B}$ by (9), where $C_{A\text{-}B,C,S}$, $C_{B\text{-}A,C,S}$, $C_{C\text{-}A,B,S}$, $C_{A,B,C\text{-}S}$, $C_{A,B\text{-}C,S}$, $C_{C,A\text{-}B,S}$ are the experimental results of the combined measurements, the sequence of which is given by columns (2–7) of the switching matrix (1), $C_{s1} = C_{A\text{-}B,C,S} + C_{B\text{-}A,C,S} + C_{C\text{-}A,B,S}$ is the total electrical capacitance of the experiment, which corresponds to the first row of the matrix AC.

Note that formula (9) can be used only after the partial capacitances $C_{A\text{-}B}$, $C_{B\text{-}C}$, C_{CA} are found.

The formulas for the parameters of other partial capacitances and dielectric loss tangents are determined according to (8), (9):

$$C_{A-B} = 0{,}5(C_{A-B,C,S} + C_{B-A,C,S} - C_{C-A,B,S} + 0 \times C_{A,B,C-S} + 0 \times C_{A,B-C,S} + 0 \times C_{C,A-B,S}); \quad (8)$$

$$\mathrm{tg}\delta_{A-B} = 0{,}5 \times \left(\frac{C_{A-B}}{C_{s1}} \mathrm{tg}\delta_{A-B,C,S} + \frac{C_{B-C}}{C_{s1}} \mathrm{tg}\delta_{B-A,C,S} - \frac{C_{C-A}}{C_{s1}} \mathrm{tg}\delta_{C-A,B,S} + 0 \times \mathrm{tg}\delta_{A,B,C-S} + 0 \times \mathrm{tg}\delta_{A-B-C,S} + 0 \times \mathrm{tg}\delta_{CA-B,S} \right). \quad (9)$$

Thus, the solution of SLAE (4) and (5) in practice is reduced to formulas that are linear combinations of measurement results taken with certain weighting factors. Calculation using them does not present any particular difficulties.

To determine the dielectric parameters of phase and belt insulation based on the method of cumulative measurements, a spatial method of creating a probing electric field in the type of paper impregnated insulation of power cables, the properties of which must be determined, is used. For this purpose, the conductors and metal shell of the power cable are switched in a way that shunts the electric field in those parts of the structure, the influence of which must be neglected.

In the case of implementing the specified method for short samples of power cables of NPPs, it is possible to conduct an examination at several values of the frequency of the sound range 0.1–10 kHz of low voltage to determine the predominant factors of the aging process over time of phase and belt paper impregnated insulation. For long-distance cables, for example, urban power networks, the use of the frequency method is limited to one power operating frequency at several values of high applied voltage. Examination of cables in operation at several values of frequency is limited by resonance phenomena between the cable's own inductance and capacitance.

Examples of practical implementation of the methodology for determining the dielectric properties of phase and belt paper impregnated insulation of power cables.

Figure 4 shows the general and determined on the basis of the proposed methodology electrical characteristics of types of electrical insulation in the form of C-tgδ diagrams for frequencies of 0.1; 1 and 10 kHz of samples of power cables of nuclear power plants for voltage of 6 kV with paper impregnated insulation in laboratory conditions. The designation of experimental data corresponds to frequencies of 0.1; 1 and 10 kHz: the total measurement results – red, green and blue colors;

determined dielectric parameters of phase and belt insulation – purple, turquoise and black colors, respectively.

For the cable sample (Fig. 4,*a*), higher values of tgδ of phase and belt insulation are observed for a frequency of 0.1 kHz, which is evidence of moistening of paper impregnated insulation during long-term operation. At the same time, belt insulation is more aged compared to phase one: tgδ values differ by more than 1.33 times for frequency of 10 kHz.

For the cable sample (Fig. 4,*b*), lower values of dielectric losses of phase and belt insulation are observed for frequency of 100 Hz. This is evidence of a lower moisture content in the insulation under the influence of the increased operating temperature of the cable during operation. At the same time, for frequency of 10 kHz, the belt insulation is also characterized by 25 % higher tgδ values compared to the phase insulation.

In any case, changing the inspection scheme leads to significant variations in tgδ, which is a sign of aging of the paper impregnated cable insulation (Fig. 4).

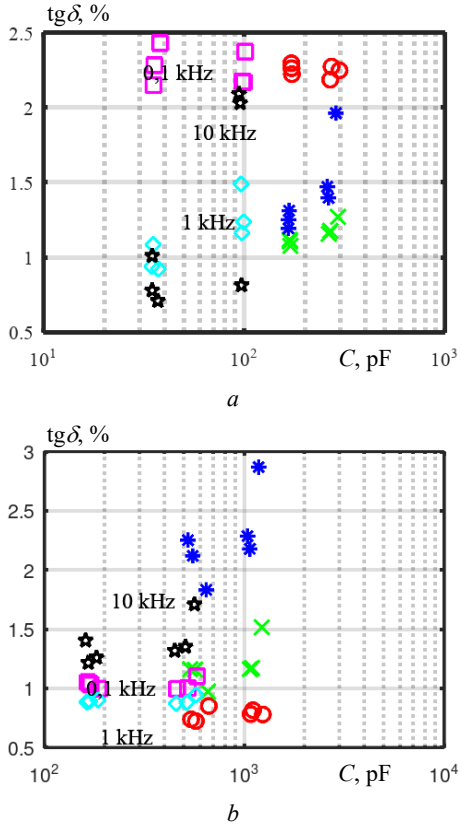

Fig. 4. Dielectric parameters of paper impregnated electrical insulation of NPP cable samples for different frequency values

Table 2–5 present the determined dielectric parameters based on the results of combined measurements of cables directly in operation of 10 kV power cable lines.

Thus, the belt insulation of phases *A*, *B* and *C* of cables (Table 2, 3) has practically the same values.

This, firstly, indirectly indicates a uniform current load during long-term operation. Secondly, the values of tgδ remain practically unchanged with an increase in the applied test voltage: the absence of air cavities. Electrical energy losses due to ionization are not observed (evidence of the uniformity of filling of dielectric wedges with an impregnating compound – Fig. 1).

Table 2

Dielectric parameters of phase and belt insulation of the AASHV-3×120 cable for voltage of 10 kV, length 240 m

Inspection scheme	Applied voltage					
	2 kV		5 kV		8 kV	
	C, nF	tgδ, %	*C*, nF	tgδ, %	*C*, nF	tgδ, %
A-S	47,9738	0,3456	49,2300	0,3475	48,6638	0,3308
B-S	48,4738	0,3376	47,8800	0,3503	48,4937	0,3348
C-S	48,7237	0,3280	48,8800	0,3334	49,0638	0,3441
A-B	12,0725	0,1802	12,0400	0,1146	12,1625	0,1318
B-C	12,4225	0,2492	12,8800	0,1799	12,1925	0,1488
C-A	12,4825	0,2202	12,0400	0,1396	12,4125	0,1418

Table 3

Dielectric parameters of phase and belt insulation of the AASHV-3×70 cable for voltage of 10 kV, length 220 m

Inspection scheme	Applied voltage					
	2 kV		5 kV		8 kV	
	C, nF	tgδ, %	*C*, nF	tgδ, %	*C*, nF	tgδ, %
A-S	29,86	0,666	29,9266	0,7265	29,9913	0,7204
B-S	29,63	0,655	29,5876	0,6312	29,5913	0,6346
C-S	29,85	0,624	29,7946	0,6534	29,7912	0,6653
A-B	7,491	0,108	7,4657	0,1311	7,3975	0,1305
B-C	7,361	0,097	7,4578	0,1211	7,4975	0,1157
C-A	7,471	0,112	7,449	0,1261	7,476	0,126

Table 4

Dielectric parameters of phase and belt insulation of cable AASHV-3×120 for voltage 10 kV, length 2470 m

a) before repair – phase *C* damaged

Inspection scheme	Applied voltage					
	2 kV		5 kV		8 kV	
	C, nF	tgδ, %	*C*, nF	tgδ, %	*C*, nF	tgδ, %
A-S	636,3	1,00	616,5	0,891	840,1	1,39
B-S	639,9	0,99	618,4	0,896	839	1,61
C-S	phase *C* damaged					
A-B	99,48	1,842	119	2,151	97,69	1,203
B-C	97,5	1,346	99,3	1,802	119,3	2,158
C-A	phase *C* damaged					

b) after repair

Inspection scheme	Applied voltage					
	2 kV		5 kV		8 kV	
	C, nF	tgδ, %	*C*, nF	tgδ, %	*C*, nF	tgδ, %
A-S	500,756	0,7640	501,062	0,8341	504,2875	0,8624
B-S	498,256	0,7774	498,162	0,8511	502,1875	0,8570
C-S	497,756	0,7600	497,462	0,8582	501,5875	0,8830
A-B	139,937	0,7164	139,675	0,7202	138,5250	0,7212
B-C	141,637	0,7252	141,475	0,7202	140,1250	0,7442
C-A	141,637	0,7452	141,475	0,7242	140,3250	0,7242

Table 5

Dielectric parameters of phase and belt insulation of the AASHV-3×95 cable for voltage of 10 kV, length 40 m

Inspection scheme	Applied voltage					
	2 kV		5 kV		8 kV	
	C, nF	tgδ, %	C, nF	tgδ, %	C, nF	tgδ, %
A-S	12,6340	0,6654	12,7731	0,7312	12,4834	0,7503
B-S	12,5230	0,6673	12,3241	0,8482	12,7184	0,7772
C-S	12,9240	1,7844	13,1081	1,8594	12,8934	1,7415
A-B	3,1630	0,3537	3,1978	0,0778	3,1433	0,1053
B-C	3,2130	0,3446	3,3227	0,0938	3,1332	0,1233
C-A	3,1620	0,2077	2,8337	0,1030	3,3583	0,0982

After repair of the damaged phase C of the power cable AASHV-3×120 (Table 4), the uniformity of aging of the belt and phase insulation of all three phases was established. After repair, the tgδ level decreased, but remained in the range from 0.6 to 0.8 %, which corresponds to moderately aged insulation [29].

The AASHV-3×95 cable (Table 5) is characterized by non-uniform current load in operation. As a result, the insulation of phase *C* has 2.3 times higher tgδ values: it is significantly aged compared to the others. The critical tgδ values for the frequency of 50 Hz correspond to the critical value of mechanical strength by the number of double bends of cable papers and have the following values: for phase insulation: 1.2673–1.3874 %; for belt insulation: 1.29–1.4886 % [36]. Additional direct current inspections in operation proved the defectiveness of the cable coupling of phase *C*.

Measurements at direct voltage allow to detect local defects of the cable line – leakage of impregnating liquid, which most often occur in connecting and end couplings [37–40].

Measurement of leakage current at direct current when applying a voltage of 40 kV allowed to determine the insulation resistance Ris of phase C of the cable line with the coupling. The product of the insulation resistance R_{is} and the electrical capacitance of phase *C* (Table 5, *C-S* = 12.924 nF) determines the self-discharge time constant of the insulation $\theta = R_{is} \cdot C$ – an objective indicator of quality that does not depend on the geometric dimensions of the insulation.

Thus, the signs of defects in elements of cable lines with paper impregnated insulation are established on the basis of the ratio of the values of tgδ of the types of cable insulation (the result of measurements on AC) and the self-discharge time constant (the result of measurements on direct current of insulation resistance and electric capacitance on AC) (Table 6).

Table 6

Classification of defects in cable lines with paper impregnated insulation [41]

Value range of θ, s	tgδ < (0,5 – 1) %	tgδ > (1 – 2) %
θ < (1 – 10)	Coupling	Coupling and cable
θ > (10 – 100)	Normal state	Cable

In the considered case, the self-discharge time constant of phase *C* is θ = 1.52 s; for phases *A* and *B*: θ = 12.14 s and 7.43 s, respectively.

Conclusions.

1. The established differences in the structure of the probing electric field in the types of paper impregnated electrical insulation made it possible to determine the share of energy accumulated in the phase, belt insulation and interphase space in the cable as a whole.

2. It has been proven that according to the inspection schemes «each of the three cores – against the grounded two others and the metal shell» and «three cores together – against the grounded shell», the probing electric field is concentrated mainly in the phase or belt insulation of the cable, respectively. This provided the basis for developing a methodology for determining the dielectric parameters of the types of electrical insulation – phase and belt insulation of power cables.

3. The methodology is based on solving a system of linear algebraic equations of the 6th order, which reflects the results of six cumulative measurements of the dielectric parameters of three-core power cables in a metal shell.

4. The results of the practical implementation of the developed methodology for assessing the differences in the properties of phase and belt insulation of NPP power cables and power network cables are presented.

5. The need to compare the results of diagnostic examinations on direct and alternating currents to increase the accuracy of assessing the technical condition of power cables with paper impregnated insulation in operation is argued.

Conflict of interest. The authors of the article declare no conflict of interest.

REFERENCES

1. Zapf M., Blenk T., Müller A.-C., Pengg H., Mladenovic I., Weindl C. Lifetime Assessment of PILC Cables with Regard to Thermal Aging Based on a Medium Voltage Distribution Network Benchmark and Representative Load Scenarios in the Course of the Expansion of Distributed Energy Resources. *Energies*, 2021, vol. 14, no. 2, art. no. 494. doi: https://doi.org/10.3390/en14020494.

2. *Assessing and Managing Cable Ageing in Nuclear Power Plants*. IAEA Nuclear Energy Series, No. NP-T-3.6. Vienna, IAEA, 2012. 96 p.

3. Šimić Z., Peinador Veira M., Banov R. Correlation between events with different safety significance in nuclear power plants. *Nuclear Engineering and Technology*, 2022, vol. 54, no. 7, pp. 2510-2518. doi: https://doi.org/10.1016/j.net.2022.01.034.

4. Hettal S., Suraci S.V., Roland S., Fabiani D., Colin X. Towards a Kinetic Modeling of the Changes in the Electrical Properties of Cable Insulation during Radio-Thermal Ageing in Nuclear Power Plants. Application to Silane-Crosslinked Polyethylene. *Polymers*, 2021, vol. 13, no. 24, art. no. 4427. doi: https://doi.org/10.3390/polym13244427.

5. *Ageing Management for Nuclear Power Plants: International Generic Ageing Lessons Learned (IGALL)*. IAEA Safety Reports Series, no. 82 (rev. 1). Vienna, IAEA, 2020. 120 p.

6. *Equipment Qualification for Nuclear Installations*. IAEA Specific Safety Guides, no. SSG-69, Vienna, 2021. 53 p.

7. Bezprozvannych G., Moskvitin Y. Aging management of cables of nuclear power plants. *Energy Saving. Power Engineering. Energy Audit*, 2022, no. 11-12 (177-178), pp. 21-33. (Ukr). doi: https://doi.org/10.20998/2313-8890.2022.11.02.

8. Mazzanti G., Montanari G.C., Dissado L.A. Electrical aging and life models: the role of space charge. *IEEE Transactions on*

Dielectrics and Electrical Insulation, 2005, vol. 12, no. 5, pp. 876-890. doi: https://doi.org/10.1109/TDEI.2005.1522183.
9. *Cable ageing in nuclear power plants report on the first and second terms (2012-2017) of the NEA cable ageing data and knowledge (CADAK) project*. Vienna, IAEA, 2018. 60 p.
10. Shaalan E.M., Ward S.A., Youssef A. Analysis of a Practical Study for Under-Ground Cable Faults Causes. *2021 22nd International Middle East Power Systems Conference (MEPCON)*, 2021, vol. 208-215. doi: https://doi.org/10.1109/MEPCON50283.2021.9686288.
11. Klimenta J., Panic M., Stojanovic M., Klimenta D., Milovanovic M., Perovic B. Thermal aging management for electricity distribution networks: FEM-based qualification of underground power cables. *Thermal Science*, 2022, vol. 26, no. 4 Part B, pp. 3571-3586. doi: https://doi.org/10.2298/TSCI220128050K.
12. Mustafa E., Afia R.S.A., Nouini O., Tamus Z.A. Implementation of Non-Destructive Electrical Condition Monitoring Techniques on Low-Voltage Nuclear Cables: I. Irradiation Aging of EPR/CSPE Cables. *Energies*, 2021, vol. 14, no. 16, art. no. 5139. doi: https://doi.org/10.3390/en14165139.
13. Kim J., Kim W., Park H.-S., Kang J.-W. Lifetime Assessment for Oil-Paper Insulation using Thermal and Electrical Multiple Degradation. *Journal of Electrical Engineering and Technology*, 2017, vol. 12, no. 2, pp. 840-845. doi: https://doi.org/10.5370/JEET.2017.12.2.840.
14. Mladenovic I., Weindl C. Artificial aging and diagnostic measurements on medium-voltage, paper-insulated, lead-covered cables. *IEEE Electrical Insulation Magazine*, 2012, vol. 28, no. 1, pp. 20-26. doi: https://doi.org/10.1109/MEI.2012.6130528.
15. Carrascal I.A., Fernández-Diego C., Casado J.A., Diego S., Fernández I., Ortiz A. Quantification of Kraft paper ageing in mineral oil impregnated insulation systems through mechanical characterization. *Cellulose*, 2018, vol. 25, no. 6, pp. 3583-3594. doi: https://doi.org/10.1007/s10570-018-1788-1.
16. Bezprozvannych G.V., Moskvitin Y.S. Physical Processes of Aging and Assessment of the Technical Condition of Power Cables with Paper-Impregnated Insulation. *2023 IEEE 4th KhPI Week on Advanced Technology (KhPIWeek)*, 2023, pp. 1-5. doi: https://doi.org/10.1109/KhPIWeek61412.2023.10312975.
17. Basu D., Gholizad B., Ross R., Gargari S.M. Thermal Aging-Based Degradation Parameters Determination for Grid-Aged Oil Paper Insulation. *IEEE Transactions on Dielectrics and Electrical Insulation*, 2023, vol. 30, no. 2, pp. 734-743. doi: https://doi.org/10.1109/TDEI.2022.3217434.
18. Kiger C.J., Hashemian H.M., Sexton C.D., Toll T.A. Research gap in management of insulation aging of medium voltage cables in nuclear power plants. *Transactions of the American Nuclear Society*, 2018, vol. 118, no. 1, pp. 593-594.
19. Kim J-S., Lee D.-J. Evaluation of nuclear plant cable aging through condition monitoring. *Nuclear Engineering and Technology.* 2004, vol. 36, no. 5, pp. 474-475.
20. Fabiani D., Suraci S.V., Bulzaga S. Aging Investigation of Low-Voltage Cable Insulation Used in Nuclear Power Plants. *2018 IEEE Electrical Insulation Conference (EIC)*, 2018, pp. 516-519. doi: https://doi.org/10.1109/EIC.2018.8481139.
21. Shafiq M., Kauhaniemi K., Robles G., Isa M., Kumpulainen L. Online condition monitoring of MV cable feeders using Rogowski coil sensors for PD measurements. *Electric Power Systems Research*, 2019, vol. 167, pp. 150-162. doi: https://doi.org/10.1016/j.epsr.2018.10.038.
22. Bezprozvannych G.V., Kostukov I.O., Moskvitin E.S. Differentiation of absorption processes in inhomogeneous insulation by curve of recovering voltage of power high voltage cables. *Technical electrodynamics*, 2021, no. 6, pp. 13-19. (Ukr). doi: https://doi.org/10.15407/techned2021.06.013.
23. Kyrylenko V.M., Kyrylenko K.V., Budko M.O., Denysiuk P.L. Reasoning of additional diagnostic parameters for electric insulation diagnostics by absorption methods. *Electrical Engineering & Electromechanics*, 2021, no. 6, pp. 39-45. doi: https://doi.org/10.20998/2074-272X.2021.6.06.
24. Bezprozvannych G.V., Moskvitin E.S., Kyessayev A.G. The absorption characteristics of the phase and zone paper-impregnated insulation of power cable at direct voltage. *Electrical Engineering & Electromechanics*, 2015, no. 5, pp. 63-68. (Rus). doi: https://doi.org/10.20998/2074-272X.2015.5.09.
25. Bezprozvannych G.V., Rudakov S.V., Moskvitin E.S. *Prevention of emergency situations by monitoring the state of insulation of multi-core cables according to the parameters of partial capacitances and tangent of dielectric losses*. *Monograph*. Kharkiv, 2013. 165 p. (Rus).
26. Kostiukov I. Measurement of Dissipation Factor of Inner Layers of Insulation in Three-Core Belted Cables. *Lighting Engineering & Power Engineering*, 2021, vol. 60, no. 1, pp. 23-30. doi: https://doi.org/10.33042/2079-424X.2021.60.1.04.
27. Cherukupalli S., Buchholz V., Colwell M., Crine J.-P., Keefe R.J. Condition assessment of distribution PILC cables from electrical, chemical, and dielectric measurements. *IEEE Electrical Insulation Magazine*, 2004, vol. 20, no. 4, pp. 6-12. doi: https://doi.org/10.1109/MEI.2004.1318834.
28. Cichecki P., Gulski E., Smit J.J., van Nes P., Ejigu A.G., de Vries F. Dielectric losses diagnosis of serviced aged oil impregnated paper insulation of HV power cables. *2009 IEEE Electrical Insulation Conference*, 2009, pp. 216-219. doi: https://doi.org/10.1109/EIC.2009.5166348.
29. Kim S.-J., Lee S., Choi W.-S., Lee B.-W. Experimental and Simulation Studies on Stable Polarity Reversal in Aged HVDC Mass-Impregnated Cables. *Energies*, 2024, vol. 17, no. 10, art. no. 2352. doi: https://doi.org/10.3390/en17102352.
30. Florkowski M., Kuniewski M., Mikrut P. Effects of mechanical transversal bending of power cable on partial discharges and dielectric-loss evolution. *IEEE Transactions on Dielectrics and Electrical Insulation*, 2024, pp. 1-1. doi: https://doi.org/10.1109/TDEI.2024.3382642.
31. Rowland S., Wang M. Fault Development in Wet, Low Voltage, Oil-Impregnated Paper Insulated Cables. *IEEE Transactions on Dielectrics and Electrical Insulation*, 2008, vol. 15, no. 2, pp. 484-491. doi: https://doi.org/10.1109/TDEI.2008.4483468.
32. Hakonseth G., Ildstad E., Furuheim K.M. Local Electric Field in Mass-Impregnated HVDC Cables. *Proceedings of the Nordic Insulation Symposium*, 2017, no. 25. doi: https://doi.org/10.5324/nordis.v0i25.2351.
33. Borghetto J., Pirovano G., Tornelli C., Contin A. Frequency Dielectric Spectroscopy and Dissipation Factor Measurements during Thermal Cycles on Different Types of MV Cable Joints. *2021 IEEE Electrical Insulation Conference (EIC)*, 2021, pp. 441-446. doi: https://doi.org/10.1109/EIC49891.2021.9611379.
34. Besprozvannych A.V., Naboka B.G., Moskvitin E.S. Inspection of the insulation of three-phase cables in a metal sheath. *Electricity*, 2010, no. 1, pp. 48-54. (Rus).
35. Besprozvannych A.V., Naboka B.G. The influence of parasitic capacitances on the results of measurements of parameters of multi-core cables when assessing their technical condition. *Electricity*, 2011, no. 5, pp. 27-36. (Rus).
36. Bezprozvannych G.V., Moskvitin E.S. Estimation criteria for degree of paper-impregnated insulated power cable ageing. *Electrical Engineering & Electromechanics*, 2013, no. 4, pp. 32-36. (Rus).
37. Su J., Wei L., Zhang P., Li Y., Liu Y. Multi-type defect detection and location based on non-destructive impedance

spectrum measurement for underground power cables. *High Voltage*, 2023, vol. 8, no. 5, pp. 977-985. doi: https://doi.org/10.1049/hve2.12331.

38. Neimanis R., Eriksson R., Papazyan R. Diagnosis of Moisture in Oil/Paper Distribution Cables – Part II: Water Penetration in Cable Insulation–Experiment and Modeling. *IEEE Transactions on Power Delivery*, 2004, vol. 19, no. 1, pp. 15-20. doi: https://doi.org/10.1109/TPWRD.2003.820430.

39. Neimanis R., Eriksson R. Diagnosis of Moisture in Oil/Paper Distribution Cables – Part I: Estimation of Moisture Content Using Frequency-Domain Spectroscopy. *IEEE Transactions on Power Delivery*, 2004, vol. 19, no. 1, pp. 9-14. doi: https://doi.org/10.1109/TPWRD.2003.820417.

40. Bonanno R., Lacavalla M. A feasibility analysis aimed at defining an alert system for Distribution MV Underground Cables. *2020 AEIT International Annual Conference (AEIT), 2020*, pp. 1-6. doi: https://doi.org/10.23919/AEIT50178.2020.9241134.

41. Naboka B.G., Bezprozvannych A.V., Moscvitin E.S., Bytko M.V., Bytko S.M., Golovan A.A. Diagnostics of power system cable lines on dielectric dissipation factor and impregnated-paper insulation self-discharge time constant. *Electrical Engineering & Electromechanics.* 2011. no. 2. pp. 65-69. (Rus).

Received 14.09.2024
Accepted 14.11.2024
Published 02.03.2025

G.V. Bezprozvannych[1]*, Doctor of Technical Science, Professor,*
Y.S. Moskvitin[1]*, PhD,*
I.O. Kostiukov[1]*, Doctor of Technical Science, Assistant Professor,*
O.M. Grechko[1]*, PhD, Assistant Professor,*
[1] National Technical University «Kharkiv Polytechnic Institute», 2, Kyrpychova Str., Kharkiv, 61002, Ukraine,
e-mail: Hanna.Bezprozvannukh@khpi.edu.ua (Corresponding Author),
yevhen.moskvitin@khpi.edu.ua; ivan.kostiukov@khpi.edu.ua; a.m.grechko@gmail.com

How to cite this article:
Bezprozvannych G.V., Moskvitin Y.S., Kostiukov I.O., Grechko O.M. Dielectric parameters of phase and belt paper impregnated insulation of power cables. *Electrical Engineering & Electromechanics*, 2025, no. 2, pp. 69-78. doi: https://doi.org/10.20998/2074-272X.2025.2.09

UDC 621.319 https://doi.org/10.20998/2074-272X.2025.2.10

T.K. Nurubeyli, A.M. Hashimov, N.E. Imamverdiyev, G.N. Mammadova

Complex physicochemical analysis of transformer oil parameters using the inductively coupled plasma mass spectrometry technique

Introduction. *Transformers are crucial and expensive components of power systems, experiencing electrical, thermal, and chemical stresses. Transformer oil analysis is important for diagnosing transformer faults and assessing its remaining service life. The oil used in transformers degrades over time due to its interaction with electrical loads and heat from the core and windings. The oil degrades into low-molecular gases and carbon particles, which affect its dielectric properties and indicate potential problems. Analysis of dissolved gases in oil allows early detection of defects such as corona or arc discharges, as well as overheating. In addition, analysis of metal content in oil helps to clarify the type and location of the fault identified by gas analysis.* ***Novelty*** *of the proposed work lies in the study of the relationship between transformer oil parameters and its quality, as well as the effect of dissolved gases. The article proposes a method for determining how changes in these parameters affect each other. The obtained data are compared with the results of mass spectrometric analysis for a more accurate assessment of the transformer condition.* ***The purpose*** *of this paper is to explore the connection between the chemical properties of transformer oil and the elemental composition determined through inductively coupled plasma mass spectrometry (ICP-MS).* ***Methods.*** *The solution to the problem was carried out using the inductively coupled plasma mass spectrometry method from Agilent Technologies 7700e (USA) to measure the concentration of metals in transformer oil.* ***Results.*** *An inverse correlation has been identified between the acidity of transformer oil and its furfural content. Experimental evidence has shown that the water content has the most significant impact on decreasing the breakdown voltage of dielectric oil. It was found that CO gas has the greatest influence on the formation of furfural. It has been established that gaseous C_2H_2 plays an important role in the formation of acidic components. Correlations were found between the oil acidity and the concentrations of copper and iron and between the breakdown voltage and the amount of lead and aluminium in the transformer oil. A high concentration of copper in the oil indicates potential issues with the transformer windings, as well as in any bronze or brass components, and the concentration of iron in significant quantities indicates problems with the transformer core and tank. Moreover, as the breakdown voltage of the oil decreases, there is a marked increase in the concentrations of lead and aluminum. This suggests that significant amounts of lead are found in the transformer solder joints, while aluminum is present in the windings and ceramic bushings.* ***Practical value.*** *The advantage of the mass spectrometric method for detecting metals in transformer oils is the ability to accurately determine the type of fault and diagnose transformer problems. Research shows that this method allows early detection of potential problems and predicts the condition of the transformer.* References 21, table 2, figures 8.

Key words: **transformer oil, furfural component, breakdown voltage, mass spectrometer, dissolved gases analysis.**

Вступ. *Трансформатори є важливими та коштовними компонентами енергосистем, які зазнають електричних, теплових та хімічних навантажень. Аналіз трансформаторної оливи важливий для діагностики несправностей трансформатора та оцінки його терміну служби, що залишився. Олива, що використовується в трансформаторах, з часом руйнується через його взаємодію з електричними навантаженнями та теплом сердечника та обмоток. Олива розкладається на низькомолекулярні гази та частинки вуглецю, що впливає на її діелектричні властивості та вказує на потенційні проблеми. Аналіз розчинених газів у оливі дозволяє завчасно виявити дефекти, такі як коронний або дуговий розряд, а також перегрів. Крім того, аналіз вмісту металу в оливі допомагає уточнити тип і місце дефекту, виявленого газовим аналізом.* ***Новизна*** *пропонованої роботи полягає у вивченні зв'язку між параметрами трансформаторної оливи та її якістю, а також впливом розчинених газів. У статті запропоновано метод визначення того, як зміни цих параметрів впливають одна на одну. Отримані дані порівнюються з результатами мас-спектрометричного аналізу для більш точної оцінки стану трансформатора.* ***Метою*** *статті є дослідження зв'язку між хімічними властивостями трансформаторної оливи та елементним складом, визначеним за допомогою мас-спектрометрії з індуктивно зв'язаною плазмою (ICP-MS).* ***Методи.*** *Рішення проблеми здійснювалося за допомогою методу мас-спектрометрії з індуктивно зв'язаною плазмою Agilent Technologies 7700e (США) для вимірювання концентрації металів у трансформаторній оливі.* ***Результати.*** *Між кислотністю трансформаторної оливи та вмістом у ній фурфуролу виявлено зворотну залежність. Експериментальні дані показали, що вміст води має найбільш значний вплив на зниження напруги пробою діелектричної оливи. Встановлено, що найбільший вплив на утворення фурфуролу має газ CO. Встановлено, що в утворенні кислотних компонентів важливу роль відіграє газоподібний C_2H_2. Були виявлені кореляції між кислотністю оливи та концентрацією міді та заліза, а також між напругою пробою та кількістю свинцю та алюмінію в трансформаторній оливі. Високий вміст міді в оливі вказує на потенційні проблеми з обмотками трансформатора, а також у будь-яких бронзових або латунних компонентах, а концентрація заліза в значних кількостях вказує на проблеми з сердечником трансформатора та баком. Крім того, у міру зниження напруги пробою оливи спостерігається помітне збільшення концентрації свинцю та алюмінію. Це свідчить про те, що значна кількість свинцю міститься в паяних з'єднаннях трансформатора, тоді як алюміній присутній в обмотках і керамічних втулках.* ***Практична цінність.*** *Перевагою мас-спектрометричного методу виявлення металів у трансформаторній оливі є можливість точного визначення типу несправності та діагностики проблем трансформатора. Дослідження показують, що цей метод дозволяє завчасно виявляти потенційні проблеми та прогнозувати стан трансформатора.* Бібл. 21, табл. 2, рис. 8.

Ключові слова: **трансформаторна олива, фурфуроловий компонент, пробивна напруга, мас-спектрометр, аналіз розчинених газів.**

Introduction. By sampling transformer oil and conducting various tests, it is possible to diagnose numerous faults in the transformer and evaluate its remaining service life and overall condition. Transformer oils, like most insulating and dielectric materials, decompose and deteriorate during prolonged use. This is attributed to the oil's role in resisting electrical loads and facilitating heat transfer from the core and windings. The condition of dielectric oil is influenced by contamination, its type, and the presence of acidic compounds like metal sulfide particles. Besides chemical degradation, dielectric oil also deteriorates due to physical contamination. When exposed to partial discharges, electrical arcs, and rising temperatures, dielectric oil breaks down into low molecular weight gases that dissolve in the oil, along with

carbon particles. The behavior of each type of insulation oil is influenced by the way carbon particles are transformed. Hence, analyzing dielectric oil is crucial for assessing the condition of a transformer and identifying its potential issues [1, 2].

Dissolved gas analysis (DGA) in insulation oil is a reliable method for detecting transformer faults early. These are typically used in transformers hydrocarbon (mineral) oils or silicones as insulating fluids because of their superior dielectric properties, heat transfer efficiency, and stability. These insulating fluids typically undergo minimal decomposition under normal conditions. However, damage can lead to the degradation of both the liquid and solid insulation materials [3]. Gases like H_2 (hydrogen), CH_4 (methane), C_2H_4 (ethane), C_2H_2 (acetylene), CO (carbon monoxide), and CO_2 (carbon dioxide) can dissolve in transformer oil, indicating decomposition caused by thermal or electrical stresses. Quantitative examination of these gases can help in detecting issues like corona, arc, spark discharge, and oil overheating, all of which can impact the transformer's operational lifespan. Furthermore, analysing metals in transformer oil supports dissolved gas analysis by specifying the nature and source of potential problems identified through gas analysis [4, 5].

High-energy faults not only damage transformer insulation materials like oil, paper, and wood but also generate metal particles that disperse into the oil. These particles can subsequently circulate throughout the transformer, mainly through the oil flow. Different components of a transformer produce distinct types of metal particles, which can manifest individually or in various compounds, and may appear in different concentrations. Identifying these particles can help narrow down the potential components contributing to failures [6].

Common metals found in transformer oil include aluminum, copper, iron, lead, silver, tin, and zinc. Two techniques used to analyze these metals in oil are mass spectrometry with inductively coupled plasma (ICP-MS) and mass spectrometry with atomic absorption. The amounts of metals in the oil must be measured using these techniques. Typically, the metal atoms in a sample are liberated by high temperature burning of the metal particles, making them amenable to accurate examination via these methods. The presence of these atoms in an atomic absorption flame or inductively coupled plasma can be determined by measuring discrete frequency absorption or positive ion emission (ICP) from the atoms, as well as the metal's ion concentration and composition. The Agilent Technologies 7700e inductively coupled plasma mass spectrometer was used in this study [7, 8].

Recently, ICP-MS has been gradually replacing flame atomic absorption spectrometry due to the significantly greater availability and performance of modern equipment while maintaining undoubted advantages, including the ability to record low detection limits for chemical elements and isotopes, down to ng/l and occasionally even pg/l levels, low consumption of the analyze, the ability to conduct multielement analysis, and high sensitivity and resolution of the analyser [9–11].

In previous studies [3–5, 12], the quality of transformer oil and the DGA have been individually investigated and quantified as parameters for assessing transformer performance or diagnosing malfunctions. However, these works did not explore the interdependencies between the electrical and physicochemical parameters of transformer oils.

The goal of the paper to approach the study of how changes in transformer oil parameters affect each other, as well as the effect of dissolved gases on oil quality. In addition, the study compares these parameters with data obtained by mass spectrometry, which serves as a criterion for assessing the condition of transformers

Materials and methods. The research used a mass spectrometer with inductively coupled plasma (Agilent Technologies 7700e, USA) to measure and assess the concentrations of metals in the transformer oil (Fig. 1) [7].

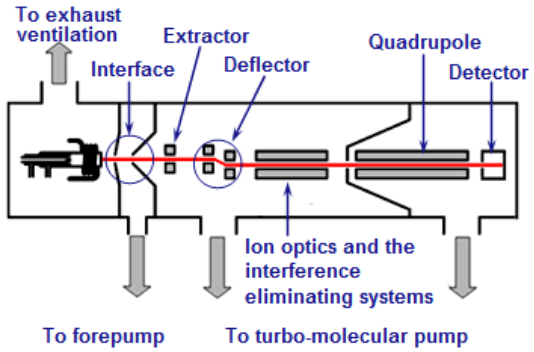

Fig. 1. Diagram of the ICP-MS Agilent 7700e [7]

To mineralize the samples, a «Speedwave Xpert» microwave system (Germany) equipped with small-volume vessels for working with microsamples was used to control the temperature (Table 1). Dispensers with volumes ranging from 100 to 1000 l and 1 to 10 ml, made by Pipet4u and Eppendorf (Germany), along with disposable tips and polypropylene tubes with capacities of 15 and 50 ml, were utilized.

Table 1

Procedure for microwave decomposition of transformer oil

Reagents	Acid		Volume		
	HNO_3 (65 %)		8 ml		
Procedure	A 100 mg (0.1 ml) sample was added to the vessel, followed by the addition of 8 ml of HNO_3 for mineralization. The mixture was then thoroughly shaken or stirred with a clean Teflon or glass rod. Before sealing the vessel, it should be allowed to sit for at least 10 min before being heated in a microwave oven according to the specified program				
Program	Step	*T*, °C	*P*, bar	*t*, min	*P*, %
	1	145	80	10	80
	2	170	80	10	80
	3	190	80	20	90
	4	50	60	10	0

To mineralize the materials and generate calibration solutions, 65 % nitric acid (HNO_3) was utilized. Furthermore, a 30 % solution of hydrogen peroxide (H_2O_2) from Suprapur (Merck, Germany) was used to quickly dissolve the samples during mineralization. The

solutions were diluted using deionized water with a resistivity of 18.2 MΩ·cm. The instrument's calibration accuracy was verified by analyzing a standard sample of drinking water.

Chromatography was used to detect the amounts of gases dissolved in the oil (H_2, CO, CO_2, CH_4, C_2H_6, C_2H_4, C_2H_2, N_2, and O_2). This was accomplished using an automated KRISTALLUX-4000 M gas chromatograph, which featured both a flame ionization detector and a thermal conductivity detector.

Experiments. Figure 1 shows a diagram of the ICP-MS Agilent 7700 instrument. The measurements were carried out on an ICP-MS system from Agilent Technologies 7700e (USA) under stable operating conditions [7–9]. The ICP-MS method is based on the use of an argon ICP as an ion source and a quadrupole mass spectrometer.

Figure 1 shows a diagram of the main parts of the instrument using an Agilent 7700e ICP-MS instrument as an example. The sample introduction system included a peristaltic pump, an atomizer, and a spray chamber. The solution of the studied substance was removed by a peristaltic pump at a speed of 0.1 ml/min. An aerosol was obtained from the sample solution and passed through a two-pass spray chamber. The fine aerosol obtained from the sample (leaving the spray chamber) directly enters a tube that directs the aerosol into a horizontally mounted plasma burner. The gas entering the three-cylinder plasma burner is called plasma, auxiliary gas, or carrier gas (supplied to the atomizer). A four-turn coil (inductor) is attached to the end of the burner, and a high-frequency signal (27.12 MHz) is supplied to it. After the plasma is enriched with electrons in a strong high-frequency field, collisions of argon atoms are ensured (i.e., plasma «combustion» is supported). At the plasma centre, the temperature reaches the range of 8000 to 10000 K. The aerosolized sample is instantly freed from the solvent and ionized. Furthermore, a beam of ions from the analysed sample is formed and introduced into the mass spectrometer through a system of cones and lenses. The ions then entered the quadrupole analyser. Only ions with a specific mass-to-charge ratio (m/z) can pass through the centre of the quadrupole under a specific combination of applied voltages.

The quadrupole provides a very fast (sawtooth) change in voltage because it can scan the entire mass range (from 2 to 260 Da) in 100 ms. As a result, mass spectra displaying the intensity vs. mass can be recorded for all elements virtually simultaneously. After passing through the quadrupole, the ions are detected by an electron multiplier. Table 2 shows some ICP-MS data from the experiments.

Table 2

Experimental mode

Plasma, generator power, W	1450
Argon flow rate, l/min	1.2
Sample supply rate, l/min	1
Mass-spectrometer resolution, Da	0.2
Vacuum without plasma, Torr	$4 \cdot 10^{-4}$
Dynamic cell, gas	Helium
Time of measurement, s	0.1–0.5

Results and discuss. The analytical findings from 50 transformers, which included dissolved gases, oil quality parameters, and metals in the oil, were utilized to determine the change or departure of oil quality parameters from one another to evaluate the transformer's performance and early diagnosis. The top results were chosen from 30 different analyses.

Carbon monoxide (CO) and carbon dioxide (CO_2) emissions found in transformer oil are indicative of a malfunction that may cause the deterioration and breakdown of paper insulation. The gases that indicate transformer overload include ethane (C_2H_6), ethylene (C_2H_4), and methane (CH_4). Acetylene gas (C_2H_2) indicates that there may have been an arc inside the transformer, which could have been brought on by a tap changer contact failure that resulted in internal shorts. The concurrent presence of methane, ethane, ethylene, carbon monoxide, and carbon dioxide gases (CH_4, C_2H_6, C_2H_4, CO and CO_2) in the dielectric oil signals the combustion of the transformer's paper insulation. The presence of hydrogen indicates the formation of partial discharges, and this gas is produced in most types of faults [13–15].

Transformer oil always contains oxygen, which leads to the formation of the gases CO and CO_2 and acidity. As the temperature rises in the transformer, oxide and acid components trigger a hydrolysis reaction, leading to the decomposition of the paper insulation. Conversely, overheating the oil also breaks down the paper insulation molecules, resulting in pyrolysis. The products of hydrolysis and pyrolysis react to form furfural, which is generated from oxygen, acid, moisture, as well as CO and CO_2 gases. The cause of transformer oil and paper insulation degradation is the acid, moisture and oxygen contained in furfural [16–19].

Figure 2 illustrates the inverse relationship between the furfural component, which forms from the degradation of the transformer's paper insulation, and the acid component. Figure 2 shows that a 1 ppm increase in the acid component results in a 0.6 ppm decrease in the furfural component. The primary causes of acid formation in transformer oil are oxygen and oil oxidation. The degradation of transformer paper insulation and the formation of furfural are attributed to processes involving oxygen, hydrolysis, and pyrolysis [20]. Figure 2 clearly demonstrates that the concentration of furfural decreases as the acid content in the transformer oil increases.

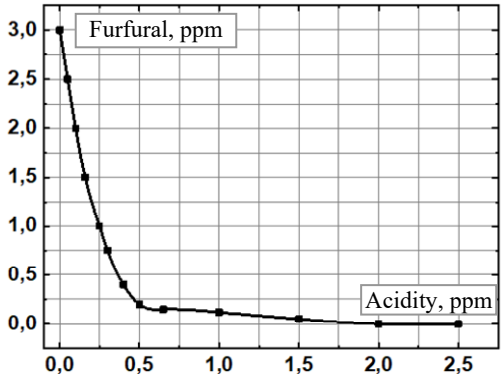

Fig. 2. Relationship between acid and furfural components of transformer oil

The dependence of furfural on the water content of the oil is depicted in Fig. 3. Apart from ambient moisture, the hydrolysis of paper insulation results in the creation of moisture within the insulating oil. As the temperature

increases, these bubbles evolve into partial discharge and hydrogen production [21].

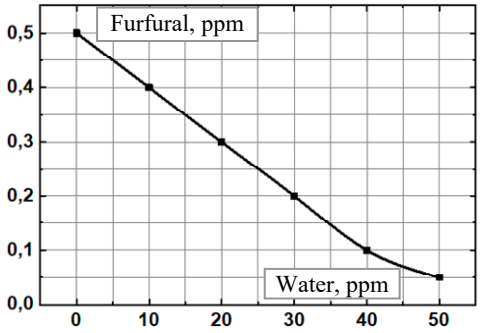

Fig. 3. Variation in furfural content with water content

Carbon monoxide is a gas produced during the decomposition of transformer paper insulation and has the most significant impact on the furfural component. Figure 4 shows that at low CO concentrations, the furfural content in the transformer oil does not change. However, as the heat increases and the paper insulation degrades, the carbon dioxide content increases, which increases the furfural content. The furfural component is a key parameter for assessing the degree of polymerization and estimating the remaining service life of transformer paper insulation.

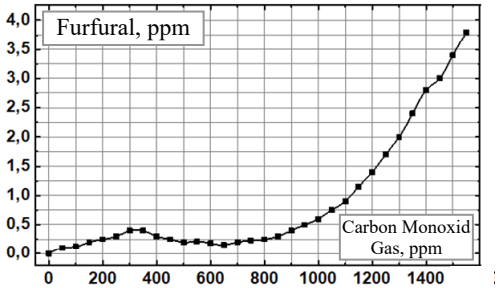

Fig. 4. Dependence of furfural on carbon monoxide

The breakdown voltage of transformer oil is a crucial indicator of its quality, reflecting its dielectric strength against factors such as arcing. The parameter exerting the most significant influence on this breakdown voltage is the water content. As the water content increases, the electrical conductivity of the oil also increases, thereby reducing its dielectric strength against electrical stress. Specifically, the breakdown voltage of the oil decreases by 1 kV for every increase of 1 ppm in water content.

Figure 5 illustrates the relationship between the concentration of copper and iron and the acidity of transformer oil. The data from the figure show that as the acidity of the oil increases, there is an exponential increase in the concentration of these metals. This confirms the correlation between oil acidity levels and the accumulation of metals such as copper and iron, which can indicate transformer issues.

Oil acidity is a critical parameter that directly affects its quality and operational safety. When the oil acidity exceeds 1 ppm, active corrosion of transformer components such as the core, windings, and tank occurs. This corrosion leads to the formation of iron and copper particles in the oil.

Copper can be found in the windings or in components made of bronze or brass, while iron is present in the core and tank of the transformer. These particles can result in significant transformer malfunctions, such as decreased electrical strength and increased risk of short circuits.

To determine the breakdown voltage of the oil, which can serve as an indicator of its contamination and degradation, a standard test cell is used. The breakdown voltage is measured according to the international standard IEC 60156, which describes the testing methodology and result interpretation. This standard allows for an objective assessment of transformer oil quality and its suitability for continued use.

Thus, the data in Figure 5 highlight the importance of monitoring oil acidity and regularly analyzing its composition to ensure the reliability and safety of transformer operation.

Threshold levels for metals in transformer oil are not universally established, but accumulating data and documented cases are making metal analysis in oil an increasingly valuable tool for the early detection of transformer faults before they escalate into serious issues. Relying on a single report for metal analysis is insufficient to fully assess the transformer's condition; establishing correlations between transformer oil parameters and elemental analysis obtained through techniques such as ICP-MS is crucial for a comprehensive understanding.

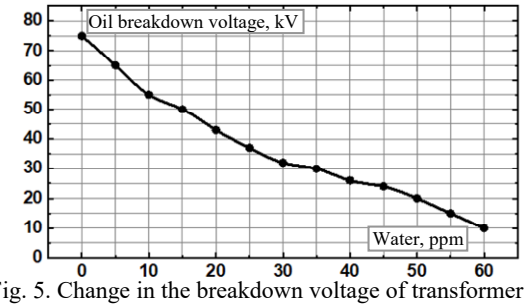

Fig. 5. Change in the breakdown voltage of transformer oil relative to the water content

Significant levels of iron and copper were detected in oils with acidity levels higher than 1 ppm. In fact, corrosion of several parts, including the transformer's core, windings, and tank, occurs as the acidity of the oil increases. As a result, iron and copper particles accumulate in the oil, causing transformer failure. Figure 6 illustrates how the amounts of iron and copper increase exponentially with the acidity of the oil. Iron is present in a transformer's core and tank, while copper is present in the windings and other bronze or brass components.

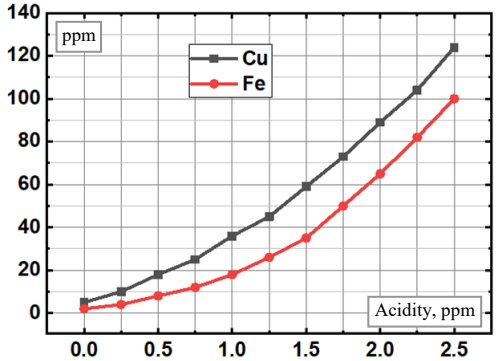

Fig. 6. Dependence of the acidity of transformer oil on the concentration of copper and iron

The primary factor affecting the transformer's performance the most is the variation in oil breakdown voltage. This is mainly influenced by the presence of contaminants and foreign particles in the dielectric oil,

which decreases both the breakdown voltage and the insulation effectiveness. Among these factors, the presence of water in the oil has the most significant impact on the breakdown voltage. According to findings in the literature, higher water content correlates directly with a reduced service life of the transformer. The value of furfural decreases with increasing temperature since the concentration of furfural is inversely related to the level of the acid component. CO_2 and CO gases have the greatest impact on transformer performance. These gases are formed when the paper insulation of the transformer decomposes into transformer oil. C_2H_6 has the most significant impact on the water content of transformer oil. Additionally, the most influential component of oil acidity is C_2H_2 gas. The advantage of using a mass spectrometric method to detect metals in transformer oils is to determine the type of fault and accurately diagnose transformer problems.

Additionally, as the breakdown voltage of the oil decreases, the concentrations of lead and aluminium increase sharply due to the decomposition of the dielectric oil under the influence of electrical voltage. The presence of particles like iron filings and impurities in dielectric oil leads to a reduction in both its breakdown voltage and dielectric strength. Figure 7 shows that at lower breakdown voltages, the concentrations of aluminium and lead increase significantly. Lead is commonly found in solder joints, connectors, and other ancillary components of transformers, while aluminum is present in the windings and ceramic bushings.

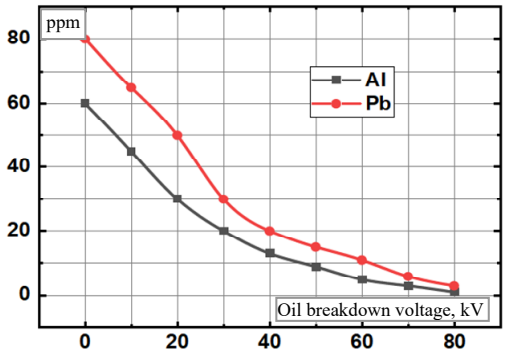

Fig. 7. Dependence of the oil breakdown voltage on the aluminium and lead concentrations

Elemental analysis of several oils revealed the presence of tin, silver, and zinc. It was experimentally revealed that a high concentration of water in the oil leads to partial discharge, which in turn increases the electrical conductivity of the oil, and sparking occurs, leading to the failure of several components of the transformer. Figure 8 shows that with a high concentration of water in the transformer oil, the concentrations of tin, silver, and zinc increase.

Tin, silver, and zinc may be present in the terminal, bolts, connectors and some peripheral components of the transformer, and their presence in the oil indicates failure of these components.

According to the findings, increasing acidity in transformer oil causes exponential increases in copper and iron concentrations. Copper levels above normally indicate problems with bronze or brass windings and components. Significant iron concentrations suggest difficulties with the transformer's core and tank, whereas large levels of aluminum indicate problems with the ceramic bushing. Tin, silver, and zinc concentrations in the oil usually indicate wear on the tips and bolts. A significant amount of lead suggests that there may be difficulties with the transformer's solder joints, connectors, and peripheral components.

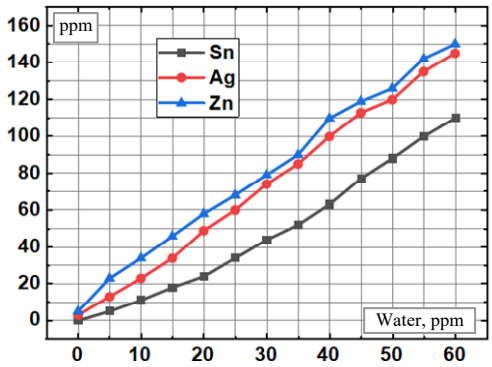

Fig. 8. Dependence of the amount of water in oil on the concentration of tin, silver, and zinc

Conclusions. The analysis revealed a significant correlation between moisture concentration, aluminum, lead, and the breakdown voltage of transformer oil. At equal concentrations, aluminum has a more pronounced effect on the breakdown voltage of the oil compared to lead.

Experimental studies have established a positive correlation between moisture content and the concentrations of tin, silver, and zinc in high-voltage transformer oil. The most critical factor affecting transformer performance is the change in the oil's breakdown voltage. The presence of particles and impurities in the oil reduces the breakdown voltage and, consequently, the insulation strength of the oil.

The most significant factor influencing the breakdown voltage is the water content in the oil. Therefore, water content is the key parameter that greatly reduces the transformer's lifespan, which aligns with previous research findings. Furfuryl alcohol is inversely proportional to oil acidity: as acidity increases, furfuryl alcohol decreases. Gases like CO_2 and CO have a major impact on transformer performance since they are formed during the decomposition of paper insulation. The gas C_2H_6 has the greatest influence on the oil's water content, while the gas C_2H_2 most significantly affects oil acidity.

The use of mass spectrometry for detecting metals in transformer oil allows for precise fault diagnosis and identification. Research indicates that with increasing oil acidity, the concentration of copper and iron rises exponentially. High levels of copper suggest issues with windings or components made of bronze or brass, while significant iron concentrations point to problems with the transformer core and tank. Aluminum is typically associated with ceramic bushings, while the presence of tin, silver, and zinc indicates wear on terminals and bolts. Elevated lead levels can indicate problems with soldered connections, connectors, and other peripheral components.

Conflict of interest. The authors declare that there is no conflict of interest.

REFERENCES

1. Somekawa T., Fujita M., Izawa Y., Kasaoka M., Nagano Y. Furfural analysis in transformer oils using laser raman spectroscopy. *IEEE Transactions on Dielectrics and Electrical*

Insulation, 2015, vol. 22, no. 1, pp. 229-231. doi: https://doi.org/10.1109/TDEI.2014.004800.
2. Zhang L., Sun L., Wu J., Han Y., Wang S., Yang C., Shen W., Guo C. Development of multi-parameter online monitoring equipment for EHV transformer bushing. *IET Science, Measurement & Technology*, 2020, vol. 14, no. 1, pp. 98-103. doi: https://doi.org/10.1049/iet-smt.2019.0262.
3. Faria G., Pereira M., Lopes G., Villibor J., Tavares P., Faria I. Evaluation of Capacitance and Dielectric Dissipation Factor of Distribution Transformers - Experimental Results. *2018 IEEE Electrical Insulation Conference (EIC)*, 2018, pp. 336-339. doi: https://doi.org/10.1109/EIC.2018.8481052.
4. Lundgaard L., Hansen W., Ingebrigtsen S. Ageing of Mineral Oil Impregnated Cellulose by Acid Catalysis. *IEEE Transactions on Dielectrics and Electrical Insulation*, 2008, vol. 15, no. 2, pp. 540-546. doi: https://doi.org/10.1109/TDEI.2008.4483475.
5. Poliakov M.O., Vasylevskyi V.V. Method for assessing unevenness of cellulose insulation layers aging of power transformers winding. *Electrical Engineering & Electromechanics*, 2022, no. 5, pp. 47-54. doi: https://doi.org/10.20998/2074-272X.2022.5.08.
6. Hernanda I.G.N.S., Mulyana A.C., Asfani D.A., Negara I.M.Y., Fahmi D. Application of health index method for transformer condition assessment. *TENCON 2014 - 2014 IEEE Region 10 Conference*, 2014, pp. 1-6. doi: https://doi.org/10.1109/TENCON.2014.7022433.
7. Nurubeili T.K. Effect of Doubly Charged Ions in Forming the Mass Spectra of Solid-State Substances in a Mass Spectrometer with Inductively Coupled Plasma. *Surface Engineering and Applied Electrochemistry*, 2018, vol. 54, no. 4, pp. 395-400. doi: https://doi.org/10.3103/S1068375518040142.
8. Nurubeyli T.K., Jafar N.S., Mammadova G.N. Improving methods for sample preparation of biological fluids by inductively coupled plasma mass spectrometry. *International Journal of Mass Spectrometry*, 2025, vol. 507, art. no. 117355. doi: https://doi.org/10.1016/j.ijms.2024.117355.
9. Ahadzade S.M., Nurubeyli T.K., Quliyev E.Z., Sultanli A.N. Technological and electrophysical parameters of ZnO varistor with impurities. *International Journal on Technical and Physical Problems of Engineering*, 2023, vol. 15, no. 2, pp. 307-311.
10. Nurubeyli T.K. Coefficient of Relative Sensitivity in Mass Spectrometers with Inductively Coupled Plasma. *Inorganic Materials: Applied Research*, 2020, vol. 11, no. 3, pp. 552-557. doi: https://doi.org/10.1134/S2075113320030351.
11. Nurubeyli T.K., Zeynalov J.I., Mammadova G.N., Imamverdiyev N.E. Improving methods for sample preparation of transformer oils by ICP-MS. *International Journal on Technical and Physical Problems of Engineering*, 2024, vol. 16, no. 1, pp. 21-26.
12. Saeid M., Zeinoddini-Meymand H., Kamel S., Khan B. Interaction of transformer oil parameters on each other and on transformer health index using curve estimation regression method. *International Transactions on Electrical Energy Systems*, 2022, vol. 2022, art. no. 7548533. doi: https://doi.org/10.1155/2022/7548533.
13. Guo H., Guo L. Health index for power transformer condition assessment based on operation history and test data. *Energy Reports*, 2022, vol. 8, pp. 9038-9045. doi: https://doi.org/10.1016/j.egyr.2022.07.041.
14. Palchykov O.O. Breakdown voltage of micron range air inclusions in capacitor paper. *Electrical Engineering & Electromechanics*, 2020, no. 6, pp. 30-34. doi: https://doi.org/10.20998/2074-272X.2020.6.05.
15. Aizpurua J.I., Stewart B.G., McArthur S.D.J., Lambert B., Cross J.G., Catterson V.M. Improved power transformer condition monitoring under uncertainty through soft computing and probabilistic health index. *Applied Soft Computing*, 2019, vol. 85, art. no. 105530. doi: https://doi.org/10.1016/j.asoc.2019.105530.
16. Zeinoddini-Meymand H., Vahidi B. Health index calculation for power transformers using technical and economical parameters. *IET Science, Measurement & Technology*, 2016, vol. 10, no. 7, pp. 823-830. doi: https://doi.org/10.1049/iet-smt.2016.0184.
17. Zhang X., Gockenbach E. Asset-Management of Transformers Based on Condition Monitoring and Standard Diagnosis [Feature Article]. *IEEE Electrical Insulation Magazine*, 2008, vol. 24, no. 4, pp. 26-40. doi: https://doi.org/10.1109/MEI.2008.4581371.
18. Chen S., Chen Y., Yu N., Pang X., Zhang L., Han Z., Feng G., Jia Y., Xu T. Aging Analysis of Transformer Mineral Insulating Oil Based on Chromatographic Furfural Content Determination. *IOP Conference Series: Materials Science and Engineering*, 2019, vol. 493, art. no. 012069. doi: https://doi.org/10.1088/1757-899X/493/1/012069.
19. Vasilevskij V.V., Poliakov M.O. Reproducing of the humidity curve of power transformers oil using adaptive neuro-fuzzy systems. *Electrical Engineering & Electromechanics*, 2021, no. 1, pp. 10-14. doi: https://doi.org/10.20998/2074-272X.2021.1.02.
20. Jahromi A., Piercy R., Cress S., Service J., Fan W. An approach to power transformer asset management using health index. *IEEE Electrical Insulation Magazine*, 2009, vol. 25, no. 2, pp. 20-34. doi: https://doi.org/10.1109/MEI.2009.4802595.
21. Costa J.V., da Silva D.F.F., Branco P.J.C. Large-Power Transformers: Time Now for Addressing Their Monitoring and Failure Investigation Techniques. *Energies*, 2022, vol. 15, no. 13, art. no. 4697. doi: https://doi.org/10.3390/en15134697.

Received 28.07.2024
Accepted 02.10.2024
Published 02.03.2025

T.K. Nurubeyli [1], *Doctor of Physical Science, Professor,*
A.M. Hashimov[1], *Academician, Doctor of Technical Science, Professor,*
N.E. Imamverdiyev[2], *Master's Degree,*
G.N. Mammadova[3], *PhD,*
[1] Institute of Physics Ministry of Science and Education of the Republic of Azerbaijan, Baku, Azerbaijan,
e-mail: t.nurubeyli@physics.science.az (Corresponding Author); a.hashimov@physics.science.az
[2] Khazar University, Baku, Azerbaijan,
e-mail: omartarana@gmail.com
[3] Nakhichevan State University, Nakhichevan, Azerbaijan,
e-mail: gulsenmemmedova@ndu.edu.az

How to cite this article:
Nurubeyli T.K., Hashimov A.M., Imamverdiyev N.E., Mammadova G.N. Complex physicochemical analysis of transformer oil parameters using the inductively coupled plasma mass spectrometry technique. *Electrical Engineering & Electromechanics*, 2025, no. 2, pp. 79-84. doi: https://doi.org/10.20998/2074-272X.2025.2.10

Матеріали приймаються за адресою:
Кафедра "Електричні апарати", НТУ "ХПІ", вул. Кирпичева, 2, м. Харків, 61002, Україна
Електронні варіанти матеріалів по e-mail: a.m.grechko@gmail.com

Довідки за телефонами: +38 067 359 46 96 Гречко Олександр Михайлович

Передплатний індекс: 01216